LAWRENCE
LIVERMORE
NATIONAL
LABORATORY

LLNL-TH-432604

Spectroscopic Investigations of Highly Charged Tungsten Ions - Atomic Spectroscopy and Fusion Plasma Diagnostics

J. Clementson

May 18, 2010

Disclaimer

This work performed under the auspices of the U.S. Department of Energy by Lawrence Livermore National Laboratory under Contract DE-AC52-07NA27344.

Spectroscopic Investigations of Highly Charged Tungsten Ions

Atomic Spectroscopy
and
Fusion Plasma Diagnostics

Joel Clementson

Lund 2010

Atomic Physics Division
Department of Physics
Faculty of Engineering LTH
Lund University
Box 118, SE-221 00 LUND
SWEDEN

Lund Reports on Atomic Physics, ISSN 0281-2762
LRAP-417
ISBN 978-91-628-8132-0

Printed in Sweden by *Media-Tryck*, Lund
May 2010

To my grandfather B.G. Svanbom
in memoriam

Sammanfattning

Atomspektra har varit ett viktigt forskningsområde inom fysiken sedan mitten av 1800-talet. Då elektromagnetisk strålning, såsom synligt ljus, ultraviolett- och röntgenstrålning, är unik för varje grundämne ger ett observerat spektrum information om vilka slags atomer som emitterar strålningen. Exempelvis så visar spektra av ett vanligt lysrör att ljuset kommer från kvicksilveratomer och olika ädelgaser. Det som avslöjas av ett spektrum är dock inte bara ämnet som utsänder ljuset. Spektra innehåller också information om de strålande atomernas omgivning. Genom studier av atomspektra kan man därför mäta exempelvis temperaturer och tätheter hos stjärnor och andra objekt som avger strålning.

Denna avhandling behandlar spektroskopiska studier av högt joniserat volfram. Volfram är ett tungt grundämne som förekommer i många tekniska tillämpningar, ofta i komponenter som behöver vara värmetåliga. Ett område där volfram förväntas bli betydande är fusionsforskning. Inom kärnfusion förenas atomkärnor av väte till helium och i processen frigörs energi. Kärnfusion har därmed potential som energikälla. Men det är inte lätt att utveckla fusionskraftverk. För att få i gång fusionsreaktioner krävs nämligen temperaturer på hundratals miljoner grader. Att värma det så kallade plasmat till sådana temperaturer är en stor utmaning och att konstruera en reaktor som kan innesluta plasmat är ännu svårare. Det är här som volfram kommer in i bilden. Volfram, som har utmärkta värmeegenskaper, kan användas som konstruktionsmaterial i fusionsreaktorer. Man kan dock förvänta sig att volframpartiklar kommer lossna från väggarna av reaktorn och blandas med det heta plasmat. De höga temperaturerna gör att de flesta av volframatomernas elektroner slits loss och kvar blir då högt joniserade atomer. Dessa volframjoner avger mycket ultraviolett- och röntgenstrålning. Studerar man volframspektra från ett fusionsplasma kan man därför uppskatta mängden volfram i plasmat, hur varmt det är, vad det har för densitet, samt hur plasmat rör sig i reaktorn.

För att volfram ska kunna användas för plasmadiagnostik behöver man veta hur volframjonernas spektra ser ut. I detta arbete har därför volframspektra studerats i laboratoriet. Våglängder och intensiteter hos spektrallinjer har mätts och deras potentiella användning inom plasmadiagnostik undersökts. Dessa studier har kompletterats med beräkningar samt mätningar vid ett fusionsexperiment. I avhandlingen presenteras förslag på volframspektra för diagnostik under olika plasmaförhållanden.

Abstract

The spectra of highly charged tungsten ions have been investigated using x-ray and extreme ultraviolet spectroscopy. These heavy ions are of interest in relativistic atomic structure theory, where high-precision wavelength measurements benchmark theoretical approaches, and in magnetic fusion research, where the ions may serve to diagnose high-temperature plasmas.

The work details spectroscopic investigations of highly charged tungsten ions measured at the Livermore electron beam ion trap (EBIT) facility. Here, the EBIT-I and SuperEBIT electron beam ion traps have been employed to create, trap, and excite tungsten ions of M- and L-shell charge states. The emitted spectra have been studied in high resolution using crystal, grating, and x-ray calorimeter spectrometers. In particular, wavelengths of $\Delta n = 0$ M-shell transitions in K-like W^{55+} through Ne-like W^{64+}, and intershell transitions in Zn-like W^{44+} through Co-like W^{47+} have been measured. Special attention is given to the Ni-like W^{46+} ion, which has two strong electric-dipole forbidden transitions that are of interest for plasma diagnostics. The EBIT measurements are complemented by spectral modeling using the Flexible Atomic Code (FAC), and predictions for tokamak spectra are presented. The L-shell tungsten ions have been studied at electron-beam energies of up to 122 keV and transition energies measured in Ne-like W^{64+} through Li-like W^{71+}. These spectra constitute the physics basis in the design of the ion-temperature crystal spectrometer for the ITER tokamak.

Tungsten particles have furthermore been introduced into the Sustained Spheromak Physics Experiment (SSPX) spheromak in Livermore in order to investigate diagnostic possibilities of extreme ultraviolet tungsten spectra for the ITER divertor. The spheromak measurement and spectral modeling using FAC suggest that tungsten ions in charge states around Er-like W^{6+} could be useful for plasma diagnostics.

List of Publications

This dissertation is based on the following papers. They will be referred to in the text by their roman numbers. The papers are included in Part III.

I Grazing-incidence spectrometer on the SSPX spheromak
J. Clementson, P. Beiersdorfer, and E. W. Magee
Rev. Sci. Instrum. **79**(10), 10F538 (2008)

II Laboratory astrophysics, QED, and other measurements using the EBIT calorimeter spectrometer at LLNL
G. V. Brown, J. S. Adams, P. Beiersdorfer, J. Clementson, M. Frankel, S. M. Kahn, R. L. Kelly, C. A. Kilbourne, D. Koutroumpa, M. Leutenegger, F. S. Porter, D. B. Thorn, and E. Träbert
AIP Conf. Proc. **1185**(1), 446-449 (2009)

III High-resolution spectroscopy of $2s_{1/2}$ - $2p_{3/2}$ transitions in W^{65+} through W^{71+}
Y. Podpaly, J. Clementson, P. Beiersdorfer, J. Williamson, G. V. Brown, and M. F. Gu
Phys. Rev. A **80**(5), 052504 (2009)

IV Wavelength measurement of $n = 3$ to $n = 3$ transitions in highly charged tungsten ions
J. Clementson and P. Beiersdorfer
Phys. Rev. A, in press (2010)

V Spectroscopy of M-shell x-ray transitions in Zn-like through Co-like W
J. Clementson, P. Beiersdorfer, G. V. Brown, and M. F. Gu
Phys. Scr. **81**(1), 015301 (2010)

VI Theoretical spectra of Ge-like through V-like W ions
J. Clementson, P. Beiersdorfer, T. Brage, and M. F. Gu
work in progress (2010)

VII X-ray spectroscopy of E2 and M3 transitions in Ni-like W
J. Clementson, P. Beiersdorfer, and M. F. Gu
Phys. Rev. A **81**(1), 012505 (2010)

VIII EUV spectroscopy on the SSPX spheromak
J. Clementson, P. Beiersdorfer, M. F. Gu, H. S. McLean, and R. D. Wood
J. Phys. Conf. **130**, 012004 (2008)

IX Spectroscopy of multiply charged titanium ions in high-density magnetic fusion plasmas
J. H. T. Clementson, P. Beiersdorfer, and R. D. Wood
J. Phys. Conf. **163**, 012018 (2009)

X Tungsten spectroscopy relevant to the diagnostics of ITER divertor plasmas
J. Clementson, P. Beiersdorfer, E. W. Magee, H. S. McLean, and R. D. Wood
J. Phys. B: At. Mol. Opt. Phys., in press (2010)

In addition to the above papers, other publications not included in the dissertation are:

XI The ITER core imaging x-ray spectrometer
P. Beiersdorfer, J. Clementson, J. Dunn, M. F. Gu, K. Morris, Y. Podpaly, E. Wang, M. Bitter, R. Feder, K. W. Hill, D. Johnson, and R. Barnsley
J. Phys. B: At. Mol. Opt. Phys., in press (2010)

XII Spectroscopy on magnetically confined plasmas using electron beam ion trap spectrometers
A. T. Graf, S. Brockington, R. Horton, S. Howard, D. Hwang, P. Beiersdorfer, J. Clementson, D. Hill, M. May, H. Mclean, R. Wood, M. Bitter, J. Terry, W. L. Rowan, J. K. Lepson, and L. Delgado-Aparicio
Can. J. Phys. **86**(1), 307-313 (2008)

XIII Extreme ultraviolet spectroscopy of low-Z ion plasmas for fusion applications
P. G. Wilcox, A. S. Safronova, V. L. Kantsyrev, U. I. Safronova, K. M. Williamson, M. F. Yilmaz, J. Clementson, P. Beiersdorfer, and K. W. Struve
Rev. Sci. Instrum. **79**(10), 10F543 (2008)

XIV Survey of the K-shell emission from heliumlike ions with an x-ray microcalorimeter
P. Beiersdorfer, G. V. Brown, J. H. T. Clementson, M. Frankel, M. F. Gu, S. M. Kahn, R. Kelley, C. A. Kilbourne, F. S. Porter, D. Thorn, and E. Träbert
J. Phys. Conf. **163**, 012022 (2009)

XV X-ray signatures of charge exchange in L-shell iron and sulfur
M. Frankel, P. Beiersdorfer, G. V. Brown, J. Clementson, M. F. Gu, and L. Schweikhard
J. Phys. Conf. **163**, 012052 (2009)

XVI Investigation of the $2p_{3/2}$-$3d_{5/2}$ line emission of Au^{53+} - Au^{69+} for diagnosing high energy density plasmas
G. V. Brown, S. B. Hansen, E. Träbert, P. Beiersdorfer, K. Widmann, H. Chen, H. K. Chung, J. H. T. Clementson, M. F. Gu, and D. B. Thorn
Phys. Rev. E **77**(6), 066406 (2008)

XVII The ITER core imaging x-ray spectrometer: X-ray calorimeter performance
P. Beiersdorfer, G. V. Brown, J. Clementson, J. Dunn, K. Morris, E. Wang, R. L. Kelley, C. A. Kilbourne, F. S. Porter, M. Bitter, R. Feder, K. W. Hill, D. Johnson, R. Barnsley
Rev. Sci. Instrum. submitted (2010)

XVIII Studies of x-ray production following charge exchange recombination between highly charged ions and neutral atoms and molecules
G. V. Brown, P. Beiersdorfer, H. Chen, J. Clementson, M. Frankel, M. F. Gu, R. L. Kelley, C. A. Kilbourne, F. S. Porter, D. B. Thorn, and B. Wargelin
J. Phys. Conf. **163**, 012051 (2009)

XIX High-resolution spectroscopy of K-shell praseodymium with a high-energy microcalorimeter
D. B. Thorn, G. V. Brown, J. H. T. Clementson, H. Chen, M. Chen, P. Beiersdorfer, K. R. Boyce, C. A. Kilbourne, F. S. Porter, and R. L. Kelley
Can. J. Phys. **86**(1), 241-244 (2008)

XX High-resolution spectroscopy with the EBIT calorimeter spectrometer
F. S. Porter, J. S. Adams, P. Beiersdorfer, G. V. Brown, J. Clementson, M. Frankel, S. M. Kahn, R. L. Kelley, and C. A. Kilbourne
AIP Conf. Proc. **1185**(1), 454-457 (2009)

XXI EUV spectroscopy on NSTX
J. K. Lepson, P. Beiersdorfer, J. Clementson, M. F. Gu, M. Bitter, L. Roquemore, R. Kaita, P. G. Cox, and A. S. Safronova
J. Phys. B: At. Mol. Opt. Phys., in press (2010)

XXII Tungsten transport in the NSTX tokamak
J. Clementson, P. Beiersdorfer, A. L. Roquemore, C. H. Skinner, D. K. Mansfield, K. Hartzfeld, and J. K. Lepson
Rev. Sci. Instrum. submitted (2010)

Acknowledgements

Foremost, I wish to thank my advisors Hans Lundberg, Peter Beiersdorfer, Sune Svanberg, and Sven Huldt. It has been a privilege to be mentored by such outstanding physicists. They have provided me with much advice and encouragement and their work have been a great source of inspiration. As my group leader, Peter has given me the freedom and support to pursue the work of my interest, which has been most appreciated.

I would like to thank friends and colleagues at the Lawrence Livermore National Laboratory, Lund University, UC Berkeley, UN Reno, and the Princeton Plasma Physics Laboratory for providing much assistance and support of which I am truly thankful. I especially want to thank Elmar Träbert for all the comments and useful suggestions on my manuscripts; Greg Brown, whom I always can come to for advice; Ming Feng Gu for always taking the time to help with calculations; Daniel Thorn, Hui Chen, and Miriam Frankel, whom I have enjoyed sharing trailer with and for the good times in the lab; Roger Hutton for helping me get a position at Livermore; Ed Magee for fixing technical problems in the lab; Tomas Brage for teaching me theoretical atomic physics; Donna Vercelli and Karen Lema-Crowe for all their admin work; Reg Wood and Harry McLean for supporting my experiments; and Alla Safronova and Jaan Lepson for good collaborations.

I am greatly thankful for my family's encouragement and enthusiasm. Thank you Mamma, Pappa, Maja, Anni, and Chris! Special thanks to Nim for all her incredible support and for always being there. I also wish to express my gratitude to my beloved late grandparents for all their inspiration.

Thanks to the Axel Victor Runnerström foundation for its generous support.

This work was performed under the auspices of the United States Department of Energy by Lawrence Livermore National Laboratory under Contract No. DE-AC52-07NA-27344.

List of Acronyms and Abbreviations

CCD	Charge-Coupled Device
CIXS	Core Imaging X-ray Spectrometer
EBIT	Electron Beam Ion Trap
ECS	EBIT Calorimeter Spectrometer
EUV	Extreme Ultraviolet
FAC	Flexible Atomic Code
FWHM	Full Width at Half Maximum
GFFS	Gold Flat Field Spectrometer
ITER	International Thermonuclear Experimental Reactor
MCF	Magnetic Confinement Fusion
QED	Quantum Electrodynamics
SFFS	Silver Flat Field Spectrometer
SSPX	Sustained Spheromak Physics Experiment
XRS	X-Ray Spectrometer

Contents

Part I

Overview

Chapter 1

Introduction

Radiative properties of atoms and plasmas are strongly linked. Spectroscopic studies can reveal information about the structure and dynamics of atoms and ions as well as provide data about the conditions of the ambient environment of the emitting atoms. Atomic spectroscopy therefore constitutes the basis for astrophysics and many of the diagnostics of laboratory plasmas.

Spectroscopic investigations of highly charged ions are often conducted in the ultraviolet and x-ray spectral regions because of the scaling of atomic structure with various powers of the nuclear charge Z. Atomic physics can therefore be explored in the study of highly charged high-Z ions, where several interactions affect the energy level systems [1]. Highly charged ions exist in high-temperature plasmas, such as those found in stars or nuclear fusion experiments.

Nuclear fusion is the process where light nuclei merge to form a heavier nucleus. These are the reactions that power the stars and fabricate the chemical elements. Research on fusion took off after World War II with efforts to create hydrogen bombs. Already these uncontrolled fusion reactions turned out to be quite challenging to achieve. As has been learned many times since, to stimulate fusion reactions in a controlled manner in the laboratory is extremely difficult [2]. A great number of schemes to confine hot fusion plasmas for power production has been conceived, most of which are based on magnetic fields for particle containment. This branch of controlled thermonuclear research is called magnetic confinement fusion (MCF) and has been a driving force for much of plasma physics research.

The most versatile method to diagnose high-temperature nuclear fusion experiments is plasma spectroscopy. The presence of highly charged ions in fusion plasmas serve as probes of the plasma conditions. Spectroscopic measurements of the emitted radiation can provide detailed knowledge of the physics of the plasma and its interactions with the surrounding vessel.

1.1 Magnetic Confinement Fusion

Magnetic fusion is the approach toward a fusion reactor that has received the most attention over the years [1]. Several designs utilizing magnetic fields have been investigated for confinement of hot hydrogen plasmas. Experiments were performed on toroidal devices already in the 1930s and 1940s in the US and the UK. This eventually resulted in larger efforts in the 1950s and 1960s when several laboratories dedicated to fusion energy research were established. In the Culham laboratory in the UK and at Los Alamos in New Mexico pinch machines were studied, and in Princeton the stellarator was invented. The stellarator is still today one of the leading contenders as a fusion reactor. Meanwhile in the Soviet Union, the tokamak device was designed. When its excellent performance was confirmed by British physicists in 1969 the tokamak became the machine of choice and has dominated magnetic fusion research since. In Livermore, so-called magnetic mirror machines were actively pursued until the mid-1980s [2,3].

Tokamaks are devices that confine plasmas in toroidal vessels by magnetic fields. They share properties with the pinch machine, which has a strong current compressing the plasma, and with the stellarator, which has external magnets in a complicated geometry to contain the plasma [2]. Around the torus there are large coils that generate a toroidal magnetic field. Together with this field, a weaker poloidal magnetic field is generated by a large current flowing through the torus. The resulting field lines have a helical shape following the torus [4]. To keep the plasma away from the wall of the torus either plasma limiters or divertors are used. A limiter is an outer boundary that defines the extent of the plasma. Magnetic divertors move the plasma-wall interactions away from the main plasma volume by shaping the poloidal field lines so that they intersect the wall in a separate chamber. This reduces ion impurities in the main plasma, and divertors are therefore often implemented in present-day machines. The toroidal plasma current in a tokamak is driven by electric fields generated by transformer action where the plasma torus acts as the second winding. The current not only generates fields to confine the plasma, it also heats it. This ohmic heating can raise the temperatures to a few keV, which is not enough for favorable fusion conditions, requiring temperatures above 10 keV. Additional heating is therefore necessary, and this is accomplished by particle beams or electromagnetic waves [4].

In the last few years fusion science has ignited with the advent of several large magnetic fusion facilities. In Greifswald, Germany, the Wendelstein 7-X stellarator is under construction, which will investigate the feasibility of the stellarator device as a reactor. A still larger project is the International Thermonuclear Experimental Reactor (ITER)[2]. The ITER tokamak is an international effort that has been under way since 1985. The project now includes the US, the Russian Federation, the EU, China, the Republic of Korea, India, and Japan. The tokamak is currently being built

[1] The other branch of fusion research is inertial confinement fusion (ICF) where the most common schemes utilize high-power lasers to compress fuel capsules to achieve fusion burn. The largest ICF effort is the National Ignition Facility (NIF) in Livermore, which has fusion ignition on the agenda for 2012.

[2] Due to the risk of bad publicity with a project title containing *thermonuclear*, the full name is often dropped and ITER is said to instead be latin for *The Path*.

in Cadarache, France and is expected to be completed around 2020. The physics goal of the project is to achieve burning deuterium-tritium plasmas with a power output of around 500 MW during 400 s discharges, corresponding to a fusion gain of Q = 10 [5]. To achieve this, ITER will be much larger than present-day tokamaks with a plasma volume of 180 m^3. The major radius (distance from tokamak center to magnetic axis) will be $R = 6.5$ m. ITER will have 18 toroidal magnets and 6 poloidal coils in addition to the center solenoid. The coils are superconducting and the vacuum vessel is therefore enclosed in a large cryostat [6]. The plasmas will have temperatures of around 25 keV [5] and be contained in a vacuum vessel with a first wall made of copper, beryllium, carbon, and tungsten [7]. These are therefore elements that can be expected to be found in the ITER plasmas as impurity ions. The divertor will likely be radiatively cooled with nitrogen and various noble gases. In addition to these elements it is also possible that ions from mid-Z elements from the structural parts of the vacuum vessel (such as Al, Cr, Fe, Ni, and Zn) can be released into the plasmas [7]. The heat and plasma impurities, including the helium ash, will be exhausted through the ITER divertor. It will consist of three targets (inner, outer, and dome) and will be located at the bottom of the vessel. The plasma strike point surfaces will initially be made of carbon fiber-reinforced carbon composite (CFC), and later replaced with tungsten targets. The ITER divertor will be made up of 54 divertor cassettes [6], see Fig. 1.2.

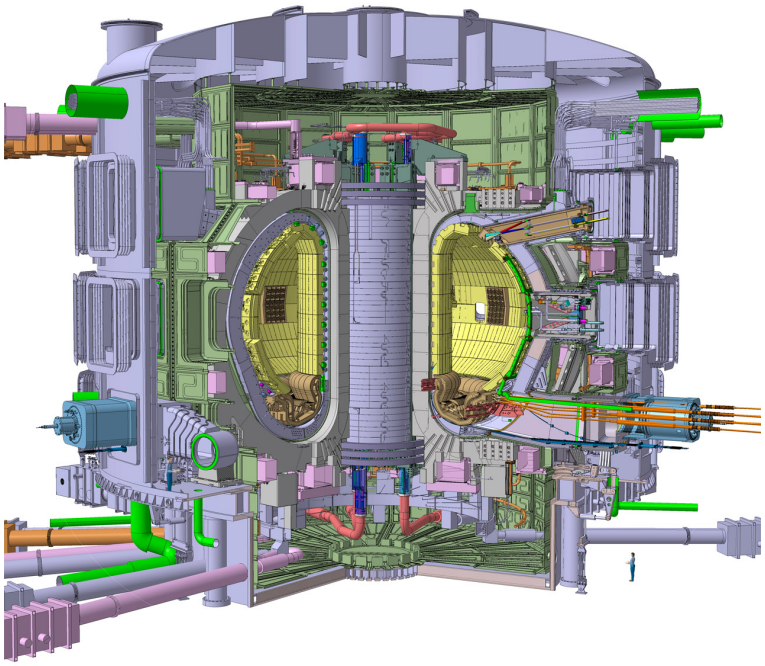

Figure 1.1: Drawing of the ITER tokamak [6]. Note the physicist to the right.

1.2 Fusion Plasma Spectroscopy

The most versatile method to diagnose high-temperature plasmas is probably that of spectroscopy. Magnetic fusion plasmas are largely optically thin [8] and the emitted radiation therefore offers a convenient way to assess the conditions of the plasmas. Consequently, spectroscopic systems are part of the diagnostics suites at most fusion experiments. The many spectroscopic techniques used in magnetic fusion can be divided into two categories: *active* and *passive* spectroscopy. Active spectroscopic techniques are those that measure the response to a disturbance posted on the plasma, such as the injection of particle or laser beams. Some of these methods include the Motional Stark Effect (MSE) for safety factor measurements (twist of the magnetic field around a torus) [9], Li-beam diagnostic for current profile measurements using the Zeeman effect [10], and charge exchange recombination spectroscopy for ion temperature and flow velocity measurements [11]. Passive spectroscopy encompasses the more traditional techniques and include emission ultraviolet and x-ray spectroscopy. These fields will likely become more important as the temperatures of fusion plasmas increase and the electromagnetic radiation shifts toward higher energies.

One of the main objectives of passive spectroscopy at fusion facilities is the monitoring of the ion impurity contents of the plasmas. Broad-band spectrometers can detect the characteristic line radiation from partly stripped ions from which particle species and concentrations can be inferred. In turn, this provides information about the origins of the ions, which can be critical for the operation of the devices. Impurity diagnostics of fusion plasmas are often performed in the ultraviolet or extreme ultraviolet regions, where a multitude of transitions from few-times ionized low- and mid-Z elements is present. A widely used spectrometer for this purpose is the SPRED (Survey Poor Resolution Extended Domain) ultraviolet instrument [12]. However, when tokamaks get larger and hotter plasmas are achieved, the presence of line radiation from low-Z impurities will mainly be at the edges of the plasma and in the divertor. In the hot core plasmas these ions will burn out and low-Z ions can therefore not be monitored by line emission spectroscopy.

The radiation from ions is characteristic of the temperature of a plasma in local thermodynamic equilibrium. Electrons are mainly responsible for the excitation and ionization of ions and the study of the charge balance of an appropriate element can thus give the electron temperature of the plasma. However, plasmas in tokamaks are often not in equilibrium because particle transport can alter the distribution of ions. This means that ionization and excitation of an ion do not necessarily occur at the same location. If the ionization balance is known for a given temperature, deviations from this distribution can therefore reveal particle transport.

In magnetic fusion plasmas the natural line widths are typically much smaller than the Doppler broadening determined by the thermal motions of the emitting ions [8]. High-resolution measurements of spectral line widths can thus be used to determine ion temperatures. The Doppler broadening of a line is determined by

$$\frac{\Delta\lambda}{\lambda} \;=\; 7.7 \;\times\; 10^{-5}\sqrt{\frac{T}{M}}$$

where $\Delta\lambda$ is the full width at half maximum (FWHM) of a gaussian profile at

wavelength λ, T is the ion temperature, and M the atomic mass [8]. Determination of ion temperatures using x-ray spectroscopy was pioneered by Bitter *et al.*, who performed the first measurements at the Princeton Large Torus (PLT) [13]. Well known from cosmology, the related spectroscopic technique of Doppler shifts can be used to measure bulk ion velocities in tokamaks and other fusion plasmas.

The intensities of certain spectral lines are sensitive to the electron densities. This is particularly true for lines originating from metastable levels, which are long lived and thereby have higher probabilities for getting quenched by electron collisions before decaying radiatively. Metastable levels can only decay by electric dipole forbidden transitions and, since these transitions scale favorably with the nuclear charge Z, highly charged ions can often provide suitable systems for density measurements. A frequently used atomic system for density diagnostics is the heliumlike ion. The $n = 1$ to $n = 2$ transitions (commonly referred to as Kα transitions) have wavelengths in a narrow region and can therefore often be observed simultaneously. The so-called *resonance* transition w ($1s^2\ ^1S_0$ - $1s2p\ ^1P_1$), *intercombination* transition y ($1s^2\ ^1S_0$ - $1s2p\ ^3P_1$) and *forbidden* transition z ($1s^2\ ^1S_0$ - $1s2s\ ^3S_1$) make up a density-sensitve spectral signature. The lines are labeled w, y, and z according to the standard notation of Gabriel [14]. The radiative lifetimes for the upper levels are very different and the level populations are thus strongly dependent on the electron density. Observations of the line ratios can therefore serve to measure densities. The heliumlike system also has the advantage of having dielectronic satellite lines nearby from doubly excited lithiumlike ions, which also can be used for electron density measurements [11].

There are several additional features of atomic spectra that can be utilized for diagnosing fusion plasmas, and a multitude of experimental schemes, both active and passive, exist to extract the information from the radiating ions. It is important to select suitable lines when performing plasma spectroscopy, as there can be more than one mechanism responsible for a spectral feature, for instance broadening of spectral lines. Also the choice of working radiation that spectroscopic system are based on must be chosen wisely. For instance, as mentioned earlier, lighter elements will burn out in the hot core of future high-temperature plasmas. Spectroscopic diagnostics then need to rely on high-Z elements for probing the interiors of the fusion plasmas. Enter tungsten.

1.3 Tungsten Spectroscopy

Tungsten is considered to be a leading candidate material for plasma-facing components in magnetic fusion devices. Discovered in 1758 by A. F. Cronstedt[3], tungsten, or wolfram, is a high-density metal with the lowest vapor pressure and highest melting point (3422 °C) of all the non-alloyed metals [16]. Tungsten has the chemical symbol W, atomic number $Z = 74$, and is located among the transition elements in the periodic table.

The reason why tungsten is such an attractive material for magnetic fusion applications is mainly the low erosion yield from plasma particles [17]. The plasma-facing

[3]Tungsten was also discovered in 1781 by Carl Wilhelm Scheele and, in pure form, in 1783 by José and Fausto D'Elhuyar [15]

surfaces in a tokamak receive very high heat loads. Not only must the wall material be able to withstand physical sputtering of particles, but it also needs to be insensitive to chemical erosion that hydrogen and impurity ions can cause the surfaces.

Despite the qualities of tungsten, the usage of high-Z elements in high-temperature plasma experiments has long been considered risky as the likelihood of contamination of the plasma is high. With too large quantities of high-Z ions in a plasma the emitted radiation poses a threat of cooling the plasma enough to prevent it from reaching fusion burn conditions. Whereas low-Z ion impurities get fully stripped in a high-temperature plasma (and thereby only contribute to radiation losses through bremsstrahlung), high-Z elements, such as tungsten, will not get fully stripped even at the highest temperatures envisioned in future fusion devices, and will hence emit line radiation. Still, as plasma experiments reach higher temperatures, the usage of high-Z materials as plasma-facing components seems necessary. Several machines have already installed tungsten parts and others are in the process. Much motivation is due to the design of the ITER divertor, where the plasma strike point targets will be made of tungsten. With the implementation of tungsten parts in fusion devices the impurity ions will likely follow. However, the ever-present radiation from tungsten ions can also be beneficial. The ions can serve as intrinsic probes to relay information about the state of the plasma.

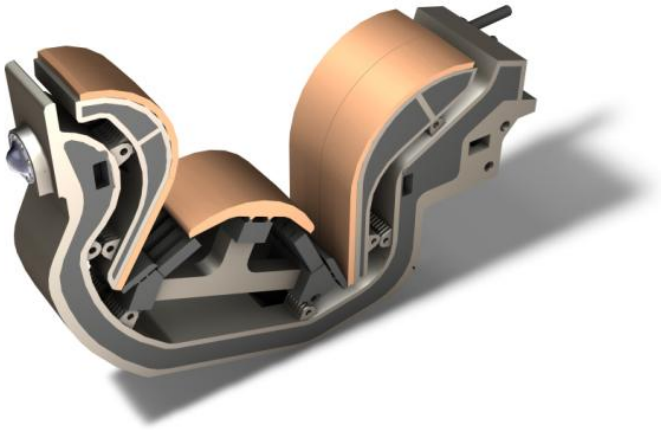

Figure 1.2: ITER divertor cassette [6]. The target plates will be made of tungsten in the second phase of the project.

The possibilities of utilizing tungsten ions to diagnose plasmas are vast. Applications include particle transport, plasma rotation, ion temperature, and electron density measurements. In order to realize the diagnostic possibilities of highly charged tungsten ions, accurate spectroscopic data must be available. X-ray spectra of tung-

sten have been studied for almost a century, see e.g. Ref. [18] and references therein. The spectra of few-times ionized tungsten have mainly been studied in the ultraviolet using sliding spark discharges, see e.g. [19–27]. Several spectroscopic measurements of higher charge states of tungsten have been performed on laser-produced plasmas, see e.g. [28–31].

Tungsten ions were first studied in fusion devices in the 1970s when it was released into the plasmas from the limiters of the Oak Ridge ORMAK and Princeton Large Torus (PLT) tokamaks [32–34]. Strong emission was observed between 30 and 70 Å and attributed to complex $n = 4$ to $n = 4$ transition arrays from many charge states around thirty times ionized tungsten. Sugar and Kaufman later evaluated the data and suggested the radiation to mainly originate from Ag-like W^{27+} [35]. These spectral features were replicated in plasmas at the TEXT tokamak, where tungsten was injected by laser blow off. The analysis by Finkenthal et al. [36] indicated that the emission bands around 50 Å are mainly due to transitions from ions lower than Pd-like W. In the early 1990s tungsten was again injected into the TEXT tokamak [37–39] for detailed investigations of Ag-like W^{27+}, Pd-like W^{28+}, and Rh-like W^{29+}. Additional investigations of the tungsten spectra at fusion experiments have been performed after injection at the ASDEX Upgrade tokamak [40] and, more recently, at the LHD device [41] and the NSTX spherical torus in Princeton [42].

The most ambitious tungsten project on a tokamak is the ASDEX Upgrade tokamak in Garching, Germany. Starting out with a tungsten divertor, the interior of ASDEX Upgrade has successively been covered with tungsten, see e.g. [43, 44]. Several spectroscopic investigations of tungsten have been performed, e.g. [40,45]. Among many measured lines a soft x-ray feature at 7.93 Å [45] has received much attention.

Several spectroscopic studies of highly ionized tungsten have also been carried out at electron beam ion traps (EBITs). At Livermore, highly charged tungsten has been studied by Beiersdorfer, who measured the neonlike tungsten spectrum in 1992 [46, 47]. Three years later, Elliott *et al.* made a high-precision measurement of one of the resonance lines in Ni-like W^{46+} to investigate its possible use for x-ray lasers [48]. Studies also include EUV spectra around 50 Å [49] and soft x-ray spectra around 6 Å [131]. Also the EBIT at the National Institute for Standards and Technology in Gaithersburg, Maryland has been employed for several tungsten measurement. These include EUV measurements of W^{39+} through W^{46+} and W^{54+} through W^{63+} by Ralchenko *et al.* [50, 51], and an x-ray measurement of nickellike and cobaltlike tungsten using an x-ray calorimeter [52]. A recent measurement from the NIST EBIT include soft x-ray wavelengths of W^{60+} through W^{63+} by Gillaspy *et al.* [53]. The Berlin electron beam ion trap has specialized on tungsten measurements of relevance to fusion research [54]. Several studies have been reported, see e.g. [55–58].

There is additional work on tungsten spectra reported, see e.g. the recent data compilation by Kramida and Shirai [59]. Also on the theory side several papers have been published. Still, the radiative data on tungsten is far from complete. As calculations of atomic structure improve in accuracy and the encounter of tungsten ions in fusion plasmas can be expected to increase, there are certainly needs for high-precision spectroscopic data of highly charged tungsten ions.

Chapter 2

Facilities

The work reported in this dissertation has been performed at two research facilities: the electron beam ion trap (EBIT) facility and the Sustained Spheromak Physics Experiment (SSPX) facility at the Lawrence Livermore National Laboratory (LLNL) in Livermore, California.

2.1 Livermore EBIT Facility

The Livermore EBIT facility is where the electron beam ion trap was invented. The first device was dubbed EBIT and was originally developed with the purpose of producing x-ray spectra from highly charged ions in support of the x-ray laser program in Livermore [60]. EBIT is based on the electron beam ion source (EBIS) and was designed by Levine and Marrs in 1985 - 1986. A few years later a second device was constructed, the EBIT-II, which has since moved to the Lawrence Berkeley National Laboratory. EBIT was rebuilt in the early 1990s to extend its operating parameters with electron-beam energies up to around 200 keV. The new device was dubbed the SuperEBIT electron beam ion trap. This machine can now be converted between SuperEBIT and EBIT and these two devices thereby cover a wide range of electron-beam energies [61, 62].

The EBIT project has proven very successful for x-ray spectroscopy and has over the years resulted in several important contributions to atomic physics. In addition, the spectroscopy program has provided a multitude of data for applications in fields such as astrophysics and plasma physics, see e.g. [5, 63–65]. Several electron beam ion traps have been built at locations all over the world, many which are based on the Livermore design. Because of this, the original device is now referred to as EBIT-I and the term EBIT has become the designation for the type of machine.

The main features of an EBIT are the electron gun assembly, the trap, and the electron-beam collector. These are displayed in Fig. 2.1, where the major components have been labeled. Below follows an overview of the EBIT-I [66, 67] and SuperEBIT [68] electron beam ion traps.

The electron beam starts out from the electron gun assembly, which consists of

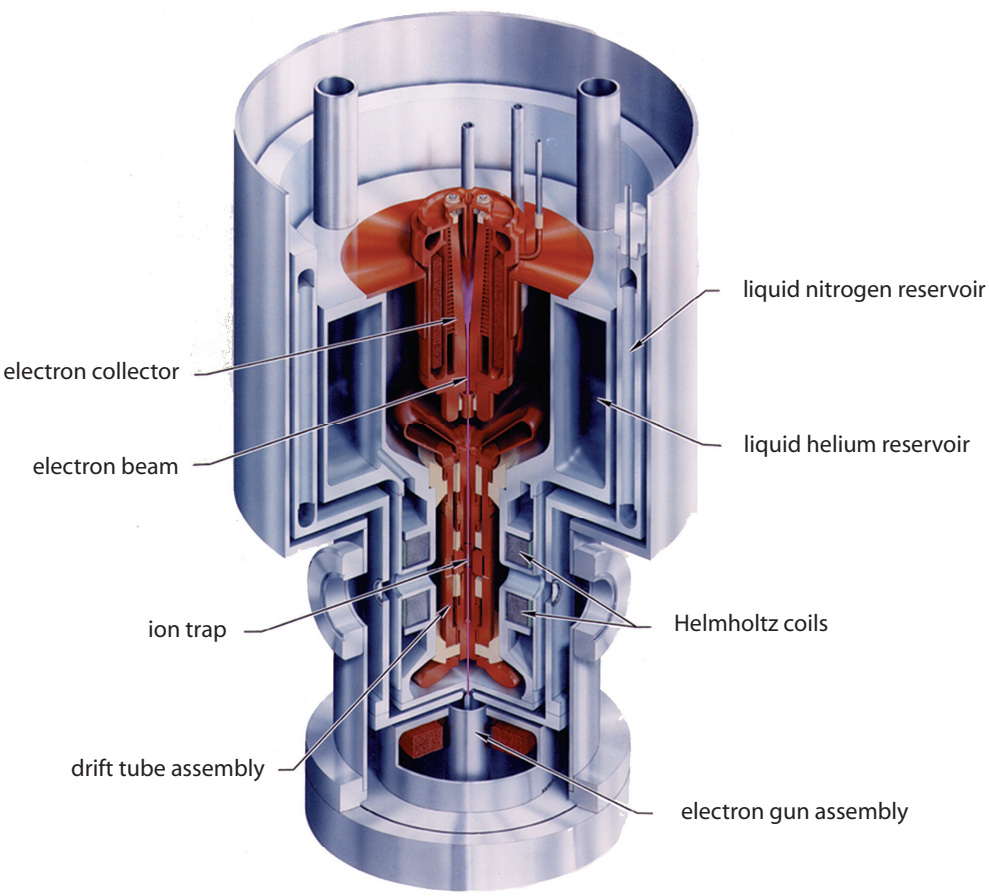

Figure 2.1: Drawing of EBIT-I from Ref. [69]. This image is also the logo of the Livermore EBIT facility.

a gun (cathode) and an anode. The gun is grounded in EBIT-I and biased to high negative voltages in SuperEBIT. The gun is heated to emit electrons from its concave surface. This thermal emission of electrons is extracted from the cathode by the anode electrode located just above. The anode voltage thereby determines the electron-beam current. Around the cathode is the so-called bucking coil located with the purpose to eliminate magnetic fields at the gun surface and thereby reduce the velocity components of the electrons in the directions perpendicular to the beam axis. Above the electron gun assembly is the beam accelerated toward the drift tube assembly, which is a series of three circular electrodes defining the ion trap.

The drift tube assembly consists of the bottom, middle, and top drift tubes. These are biased to relatively low voltages, typically up to 400 V, to create a potential well along the electron-beam axis. The trapping of ions and their interaction with the

electron beam occur in a 2 cm region inside the middle drift tube. The depth of the potential well is chosen based on the element of study. Heavy elements are generally better confined in a shallow trap[1], whereas lighter ions need a deeper trap to avoid getting pushed out by heavier elements. The whole drift tube assembly is biased to high positive voltages up to around 30 kV. This voltage, in addition to the middle drift tube potential and the electron space charge of the trap, is what determines the kinetic energy of the electrons when they interact with the trapped ions. In SuperEBIT, the high negative potential that the cathode floats at must also be added to determine the energy of the electrons when they reach the trap. The drift tube assembly and the potential wells of the trap are illustrated in Fig. 2.2. The middle drift tube has six radial view ports to which spectrometers, solid-state detectors, and ion injection systems can be connected.

The x-ray emission rate from the electron-ion interactions in the trap is proportional to the electron current density and it is therefore of importance to have a high electron density in the trap [62]. This is achieved by compressing the beam with a strong magnetic field. Around the drift tube assembly a pair of superconducting Helmholtz coils is located. In a Helmholtz geometry, two identical coils are placed on a common axis separated by a distance that equals the coil radius. When the same current is supplied through the coils the generated magnetic field is nearly parallel and homogeneous in the area around the common axis. The Helmholtz coils at the Livermore EBITs produce a 3 T field at a coil current of 160 A. This strong magnetic field ensures that the electron beam is compressed to a high (around 10^{11-12} cm^{-3}) and uniform electron density in the trap region. The cross section of the electron beam is therefore very narrow in the trap region, typically around 60 μm. The space charge of the electron beam makes a radial trap for the ions.

After the small trap volume the electron beam continues through the top drift tube toward the electron collector located above. The collector consists of an electrode and a magnet. The field of the collector magnet is in the opposite direction to the Helmholtz field and serves to expand the electron beam radially so that it will intersect the inner walls of the electrode and terminate. A lot of energy is thereby deposited to the collector and for this reason external cooling is required. A reservoir of liquid nitrogen (LN_2) is therefore surrounding the collector.

The superconducting Helmholz coils also need to be cooled given the heat generated by the large current. Around the coils flows liquid helium (LHe), keeping the magnet at 4 K. The LHe also keeps the drift tubes cold, making the walls of the trap act as cryopumps. Around the LHe reservoir is a shield of LN_2.

There are several methods to introduce ions into the EBIT trap. For most gaseous elements a ballistic gas injection system works well. Atomic and simple molecular gases, such as carbon dioxide, nitrogen, and the noble gases, are introduced this way. These gases are often used for wavelength calibration of spectra and for evaporative cooling of trapped ions; see below. More complex molecules such as iron pentacarbonyl, $Fe(CO)_5$, and trimethylaluminum (TMA) are also commonly used. The neutral atoms or molecules stream through a nozzle controlled by a thermo valve

[1]So long as the element is lighter than tungsten, which exists in the EBITs as an impurity originating from the electron gun.

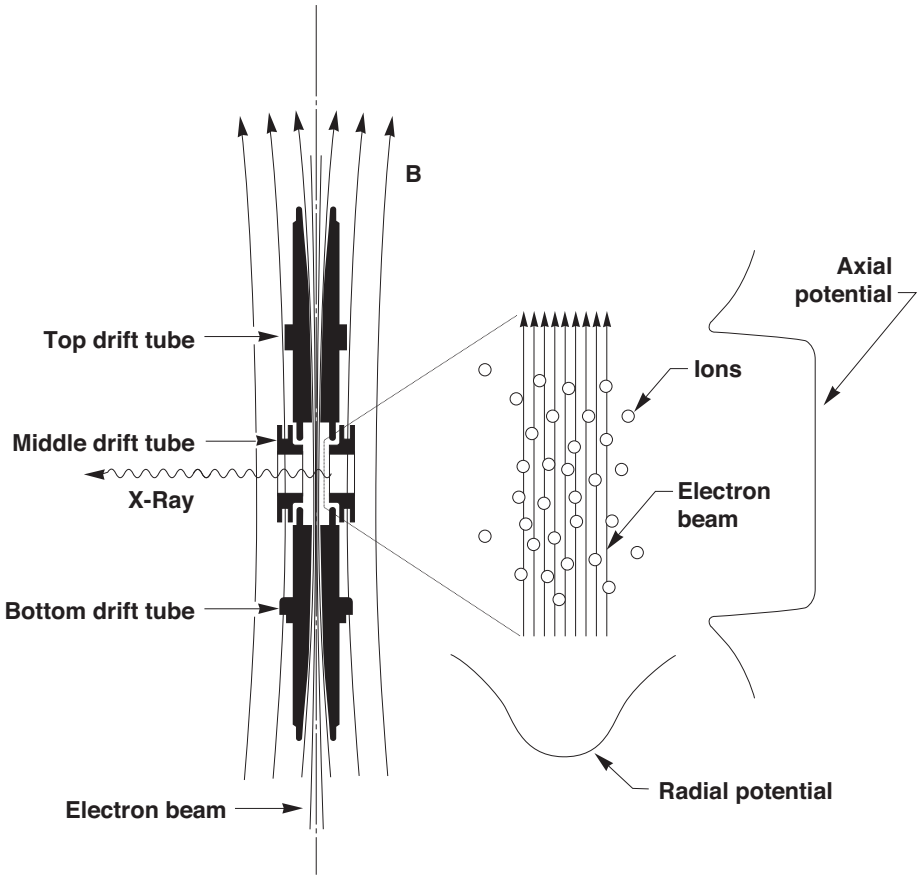

Figure 2.2: EBIT drift tube assembly. Radial view ports through the middle drift tube allow for x-rays to be observed. The geometries of the drift tubes are chosen to fit the direction of the magnetic field lines from the Helmholtz coils. The drawing to the right illustrates the potential wells of the trap. Figure courtesy of P. Beiersdorfer.

into the EBIT vacuum chamber [70].

Other substances are injected into the EBITs by means of sublimation. Sublimation injectors essentially consist of a container of material connected to one of the ports of EBIT. In order to increase the vaporization of material some bottles need external heating, which is provided by wrapping heater tapes around the containers. For some of the work reported in this dissertation, tungsten hexacarbonyl, $W(CO)_6$, has been injected into SuperEBIT by sublimation.

Solid elements can be introduced into the trap by employing a laser-ablation sys-

tem [71]. This relatively new method works by having a Q-switched Nd:YAG laser strike the surface of a target and sputter off particles. This vaporized material shoots away from the target surface and through collimation slits into EBIT. Due to the magnetic fields surrounding the trap, only neutral particles reach the beam as electrons and ions get deflected. This injection method works well for certain elements whereas it has proven less useful for others. This is not yet well understood.

Another common method of injection for metals is the MeVVA source. The Metal Vapor Vacuum Arc (MeVVA) is located at the top of EBIT and works by sputtering ions off from an electrode using high-voltage discharges. These pulses of low charge state ions are accelerated into EBIT through the collector. One of the big advantages with the MeVVA is that the timing of the ion injection is well controlled. A bundle of ions can, for instance, be introduced into the trap at the beginning of every trap cycle. These ions will become successively ionized and a large fraction of them reach the maximum charge state energetically available. The charge state distribution therefore typically becomes peaked. At the end of the cycle the trap is emptied and replenished with fresh ions and a new cycle begins. This controlled temporal injection is similar to the laser injection, where the number and timing of laser shots easily can be set. This contrasts to the continuous injection methods of the gas and sublimation injectors, where neutral atoms constantly are supplied to the trap. In these cases, the charge state distributions often have a larger spread between charge states.

Low-Z ions are often injected continuously into the trap using the gas injector for evaporative cooling of high-Z ions in the trap. This method is very effective in lowering the temperature of the ions and confining them for longer periods of time in the trap. Low-Z ions equilibrate with the high-Z ions in the trap until they have approximately the same temperature. However, ions with low charge states escape the trap much easier and thus carry away kinetic energy from the trap, resulting in cooling of the high-Z ions [72].

2.2 SSPX Spheromak Facility

The Sustained Spheromak Physics Experiment (SSPX) was an Innovative Confinement Concept (ICC) project in Livermore. The spheromak was in operation from 1999 to 2007 with the mission to examine the feasibility of the spheromak concept as a fusion reactor. Specifically, the goal of SSPX was to investigate magnetic field generation and energy confinement [73,74]. Spheromaks are magnetic confinement devices with several attractive features, of which the most appealing is that the plasma is confined primarily using self-generated fields seeded by small, simple solenoidal magnets. There is no need for large, high field, torus-linked coils, which is a big advantage over the tokamak and stellarator devices. Spheromaks are also smaller in size than the conventional fusion machines. These are useful properties for a reactor as it makes it cheaper both to construct and maintain. Albeit the engineering aspects of a spheromak might be advantageous, the physics of spheromak plasmas is most complicated.

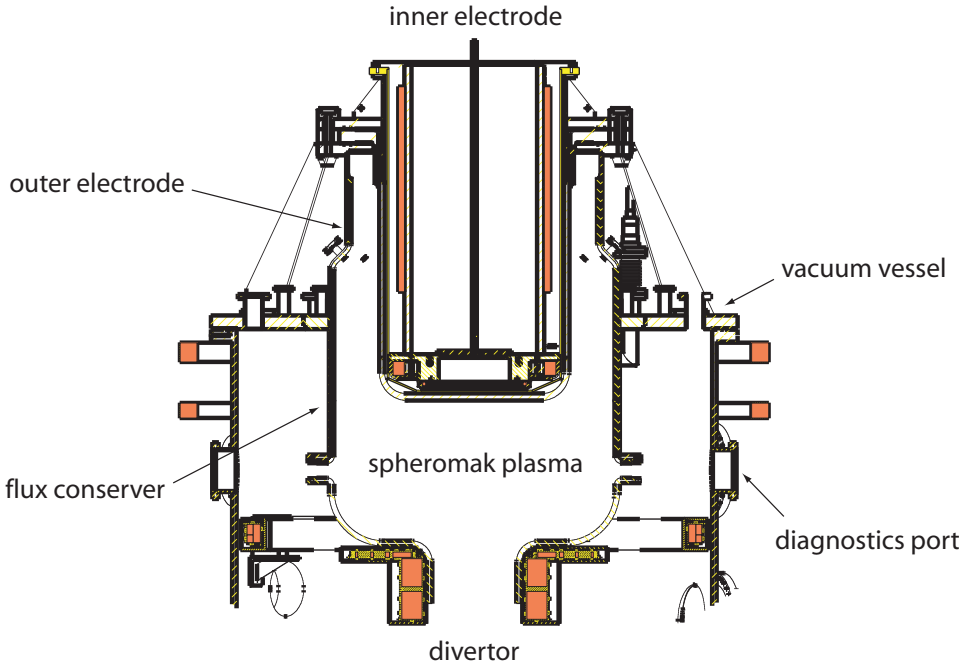

Figure 2.3: Drawing of SSPX displaying the cross section of the spheromak. Figure courtesy of H. S. McLean.

Figure 2.3 displays a drawing of the cross section of the SSPX spheromak where the major components are labeled. The plasma itself, often called a spheromak, is confined within the so-called flux conserver, a 12 mm thick container of copper with a 100 μm coating of tungsten on its plasma-facing surfaces to reduce sputtering [74,75]. The 1 m diameter flux conserver is separated at the mid-plane to allow for access of diagnostic instrumentation. The flux conserver is surrounded by the vacuum vessel, which keeps SSPX at background pressures around 10^{-8} Torr.

The plasmas are created with the spheromak injector, which comprises the upper half of SSPX. The injector consists of a magnetized coaxial gun with an inner electrode (cathode), and an outer electrode (anode). A few seconds before a discharge is initiated the coils in the gun are turned on to let magnetic fields diffuse through the flux conserver, whereupon hydrogen gas is puffed into the region between the electrodes using fast gas valves. A formation capacitor bank is then discharged and gun currents of around 500 kA supplied to the electrodes. [76]. This causes the hydrogen gas between the electrodes to break down and create a plasma, which is ejected from the gun region toward the main volume of the flux conserver. When the plasma has expanded to occupy the flux conserver some of the field lines near the injector will reconnect and form closed magnetic field lines. The plasma thereby gets confined in a toroidal spheromak plasma with a major radius of $R = 0.31$ m and minor radius of

$a = 23$ cm. A sustainment capacitor bank is arranged as a constant current power supply to maintain the spheromak plasma [74].

Typical SSPX plasmas lasted 4 ms and achieved electron temperatures around 100 - 200 eV. Some of the SSPX peak performance parameters include electron temperatures above 500 eV, plasma durations of 9 ms, and toroidal plasma currents around 1 MA [77].

The SSPX spheromak was a well diagnosed experiment [78]. The instrumental suite included a Thomson scattering system, H-alpha array, magnetic coils [78], and a Doppler spectrometer [79]. A layout of the diagnostics is shown in Paper I. Initially, a SPRED instrument [12] was used to measure impurity ions in the ultraviolet range. In 2006 this instrument was replaced with the high-resolution extreme ultraviolet Silver Flat Field Spectrometer (SFFS). The SFFS was connected to a beam line tangential to the magnetic axis of the spheromak. The line-integrated data therefore covered both the cooler edges as well as the hotter plasma at the center. The SFFS spectrometer is described in Chapter 3.

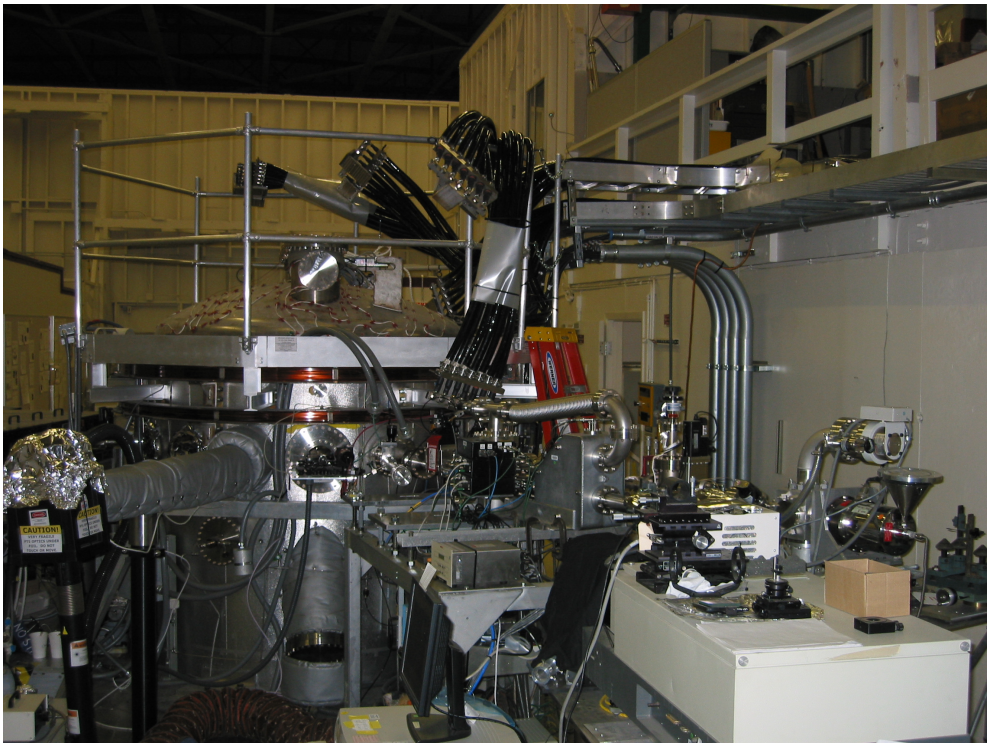

Figure 2.4: The SSPX spheromak in Livermore. At the right is the SFFS spectrometer.

Chapter 3

Instrumentation

The experimental investigations reported in this dissertation have been performed using two grating spectrometers, two crystal spectrometers, and two x-ray calorimeter spectrometers. The characteristics of these instruments are described in this chapter.

3.1 Grating Spectrometers

Grating spectrometers are useful instruments for the study of extreme ultraviolet (EUV) and soft x-ray spectra. Grating instruments have been employed at tokamak facilities since the 1970s and have often been the main instrument for plasma impurity monitoring. At EBIT facilities, these spectrometers were first used a little over a decade ago, then with focus on atomic astrophysics.

The reason why the soft x-ray and EUV ranges are so useful for plasma diagnostics is that many strong atomic transitions fall in this range. The L-shell emission from few-times ionized low-Z elements such as carbon and oxygen, which are common impurities in magnetic fusion plasmas, produce many strong lines in the EUV; see e.g. Paper VIII. K-shell emission from these elements can be observed in first order in the soft x-ray or in higher orders in the EUV. Other common plasma impurity species such as titanium, iron, and nickel have strong M-shell transitions that fall in the EUV. Also high-Z elements, such as tungsten, have much emission in the EUV and soft x-ray regions originating from a wide range of charge states. Grating reflectivities are low for high-energy photons and grating spectrometers for the short-wavelength EUV and soft x-ray regimes are therefore operated at grazing incidence.

3.1.1 Silver Flat Field Spectrometer

The Silver Flat Field Grating Spectrometer (SFFS) is a grazing-incidence EUV instrument also known as the Long Wavelength Extreme Ultraviolet Spectrometer (LoWEUS) depending on which facility it is fielded at. The SFFS was originally designed to be used for laboratory astrophysics measurements at the Livermore electron beam ion traps. A description of an early version of the instrument is given by

Beiersdorfer *et al.* in Ref. [80]. The spectrometer has since been upgraded and also used at the SSPX spheromak; see Paper I and Ref. [81], and the NSTX tokamak in Princeton [42, 82].

The spectrometer employs spherical gratings with a radius of curvature of $R = 5.6$ m. For the measurements reported in this dissertation a Hitachi grating with an average groove density of 1200 lines/mm has been used [83]. The grating has a gold-covered surface of 30 mm groove length by 50 mm groove distance and is blazed for a grazing angle of 3.2°. When the spectrometer is used at an EBIT it does not need an entrance slit as the electron-beam width is sufficiently narrow to act as a line source. However, for use at SSPX or NSTX, which are extended light sources, slit apertures of widths 100 and 30 μm have been used. The slits are placed at a distance of 237 mm from the grating, which also is the distance of the detector to the grating. Various liquid nitrogen cooled charge-coupled device (CCD) cameras have been used as detectors. At SuperEBIT and SSPX, see Fig. 3.1, a Photometrics back-illuminated 1024 by 1024 pixel CCD was used (with 25 μm pixel size), and at EBIT-I and NSTX measurements have been carried out using back-illuminated Princeton Instruments cameras with 1300 by 1340 pixel chip sizes (with 20 μm pixel size).

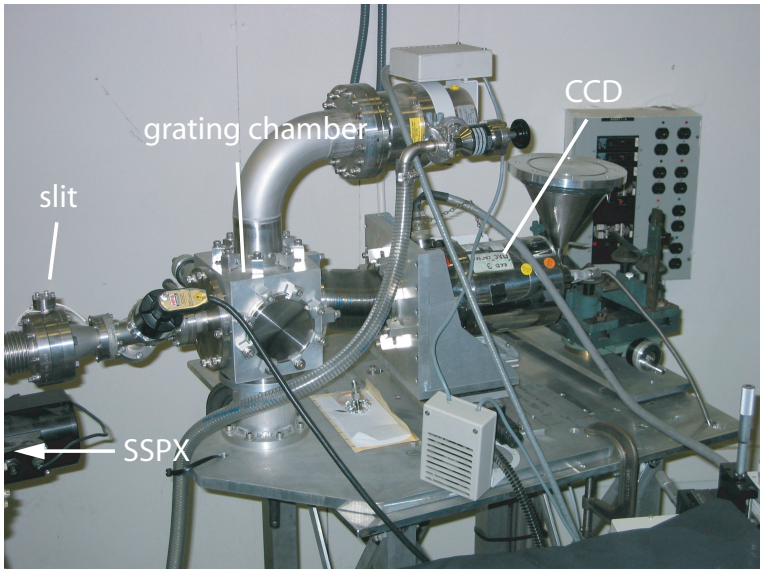

Figure 3.1: The Silver Flat Field Spectrometer at SSPX. The SFFS is connected to a tangential beam line to the spheromak, which is approximately 2 m from the spectrometer.

The detector can be translated along the optical axis to adjust the focus. The detector mount is connected to a bellows so that it can be moved along the dispersion direction to cover the 20 - 450 Å range, i.e. the whole EUV region and parts of the soft x-ray range. Depending on camera position, bandwidths of 100 - 200 Å are

achieved. For such broad wavelength coverage the focus necessarily varies across the camera. This is illustrated in Fig. 3.2, where an oxygen spectrum in the 18 - 158 Å interval is shown, acquired at EBIT-I at an electron-beam energy of 2.1 keV. The short wavelength side of the spectrum (H-like O VIII and He-like O VII) has a resolution of around 0.2 Å FWHM whereas the lines around 130 Å (Li-like O VI and Be-like O V) have line widths of around 0.4 Å. This good resolution over such a broad spectral range makes the SFFS spectrometer an excellent instrument for plasma impurity diagnostics.

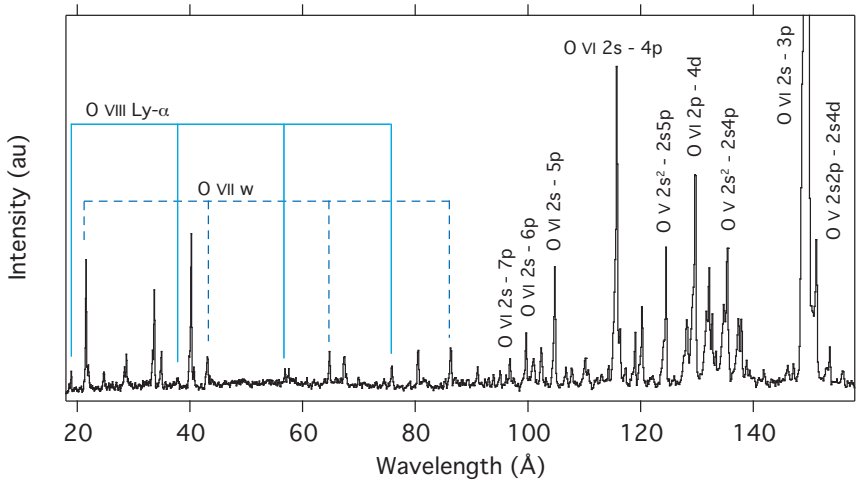

Figure 3.2: Oxygen spectrum taken with the SFFS at EBIT-I at an electron-beam energy of 2.1 keV. The first four orders of the K-shell resonance lines are shown together with some high-n series in lithiumlike and berylliumlike oxygen. Also shown at the short wavelength side are K-shell lines from carbon and nitrogen ions.

Paper X and Chapter 6 describe measurements of few-times ionized tungsten performed with the SFFS at the SSPX spheromak.

3.1.2 Gold Flat Field Spectrometer

The Gold Flat Field Spectrometer (GFFS) is a very high resolution soft x-ray and EUV spectrometer at the Livermore EBIT facility; see Fig. 3.3. The spectrometer was designed for high-precision QED [84] and hyperfine-structure [85] measurements and for investigations of atomic spectra for the interpretation of astrophysical data obtained with space-based instruments [86]. The design has proven so successful that a similar spectrometer has been built for use on laser-produced plasmas at the Jupiter Laser Facility in Livermore [87, 88] and one is presently being constructed for NSTX, where it will study spectra of interest for plasma diagnostics and astrophysics.

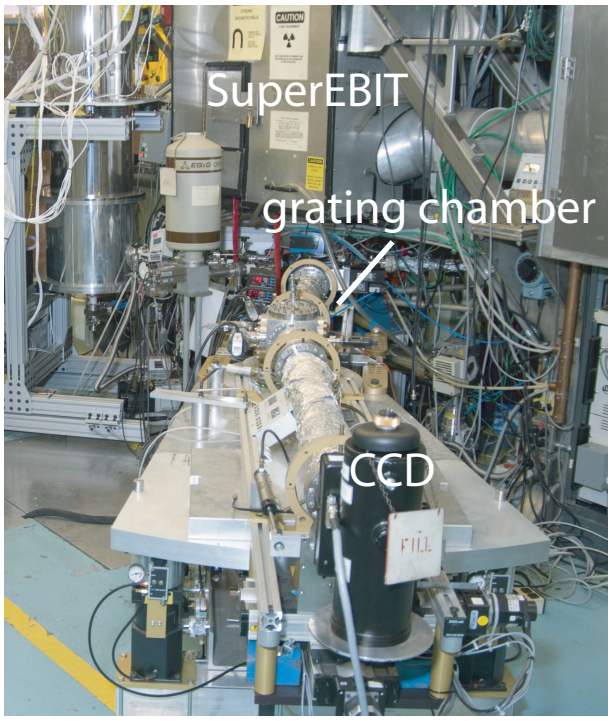

Figure 3.3: The Gold Flat Field Spectrometer at SuperEBIT.

The GFFS utilizes an $R = 44.3$ m varied space groove grating with an average groove density of 2400 lines/mm. The spherical grating is gold covered and mounted at a grazing angle of about 2° to SuperEBIT [86]. The GFFS can field both CCD cameras and micro channel plate (MCP) detectors. In this work Princeton Instruments CCD detectors were used. These cameras have pixel sizes of 20 μm and arrays of 1300 by 1340 pixels. As the spectrometer operates without any imaging slit, the CCD resolution allows for upper estimates of the electron-beam width. For instance, the lines in the neon spectrum shown below have line widths of approximately 3.5 pixels, which correspond to an electron beam narrower than 70 μm. To minimize mechanical vibrations, and thus broadening of spectral lines, the GFFS is mounted on a stabilizing system, where the grating and detector rest on a compressed-air bearing [86].

Figure 3.4 displays a spectrum of highly charged neon in the 9 - 15 Å interval. This is a 45 minute exposure from SuperEBIT where neon gas was injected to a 8.25 keV electron beam. The Lyman series in H-like Ne X and the K series in He-like Ne IX are shown up to $n = 4$ and 6, respectively. As the detector is located far from the grating, the focal field is nearly flat and the resolution is very uniform across the detector, approximately 15 mÅ, corresponding to resolving powers $R = \lambda/\Delta\lambda$ between 600 and 1000. The GFFS can be set up to operate from just below 10 Å to around 120 Å. With a CCD detector the GFFS bandwidth in the short-wavelength regime is about 5 Å, whereas the coverage is roughly 10 Å for the long wavelengths.

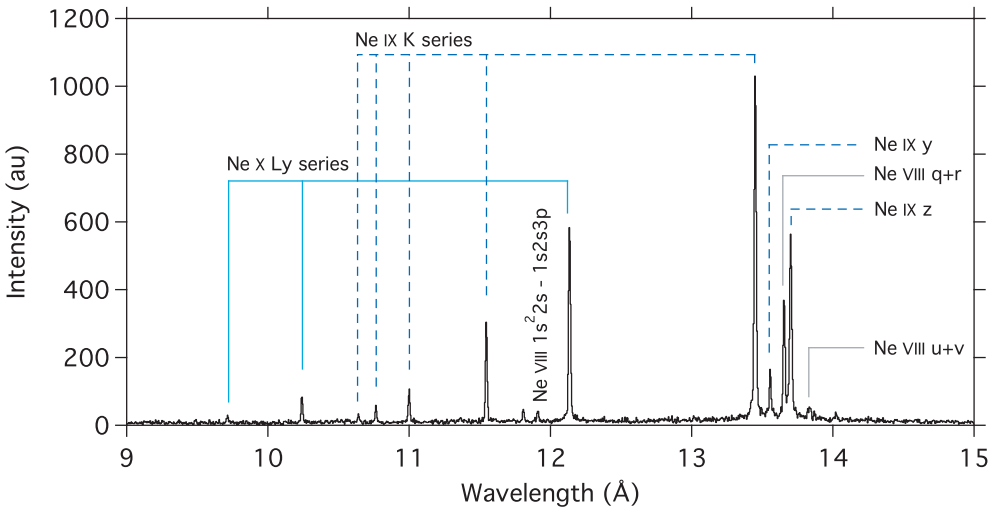

Figure 3.4: Neon spectrum taken with the GFFS at SuperEBIT at an electron-beam energy of 8.25 keV. The resonance series in He-like Ne IX and H-like Ne X are shown together with Li-like Ne VIII satellite lines.

The GFFS has been used for high-precision wavelength measurements of $\Delta n = 0$ M-shell transitions in highly charged tungsten ions in the 19 - 25 Å interval at SuperEBIT. This work is described in Paper IV and Chapter 5.

3.2 Crystal Spectrometers

Crystal spectrometers have proven very powerful for plasma diagnostics on tokamaks. Since measurements of the Doppler broadening of the He-like Fe^{24+} line w were performed on the Princeton PLT tokamak by Bitter *et al.* in 1978 [13], crystal spectrometers have been used for ion-temperature measurements on many magnetic fusion experiments. Crystal spectrometers have also been the instruments of choice for high-precision measurements of x-ray wavelengths on electron beam ion traps. At Livermore, a variety of spectrometer types have been implemented, from cylindrically bent crystals operated in the von Hámos and Johann geometries to broadband and high-resolution flat-crystal instruments. This dissertation includes measurements performed at SuperEBIT using two of these flat-crystal spectrometers.

A crystal diffracts radiation according to Bragg's law,

$$n\lambda = 2dsin\theta$$

where n is the diffraction order, λ the wavelength, d the crystal lattice spacing, and θ the Bragg angle, measured from the face of the crystal. The type of crystal and its cut determine the $2d$ spacing and thereby the available wavelengths that can be

diffracted. The resolving power R of a crystal spectrometer can be expressed as

$$R = \frac{\lambda}{\Delta\lambda} = \frac{1}{\Delta\theta} tan\theta$$

where $\Delta\theta$ is the angular resolution. The resolving power is thus determined by the Bragg angle and the angular resolution. The spectral resolution increases as the Bragg angle approaches 90° or when the angular resolution decreases. The angular resolution is a combination of the source width (or spectrometer entrance slit), the detector resolution, the spectrometer geometry, and the intrinsic resolution of the crystal.

3.2.1 Blue Spectrometer

The Blue spectrometer at the Livermore EBIT facility was built to measure Fe L-shell spectra. The spectrometer design is clever in that it allows for the use of two crystal and detector systems in the same vacuum chamber. This means that two adjacent or separated wavelength bands can be measured using the same EBIT viewport. If used in conjunction with the sister instrument - the Orange spectrometer - very broad spectral coverage can be achieved; up to 9 Å for wavelengths below 21 Å [89].

The spectrometer employs long flat crystals that are positioned close to the entrance port of the instrument and can be operated at Bragg angles up to 58°. For the work reported in the dissertation, an 11 cm long, 1.2 cm high ammonium dihydrogen phosphate (ADP) crystal was used with a $2d$ spacing of 10.640 Å at the (101) plane.

Both the Blue and the Bradley II spectrometer (see below) make use of Ordela single wire position-sensitive proportional counters (PSPCs) as detectors. The PSPCs are filled with P-10 gas (90 % argon 10 % methane), which flows through the detector at a rate of approximately 1 mm^3s^{-1}. The detector is located 25.4 cm from the crystal [89]. The PSPCs are controlled and read out using a CAMAC multi-parameter data acquisition system developed for spectroscopic applications [90].

The $2s_{1/2}$ - $2p_{3/2}$ transitions in F-like W^{65+} through Li-like W^{71+} have been measured with the Blue spectrometer and are reported in Paper III and in Chapter 4. The spectrometer has furthermore been used to measure the wavelengths and relative intensities and polarizations of the electric dipole forbidden transitions in Ni-like W^{46+}; see Paper VII and Chapter 5.

3.2.2 Bradley II Spectrometer

The high-resolution flat-crystal spectrometer at the Livermore EBIT facility is dubbed Bradley II. In order to achieve very high spectral resolution the spectrometer is designed to operate at large Bragg angles. The significant difference from its predecessor, the Bradley I, is that the crystal is positioned at the back of the vacuum chamber, approximately 93 cm from the electron beam. This increase of the spectrometer geometry decreases the spectral range and allows for very large Bragg angles to be attained, up to 85° [91]. For the measurement reported in this work a quartz crystal with a $2d$ spacing 8.350 Å was used at an angle of 72°.

Just as the Blue spectrometer, the Bradley II has its optical plane perpendicular to the direction of the electron beam. Crystals are sensitive to polarization and have different reflectivities in the directions parallel and perpendicular to the electron beam. This property can be used to measure the relative polarization of lines using two crystals. The reflectivity also depends on the Bragg angle of the crystal, and the large Bragg angles achieved with the Bradley II therefore are associated with high reflectivities [91].

The Bradley II instrument has been used in conjunction with the Blue spectrometer to measure the relative line intensities and polarization of the magnetic-octupole and electric-quadrupole transitions in nickellike tungsten. This measurement is reported in Paper VII and in Chapter 5.

3.3 X-ray Calorimeter Spectrometers

X-ray calorimeters are also known as microcalorimeters and quantum calorimeters. These relatively new instruments are gaining popularity in x-ray spectroscopy. The first x-ray calorimeter used at an EBIT facility was developed in Livermore; see e.g. Refs. [92–94] and consisted of a single heat absorber. In 2000, the Livermore EBIT group started a collaboration with the NASA Goddard Space Flight Center (GSFC). At GSFC x-ray calorimeters are developed for x-ray satellite missions. Three generations of multi-pixel NASA instruments have been implemented in Livermore, where they have been utilized for numerous laboratory astrophysics and atomic physics measurements.

The benefits of x-ray calorimeters are the broad spectral coverage in addition to good spectral resolution. Although having high resolving powers, crystal spectrometers are limited in bandwidth. Solid-state detectors, on the other hand, cover wide energy ranges but often have poor resolution. X-ray calorimeters are also unique in other ways. For instance, since the detectors are energy dispersive[1] the spectral lines are uniquely determined by the photon energies; the concept of orders does not exist. For spectral surveys this is often a good property as high-order lines otherwise can interfere with the spectral features of interest. X-ray calorimeters are also insensitive to polarization. For measurements on an EBIT this can be important because the unidirectional electron beam makes EBIT a highly polarized light source.

3.3.1 XRS Spectrometer

The second generation of GSFC x-ray calorimeters at the Livermore EBIT facility is known as the X-Ray Spectrometer (XRS) or XRS/EBIT to distinguish it from its sister instrument onboard the Astro-E2/Suzaku x-ray observatory [2]. The XRS detector consists of a 6×6 array of silicon thermistors where 28 HgTe heat absorbers and four Bi absorbers are attached. Each pixel element has an area of $624 \times 624\ \mu\text{m}^2$ [95]. The XRS has an approximate energy resolution $\Delta E = 6$ eV at 6 keV and $\Delta E = 60$ eV

[1] X-ray calorimeters are sometimes called non-dispersive instruments to separate them from the more common wavelength-measuring spectrometers.

[2] This instrument failed shortly after launch in 2005.

at 60 keV, and a dynamic range of 100 eV up to 100 keV [96]. It was in operation at SuperEBIT from 2003 to the fall of 2007 when it was replaced as the main x-ray calorimeter instrument by the ECS spectrometer; see below.

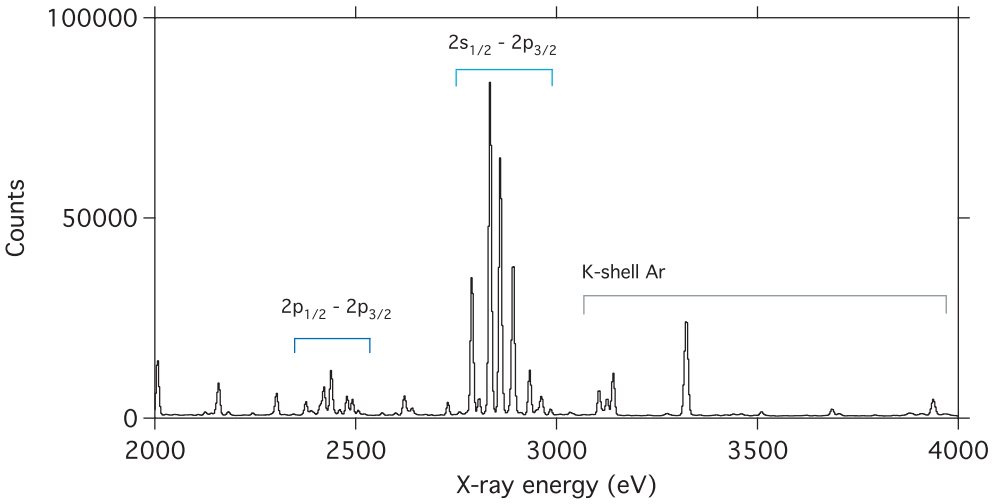

Figure 3.5: XRS spectrum of highly charged bismuth measured at SuperEBIT at $E = 116$ keV.

The large number of heat absorbers allows for good counting statistics. When the counts from the individual pixels are added strong signals are achieved, especially when data from several run days are added. A good example of this is shown in Fig. 3.5, where $\Delta n = 0$ L-shell transitions in highly charged bismuth ions are displayed. These ions were studied with the XRS at SuperEBIT at an electron-beam energy of 116 keV [97]. The spectrum displays the electric dipole (E1) $2s_{1/2}$ - $2p_{3/2}$ and the magnetic dipole (M1) $2p_{1/2}$ - $2p_{3/2}$ transitions in F-like Bi^{74+} through Li-like Bi^{80+}. These transitions have also been studied in highly charged tungsten ions; see Paper III and Chapter 4.

The usefulness of the XRS as a broadband plasma diagnostic is illustrated with Fig. 3.6, where K-shell emission from several low-Z ions are observed. Line widths are around 6.5 eV FWHM. In this spectrum, Lyman and K series of hydrogen- and heliumlike oxygen, sodium, silicon, phosphorus, sulfur, chlorine, argon, and potassium ions are observed. K-shell lines are often used for energy calibration of x-ray calorimeter data as the transition energies are well known from both theory and experiment [98].

The XRS spectrometer has measured M-shell transition energies in Zn-like W^{44+} through Co-like W^{47+}; see Paper V and Chapter 5.

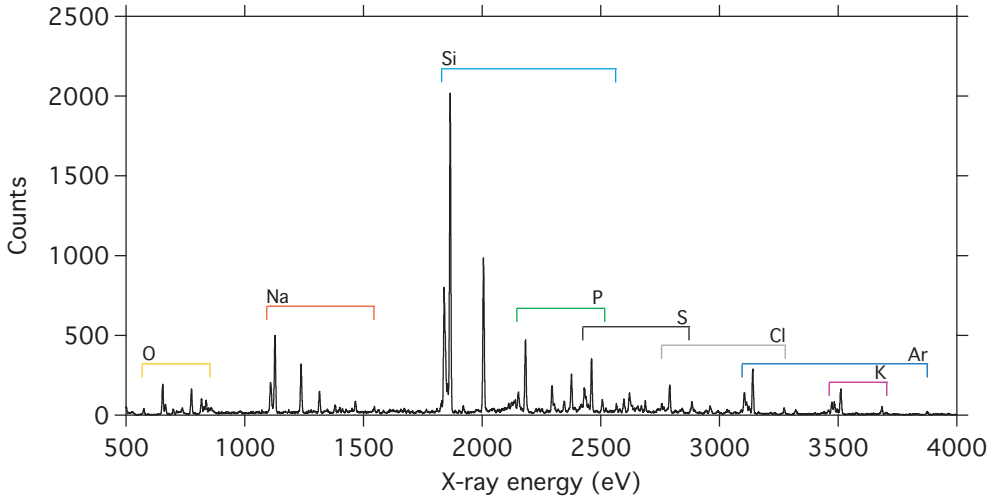

Figure 3.6: XRS spectrum of low-Z ions observed at SuperEBIT.

3.3.2 ECS Spectrometer

The EBIT Calorimeter Spectrometer (ECS) is the latest x-ray calorimeter in Livermore. The instrument has succeeded the role of the XRS as the main diagnostic of EBIT plasmas.

Similar to the XRS spectrometer, the ECS instrument is made up of a 6 $\times$ 6 array with 32 heat absorber elements. Eighteen of these are used for measurements in the 50 eV through 12 keV spectral interval with a quantum efficiency of 95 % and a spectral resolution of 4.5 eV at 6 keV. The other 14 pixels cover the 300 eV through 100 keV interval, and have a quantum efficiency of 32 % at 60 keV and a resolution of 33 eV; see Paper II and Ref. [99].

Tungsten spectroscopy of charge states isoelectronic to germanium through titanium has been carried out with the ECS spectrometer at EBIT-I. This is described in Chapter 5. The ECS has furthermore been used to measure L-shell transition energies in Mg-like W^{62+} through Li-like W^{71+} ions at SuperEBIT; see Chapter 4.

Part II

Tungsten Spectroscopy

Chapter 4

L-shell Tungsten

Future magnetic fusion devices, such as the ITER tokamak, will have sufficiently high temperatures for the tungsten charge state distributions to peak at the L-shell ions. The minimum energy to remove the 3s electron in sodiumlike tungsten is 7.1 keV, and energies in excess of 19.6 keV are required to reach the K shell [100]. According to the calculations by Gu reported in Ref. [101] and shown in Figs. 4.1 and 5.8, Ne-like W^{64+} has a fractional abundance of more than 10 % in the electron temperature interval between 12 and 33 keV. This wide temperature range in addition to the relatively simple spectrum make neonlike tungsten valuable for diagnostics of tokamak plasmas.

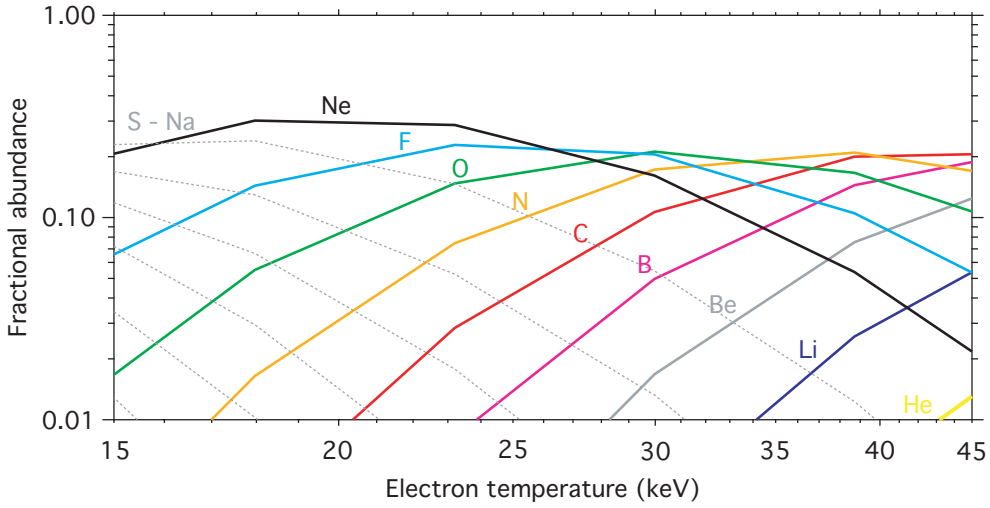

Figure 4.1: Tungsten charge balance for electron temperatures between 15 and 45 keV. Calculations by Gu [101].

L-shell tungsten spectra are proposed as the core plasma diagnostic of the ITER tokamak. The current design of the core imaging x-ray spectrometer (CIXS), which

will be the main instrument for measurements of ion-temperature profiles of the central ITER plasmas, is based on the $2p_{3/2}$ - $3d_{5/2}$ transition in Ne-like W^{64+} [101]. Due to the large plasma volume of ITER, charge exchange recombination spectroscopy, which is used in many present-day tokamaks for ion-temperature measurements, is not feasible because it is difficult for diagnostic neutral beams to penetrate into the central plasma. X-ray spectroscopy of highly charged tungsten ions therefore offers an attractive option.

The strong resonance lines in Ne-like W^{64+} have previously been measured at EBIT-I using high-resolution crystal spectroscopy [46, 47], and recently by Biedermann *et al.*, who observed some of the neonlike through siliconlike tungsten lines at the Berlin EBIT [57]. Dielectronic and radiative recombination lines have furthermore been observed at the Berlin EBIT [58] and at the Tokyo EBIT [102] using low-resolution germanium solid-state detectors.

The L-shell tungsten spectra have been investigated at Livermore. Here, SuperEBIT was employed to create and excite these highly charged ions, which were studied at electron-beam energies around 23.5, 51, 103, and 122 keV. The ECS spectrometer surveyed the L-shell emission from 0.5 keV up to 14 keV, thereby covering both the $n = 2$ - $n' = 2$ intrashell transitions at x-ray energies between 1 and 2 keV, and the $n = 2$ - $n' = 3$ transitions between 8 and 12 keV. High-resolution spectra of the $2s_{1/2}$ - $2p_{3/2}$ transitions were studied with the Blue crystal spectrometer; see Paper III. An overview of the L-shell emission is displayed in Fig. 4.2. This spectrum is from the ECS spectrometer taken at a beam energy of 51 keV.

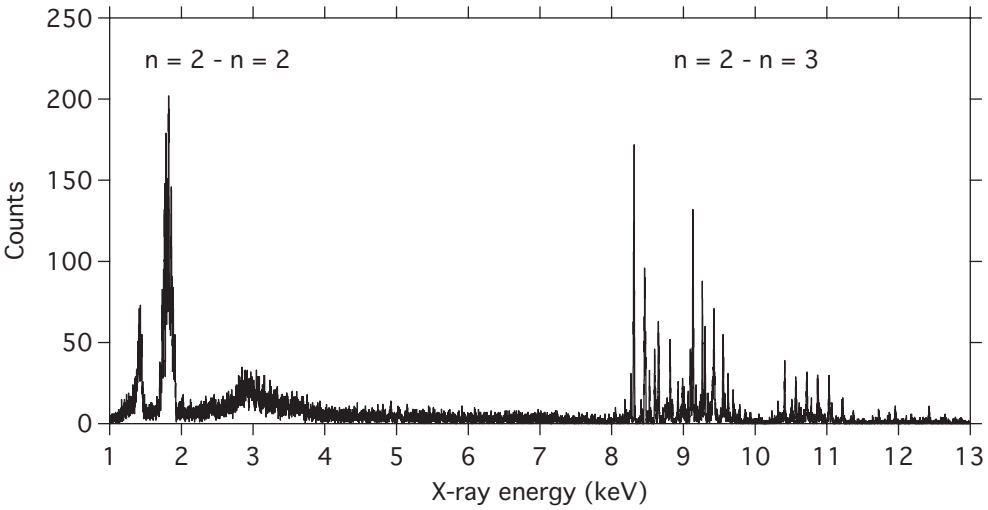

Figure 4.2: Measured SuperEBIT tungsten spectrum with the ECS spectrometer at an electron-beam energy of 51 keV.

To aid the line identification of the measured spectra the transition energies and line emissivities of the tungsten ions were calculated using the FAC code [103]. Spectra

were calculated for electron-beam energies of 25, 50, 100, and 125 keV and densities of 1×10^{12} cm^{-3}. Included configuration state functions for the L-shell ions are listed in Table 4.1. Configuration state functions used for the calculations of the M-shell ions, which were calculated with the frozen-core approximation, are listed in Paper IV.

Table 4.1: Configuration state functions for the tungsten L-shell ions used in the FAC calculations. n = 3, 4, 5. l = 0, 1, ..., n - 1.

Ne-like W^{64+}	F-like W^{65+}	O-like W^{66+}	N-like W^{67+}
$1s^22s^22p^6$	$1s^22s^22p^5$	$1s^22s^22p^4$	$1s^22s^22p^3$
$1s^22s^22p^5nl$	$1s^22s2p^6$	$1s^22s2p^5$	$1s^22s2p^4$
$1s^22s2p^6nl$	$1s^22s^22p^4nl$	$1s^22p^6$	$1s^22p^5$
$1s2s^22p^6nl$	$1s^22s2p^5nl$	$1s^22s^22p^3nl$	$1s^22s^22p^2nl$
	$1s^22p^6nl$	$1s^22s2p^4nl$	$1s^2$ 2s $2p^3nl$
	$1s2s^22p^6$	$1s^22p^5nl$	$1s^22p^4nl$
	$1s2s^22p^5nl$	$1s2s^22p^5$	$1s2s^22p^4$
	$1s2s2p^6nl$	$1s2s2p^6$	$1s2s2p^5$
		$1s2s^22p^4nl$	$1s2p^6$
		$1s2s2p^5nl$	$1s2s^22p^3nl$
		$1s2p^6nl$	$1s2s2p^4nl$
			$1s2p^5nl$
C-like W^{68+}	B-like W^{69+}	Be-like W^{70+}	Li-like W^{71+}
$1s^22s^22p^2$	$1s^22s^22p$	$1s^22s^2$	$1s^22s$
$1s^22s2p^3$	$1s^22s2p^2$	$1s^22s2p$	$1s^22p$
$1s^22p^4$	$1s^22p^3$	$1s^22p^2$	$1s^2nl$
$1s^22s^22pnl$	$1s^22s^2nl$	$1s^22snl$	$1s2s^2$
$1s^22s2p^2nl$	$1s^22s2pnl$	$1s^22pnl$	1s2s2p
$1s^22p^3nl$	$1s^22p^2nl$	$1s2s^22pnl$	$1s2p^2$
$1s2s^22p^3$	$1s2s^22p^2$	$1s2s2p^2nl$	$1s2snl$
$1s2s2p^4$	$1s2s2p^3nl$	$1s2p^3nl$	1s2pnl
$1s2p^5$	$1s2p^4nl$	$1s2s^2nl$	
$1s2s^22p^2nl$	$1s2s^22pnl$	1s2s2pnl	
$1s2s2p^3nl$	$1s2s2p^2nl$	$1s2p^2nl$	
$1s2p^4nl$	$1s2p^3nl$		

4.1 Intrashell Transitions

The $\Delta n = 0$ intrashell x-ray transitions in F-like W^{65+} through Li-like W^{71+} have been measured with the Blue crystal spectrometer and the ECS x-ray calorimeter. The measurements with the crystal spectrometer cover the $2s_{1/2}$ - $2p_{3/2}$ transitions and are reported in Paper III. The ECS data extend the spectral coverage and also include the $2p_{1/2}$ - $2p_{3/2}$ transitions.

4.1.1 Atomic Spectroscopy

Resonance transitions in few-electron ions provide good opportunities for high-precision measurements and theoretical predictions. Previously, the $2s_{1/2}$ - $2p_{3/2}$ transition has been measured in Li-like Bi^{80+} [104] and Li-like U^{89+} [105]. The measurement of this spectral transition in Li-like W^{71+} therefore provides isoelectronic data for high-Z ions. Such studies are important in atomic theory because the energy level structures of high-Z multi-electron ions are functions of nuclear-charge dependent QED and relativistic effects, as well as electron correlation. The measurement reported here covers resonance transitions from lithiumlike up to fluorinelike tungsten and thus provides benchmark data for future high-precision calculations.

The $n = 2$ - $n' = 2$ intrashell transitions were measured with both the Blue crystal spectrometer and the ECS x-ray calorimeter spectrometer. The good counting statistics and wide energy coverage of the ECS allowed for the determination of additional line positions and improvements on some of the $2s_{1/2}$ - $2p_{3/2}$ transitions also observed with the crystal spectrometer. The $2p_{1/2}$ - $2p_{3/2}$ transitions around 1400 eV were observed; however, only a few of these M1 transitions could also be measured as most of them were blended prohibiting a clear determination of the transition energies.

For the ECS measurement 14 of the 36 heat absorber elements were used. The detector temperature was set to the higher operating point of 65 mK in order to also cover the $n = 2$ to n - 3 transitions at higher photon energies. This also meant, however, that the spectral resolution was lowered, and line widths of around 7 eV were achieved. The voltage response for absorbed photons is slightly different for each pixel and the recorded signals were therefore voltage corrected before adding the data. Spectra were acquired over a two-week period and drifts in the electronics were noticed to cause line shifts below 0.2 eV. The spectrometer was energy calibrated with K-shell emission from hydrogen- and heliumlike oxygen, aluminum, and argon ions. A systematic energy shift was noticed and corrected for. The resulting calibration curve is believed to be accurate to within 0.5 eV. ECS spectra were acquired at electron-beam energies around 23.5, 51, 103, and 122 keV. The data from each energy have been summed to form a data set. These are displayed in Fig. 4.3.

Synthetic spectra were calculated using FAC to support line identifications. These spectra were modeled at electron-beam energies of 25, 50, 100, and 125 keV at an electron density of 1×10^{12} cm^{-3}. The lines profiles were set to 7 eV FWHM, corresponding to the instrumental resolution of the ECS spectrometer. The charge balances were estimated based on the number of counts in the strong resonance lines and the calculated line emissivities. The lines from carbonlike and berylliumlike tungsten were blended and the fractional abundances of these ions were therefore interpolated. The estimated charge balances are shown in Fig. 4.4. The calculated spectra are displayed together with the experimental spectra in Fig. 4.3. The $2s_{1/2}$ - $2p_{2/3}$ spectral signatures are well reproduced by the calculations. The M1 transitions around 1400 eV appear less intense than the experimental data. The calculations show that these lines are strongly blended.

Line Ne-1 is a 2-electron 1-photon electric-dipole transition only observed in the 23.5 keV spectrum. The calculations show that there are additional neonlike tungsten lines just below 1900 eV; however, they are blended with the much stronger oxygen-

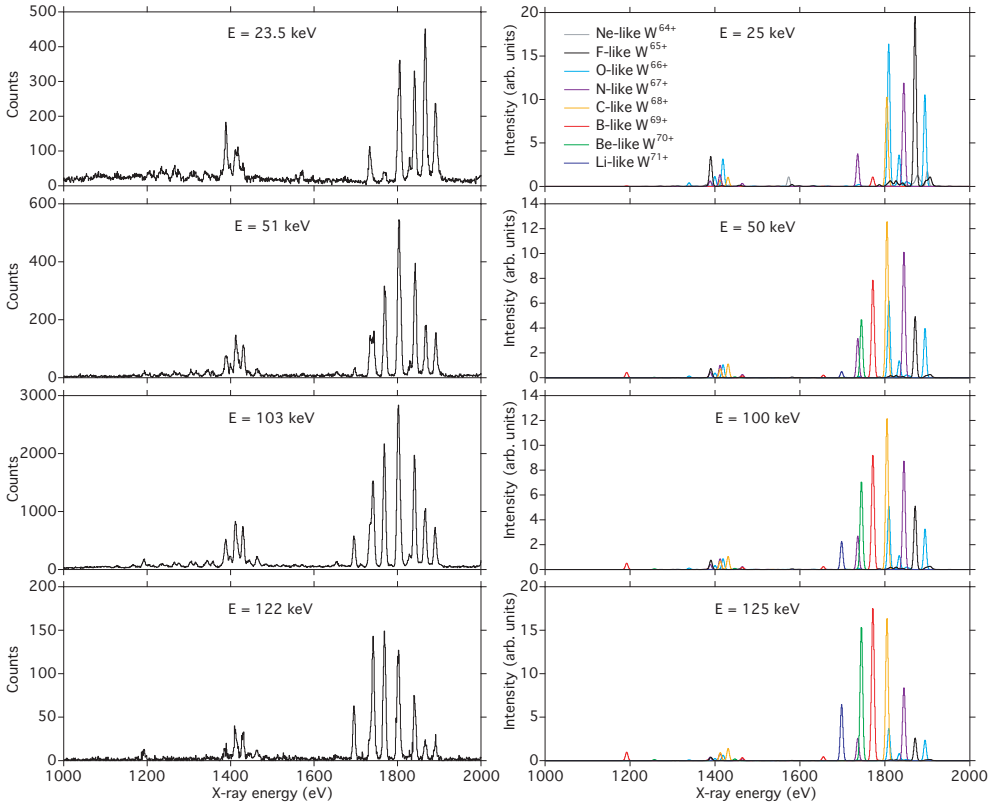

Figure 4.3: Tungsten $\Delta n = 0$ L-shell transitions. **Left**: Experimental spectra from SuperEBIT using the ECS spectrometer. **Right**: Synthetic spectra calculated using FAC.

and fluorinelike resonance lines.

Fluorinelike tungsten was observed in all data sets. The strong F-1 line was difficult to measure in the crystal data as it is possibly blended with the He-like Si^{12+} line w. The influence of the silicon in the ECS spectra is likely small. Still, the statistical uncertainty has been doubled to account for any small shifts. Line F-2 at 1388.9(5) eV is an M1 transition and the line position was determined in the 23.5 keV spectrum as the line was blended with nitrogenlike tungsten in the other data sets. Here the statistical uncertainty was doubled as well.

There are three E1 oxygenlike tungsten lines. O-1 was measured with the crystal spectrometer. Here, this line is blended with the strong carbonlike tungsten line C-1 prohibiting a determination of the line position. O-2 blends with neonlike tungsten in the 23.5 keV spectrum, and the line position is therefore averaged with the other data sets. O-3 at 1829.0(9) eV is measured in the 23.5 keV spectrum as it is not resolved in the other data sets. The statistical uncertainty has been doubled. There are also

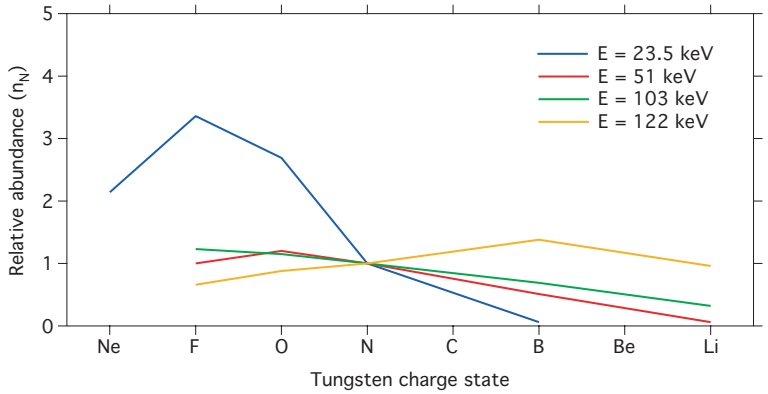

Figure 4.4: Estimated tungsten charge balance.

two M1 $2p_{1/2}$ - $2p_{3/2}$ oxygenlike tungsten transitions observed that were too blended to determine their positions with any accuracy.

The two strong N-like W^{67+} E1 transitions N-1a and N-1b could not be resolved with the ECS spectrometer. The average line position from all four data sets is 1841.5(5) eV, which is in good agreement with the crystal data. Line N-2 is determined in the 23.5 keV spectrum as it is blended with Be-1 at higher beam energies. Although the calculations suggest the Be-like W^{70+} line not to be present at 23.5 keV, the statistical uncertainty has nevertheless been doubled. One M1 $2p_{1/2}$ - $2p_{3/2}$ nitrogenlike tungsten line is also observed but its energy was not measured, as it is blended.

The C-1 line is blended with the O-1 line in most data sets. However, the feature is narrow in the 122 keV spectrum and the calculations indicate that the oxygenlike line only has a small contribution. The line position is therefore determined in the 122 keV spectrum and the statistical uncertainty doubled. Line C-2 is an E2 $2p_{1/2}$ - $2p_{3/2}$ transition. The 51, 103, and 122 keV data sets give an average line-position value of 1429.7(5).

The two strong B-like W^{69+} lines B-1a and B-1b, which are resolved in the crystal data, are blended in the ECS spectra. An average line position from all data sets give a line position of 1768.9(5) eV, in good agreement with the crystal measurement. The much weaker E1 transition B-2 is observed at 1654.0(6) eV in the 103 keV spectrum. A weak boronlike M1 line is also observed around 1463 eV, but the observed feature is an overlap with an M1 nitrogenlike line and the line position cannot be determined. Line B-3 is a 2-electron 1-photon E1 transition that was measured in the 103 keV data set.

Be-1 is measured in the 122 keV spectrum. It has a shoulder from N-2 and the statistical uncertainty has therefore been doubled.

The transition energy of Li-1 is the average value from the 103 and 122 keV spectra. The good counting statistics allows for the determination of the line position to within 0.5 eV, corresponding to an uncertainty of 0.03 %.

All measured line positions with the ECS spectrometer agree with the crystal

spectrometer data within the experimental error bars except line F-1. This line was only resolved in one of the crystal spectrometer data sets. There were trace amounts of silicon in the trap; however, the abundance of He-like Si^{14+} is expected to be very low and any overlap of the Si w line with F-1 should be very slight.

Table 4.2: Tungsten $\Delta n = 0$ L-shell transition energies. Experimental data from the ECS x-ray calorimeter spectrometer and the Blue crystal spectrometer. Theoretical energies from FAC. Units in electronvolts.

Line	Lower level	Upper level	ECS	Blue	FAC
B-3	$(2s_{1/2}2p^2_{1/2})_{1/2}$	$(2s^22p_{3/2})_{3/2}$	1192.5(6)		1191.6
F-2	$(2s^22p^2_{1/2}2p^3_{3/2})_{3/2}$	$(2s^22p_{1/2}2p^4_{3/2})_{1/2}$	1388.9(6)		1389.8
C-2	$(2s^22p^2_{1/2})_0$	$(2s^22p_{1/2}2p_{3/2})_2$	1429.7(5)		1430.4
Ne-1	$(2s^22p^2_{1/2}2p^3_{3/2}3s_{1/2})_1$	$(2s^22p_{1/2}2p^4_{3/2}3p_{1/2})_0$	1570.7(8)		1573.2
B-2	$(2s^22p_{1/2})_{1/2}$	$(2s_{1/2}2p_{1/2}2p_{3/2})_{3/2}$	1654.0(6)		1654.6
Li-1	$(2s_{1/2})_{1/2}$	$(2p_{3/2})_{3/2}$	1696.2(5)	1697(1)	1697.7
N-2	$(2s^22p^2_{1/2}2p_{3/2})_{3/2}$	$(2s_{1/2}2p^2_{1/2}2p^2_{3/2})_{5/2}$	1733.9(8)	1734(1)	1735.6
Be-1	$(2s^2)_0$	$(2s_{1/2}2p_{3/2})_1$	1741.4(6)	1741(1)	1744.2
B-1a	$(2s^22p_{1/2})_{1/2}$	$(2s_{1/2}2p_{1/2}2p_{3/2})_{1/2}$		1767(1)	1769.7
B-1b	$(2s^22p_{1/2})_{1/2}$	$(2s_{1/2}2p_{1/2}2p_{3/2})_{3/2}$		1769(1)	1772.0
C-1	$(2s^22p^2_{1/2})_0$	$(2s_{1/2}2p^2_{1/2}2p_{3/2})_1$	1802.0(8)	1801(2)	1804.4
O-1	$(2s^22p^2_{1/2}2p^2_{3/2})_2$	$(2s_{1/2}2p^2_{1/2}2p^3_{3/2})_2$		1806(2)	1808.8
O-3	$(2s^22p^2_{1/2}2p^2_{3/2})_0$	$(2s_{1/2}2p^2_{1/2}2p^3_{3/2})_1$	1829.0(9)		1833.3
N-1a	$(2s^22p^2_{1/2}2p_{3/2})_{3/2}$	$(2s_{1/2}2p^2_{1/2}2p^2_{3/2})_{1/2}$		1840(2)	1842.9
N-1b	$(2s^22p^2_{1/2}2p_{3/2})_{3/2}$	$(2s_{1/2}2p^2_{1/2}2p^2_{3/2})_{3/2}$		1842(2)	1844.7
F-1	$(2s^22p^2_{1/2}2p^3_{3/2})_{3/2}$	$(2s_{1/2}2p^2_{1/2}2p^4_{3/2})_{1/2}$	1866.5(5)	1871(2)	1870.7
O-2	$(2s^22p^2_{1/2}2p^2_{3/2})_2$	$(2s_{1/2}2p^2_{1/2}2p^3_{3/2})_1$	1890.8(5)	1891(2)	1894.0

4.1.2 Fusion Plasma Diagnostics

The strong $2s_{1/2}$ - $2p_{3/2}$ transitions suggest that the lines may be of interest for fast time-resolved charge-balance measurements. To investigate this possibility the tungsten spectra were modeled under tokamak-like conditions. Using FAC, the line emissivities were calculated for all the charge states with fractional abundances above 1 %, as shown in Fig. 4.1, for electron temperatures of 15, 25, 35, and 45 keV. The spectra were calculated for $n_e = 1 \times 10^{14}$ cm^{-3} and the line widths set to correspond to the Doppler broadening. Here, the ion temperatures were assumed equal to the electron temperatures. The line widths at $E = 1800$ eV vary from 1.25 eV to 2.17 eV FWHM. Level population mechanisms include collisional excitation and deexcitation, radiative cascades, and autoionization. Dielectronic recombination is included to the lowest levels of the daughter ion for all charge states above Al-like W^{61+}. The calculated spectra are displayed in Fig. 4.5, where the charge states of the strong lines are indicated.

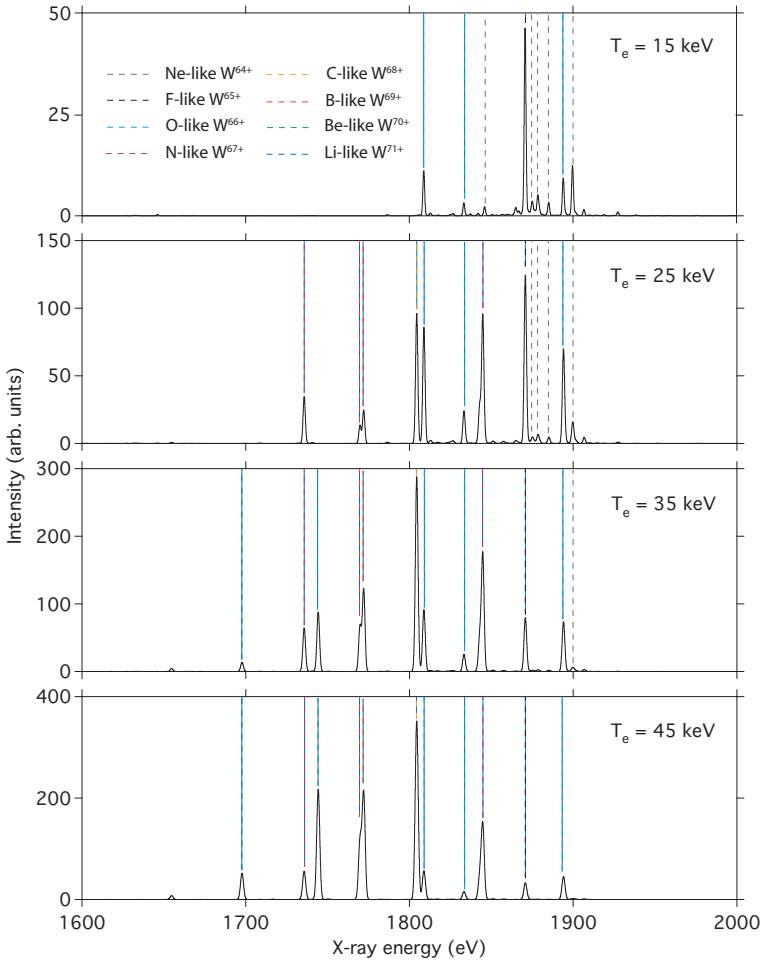

Figure 4.5: Theoretical spectra of tungsten modeled at $n_e = 1 \times 10^{14}$ cm^{-3}.

The spectral region between 1700 and 1900 eV contains several strong lines from the intrashell tungsten transitions. At each temperature, many charge states are present. In addition, the strong lines are resolved and, hence, this region should be suitable to infer the tungsten charge balance of a high-temperature tokamak plasma. This, in turn, could give information on the electron temperature and plasma transport. Even relatively small amounts of tungsten may be useful for diagnostics as these highly charged ions radiate plenty. For instance, each Li-like W^{71+} ion radiates more than 900 photons/s in the $2s_{1/2}$ - $2p_{3/2}$ transition at a temperature of 35 keV. If the concentrations of tungsten are sufficiently high, the L-shell spectra may even allow for fast time-resolved measurements.

4.2 Intershell Transitions

The $n = 2$ to $n = 3$ transitions in highly charged tungsten ions are of special interest since they constitute the physics basis of the CIXS crystal spectrometer that will measure the ion temperatures of ITER plasmas. It is especially the high fractional abundance of the neonlike charge state and the fact that tungsten will be an indigenous element in ITER plasmas that make this such an attractive diagnostic. Neonlike spectra have been studied extensively in tokamak plasmas for elements up to europium ($Z = 63$), see e.g. [106–109]. Ne-like W^{64+}; however, is not yet that well known. It has previously been measured by Beiersdorfer at EBIT-I [46, 47] and by Biedermann *et al.* at the Berlin EBIT [57].

4.2.1 Atomic Spectroscopy

Neonlike ions have 36 singly excited $2l3l'$ energy levels. This makes the neonlike spectrum comparatively simple as only a few resonance transitions are readily observable. Among these strong x-ray lines are seven E1 transitions, dubbed 3A through 3G, and five E2 transitions, labeled E2L, E2M, E2U, E2S, and E2T. The transition from the lowest excited level $(2p_{3/2}3s_{1/2})_2$ proceeds to the ground state via an M2 transition. This transition is energetically very close to the 3G line, which originates from the sister level of the same configuration, $(2p_{3/2}3s_{1/2})_1$. The second strong feature in the neonlike spectrum is the 3D transition from the $(2p_{3/2}3d_{5/2})_1$ level.

Table 4.3: Theoretical transition energies, transition probabilities and line emissivities of Ne-like W^{64+} calculated using FAC. Emissivities are calculated for $n_e = 1 \times 10^{14}$ cm^{-3} and $T_e = 25$ keV.

Line	Lower level	Upper level	ΔE (eV)	A (s^{-1})	ϵ (s^{-1}ion^{-1})
M2	$(2s^22p^6)_0$	$(2s^22p^2_{1/2}2p^3_{3/2}3s_{1/2})_2$	8293.4	4.12×10^9	90
3G	$(2s^22p^6)_0$	$(2s^22p^2_{1/2}2p^3_{3/2}3s_{1/2})_1$	8302.0	1.50×10^{14}	339
E2L	$(2s^22p^6)_0$	$(2s^22p^2_{1/2}2p^3_{3/2}3p_{1/2})_2$	8444.2	9.21×10^{11}	72
E2M	$(2s^22p^6)_0$	$(2s^22p^2_{1/2}2p^3_{3/2}3p_{3/2})_2$	8834.6	9.22×10^{11}	17
3E	$(2s^22p^6)_0$	$(2s^22p^2_{1/2}2p^3_{3/2}3d_{3/2})_1$	8990.1	7.84×10^{13}	31
3D	$(2s^22p^6)_0$	$(2s^22p^2_{1/2}2p^3_{3/2}3d_{5/2})_1$	9120.6	2.88×10^{15}	732
3F	$(2s^22p^6)_0$	$(2s^22p_{1/2}2p^4_{3/2}3s_{1/2})_1$	9683.8	3.65×10^{13}	51
3B	$(2s^22p^6)_0$	$(2s_{1/2}2p^63p_{1/2})_1$	10316.8	6.81×10^{14}	81
3C	$(2s^22p^6)_0$	$(2s^22p_{1/2}2p^4_{3/2}3d_{3/2})_1$	10404.0	1.49×10^{15}	231
3A	$(2s^22p^6)_0$	$(2s_{1/2}2p^63p_{3/2})_1$	10705.9	4.55×10^{14}	44
4D	$(2s^22p^6)_0$	$(2s^22p^2_{1/2}2p^3_{3/2}4d_{5/2})_1$	11950.9	9.77×10^{14}	101
4C	$(2s^22p^6)_0$	$(2s^22p_{1/2}2p^4_{3/2}4d_{3/2})_1$	13295.4	6.31×10^{14}	39

The ECS x-ray calorimeter observed the $n = 2$ to $n = 3$, 4 spectra in the 8 - 14 keV x-ray interval at electron-beam energies around 23.5, 51, and 103 keV. The 7 - 13 keV interval was energy calibrated with K-shell emission from highly charged iron and krypton ions. The signals from each of the 14 pixels used for the measurement

was voltage corrected to account for the slightly different thermal response of the heat absorbers. The data at each beam energy have been added to form a data set.

The measured lines were identified with the theoretical spectra calculated using FAC. Theoretical transition energies and line emissivities from Si-like W^{60+} through Li-like W^{71+} were compared with the experimental spectra. Calculated energies and transition probabilities for the observed Ne-like W^{64+} lines are listed in Table 4.3.

All data sets are dominated by the neonlike tungsten spectrum. The observed Ne-like W^{64+} lines are listed in Table 4.3 and labeled in Figs. 4.6 and 4.7. The 23.5 keV spectrum is displayed in Fig. 4.6, where also the expected coverage of the CIXS instrument is indicated. The strong lines are labeled according to charge state. In addition to the neonlike tungsten lines, the observed features are mainly from sodium-, magnesium-, aluminum-, fluorine-, and oxygenlike tungsten ions. The lines from these adjacent ions, though, are all much weaker than neonlike tungsten.

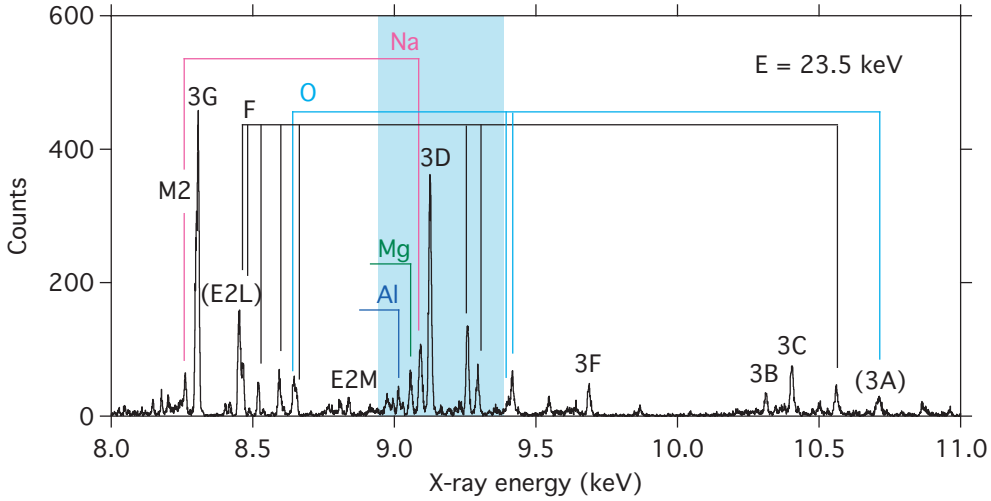

Figure 4.6: Tungsten intershell spectrum measured with the ECS spectrometer at SuperEBIT at an electron-beam energy of 23.5 keV. The approximate region covered by CIXS is indicated by the shaded area. The stronger lines are labeled by charge state and the Ne-like W^{64+} lines according to transition. Lines E2L and 3A are blended with F-like W^{65+} and O-like W^{66+} lines, respectively.

The $E = 103$ keV data set reveals all the L-shell tungsten charge states. The ECS spectrum is shown in Fig. 4.7, where it is divided in two sections for clarity. Here, the fluorine-, oxygen-, and nitrogenlike tungsten lines are quite strong. The higher charge states show mainly between 10 and 12 keV. At yet higher x-ray energies two $\Delta n = 2$ neonlike tungsten transition are observed, lines 4D and 4C from the $(2p_{3/2}4d_{5/2})_1$ and $(2p_{1/2}4d_{3/2})_1$ levels to the ground state.

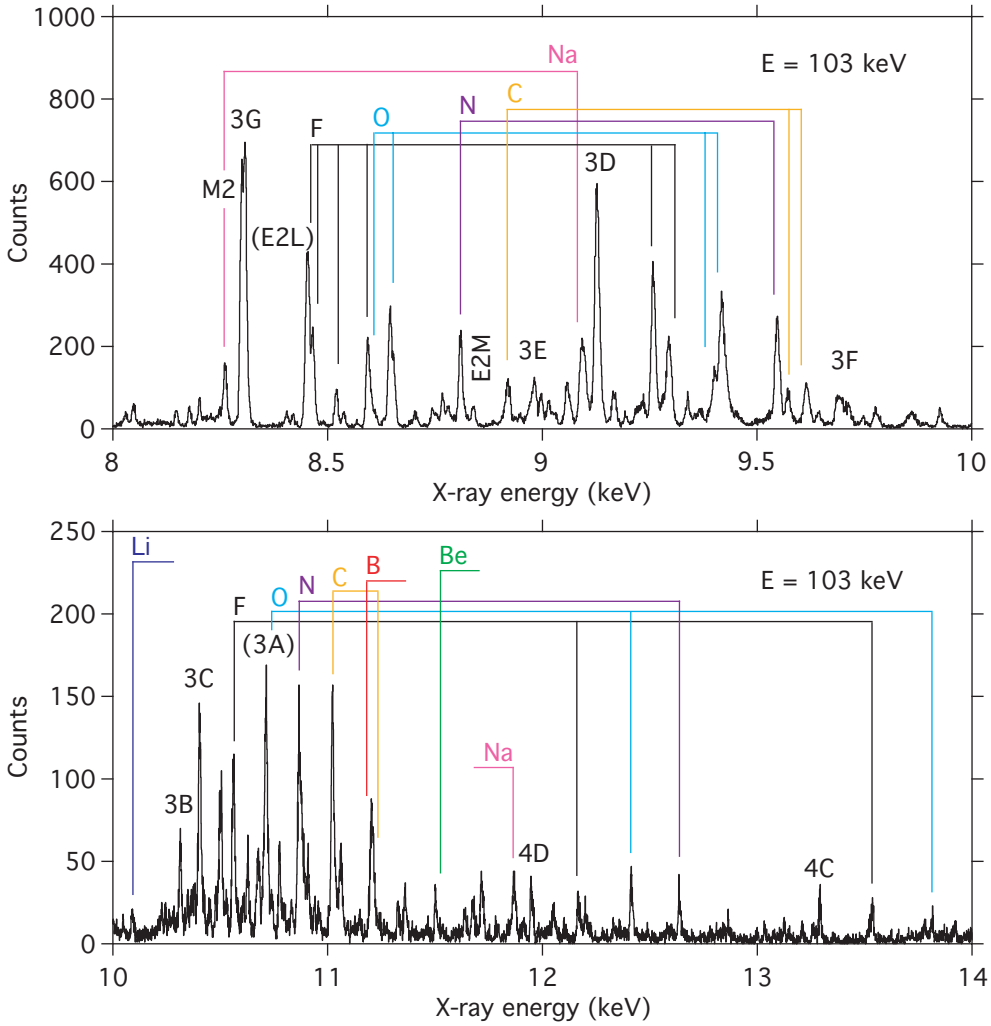

Figure 4.7: Tungsten L-shell spectrum measured with the ECS spectrometer at SuperEBIT at $E = 103$ keV. The stronger lines are labeled by charge state and the Ne-like W^{64+} lines according to transition. Lines E2L and 3A are blended with F-like W^{65+} and O-like W^{66+} lines, respectively. **Top**: The 8 - 10 keV interval includes the region around 3D proposed for the CIXS instrument. **Bottom**: The 10 - 14 keV range include all the L-shell spectra.

4.2.2 Fusion Plasma Diagnostics

The CIXS crystal spectrometer will be one of the main diagnostics of the ITER core plasmas. The objectives of the instrument are to establish ion and electron temperature profiles and toroidal and poloidal rotation velocities. Tungsten is chosen

as the working radiation and therefore underlies the design of CIXS, which is described in Ref. [101]. One of the main reasons for selecting the tungsten L-shell emission is because tungsten is the only indigenous high-Z element in ITER. Even the high temperatures expected in the center plasmas will not be enough to strip tungsten of its electrons, cf. Fig. 4.1, and thus tungsten ions will serve as intrinsic probes of the core conditions. CIXS will focus on the spectral region around the 3D line in Ne-like W^{64+} and the neighboring lines from adjacent charge states. This region therefore allows the tungsten charge balance to be inferred in addition to Doppler broadening measurements for ion temperature profiles and the Doppler shift measurements for velocity determinations.

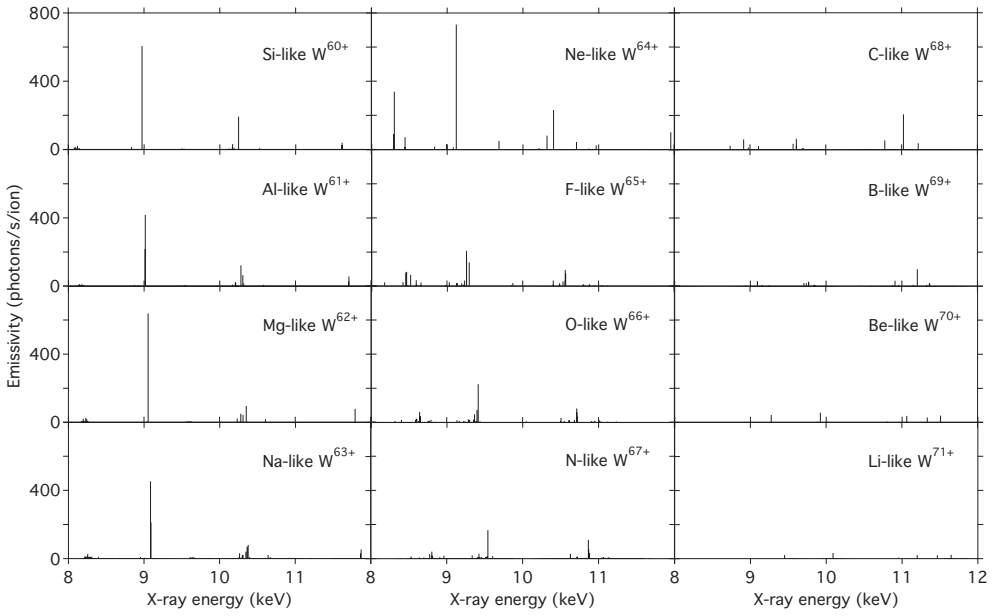

Figure 4.8: Line emissivities of tungsten calculated at $n_e = 1 \times 10^{14}$ cm^{-3} and $T_e = 25$ keV.

Theoretical spectra of highly charged tungsten ions have been calculated for tokamak plasmas in the spectral region from 7 keV to 14 keV. Line intensities as functions of electron temperature are necessary to know in order to establish accurate ion-temperature profiles. The spectra of Si-like W^{60+} through Li-like W^{71+} were calculated for plasma densities of $n_e = 1 \times 10^{14}$ cm^{-3} and electron temperatures between 15 keV and 45 keV. Excitation mechanisms include electron impact, radiative cascades, autoionization, and dielectronic recombination for charge states above Al-like W^{61+}. Figure 4.8 displays the calculated line emissivities between 8 and 12 keV at $T_e = 25$ keV. The neonlike tungsten ion line emissivities are listed in Table 4.3.

Chapter 5

M-shell Tungsten

This chapter reports on M-shell tungsten spectra. This includes not only the spectra from ions with an $n = 3$ valence electron, but also spectra from those ions with only a few electrons in the $n = 4$ shell, which have strong transitions to $n = 3$, such as e.g. copper- and zinclike tungsten ions.

5.1 Intrashell Transitions

Paper IV reports on a high-precision measurement of the $3s_{1/2}$ - $3p_{3/2}$ lines in Na-like W^{63+} and Mg-like W^{62+}, and the $3p_{1/2}$ - $3d_{3/2}$ lines in Al-like W^{61+} and Si-like W^{60+}. The measurement also includes corresponding transitions in ions down to K-like W^{55+} in the 19 - 25 Å soft x-ray region. A measured spectrum of tungsten is shown in Fig. 5.1 together with nitrogen and oxygen K-shell reference spectra. These spectra display filtered data from one run day with the SuperEBIT electron beam ion trap at an electron-beam energy of 23.5 keV using the Gold Flat Field Spectrometer (GFFS). By adding data from four days, 20 $\Delta n = 0$ transitions from K-like W^{55+} to Ne-like W^{64+} could be identified and measured.

5.1.1 Atomic Spectroscopy

The resonance lines from ions with only one or a few electrons outside the last closed shell are of interest in atomic structure theory as they provide good test systems for atomic modeling. Several authors have calculated the $3s_{1/2}$ - $3p_{3/2}$ transition in sodiumlike ions, which only have one valence electron outside the filled L shell. Such calculations need experimental verification and most $3s_{1/2}$ - $3p_{3/2}$ lines in sodiumlike ions up to Xe^{43+} have been measured. For higher-Z ions, however, not that many measurements exist. Especially, there are no previous high-precision measurements reported that could guide theory for sodiumlike ions between Cs^{44+} and Pt^{67+}.

The new Na-like W^{63+} wavelength measurement is shown in Fig. 5.2 together with earlier high-Z measurements in the sodium isoelectronic sequence. The measurements are compared with *ab initio* calculations by Kim and Cheng [110], Johnson *et al.* [111],

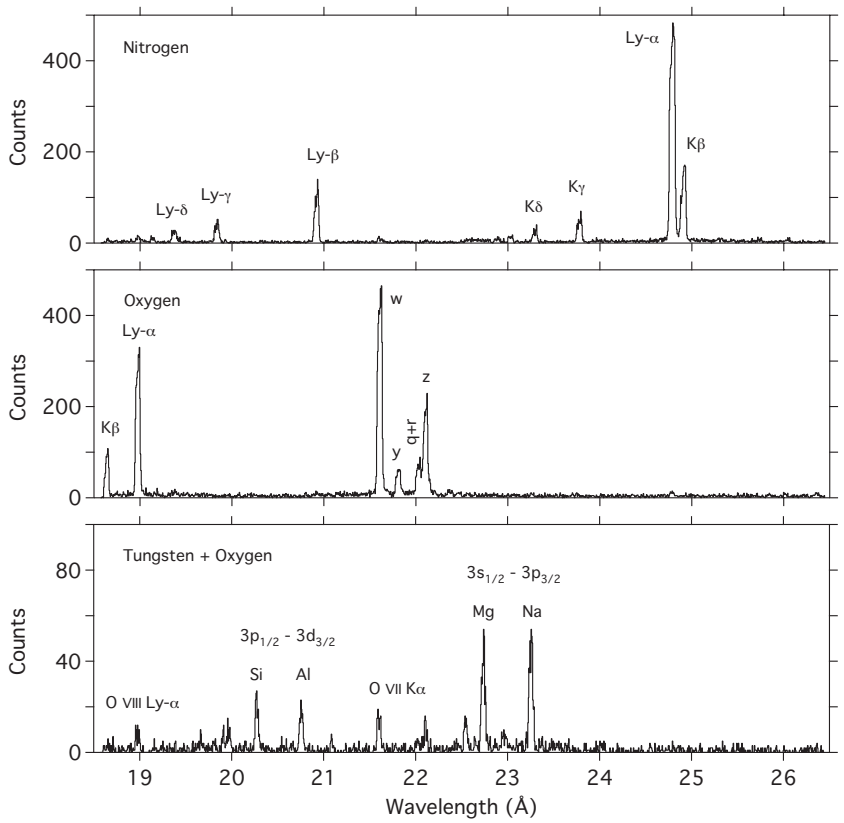

Figure 5.1: Nitrogen, oxygen, and tungsten spectra from one run day at SuperEBIT with the GFFS.

Baik *et al.* [112], Kim *et al.* [113], Seely *et al.* [114], and Blundell [115], and semi-empirical calculations of Ivanov and Ivanova [116], Kim *et al.* [113], and Seely *et al.* [114,117]. All data points are normalized to the theory of Seely *et al.* [114]. Note that the wavelengths calculated by Kim and Cheng [110], Johnson *et al.* [111], and Blundell [115] have been interpolated.

Most of the previous $3s_{1/2}$ - $3p_{3/2}$ measurements in high-Z sodiumlike ions have been performed on electron beam ion traps. Träbert *et al.* measured Xe^{43+} on SuperEBIT [118], Cowan *et al.* studied Pt^{67+} on EBIT-II [119], Gillaspy *et al.* made use of the NIST EBIT to study Hf^{61+}, Ta^{62+}, W^{63+}, and Au^{68+} [53], and Beiersdorfer *et al.* measured Pb^{71+} [120] and U^{81+} [121] on SuperEBIT and EBIT-I. Seely *et al.* studied laser-produced plasmas for the measurement of Cs^{44+} at the Rochester OMEGA laser [122] and of Gd^{53+} at the Livermore Nova laser [114]. Seely *et al.* have also reported a measurement of Xe^{43+} [114,124]. Another high-precision measurement of Pb^{71+} was performed with the Unilac accelerator at GSI, Darmstadt by Simionivici *et al.* [123]. Together with the measurements of Pt, Pb, and U, the new W data point map out the high-Z dependence on the sodiumlike resonance transition.

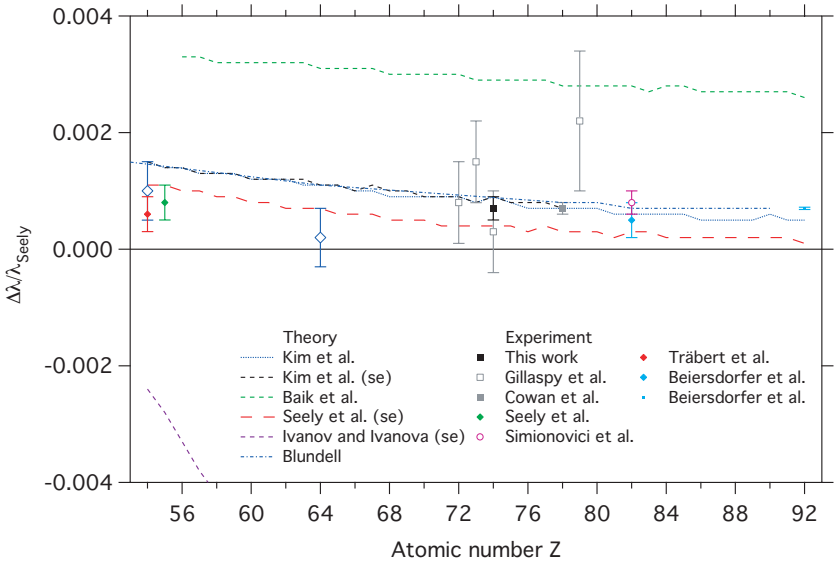

Figure 5.2: Measured and calculated $3s_{1/2}$ - $3p_{3/2}$ transitions in high-Z sodiumlike ions. Theory from Refs. [110–117], where numbers from Refs. [110,111] are off the scale. Values for Refs. [110,111,115] are interpolated. Experimental data from Paper IV and Refs. [53, 114, 118–123]. All data are normalized to calculations by Seely *et al.* [114].

Two-electron systems, i.e. ions having two valence electrons outside the last closed shell, such as heliumlike, magnesiumlike, and zinclike ions, are already much more complicated than the one-electron systems. Especially the structure of high-Z ions, where strong relativistic and quantum-electrodynamic (QED) effects add to electron-correlation contributions are challenging systems. Spectroscopic measurements of the $3s^2$ - $3s_{1/2}3p_{3/2}$ transition in high-Z magnesiumlike ions have been performed by Träbert *et al.* for Xe^{42+} on SuperEBIT [118], by Seely *et al.* for Cs^{43+} at OMEGA [122], for Hf^{60+}, Ta^{61+}, W^{62+}, and Au^{67+} by Gillaspy *et al.* at the NIST EBIT [53], by Beiersdorfer and Wargelin for Pb^{70+} at EBIT-I [120], and by Chen *et al.* for U^{80+} on EBIT-I [125]. Available wavelength calculations for high-Z magnesiumlike ions have widely disparate predictions, as seen in Fig. 5.3, where the measurements of the $3s^2$ - $3s_{1/2}3p_{3/2}$ transition, including the new data point on Mg-like W^{62+}, are compared to *ab initio* calculations by Cheng and Johnson [126], Marques *et al.* [127], Zou and Froese Fischer [128], and Shorer *et al* [129], and the semi-empirical calculations of Ivanova *et al* [130]. The wavelengths by Refs. [128–130] have been interpolated. It is clear that additional measurements are required to guide atomic theory, especially for magnesiumlike ions between Cs^{43+} and W^{62+}.

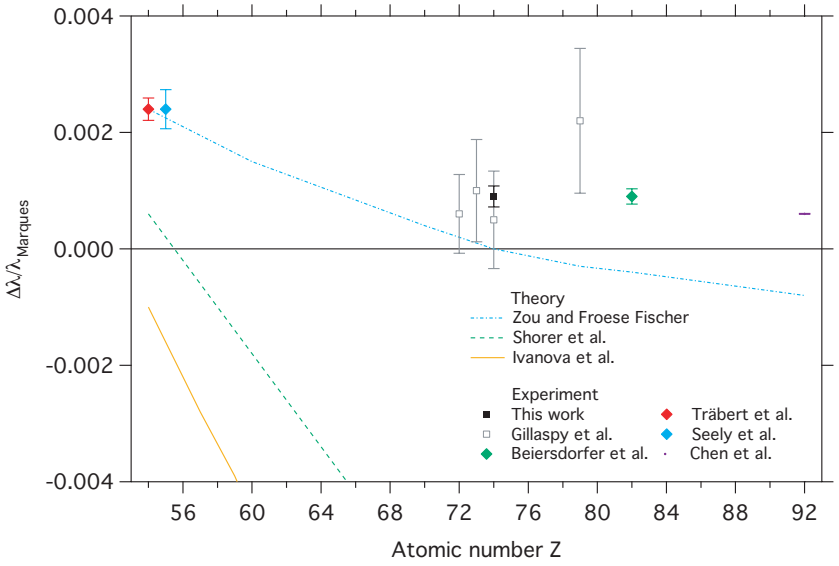

Figure 5.3: Measured and calculated $3s^2$ - $3s_{1/2}3p_{3/2}$ transitions in high-Z magnesiumlike ions. Theory from Refs. [127–130], where numbers from Ref. [126] are off the scale. Values for Refs. [128–130] have been interpolated. Experimental data from Paper IV and Refs. [53,118,120,122,125]. All data are normalized to calculations by Marques *et al.* [127].

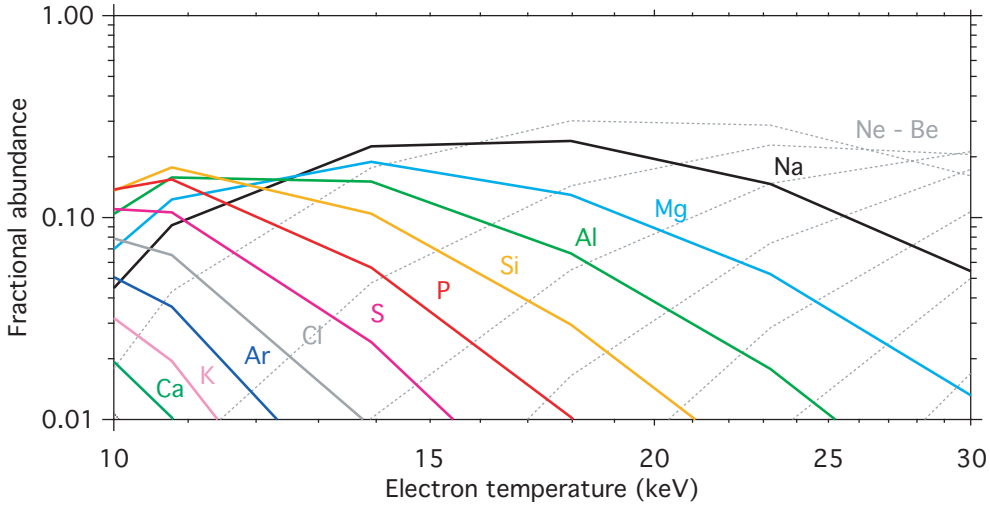

Figure 5.4: Tungsten charge balance for electron temperatures between 10 and 30 keV. Calculations by Gu [101].

5.1.2 Fusion Plasma Diagnostics

The core plasmas of ITER will have electron densities of 10^{14} cm^{-3} and electron and ion temperatures in the 10 - 30 keV interval. As demonstrated by the ionization-balance calculations by Gu reported in Ref. [101], sodiumlike and magnesiumlike tungsten ions are abundant in this range. These calculations are done for electron densities of 10^{14} cm^{-3} and include charge states from nickellike to heliumlike tungsten. A similar diagram is displayed in Fig. 5.4, where all charge states with fractional abundances above 1 % in the 10 - 30 keV interval are shown. In this temperature interval both M- and L-shell tungsten ions are abundant. However, only the M-shell ions radiate significantly at wavelengths above 10 Å. The L-shell ions emit most of their energy in $n = 2$ - $n' = 2$ and $n = 2$ - $n' = 3$ transitions, but even so, these short-wavelength transitions are much weaker than the M-shell transitions. Furthermore, the $\Delta n = 0$ transitions are the strongest lines in the spectra of highly charged M-shell tungsten ions. This makes the 10 - 60 Å soft x-ray interval that the Livermore GFFS spectrometer can cover very interesting for plasma spectroscopy. Calculated line emissivities in this spectral region for plasmas with $T_e = 20$ keV and $n_e = 10^{14}$ cm^{-3} are shown in Fig. 5.5. Especially the 19 - 25 Å interval has strong spectral lines from several charge states, and is therefore promising for diagnosing ITER plasmas in the 10 - 30 keV temperature range. For diagnostics of plasmas with somewhat lower temperatures, the wavelength region of 30 - 40 Å could be useful as the $3p_{3/2}$ - $3d_{5/2}$ emission from several tungsten ions fall in this range.

The tungsten emission from tokamak plasmas have been modeled with FAC and is shown between 15 and 30 Å in Fig. 5.6. The spectra are calculated for thermal equilibrium at an electron density of $n_e = 1 \times 10^{14}$ cm^{-3} and temperatures T_e of 10, 20, and 30 keV. Charge states from Ca-like W^{54+} to Ne-like W^{64+} have been included in fractional abundances similar to Fig. 5.4. The included configuration state functions for the ions are listed in Paper IV. The line profiles are modeled with Gaussian distributions with line widths corresponding to the Doppler broadening (the ion temperatures are assumed identical to the electron temperatures). Line widths will thus vary from about 13 to 22 mÅ FWHM. A spectrometer with a resolving power of greater than 2000 is therefore required to measure the ion temperatures. This is comparable to the achievable resolution with the GFFS. However, the line widths measured with the GFFS are limited by the electron-beam width of SuperEBIT. On a tokamak, however, imaging slits are required and slit widths of around 10 μm together with a smaller pixel-size CCD detector would probably decrease the line widths. The spectral coverage is also sufficiently wide to observe the emission from several charge states. This would allow for measurements of the charge balance or of the tungsten abundance. A spectrometer similar to the Livermore design would therefore work very well for diagnostics of high-temperature fusion plasmas.

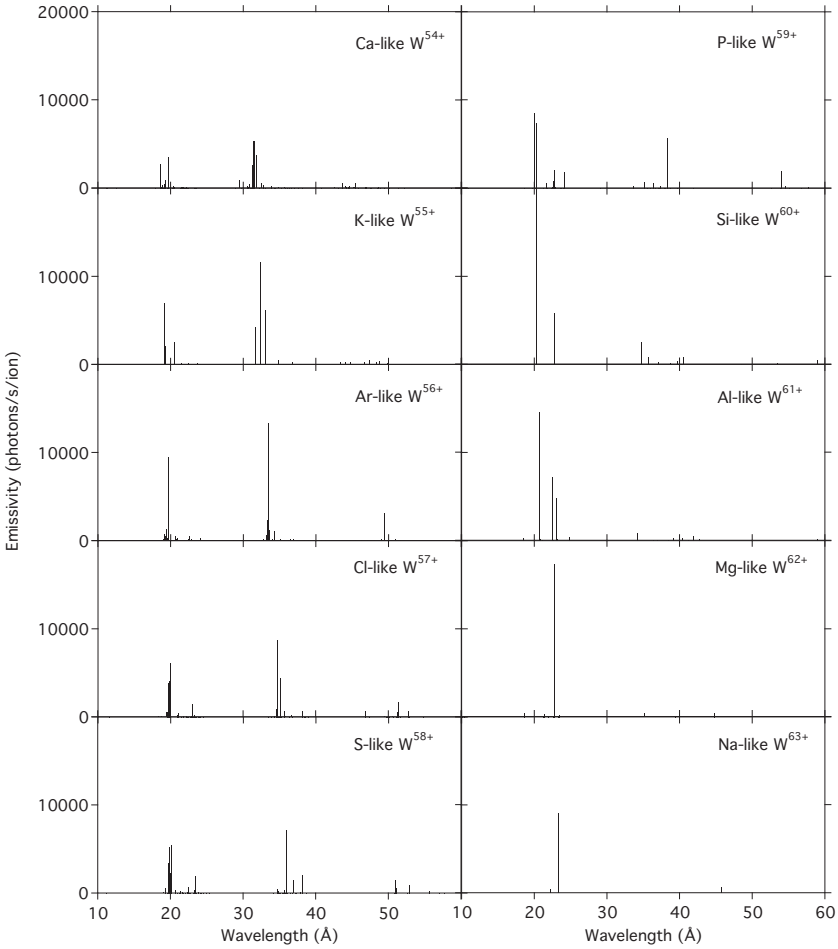

Figure 5.5: Calculated spectra of M-shell tungsten ions in the 10 - 60 Å soft x-ray range for an electron temperature of $T_e = 20$ keV and density of $n_e = 1 \times 10^{14}$ cm^{-3}. The $3p_{1/2}$ - $3d_{3/2}$ line in Si-like W^{60+} has a line emissivity of just above 20 000 photons/s/ion.

5.2 Intershell Transitions

The ions around nickellike tungsten have strong M-shell transitions. In particular, the intershell x-ray transitions connecting the 3d subshell between 2000 and 2500 eV are very intense. Many of these transitions have been studied previously, both on EBITs [52, 57, 65, 131, 132] and on laser-produced plasmas, see e.g. [28–31, 133–135]. These transitions have also been observed at the ASDEX Upgrade tokamak [45] and can be expected to be a common feature in future tokamak plasmas.

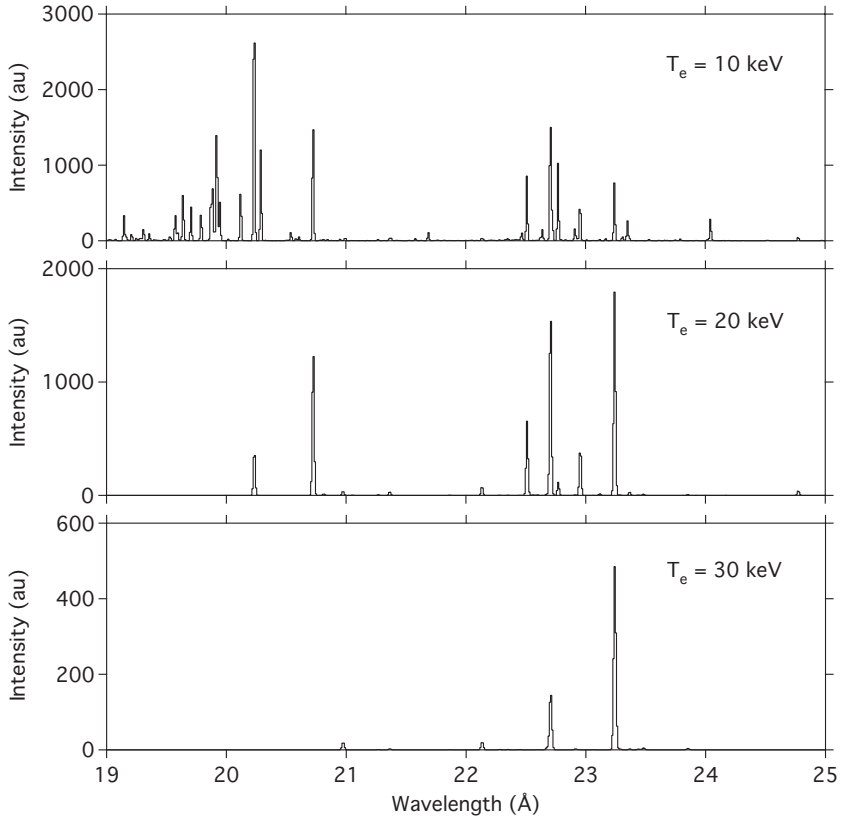

Figure 5.6: Calculated soft x-ray spectrum of tungsten at $n_e = 1 \times 10^{14}$ cm^{-3} for $T_e = 10$, 20, and 30 keV.

5.2.1 Atomic Spectroscopy

Paper V reports on broad-band spectra of Zn-like W^{44+} through Co-like W^{47+} measured at SuperEBIT with the XRS spectrometer. Spectra were studied in the 1500 - 3600 eV x-ray range and transitions with upper levels including $n = 8$ were measured. The work identified several new lines and improved the accuracies of previously measured transition energies.

An extension of the work presented in Paper V has been performed at EBIT-I using the ECS spectrometer [136], with the purpose to study the $\Delta n = 1$ transitions of higher charge states than reported in Paper V. Here, the tungsten was supplied to the EBIT-I trap using a sublimation injector containing tungsten hexacarbonyl, $W(CO)_6$. The tungsten gas was injected at low pressures (around $5 - 9 \times 10^{-8}$ Torr) to the trap. The ions were stored in cycles of two minutes before the trap was emptied in order to improve the charge balance, which typically shifts toward lower charge states when ions are supplied continuously to the trap. To favor the storing of highly charged ions, the trap voltage was set to only 50 V. In addition, neon gas was injected

to the trap at 5×10^{-8} Torr to provide evaporative cooling of the heavy tungsten ions. The much lighter neon ions equilibrate with the tungsten ions but, due to the lower charge, are not as deeply trapped. Neon ions that leave the trap carries away energy and thereby cool the trapped tungsten ions. The neon also served to provide energy-calibration lines for the tungsten spectra. Dedicated calibration spectra were also taken with both neon and argon. Data were acquired at electron-beam energies from 4.0 keV up to 6.5 keV. With beam currents of 110 mA the electron densities were estimated to be around 4×10^{12} cm^{-3}.

To support line identification of the EBIT data, the M-shell spectra of tungsten ions isoelectronic to germanium, W^{42+}, through titanium, W^{52+}, were calculated using the FAC code [103]. Synthetic EBIT spectra of Zn-like W^{42+} through Co-like W^{47+} are presented in Paper V. For the EBIT-I data, the calculated spectra were modeled with 4.5 eV line widths, corresponding to the experimental resolution of the ECS spectrometer. The spectra of Ga-like W^{43+} through Fe-like W^{48+} have also been calculated for tokamak plasmas, which are presented in Paper VI. The structure and spectra of the six tungsten ions are calculated and transition energies, oscillator strengths, and transition probabilities are tabulated. The line emissivities are also listed for plasmas of densities $n_e = 1 \times 10^{14}$ cm^{-3} and electron temperatures chosen about 50 % higher than the peak abundance temperature for each charge state, according to the charge-balance calculations by Pütterich *et al.* [137].

5.2.2 Fusion Plasma Diagnostics

The large number of transitions from several charge states centered around the nickellike tungsten spectrum provides good charge balance and ion abundance diagnostic possibilites. Especially the $3d_{3/2}$ - $4f_{5/2}$ transitions are suitable for plasma spectroscopy since these are strong and the individual charge states are relatively easy to separate. This is illustrated in Fig. 5.7, where the 2000 - 2500 eV spectral interval is displayed. The experimental spectrum is from the recent ECS measurement on EBIT-I at an electron-beam energy of 6.5 keV. The figure also shows calculated M-shell spectra of Ge-like W^{42+} through Ti-like W^{52+} modeled at the EBIT plasma parameters, $n_e = 4 \times 10^{12}$ cm^{-3} and $E = 6.5$ keV with 4.5 eV FWHM line widths, corresponding to the resolution of the ECS spectrometer. The charge balance is estimated from the calculated line emissivities and the measured intensities of the strong lines. No lines from Zn-like W^{44+} or Ga-like W^{43+} were resolved and the relative abundances of these ions are interpolated between the inferred Ge-like W^{42+} and Cu-like W^{45+} fractional abundances. The estimated charge balance is shown in Fig. 5.8, where the abundances are presented relative to the nickellike tungsten abundance.

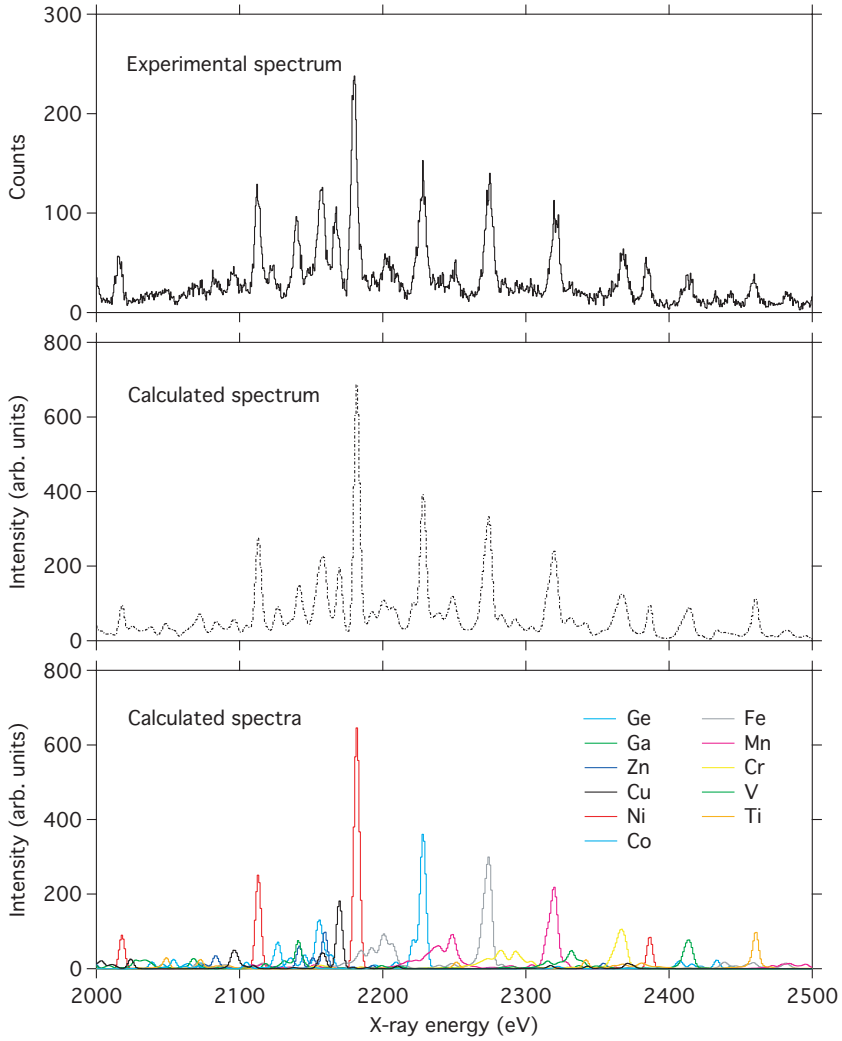

Figure 5.7: 3d - 4f transitions in Ge-like W^{42+} through Ti-like W^{52+}. **Top**: Measured spectrum at EBIT-I with the ECS spectrometer at an electron-beam energy of 6.5 keV. **Middle**: Synthetic spectrum calculated using FAC. **Bottom**: Calculated spectra using FAC.

5.3 E1-Forbidden Transitions in Ni-like W

Excited levels that are the lowest above ground and that have a total angular momentum J that differs from that of the ground level by more than 1 $\hbar$ or have the same parity than the ground level are metastable. These levels can have large populations due to radiative cascades. The levels can only radiatively decay via electric dipole (E1) forbidden transitions and are therefore sensitive to collisional quenching. However,

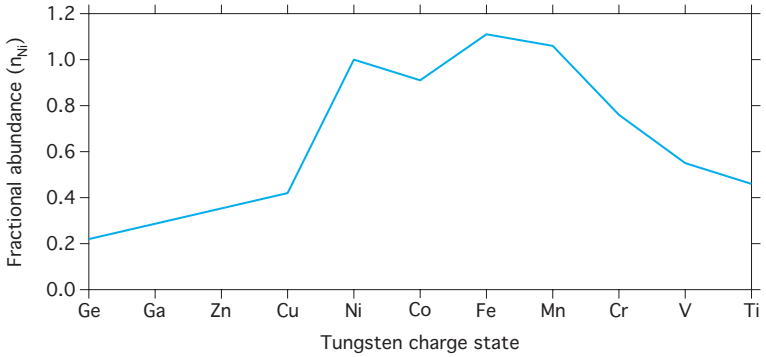

Figure 5.8: Estimated EBIT-I charge balance at $E = 6.5$ keV with tungsten hexacarbonyl injection.

if the plasma density is sufficiently low, then E1-forbidden transitions can compete as a depopulation mechanism with the collisional decay. This is especially true for high-Z systems, because the transition probabilities for these radiative multipoles are strongly dependent on the nuclear charge.

Forty-six times ionized tungsten is isoelectronic to nickel and is predicted to be one of the most abundant tungsten charge states in tokamak plasmas. According to calculations by Pütterich *et al.* [137], the ion has a fractional abundance of more than 10 % over the 3 - 7 keV electron-temperature interval. This is typical temperatures at which present-day tokamaks operate at and what the ITER tokamak will have during ohmic plasmas. Nickellike high-Z ions have a ground configuration of $3s^2 3p^6 3d^{10}$ with the first excited levels being $(3d_{5/2} 4s_{1/2})_{3,2}$. These levels can only decay radiatively through magnetic-octupole (M3) and electric-quadrupole (E2) transitions, respectively. The nickellike system is thus analogous to the closed-shell ions isoelectronic to helium and neon, whose lowest levels decay through magnetic-dipole (M1) and magnetic-quadrupole (M2) transitions, respectively [138].

The first magnetic-octupole transitions were observed in the spectra of Ni-like Th^{62+} and U^{64+} ions at EBIT-I in 1991 by Beiersdorfer *et al.* [138]. The same transition has later been studied in Ni-like Xe^{26+}, Cs^{27+}, and Ba^{28+} ions at EBIT-I and SuperEBIT in 2005 - 2007 by Träbert *et al.* [139–141].

The E2 and M3 lines have attracted much attention in the nickellike tungsten spectrum. The lines were first observed as an unresolved feature at the ASDEX Upgrade tokamak by Neu *et al.* [45] and interpreted as the E2 transition. Still, the intensity of the line could not be explained by theory [43, 137, 142]. Loch *et al.* [143] and Ralchenko *et al.* [52, 144] suggested that the feature could be a blend of the E2 and M3 lines. The unresolved feature has also been observed at the NIST EBIT [52] and at SuperEBIT; see Paper V.

The wavelengths, or corresponding energy levels, of the two tungsten transitions were first calculated by Zhang *et al.* in 1991 [145] and have been followed by predictions from Fournier in 1998 [146], Aggarwal *et al.* in 2000 [147], Safronova *et al.* in 2006 [148], Ballance and Griffin in 2006 [149], and Ralchenko *et al.* in 2006 [52].

5.3.1 Atomic Spectroscopy

Described in Paper VII is a measurement at SuperEBIT where the two electric dipole-forbidden Ni-like W^{46+} lines have been resolved. The tungsten lines were measured with the Blue and the Bradley II crystal spectrometers for electron-impact excitation energies from 3.3 to 5.4 keV. The wide wavelength coverage of the Blue spectrometer was used to determine the wavelengths of the lines. Figure 5.9 shows K-shell lines from sodium and aluminum that were used for wavelength calibration. A high-resolution spectrum obtained with the Bradley II spectrometer is displayed in Fig. 5.10, which shows the two tungsten lines for an electron excitation energy of 4.2 keV.

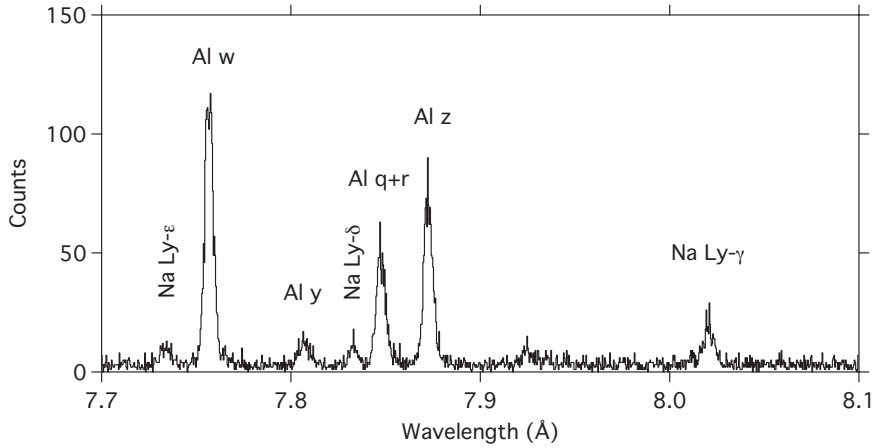

Figure 5.9: Broad band crystal spectrum showing the Lyman series of H-like Na XI and the Kα lines of He-like Al XII together with dielectronic satellite lines of Li-like Al XI.

The wavelengths of the lines have been calculated using the FAC code, written by Gu [103]. FAC has also been used in the calculations by Ralchenko *et al.* [52,144] and Safronova *et al.* [65]. In addition, the polarization and intensities of the lines were modeled with FAC for various plasma conditions. Previously, Ralchenko had studied the line intensities using the NOMAD code [144].

5.3.2 Fusion Plasma Diagnostics

The unresolved tungsten feature has been utilized at the ASDEX Upgrade tokamak to infer tungsten concentrations for plasmas in the 2.1 - 5.5 keV electron-temperature interval [137,150]. Yet, resolving the line into its two constituents allows for additional diagnostic possibilities.

As lines that originate from metastable levels are sensitive to electron collisions they are well suited for density diagnostics, as noted in e.g. Refs. [151, 152]. The density dependence and population mechanisms of the E2 and M3 lines in nickellike ions were studied by Beiersdorfer *et al.* in 1991 [138]. For nickellike tungsten, density effects on the M3 line intensity was first discussed by Loch *et al* in 2006 [143].

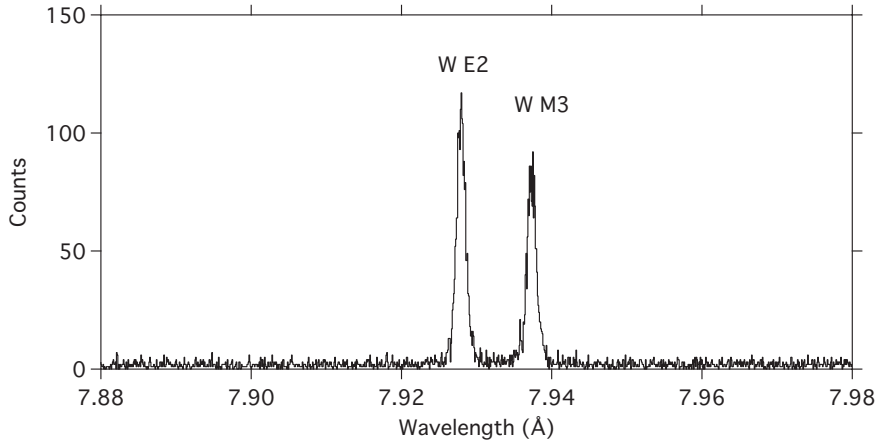

Figure 5.10: High-resolution spectrum of the tungsten E2 and M3 lines measured at SuperEBIT at an electron-beam energy of 4.2 keV.

Calculations of the density dependence on four electric dipole-forbidden transitions in Ni-like W^{46+} were later presented by Ralchenko [144], who suggested that the E2 and M3 line ratios could be used as tokamak density diagnostics.

To investigate the plasma-diagnostics potential of the lines, the intensities were measured at several electron excitation energies at SuperEBIT. Very little variation on the relative intensities was observed suggesting the line pair to be insensitive to electron temperature. This is also confirmed by the FAC calculations, shown in Paper VII. The FAC calculations demonstrate however, as expected for E1-forbidden transitions, that the relative line intensities are very much sensitive to electron densities. This was also noted by Ralchenko [144], who pointed out that the relative line intensities change in the density interval of typical tokamak plasmas.

The wavelength separation of the two lines was measured to be 9.3(2) mÅ, which is sufficient for the line profiles to be utilized for ion-temperature measurements. The intensity and Doppler broadening of the two lines have been calculated for temperatures from 1 - 7 keV, as shown in Fig. 5.11, where the lines are modeled with Gaussian profiles. The ion temperatures have been assumed equal to the electron temperatures. The two lines are excellent candidates for measurements of both the electron density and ion temperature of tokamak plasmas.

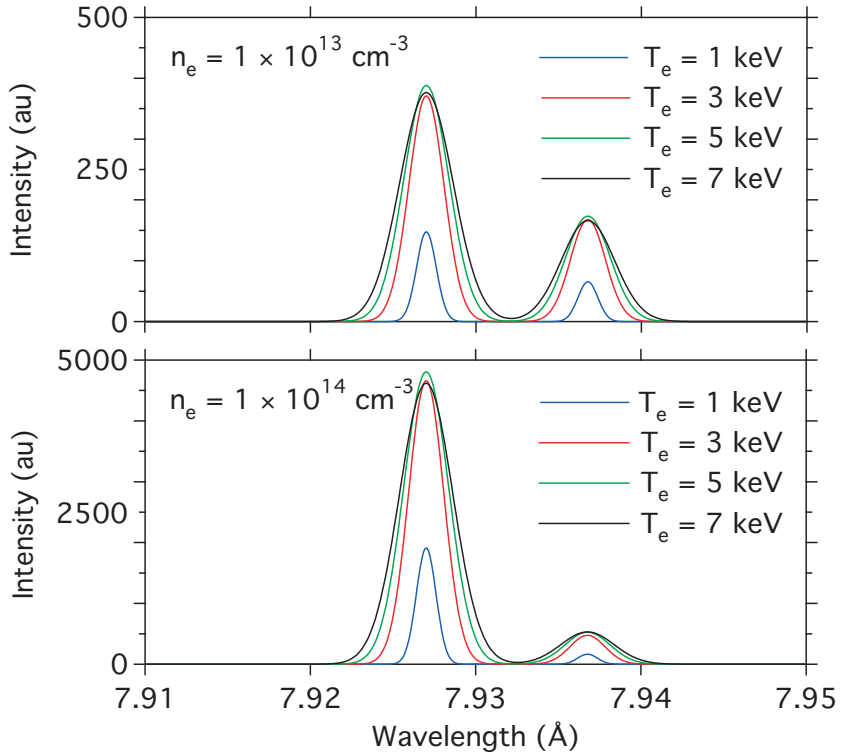

Figure 5.11: Calculated line profiles of the two nickellike tungsten lines E2 and M3 for electron temperatures of 1, 3, 5, and 7 keV for two densities: upper $n_e = 1 \times 10^{13}$ cm^{-3} and bottom $n_e = 1 \times 10^{14}$ cm^{-3}.

Chapter 6

Spheromak Spectroscopy

Spectroscopic investigations of tungsten ions in high-density magnetic fusion plasmas are relevant for the diagnostics development of the ITER divertor. Tungsten is planned as plasma-facing material for the divertor targets, and sputtering from the surfaces will therefore introduce tungsten ions in the divertor plasmas. The expected temperatures of the main divertor volume will be from 25 to 100 eV, with peak electron temperatures around 150 eV close to the X point [153].

The Sustained Spheromak Physics Experiment (SSPX) facility provided a suitable radiation source to simulate tungsten emission from ITER divertor plasmas. The SSPX spheromak had typical electron densities of 10^{14-15} cm^{-3} and temperatures around 100 eV. These high-density magnetic fusion plasmas therefore matched the expected divertor conditions well. Tungsten existed as an intrinsic impurity in the SSPX spheromak, because the copper flux conserver was spray coated with a 100 μm layer of tungsten [154]. To utilize SSPX plasmas for tungsten spectroscopy the spectra from other impurity ions had to be known. An extensive effort to measure impurity ions in the 60 to 450 Å interval was performed using the Silver Flat Field Spectrometer (SFFS); see Paper I.

Low-Z ions were abundant in the SSPX plasmas. The EUV spectra were usually dominated by boronlike, berylliumlike, and lithiumlike oxygen ions; see Papers I and VIII. Carbon and nitrogen ions were occasionally observed but usually only from relatively weak lines. Certain SSPX experiments injected boron nitride covered probes [155] into the spheromak, which caused nitrogen and boron to be released into the plasmas. The Kα lines of heliumlike boron were studied at 60 Å and used to estimate the plasma parameters of SSPX; see Paper VIII.

Of the mid-Z elements only titanium and copper were found in the SSPX plasmas. The copper ions originated from the walls of the flux conserver, whereas titanium ions were introduced by a gettering system. To confirm the identification of titanium lines, measurements were performed where the titanium features were studied in connection with titanium gettering. This work is reported in Paper IX.

To investigate the feasibility of tungsten EUV spectra for ITER divertor diagnostics an injection experiment of tungsten hexacarbonyl was performed at SSPX. This is described in Paper X. A special sublimation injector was constructed and mounted

on one of the diagnostics port, which allowed for the injection of tungsten during the hydrogen prefilled phase before each discharge. By changing the amount of injected material and study how the spectra changed, tungsten candidate lines could be identified.

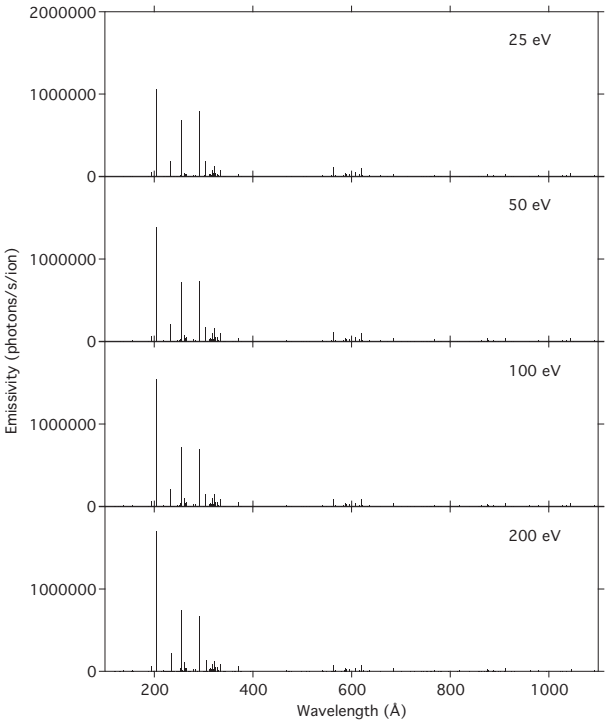

Figure 6.1: Calculated Er-like W^{6+} spectra at $n_e = 10^{15}$ cm^{-3}.

The tungsten measurements were supported by spectral modeling using the Flexible Atomic Code (FAC) [103]. The few-times charged tungsten ions expected in low-temperature divertor plasmas are difficult to model and calculated wavelengths are therefore believed to only be accurate to within 20 Å. Synthetic spectra have been calculated for $n_e = 10^{14}$ and 10^{15} cm^{-3}. Figure 6.1 shows Er-like W VII calculated at $n_e = 10^{15}$ cm^{-3}. The relative line intensities are very similar to those spectra calculated at $n_e = 10^{14}$ cm^{-3}, which are displayed in Paper X. The spectrum of Er-like W^{6+} has potential for diagnostics due to its closed-shell structure. The ion will likely be abundant in the ITER divertor and the spectrum is relatively simple. The transitions between 200 and 300 Å could, for instance, be used to infer tungsten concentrations. From the calculated line emissivities of Tm-like W VI it seem that the two 5d - 5f transitions with wavelengths just below 400 Å might be sensitive to electron temperature. The experimental and theoretical investigations indicate that EUV spectroscopy of tungsten could be a valuable diagnostic for ITER divertor plasmas.

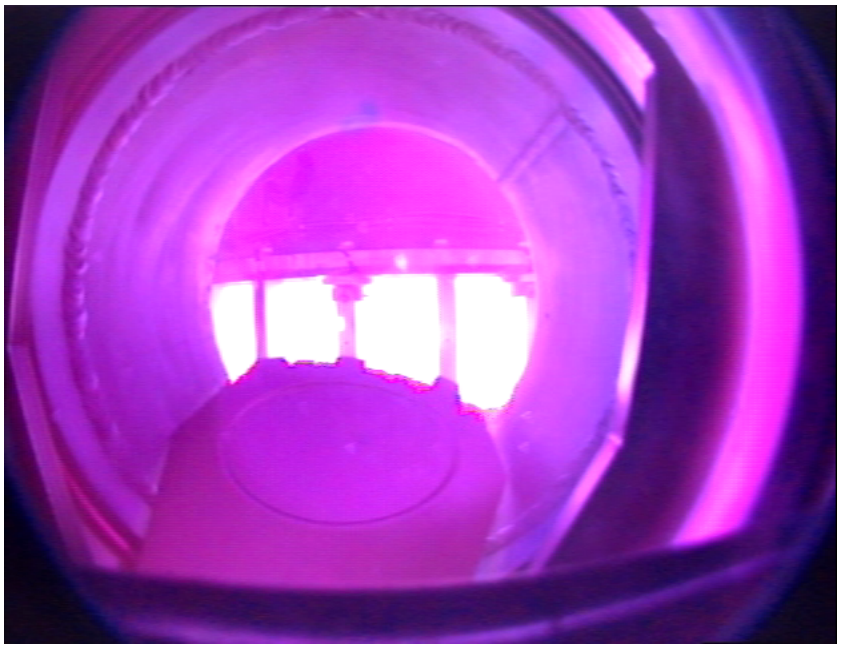

Figure 6.2: Plasma discharge at the SSPX spheromak during the tungsten experiment.

References

[1] I. Martinson, "The spectroscopy of highly ionised atoms," *Rep. Prog. Phys.*, vol. 52, pp. 157–225, Feb 1989.

[2] C. Seife, *Sun in a Bottle - The Strange History of Fusion and the Science of Wishful Thinking*. Viking Penguin, 2008.

[3] C. M. Braams and P. E. Stott, *Nuclear Fusion - Half a Century of Magnetic Confinement Fusion Research*. Taylor & Francis Group, 2002.

[4] J. Wesson, *Tokamaks*. Oxford University Press, 1997.

[5] C. H. Skinner, "Applications of EBIT to magnetic fusion diagnostics," *Can. J. Phys.*, vol. 86, pp. 285–290, Jan 2008.

[6] http://www.iter.org, May 15, 2010.

[7] N. J. Peacock, M. G. O'Mullane, R. Barnsley, and M. Tarbutt, "Anticipated X-ray and VUV spectroscopic data from ITER with appropriate diagnostic instrumentation," *Can. J. Phys.*, vol. 86, pp. 277–284, Jan 2008.

[8] B. C. Stratton, M. Bitter, K. W. Hill, D. L. Hillis, and J. T. Hogan, "Passive spectroscopic diagnostics for magnetically confined fusion plasmas," *Fusion Sci. Technol.*, vol. 53, pp. 431–486, Feb 2008.

[9] F. M. Levinton, "The motional Stark effect: Overview and future development," *Rev. Sci. Instrum.*, vol. 70, pp. 810–814, Jan 1999.

[10] R. J. Jayakumar, S. L. Allen, K. H. Burrell, L. L. Lao, M. A. Makowski, C. C. Petty, and D. M. Thomas, "Current profile measurements on the DIII-D tokamak," *Fusion Sci. Technol.*, vol. 48, pp. 852–863, Oct 2005.

[11] H. R. Griem, *Principles of Plasma Spectroscopy*. Cambridge University Press, 1997.

[12] R. J. Fonck, A. T. Ramsey, and R. V. Yelle, "Multichannel grazing-incidence spectrometer for plasma impurity diagnosis: SPRED," *Appl. Opt.*, vol. 21, pp. 2115–2123, Jun 1981.

[13] M. Bitter, S. von Goeler, R. Horton, M. Goldman, K. W. Hill, N. R. Sauthoff, and W. Stodiek, "Doppler-broadening measurements of x-ray lines for determination of the ion temperature in tokamak plasmas," *Phys. Rev. Lett.*, vol. 42, pp. 304–308, Jan 1979.

[14] A. H. Gabriel, "Dielectronic satellite spectra for highly-charged helium-like lines," *Mon. Not. R. Ast. Soc.*, vol. 160, pp. 99–119, 1972.

[15] J.-Ö. Swahn, ed., *Bra Böckers Lexikon.* Bokförlaget Bra Böcker, 1990.

[16] http://en.wikipedia.org/wiki/Tungsten, May 15, 2010.

[17] R. Neu, "Tungsten as a plasma facing material in fusion devices," Dec 2003. Habilitationsschrift, Eberhard-Karls-Universität zu Tübingen.

[18] E. Dershem, "Wave-lengths of the tungsten x-ray spectrum," *Phys. Rev.*, vol. 11, pp. 461–476, Jun 1918.

[19] L. Iglesias, V. Kaufman, O. Garcia-Riquelme, and F. R. Rico, "Analysis of the fourth spectrum of tungsten (W IV)," *Phys. Scr.*, vol. 31, pp. 173–183, Mar 1985.

[20] S. S. Churilov, R. R. Kildiyarova, and Y. N. Joshi, "Analyses of the $5d^2$-5d7p transitions in the Ta IV and W V spectra," *Can. J. Phys.*, vol. 74, pp. 145–149, 1996.

[21] R. R. Kildiyarova, S. S. Churilov, Y. N. Joshi, and A. N. Ryabtsev, "Analysis of the 5d5f configuration of trebly ionized tantalum and quadruply ionized tungsten: Ta IV and W V," *Phys. Scr.*, vol. 53, pp. 454–460, 1996.

[22] F. G. Meijer, "The fifth spectrum of tungsten, W V," *Physica*, vol. 141C, pp. 230–236, 1986.

[23] F. G. Meijer, "The sixth spectrum of tungsten, W VI," *Physica*, vol. 73, pp. 415–420, Apr 1974.

[24] V. Kaufman and J. Sugar, "Wavelengths, classifications, and ionization energies in the isoelectronic sequences from Yb II and Yb III through Bi XV and Bi XVI," *J. Opt. Soc. Am.*, vol. 66, pp. 1019–1025, Oct 1976.

[25] J. Sugar and V. Kaufman, "Identification of 5g and 6g terms and revised ionization energies in the Yb II $4f^{14}nl$ isoelectronic sequence," *J. Opt. Soc. Am.*, vol. 69, pp. 141–143, Jan 1979.

[26] J. Sugar and V. Kaufman, "Seventh spectrum of tungsten (W VII); resonance lines of Hf V," *Phys. Rev. A*, vol. 12, pp. 994–1012, Sep 1975.

[27] J. F. Wyart, V. Kaufman, and J. Sugar, "The $4f^{13}5f$ configuration in the isoelectronic sequence of Yb III," *Phys. Scr.*, vol. 23, pp. 1069–1078, Jun 1981.

[28] P. Mandelbaum, M. Klapisch, A. Bar-Shalom, J. L. Schwob, and A. Zigler, "Classification of x-ray spectra from laser produced plasmas of atoms from Tm to Pt in the range 6-9 Å," *Phys. Scr.*, vol. 27, pp. 39–53, 1983.

[29] J. F. Wyart, C. Bauche-Arnoult, J. C. Gauthier, J. P. Geindre, P. Monier, M. Klapisch, A. Bar-Shalom, and A. Cohn, "Density-sensitive electric quadrupole decays in Ni-like ions observed in laser-produced plasmas," *Phys. Rev. A*, vol. 34, pp. 701–704, Jul 1986.

[30] N. Tragin, J. P. Geindre, P. Monier, J. C. Gauthier, C. Chenais-Popovics, J. F. Wyart, and C. Bauche-Arnoult, "Extended analysis of the x-ray spectra of laser-irradiated elements in the sequence from tantalum to lead," *Phys. Scr.*, vol. 37, pp. 72–82, 1988.

[31] A. Zigler, M. Klapisch, and P. Mandelbaum, "Interpretation of laser produces Au and W x-ray spectra in the 3 keV range," *Phys. Lett. A*, vol. 117, pp. 31–35, Jul 1986.

[32] R. C. Isler, R. V. Neidigh, and R. D. Cowan, "Tungsten radiation from tokamak-produced plasmas," *Phys. Lett.*, vol. 63 A, pp. 295–297, Nov 1977.

[33] E. Hinnov and M. Mattioli, "Observations of multiply ionized tungsten radiation in the PLT discharges," *Phys. Lett.*, vol. 66 A, pp. 109–111, May 1978.

[34] E. Hinnov, K. Bol, D. Dimock, R. J. Hawryluk, D. Johnson, M. Mattioli, E. Meservey, and S. von Goeler, "Effects of tungsten radiation on the behaviour of PLT tokamak discharges," *Nucl. Fusion*, vol. 18, no. 9, pp. 1305–1307, 1978.

[35] J. Sugar and V. Kaufman, "Tokamak-generated tungsten radiation identified in Ag I isoelectronic sequence (W XXVIII," *Phys. Rev. A*, vol. 21, pp. 2096–2098, Jun 1980.

[36] M. Finkenthal, L. K. Huang, S. Lippmann, H. W. Moos, P. Mandelbaum, J. L. Schwob, M. Klapisch, and TEXT Group, "Soft x-ray bands of highly ionized tungsten, gold and lead emitted by the TEXT tokamak plasma," *Phys. Lett. A*, vol. 127, pp. 255–258, Feb 1988.

[37] J. Sugar, V. Kaufman, and W. L. Rowan, "Observation of Pd-like resonance lines through Pt^{32+} and Zn-like resonance lines of Er^{38+} and Hf^{42+}," *J. Opt. Soc. Am. B*, vol. 10, pp. 799–801, May 1993.

[38] J. Sugar, V. Kaufman, and W. L. Rowan, "Spectra of Ag I isoelectronic sequence observed from Er^{21+} to Au^{32+}," *J. Opt. Soc. Am. B*, vol. 10, pp. 1321–1325, Aug 1993.

[39] J. Sugar, V. Kaufman, and W. L. Rowan, "Rh I isoelectronic sequence observed from Er^{23+} to Pt^{33+}," *J. Opt. Soc. Am. B*, vol. 10, pp. 1977–1979, Nov 1993.

[40] K. Asmussen, K. B. Fournier, J. M. Laming, R. Neu, J. F. Seely, R. Dux, W. Engelhardt, J. C. Fuchs, and ASDEX Upgrade Team, "Spectroscopic investigations of tungsten in the EUV region and the determination of its concentration in tokamaks," *Nucl. Fusion*, vol. 38, pp. 967–986, Jul 1998.

[41] M. B. Chowdhuri, S. Morita, M. Goto, H. Nishimura, K. Nagai, and S. Fujioka, "Line analysis of EUV spectra from molybdenum and tungsten injected with impurity pellets in LHD," *Plasma and Fusion Res.*, vol. 2, p. S1060, 2007.

[42] J. Clementson, P. Beiersdorfer, A. L. Roquemore, C. H. Skinner, D. K. Mansfield, K. Hartzfeld, and J. K. Lepson, "Tungsten transport in the NSTX tokamak," *Rev. Sci. Instrum.*, 2010. submitted.

[43] R. Neu, R. Dux, A. Kallenbach, T. Pütterich, M. Balden, J. C. Fuchs, A. Herrmann, C. F. Maggi, M. O'Mullane, R. Pugno, I. Radivojevic, V. Rohde, A. C. C. Sips, W. Suttrop, A. Whiteford, and the ASDEX Upgrade team, "Tungsten: an option for divertor and main chamber plasma facing components in future fusion devices," *Nucl. Fusion*, vol. 45, pp. 209–218, 2005.

[44] R. Neu, C. Hopf, T. Kallenbach, Pütterich, R. Dux, H. Greuner, O. Gruber, A. Herrmann, K. Krieger, H. Maier, V. Rohde, and ASDEX Upgrade Team, "Operational conditions in a W-clad tokamak," *J. Nucl. Mater.*, vol. 367-370, pp. 1497–1502, Aug 2007.

[45] R. Neu, K. B. Fournier, D. Schlögl, and J. Rice, "Observations of x-ray spectra from highly charged tungsten ions in tokamak plasmas," *J. Phys. B: At. Mol. Opt. Phys.*, vol. 30, pp. 5057–5067, 1997.

[46] P. Beiersdorfer, "Spectroscopy of highly charged multi-electron ions," in *VIth International conference on the physics of highly charged ions* (P. Richard, M. Stöckli, C. L. Cocke, and C. D. Lin, eds.), vol. 274 of *AIP Conference Proceedings*, pp. 365–374, Jun 1993.

[47] P. Beiersdorfer, 1992. unpublished data.

[48] S. R. Elliott, P. Beiersdorfer, B. J. MacGowan, and J. Nilsen, "Measurements of line overlap for resonant spoiling of x-ray lasing transitions in nickel-like tungsten," *Phys. Rev. A*, vol. 52, pp. 2689–2692, Oct 1995.

[49] S. B. Utter, P. Beiersdorfer, and E. Träbert, "Electron-beam ion-trap spectra of tungsten in the EUV," *Can. J. Phys.*, vol. 80, pp. 1503–1515, Dec 2002.

[50] Y. Ralchenko, J. Reader, J. M. Pomeroy, J. N. Tan, and J. D. Gillaspy, "Spectra of W^{39+}-W^{47+} in the 12-20 nm region observed with an EBIT light source," *J. Phys. B: At. Mol. Opt. Phys.*, vol. 40, pp. 3861–3875, 2007.

[51] Y. Ralchenko, I. N. Draganic, J. N. Tan, J. D. Gillaspy, J. M. Pomeroy, J. Reader, U. Feldman, and G. E. Holland, "EUV spectra of highly-charged ions W^{54+}-W^{63+} relevant to ITER diagnostics," *J. Phys. B: At. Mol. Opt. Phys.*, vol. 41, p. 021003, 2008.

[52] Y. Ralchenko, J. N. Tan, J. D. Gillaspy, and J. M. Pomeroy, "Accurate modeling of benchmark x-ray spectra from highly charged ions of tungsten," *Phys. Rev. A*, vol. 74, p. 042514, Oct 2006.

[53] J. D. Gillaspy, I. N. Draganić, Y. Ralchenko, J. Reader, J. N. Tan, J. M. Pomeroy, and S. M. Brewer, "Measurement of the D-line doublet in high-Z highly charged sodiumlike ions," *Phys. Rev. A*, vol. 80, p. 010501(R), 2009.

[54] C. Biedermann, A. Förster, G. Fußmann, and R. Radtke, "First results from the Berlin EBIT," *Phys. Scr.*, vol. T73, pp. 360–361, 1997.

[55] R. Radtke, C. Biedermann, J. L. Schwob, P. Mandelbaum, and R. Doron, "Line and band emission from tungsten ions with charge 21+ to 45+ in the 45-70-Å range," *Phys. Rev. A*, vol. 64, p. 012720, Jul 2001.

[56] C. Biedermann, R. Radtke, J.-L. Schwob, P. Mandelbaum, R. Doron, T. Fuchs, and G. Fußmann, "EUV spectroscopy of highly charged tungsten ions relevant to hot plasmas," *Phys. Scr.*, vol. T92, pp. 85–88, 2001.

[57] C. Biedermann, R. Radtke, R. Seidel, and T. Pütterich, "Spectroscopy of highly charged tungsten ions relevant to fusion plasmas," *Phys. Scr.*, vol. T134, p. 014026, 2009.

[58] C. Biedermann, R. Radtke, R. Seidel, and E. Behar, "Dielectronic and radiative recombination of Si- to N-like ions," *J. Phys. Conf.*, vol. 163, p. 012034, 2009.

[59] A. E. Kramida and T. Shirai, "Energy levels and spectral lines of tungsten, W III through W LXXIV," *At. Data Nucl. Data Tables*, vol. 95, pp. 305–474, 2009.

[60] J. Nilsen, "The role of EBIT in X-ray laser research," *Can. J. Phys.*, vol. 86, pp. 19–23, Jan 2008.

[61] P. Beiersdorfer, "A "brief" history of spectroscopy on EBIT," *Can. J. Phys.*, vol. 86, pp. 1–10, Jan 2008.

[62] R. E. Marrs, "Milestones in EBIT spectroscopy and why it almost did not work," *Can. J. Phys.*, vol. 86, pp. 11–18, Jan 2008.

[63] J. K. Lepson, P. Beiersdorfer, M. Bitter, and S. M. Kahn, "Laboratory astrophysics in the extreme ultraviolet," *Can. J. Phys.*, vol. 86, pp. 175–182, Jan 2008.

[64] M. B. Schneider, R. Mancini, K. Widmann, K. B. Fournier, G. V. Brown, H. K. Chung, H. A. Baldis, K. Cone, S. B. Hansen, M. J. May, D. Thorn, and P. Beiersdorfer, "An overview of EBIT data needed for experiments on laser-produced plasmas," *Can. J. Phys.*, vol. 86, pp. 259–266, Jan 2008.

[65] A. S. Safronova, V. L. Kantsyrev, P. Neill, U. I. Safronova, D. A. Fedin, N. D. Ouart, M. F. Yilmaz, G. Osborne, I. Shrestha, K. Williamson, T. Hoppe, C. Harris, P. Beiersdorfer, and S. Hansen, "The importance of EBIT data for Z-pinch plasma diagnostics," *Can. J. Phys.*, vol. 86, pp. 267–276, Jan 2008.

[66] M. A. Levine, R. E. Marrs, J. R. Henderson, D. A. Knapp, and M. B. Schneider, "The electron beam ion trap: a new instrument for atomic physics measurements," *Phys. Scr.*, vol. T22, pp. 157–163, 1988.

[67] M. A. Levine, R. E. Marrs, J. N. Bardsley, P. Beiersdorfer, C. L. Bennett, M. H. Chen, T. Cowan, D. Dietrich, J. R. Henderson, D. A. Knapp, A. Osterheld, B. M. Penetrante, M. B. Schneider, and J. H. Scofield, "The use of an electron beam ion trap in the study of highly charged ions," *Nucl. Instr. and Meth.*, vol. B43, pp. 431–440, Sep 1989.

[68] D. A. Knapp, R. E. Marrs, S. R. Elliott, E. W. Magee, and R. Zasadzinski, "A high-energy electron beam ion trap for production of high-charge high-Z ions," *Nucl. Instrum. Methods Phys. Res. A*, vol. 334, pp. 305–312, Oct 1993.

[69] P. Beiersdorfer, "Laboratory x-ray astrophysics," *Annu. Rev. Astron. Astr.*, vol. 41, pp. 343–390, 2003.

[70] K. Widmann, *High-resolution spectroscopic diagnostics of very high-temperature plasmas in the hard x-ray regime.* PhD thesis, Technische Universität Graz, 1998.

[71] A. M. Niles, E. W. Magee, D. B. Thorn, G. V. Brown, H. Chen, and P. Beiersdorfer, "Laser ablation system for the injection of neutral materials into an electron beam ion trap," *Rev. Sci. Instrum.*, vol. 77, p. 10F106, 10 2006.

[72] M. B. Schneider, M. A. Levine, C. L. Bennett, J. R. Henderson, D. A. Knapp, and R. E. Marrs, "Evaporative cooling of highly charged ions in EBIT: An experimental realization," in *International symposium on electron beam ion sources and their applications*, vol. 188 of *AIP Conference Proceedings*, pp. 158–165, Jun 1989.

[73] H. S. McLean, R. D. Wood, D. N. Hill, E. B. Hooper, B. Hudson, R. J. Jayakumar, L. L. LoDestro, J. M. Moller, C. A. Romero-Talamás, T. A. Casper, B. I. Cohen, T. K. Fowler, L. D. Pearlstein, J. D. King, E. C. Morse, E. D. Mezonlin, J. Titus, J. A. Johnson III, J. H. T. Clementson, and C. R. Sovinec, "Final results from the SSPX spheromak program," 2008. Abstract, LLNL-ABS-402887, Innovative Confinement Concepts Workshop, June 24-27, 2008, Reno, Nevada.

[74] R. D. Wood, D. N. Hill, E. B. Hooper, S. Woodruff, H. S. McLean, and B. W. Stallard, "Improved operation of the SSPX spheromak," *Nucl. Fusion*, vol. 45, pp. 1582–1588, Dec 2005.

[75] R. D. Wood, D. N. Hill, E. B. Hooper, D. Buchenauer, H. McLean, Z. Wang, S. Woodruff, and G. Wurden, "Particle control in the sustained spheromak physics experiment," *J. Nucl. Mater.*, vol. 290-293, pp. 513–517, Mar 2001.

[76] H. S. McLean, R. D. Wood, B. I. Cohen, E. B. Hooper, D. N. Hill, J. M. Moller, C. Romero-Talamas, and S. Woodruff, "Transport and fluctuations in high temperature spheromak plasmas," *Phys. Plasmas*, vol. 13, p. 056105, May 2006.

[77] B. Hudson, R. D. Wood, H. S. McLean, E. B. Hooper, D. N. Hill, J. Jayakumar, J. Moller, D. Montez, C. A. Romero-Talamás, T. A. Casper, J. A. Johnson III, L. L. LoDestro, E. Mezonlin, and L. D. Pearlstein, "Energy confinement and magnetic field generation in the SSPX spheromak," *Phys. Plasmas*, vol. 15, p. 056112, May 2008.

[78] H. S. McLean, A. Ahmed, D. Buchenauer, D. Den Hartog, C. W. Domier, D. N. Hill, C. Holcomb, E. B. Hooper, E. C. Morse, M. Nagata, Y. Roh, B. Stallard, R. D. Wood, S. Woodruff, G. Wurden, Z. Wang, and SSPX Team, "Plasma diagnostics for the sustained spheromak physics experiment," *Rev. Sci. Instrum.*, vol. 72, pp. 556–561, Jan 2001.

[79] J. D. King, H. S. McLean, R. D. Wood, C. A. Romero-Talamás, J. M. Moller, and E. C. Morse, "An ion Doppler spectrometer instrument for ion temperature and flow measurements on SSPX," *Rev. Sci. Instrum.*, vol. 79, p. 10F535, Oct 2008.

[80] P. Beiersdorfer, J. R. Crespo López-Urrutia, P. Springer, S. B. Utter, and K. L. Wong, "Spectroscopy in the extreme ultraviolet on an electron beam ion trap," *Rev. Sci. Instrum.*, vol. 70, pp. 276–279, Jan 1999.

[81] A. T. Graf, S. Brockington, R. Horton, S. Howard, D. Hwang, P. Beiersdorfer, J. Clementson, D. Hill, M. May, H. Mclean, R. Wood, M. Bitter, J. Terry, W. L. Rowan, J. K. Lepson, and L. Delgado-Aparicio, "Spectroscopy on magnetically confined plasmas using electron beam ion trap spectrometers," *Can. J. Phys.*, vol. 86, pp. 307–313, Jan 2008.

[82] J. K. Lepson, P. Beiersdorfer, J. Clementson, M. F. Gu, M. Bitter, L. Roquemore, R. Kaita, P. G. Cox, and A. S. Safronova, "EUV spectroscopy on NSTX," *J. Phys. B: At. Mol. Opt. Phys.*, 2010. in press.

[83] T. Kita, T. Harada, N. Nakano, and H. Kuroda, "Mechanically ruled aberration-corrected concave gratings for a flat-field grazing-incidence spectrograph," *Appl. Opt.*, vol. 22, pp. 512–513, Feb 1983.

[84] P. Beiersdorfer, H. Chen, D. B. Thorn, and E. Träbert, "Measurement of the two-loop Lamb shift in lithiumlike U^{89+}," *Phys. Rev. Lett.*, vol. 95, p. 233033, Dec 2005.

[85] P. Beiersdorfer, E. Träbert, G. V. Brown, H. Chen, J. Clementson, and D. Thorn, "Measurement of the 2s hyperfine splitting in Bi^{80+}," in *Abstract book of the XXV International Conference on Photonics, Electronic and Atomic Collisions*, 2007.

[86] P. Beiersdorfer, E. W. Magee, E. Träbert, H. Chen, J. K. Lepson, M.-F. Gu, and M. Schmidt, "Flat-field grating spectrometer for high-resolution soft x-ray and extreme ultraviolet measurements on an electron beam ion trap," *Rev. Scr. Instrum.*, vol. 75, pp. 3723–3726, Oct 2004.

[87] J. Dunn, E. W. Magee, R. Shepard, H. Chen, S. B. Hansen, S. J. Moon, G. V. Brown, M.-F. Gu, P. Beiersdorfer, and M. A. Purvis, "High resolution soft x-ray spectroscopy of low Z K-shell emission from laser-produced plasmas," *Rev. Sci. Instrum.*, vol. 79, p. 10E314, Oct 2008.

[88] J. Dunn, P. Beiersdorfer, G. V. Brown, and E. W. Magee, "Calibration of a high resolution soft x-ray spectrometer," in *X-Ray Lasers 2008, Proceedings of the 11th International Conference, August 17-22, 2008, Belfast, UK* (C. L. S. Lewis and D. Riley, eds.), vol. 130 of *Springer Proceedings in Physics*, pp. 461–467, 2009.

[89] G. V. Brown, P. Beiersdorfer, and K. Widmann, "Wide-band, high-resolution soft x-ray spectrometer for the Electron Beam Ion Trap," *Rev. Sci. Instrum.*, vol. 70, pp. 280–283, Jan 1999.

[90] P. Beiersdorfer, G. V. Brown, L. Hildebrandt, K. L. Wong, and R. Ali, "Multi-parameter data acquisition system for spectroscopy," *Rev. Sci. Instrum.*, vol. 72, pp. 508–512, Jan 2001.

[91] P. Beiersdorfer, J. R. Crespo López-Urrutia, E. Förster, J. Mahiri, and K. Widmann, "Very high resolution soft x-ray spectrometer for an electron beam ion trap," *Rev. Sci. Instrum.*, vol. 68, pp. 1077–1079, Jan 1997.

[92] M. LeGros, E. Silver, D. Schneider, J. McDonald, S. Bardin, R. Schuch, N. Madden, and J. Beeman, "The first high resolution, broad band x-ray spectroscopy of ion-surface interactions using a microcalorimeter," *Nucl. Instr. and Meth.*, vol. A 357, pp. 110–114, 1995.

[93] E. Silver, H. Schnopper, S. Bandler, S. Murray, N. Madden, D. Landis, J. Beeman, E. Haller, M. Barbera, G. Tucker, J. Gillaspy, E. Takacs, and J. Porto, "Laboratory astrophysics and microanalysis with NTD-germanium-based X-ray microcalorimeters," *Nucl. Instr. and Meth.*, vol. A 444, pp. 156–160, 2000.

[94] P. Beiersdorfer, "Spectroscopy with trapped highly charged ions," *Phys. Scr.*, vol. T134, p. 014010, May 2009.

[95] G. V. Brown, P. Beiersdorfer, K. R. Boyce, H. Chen, M. F. Gu, S. M. Kahn, R. L. Kelley, C. A. Kilbourne, M. May, F. S. Porter, A. E. Szymkowiak, D. Thorn, and K. Widmann, "Laboratory astrophysics and atomic physics using the NASA/GSFC microcalorimeter spectrometers at the LLNL electron beam ion trap and radiation properties facility," *Nucl. Instr. and Meth.*, vol. A 559, pp. 623–625, Apr 2006.

[96] F. S. Porter, G. V. Brown, K. R. Boyce, R. L. Kelley, C. A. Kilbourne, P. Beiersdorfer, H. Chen, S. Terracol, S. M. Kahn, and A. E. Szymkowiak, "The Astro-E2 x-ray spectrometer/EBIT microcalorimeter x-ray spectrometer," *Rev. Sci. Instrum.*, vol. 75, pp. 3772–3774, Oct 2004.

[97] J. Clementson, P. Beiersdorfer, G. V. Brown, H. Chen, D. B. Thorn, and E. Träbert, 2006. unpublished data.

[98] P. Beiersdorfer, G. V. Brown, J. H. T. Clementson, M. Frankel, M. F. Gu, S. M. Kahn, R. Kelley, C. A. Kilbourne, F. S. Porter, D. Thorn, and E. Träbert, "Survey of the K-shell emission from heliumlike ions with an X-ray microcalorimeter," *J. Phys. Conf.*, vol. 163, p. 012022, Apr 2009.

[99] F. S. Porter, J. S. Adams, P. Beiersdorfer, V. Brown, Gregory, J. Clementson, M. Frankel, S. K. Kahn, R. L. Kelley, and C. A. Kilbourne, "High-resolution x-ray spectroscopy with the EBIT Calorimeter Spectrometer," in *The thirteen international workshop on Low Temperature Detectors - LTD 13* (B. Cabrera, A. Miller, and B. Young, eds.), vol. 1185 of *AIP Conference Proceedings*, pp. 454–457, Dec 2009.

[100] A. E. Kramida and J. Reader, "Ionization energies of tungsten ions: W^{2+} through W^{71+}," *At. Data Nucl. Data Tables*, vol. 92, pp. 457–479, 2006.

[101] P. Beiersdorfer, J. Clementson, J. Dunn, M. F. Gu, K. Morris, Y. Podpaly, E. Wang, M. Bitter, R. Feder, K. W. Hill, D. Johnson, and R. Barnsley, "The ITER core imaging x-ray spectrometer," *J. Phys. B: At. Mol. Opt. Phys.*, 2010. in press.

[102] H. Watanabe, N. Nakamura, D. Kato, T. Nakano, and S. Ohtani, "X-ray spectra from neon-like tungsten ions in the interaction with electrons," *Plasma and Fusion Res.*, vol. 2, p. 027, 2007.

[103] M. F. Gu, "The flexible atomic code," *Can. J. Phys.*, vol. 86, no. 5, pp. 675–689, 2008.

[104] P. Beiersdorfer, A. L. Osterheld, J. H. Scofield, J. R. Crespo López-Urrutia, and K. Widmann, "Measurement of QED and hyperfine splitting in the $2s_{1/2}$-$2p_{3/2}$ x-ray transition in Li-like $^{209}Bi^{80+}$," *Phys. Rev. Lett.*, vol. 80, pp. 3022–3025, Apr 1998.

[105] P. Beiersdorfer, D. Knapp, R. E. Marrs, S. R. Elliott, and M. H. Chen, "Structure and Lamb shift of $2s_{1/2}$-$2p_{3/2}$ levels in in lithiumlike U^{89+} through neonlike U^{82+}," *Phys. Rev. Lett.*, vol. 71, pp. 3939–3942, Dec 1993.

[106] P. Beiersdorfer, *High-resolution studies of the x-ray transitions in highly charged neonlike ions on the PLT tokamak*. PhD thesis, Princeton University, Feb 1988.

[107] P. Beiersdorfer, S. von Goeler, M. Bitter, E. Hinnov, R. Bell, S. Bernabei, J. Felt, K. W. Hill, R. Hulse, J. Stevens, S. Suckewer, J. Timberlake, A. Wouters, M. H.

Chen, J. H. Scofield, D. D. Dietrich, M. Gerassimenko, E. Silver, R. S. Walling, and P. L. Hagelstein, "X-ray transitions in highly charged neonlike ions," *Phys. Rev. A*, vol. 37, pp. 4153–4162, Jun 1988.

[108] E. Källne, J. Källne, and R. J. Cowan, "High-resolution x-ray spectra from molybdenum ions in the Alcator-C tokamak," *Phys. Rev. A*, vol. 27, pp. 2682–2697, May 1983.

[109] J. E. Rice, K. B. Fournier, J. A. Goetz, E. S. Marmar, and J. L. Terry, "X-ray observations of 2l-nl' transitions and configuration-interaction effects from Kr, Mo, Nb, and Zr in near neon-like charge states from tokamak plasmas," *J. Phys. B: At. Mol. Opt. Phys.*, vol. 33, pp. 5435–5462, Dec 2000.

[110] Y.-K. Kim and K.-T. Cheng, "Transition probabilities for the resonance transitions of Na-like ions," *J. Opt. Soc. Am.*, vol. 68, pp. 836–842, Jun 1978.

[111] W. R. Johnson, S. A. Blundell, and J. Sapirstein, "Many-body perturbation-theory calculations of energy levels along the sodium isoelectronic sequence," *Phys. Rev. A*, vol. 38, pp. 2699–2706, Sep 1988.

[112] D. H. Baik, Y. G. Ohr, K. S. Kim, J. M. Lee, P. Indelicato, and Y.-K. Kim, "Electric dipole, electric quadrupole, and magnetic dipole transition probabilities of Na-like ions, $56 \leq Z \leq 92$," *At. Data Nucl. Data Tables*, vol. 47, pp. 177–203, Mar 1991.

[113] Y.-K. Kim, D. H. Baik, P. Indelicato, and J. P. Deslaux, "Resonance transition energies of Li-, Na-, and Cu-like ions," *Phys. Rev. A*, vol. 44, pp. 148–166, Jul 1991.

[114] J. F. Seely, C. M. Brown, U. Feldman, J. O. Ekberg, C. J. Keane, B. J. MacGowan, D. R. Kania, and W. E. Behring, "Wavelengths and energy levels for the Na I isoelectronic sequence Y^{28+} through U^{81+}," *At. Data Nucl. Data Tables*, vol. 47, pp. 1–15, Jan 1991.

[115] S. A. Blundell, "Calculations of the screened self-energy and vacuum polarization in Li-like, Na-like, and Cu-like ions," *Phys. Rev. A*, vol. 47, pp. 1790–1803, Mar 1993.

[116] L. N. Ivanov and E. P. Ivanova, "Atomic ion energies for Na-like ions by a model potential method Z = 25-80," *At. Data Nucl. Data Tables*, vol. 24, pp. 95–109, Aug 1979.

[117] J. F. Seely and R. A. Wagner, "QED contributions to the 3s-3p transitions in highly charged Na-like ions," *Phys. Rev. A*, vol. 41, pp. 5246–5249, May 1990.

[118] E. Träbert, P. Beiersdorfer, J. K. Lepson, and H. Chen, "Extreme ultraviolet spectra of highly charged Xe ions," *Phys. Rev. A*, vol. 68, p. 042501, 2003.

[119] T. E. Cowan, C. L. Bennett, D. D. Dietrich, J. V. Bixler, C. J. Hailey, J. R. Henderson, D. A. Knapp, M. A. Levine, R. E. Marrs, and M. B. Schneider, "Precision measurement of the $3s_{1/2}$-$3p_{3/2}$ transition energy in Na-like platinum ions," *Phys. Rev. Lett.*, vol. 66, pp. 1150–1153, Mar 1991.

[120] P. Beiersdorfer and B. J. Wargelin, "Low energy x-ray spectrometer for an electron beam ion trap," *Rev. Sci. Instrum.*, vol. 65, pp. 13–17, Jan 1994.

[121] P. Beiersdorfer, E. Träbert, H. Chen, M.-H. Chen, M. J. May, and A. L. Osterheld, "Measurement of the $3s_{1.2}$-$3p_{3/2}$ resonance line in Na-like U^{81+}," *Phys. Rev. A*, vol. 67, p. 052103, 2003.

[122] J. F. Seely, U. Feldman, C. M. Brown, M. C. Richardson, D. D. Dietrich, and W. E. Behring, "Transitions in Na-like and Mg-like ions of In, Sb, I, and Cs," *J. Opt. Soc. Am. B*, vol. 5, pp. 785–788, Apr 1988.

[123] A. Simionovici, D. D. Dietrich, R. Keville, T. Cowan, P. Beiersdorfer, M. H. Chen, and S. Blundell, "Soft-x-ray spectroscopy of $\Delta n = 0$, $n = 3$ transitions in highly stripped lead," *Phys. Rev. A*, vol. 48, pp. 3056–3061, Oct 1993.

[124] J. F. Seely, U. Feldman, A. W. Wouters, J. L. Schwob, and S. Suckewer. unpublished.

[125] M. H. Chen, K. T. Cheng, P. Beiersdorfer, and J. Sapirstein, "Transition energies of the 3s-$3p_{3/2}$ resonance lines in sodiumlike to phosphoruslike uranium," *Phys. Rev. A*, vol. 68, p. 022507, 2003.

[126] K. T. Cheng and W. R. Johnson, "Excitation energies and line strengths in the Mg isoelectronic sequence," *Phys. Rev. A*, vol. 16, pp. 263–272, Jul 1977.

[127] J. P. Marques, F. Parente, and P. Indelicato, "Hyperfine quenching of the $1s^2 2s^2 2p^6 3s 3p^3 P_0$ level in magnesium-like ions," *At. Data Nucl. Data Tables*, vol. 55, pp. 157–170, Sep 1993.

[128] Y. Zou and C. Froese Fischer, "Multiconfiguration Dirac-Hartree-Fock calculations of the forbidden transitions between $3s^2\ {}^1S_0$, $3s3p\ {}^3P_{0,1,2}$, $^1P_1$ states for Mg-like ions," *J. Phys. B: At. Mol. Opt. Phys.*, vol. 34, pp. 915–931, 2001.

[129] P. Shorer, C. D. Lin, and W. R. Johnson, "Oscillator strengths for the magnesium isoelectronic sequence," *Phys. Rev. A*, vol. 16, pp. 1109–1116, Sep 1977.

[130] E. P. Ivanova, L. N. Ivanov, and M. A. Tsirekidze, "Energy levels of Mg-like ions calculated in the model-potential relativistic perturbation theory: Z = 25-84," *At. Data Nucl. Data Tables*, vol. 35, pp. 419–428, Nov 1986.

[131] P. Neill, C. Harris, A. S. Safronova, S. Hamasha, S. Hansen, U. I. Safronova, and P. Beiersdorfer, "The study of x-ray M-shell spectra of W ions from the Lawrence Livermore National Laboratory Electron Beam Ion Trap," *Can. J. Phys.*, vol. 82, pp. 931–942, 2004.

[132] A. Shlyaptseva, D. Fedin, S. Hamasha, C. Harris, V. Kantsyrev, P. Neill, N. Ouart, U. I. Safronova, P. Beiersdorfer, K. Boyce, G. V. Brown, R. Kelley, C. A. Kilbourne, and F. S. Porter, "Development of M-shell x-ray spectroscopy and spectropolarimetry of z-pinch tungsten plasmas," *Rev. Sci. Instrum.*, vol. 75, pp. 3750–3752, Oct 2004.

[133] M. Klapisch, P. Mandelbaum, A. Barshalom, J. L. Schwob, A. Zigler, and S. Jackel, "Identification of 3d-4p transitions in Co-like W XLVIII and Tm XLIII and in Cu-like W XLVI and Tm XLI from laser-produced plasmas," *J. Opt. Soc. Am.*, vol. 71, pp. 1276–1281, Oct 1981.

[134] A. Zigler, H. Zmora, N. Spector, M. Klapisch, J. L. Schwob, and A. Bar-Shalom, "Identification of the spectra of Hf XLV, Ta XLVI, W XLVII, and Re XLVIII isoelectronic to Ni I in laser-produced plasmas," *J. Opt. Soc. Am.*, vol. 70, pp. 129–132, Jan 1980.

[135] P. Mandelbaum, M. Klapisch, A. Bar-Shalom, J. L. Schwob, and A. Zigler, "Classification of Cu-I like 3p-4s and 3p-4d transitions in x-ray spectra from laser-produced plasmas of atoms from Tm to Re in the range 4-8 Å," *Phys. Lett.*, vol. 99A, pp. 84–88, Nov 1983.

[136] A. S. Safronova, J. Clementson, P. Beiersdorfer, *et al.*, 2009. unpublished data.

[137] T. Pütterich, R. Neu, R. Dux, A. D. Whiteford, M. G. O'Mullane, and the ASDEX Upgrade team, "Modelling of measured tungsten spectra from ASDEX upgrade and predictions for ITER," *Plasma Phys. Control. Fusion*, vol. 50, p. 085016, 2008.

[138] P. Beiersdorfer, A. L. Osterheld, J. Scofield, B. Wargelin, and R. E. Marrs, "Observation of magnetic octupole decay in atomic spectra," *Phys. Rev. Lett.*, vol. 67, pp. 2272–2275, Oct 1991.

[139] E. Träbert, P. Beiersdorfer, G. V. Brown, S. Terracol, and U. I. Safronova, "On the metastable level in Ni-like ions," *Nucl. Instrum. Methods Phys. Res. B*, vol. 235, pp. 23–27, Jul 2005.

[140] E. Träbert, P. Beiersdorfer, G. V. Brown, K. Boyce, R. L. Kelley, C. A. Kilbourne, F. S. Porter, and A. Szymkowiak, "Time-resolved soft-x-ray spectroscopy of a magnetic octupole transition in nickel-like xenon, cesium, and barium ions," *Phys. Rev. A*, vol. 73, p. 022508, Feb 2006.

[141] E. Träbert, P. Beiersdorfer, and G. V. Brown, "Observation of hyperfine mixing in measurements of a magnetic octupole decay in isotopically pure nickel-like Xe129 and Xe132 ions," *Phys. Rev. Lett.*, vol. 98, p. 263001, Jun 2007.

[142] R. Neu, K. B. Fournier, D. Bolshukhin, and R. Dux, "Spectral lines from highly charged tungsten ions in the soft-x-ray region for quantitative diagnostics of fusion plasmas," *Phys. Scr.*, vol. T92, pp. 307–310, 2001.

[143] S. D. Loch, M. S. Pindzola, C. P. Ballance, D. C. Griffin, A. D. Whiteford, and T. Pütterich, "Modeling the spectral emission from tungsten in tokamaks," in *18th International Conference on Spectral Line Shapes* (E. Oks and M. Pindzola, eds.), vol. CP874 of *AIP Conference Proceedings*, pp. 233–241, American Institute of Physics, Nov 2006.

[144] Y. Ralchenko, "Density dependence of the forbidden lines in Ni-like tungsten," *J. Phys. B: At. Mol. Opt. Phys.*, vol. 40, pp. F175–F180, Jun 2007.

[145] H. L. Zhang, D. H. Sampson, and C. J. Fontes, "Relativistic distorted-wave collision strengths and oscillator strengths for the 33 Ni-like ions with 60 $\leq$Z$\leq$92," *At. Data Nucl. Data Tables*, vol. 48, pp. 91–163, May 1991.

[146] K. B. Fournier, "Atomic data and spectral line intensities for highly ionized tungsten (Co-like W^{47+} to Rb-like W^{37+}) in a high-temperature, low-density plasma," *At. Data Nucl. Data Tables*, vol. 68, pp. 1–48, Jan 1998.

[147] K. M. Aggarwal, P. H. Norrington, K. L. Bell, F. P. Keenan, G. J. Pert, and S. J. Rose, "Radiative rates for allowed transitions in Ni-like Nd, Sm, Eu, Ta, and W," *At. Data Nucl. Data Tables*, vol. 74, pp. 157–255, Mar 2000.

[148] U. I. Safronova, A. S. Safronova, S. M. Hamasha, and P. Beiersdorfer, "Relativistic many-body calculations of multipole (E1, M1, E2, M2, E3, and M3) transition wavelengths and rates between 3^{-1}4l' excited and ground states in nickel-like ions," *At. Data Nucl. Data Tables*, vol. 92, pp. 47–104, 2006.

[149] C. P. Ballance and D. C. Griffin, "Relativistic radiatively damped *R*-matrix calculation of the electron-impact excitation of W^{46+}," *J. Phys. B: At. Mol. Opt. Phys.*, vol. 39, pp. 3617–3628, 2006.

[150] T. Pütterich, R. Neu, R. Dux, and ASDEX Upgrade Team, "Spectroscopic diagnostic of tungsten in fusion plasmas," in *34th EPS Conference on Plasma Physics*, vol. 31F of *Europhysics Conference Abstracts*, pp. P–5.103, 2007.

[151] R. W. P. McWhirter, "Review paper a5. data needs, priorities and accuracies for plasma spectroscopy," *Phys. Rep.*, vol. 37, pp. 165–209, Feb 1978.

[152] R. Mewe, "X-ray spectroscopy of stellar coronae," *The Astron. Astrophys. Rev.*, vol. 3, pp. 127–168, Jun 1991.

[153] ITER Physics Expert Group on Divertor, ITER Physics Expert Group on Divertor Modelling and Database, and ITER Physics Basis Editors, "Power and particle control," *Nucl. Fusion*, vol. 39, no. 12, pp. 2391–2469, 1999.

[154] R. D. Wood, D. N. Hill, E. B. Hooper, H. S. McLean, D. Ryutov, and S. Woodruff, "Comparison of deuterium and hydrogen experiments in the Sustained Spheromak Physics Experiment," *J. Nucl. Mater.*, vol. 337-339, pp. 548–552, Mar 2005.

[155] C. A. Romero-Talamás, E. B. Hooper, D. N. Hill, B. I. Cohen, H. S. McLean, R. D. Wood, and J. M. Moller, "Comparison between experimental measurements and numerical simulations of spheromak formation in SSPX," *J. Fusion Energy*, vol. 26, pp. 169–172, Jun 2007.

Comments on papers

In addition to the measurements reported in this dissertation, I have performed several EBIT measurements where the data sets are not yet analyzed. These measurements include determination of x-ray transition energies in M-shell platinum and uranium ions, and in L-shell bismuth ions. Data not yet evaluated also include EUV spectra of tungsten and nickel. As a certified EBIT operator I have assisted other researchers on their projects. This has often included operating the SuperEBIT and EBIT-I electron beam ion traps and helping out with measurements.

I have furthermore worked as a visiting researcher at the Princeton Plasma Physics Laboratory. The work in Princeton focused on EUV spectroscopy at the NSTX tokamak, where my main project was a tungsten injection experiment.

Paper I

This paper describes the EUV grating spectrometer used at the SSPX spheromak. The design of the instrument and some examples of its use are discussed. I performed the measurements reported and wrote the text for the paper.

Paper II

The paper describes some recent measurements using x-ray calorimeter spectrometers at the Livermore EBIT laboratory. I have been involved in some of the measurements reported and I provided one of the figures in the paper.

Paper III

The $2s_{1/2}$ - $2p_{3/2}$ transitions in F-like W^{65+} through Li-like W^{71+} have been measured with a crystal spectrometer at the SuperEBIT electron beam ion trap. I helped run the experiment and FAC calculations and assisted with the manuscript.

Paper IV

The wavelengths of $n = 3$ to $n = 3$ transitions in K-like W^{55+} through Ne-like W^{64+} have been measured using a high-resolution grating spectrometer at the SuperEBIT electron beam ion trap. Twenty wavelengths between 19 and 25 Å were measured and compared to calculations using the FAC code and theoretical predictions along the sodium and magnesium isoelectronic sequences. I was in charge of the measurement, collected most of the data, performed the FAC calculations and the analysis, and wrote the manuscript.

Paper V

The transition energies of M-shell tungsten ions were measured using an x-ray calorimeter at the SuperEBIT electron beam ion trap. I was in charge of the experiment and acquired most of the data. I did the calculations and analysis and wrote the paper.

Paper VI

This manuscript is in preparation and reports on theoretical calculations on six tungsten spectra. Presented data include transition energies, oscillator strengths, transition probabilities, and line emissivities for M-shell transitions in Ga-like W^{43+} through Fe-like W^{48+}. I have performed the calculations and written the manuscript.

Paper VII

Two strong electric-dipole forbidden x-ray transitions have been studied using two crystal spectrometers at the SuperEBIT electron beam ion trap. The measurements include wavelengths, relative intensities, and relative polarizations of the two tungsten lines. Atomic calculations and plasma modeling complement the measurements. The potential of the lines for diagnostics of tokamak plasmas is discussed. I ran the experiment, collected most of the data, was responsible for the data analysis, performed the calculations, and wrote the paper.

Paper VIII

This paper gives an overview of the spectroscopic efforts at the SSPX spheromak. The experimental setup is described and some results are presented. Data are compared with calculations and the plasma parameters of SSPX are estimated. I performed the measurements and analysis, and wrote the manuscript.

Paper IX

Titanium was injected into the SSPX spheromak using a gettering system to support line identifications in EUV spectra. I was in charge of the measurement and collected the data. I am furthermore responsible for the analysis and writing of the manuscript.

Paper X

This paper describes injection of tungsten hexacarbonyl into the SSPX spheromak. The similarities of SSPX plasmas with ITER divertor plasmas were utilized to simulate tungsten emission from ITER. The measurement was then complemented with calculations. The possibility of using tungsten EUV spectroscopy for diagnostics of the ITER divertor is discussed. I collected and evaluated the data, performed the spectral modeling, and wrote the paper.

Part III

Papers

Paper I

Grazing-incidence spectrometer on the SSPX spheromak[a)]

J. Clementson,[b)] P. Beiersdorfer, and E. W. Magee
Lawrence Livermore National Laboratory, Livermore, California 94550, USA

(Presented 15 May 2008; received 7 May 2008; accepted 9 July 2008; published online 31 October 2008)

The silver flat field spectrometer (SFFS) is a high-resolution grazing-incidence diagnostic for magnetically confined plasmas. It covers the wavelength range of 25–450 Å with a resolution of $\Delta\lambda=0.3$ Å full width at half maximum. The SFFS employs a spherical 1200 lines/mm grating for flat-field focusing. The imaging is done using a backilluminated Photometrics charge-coupled device camera allowing a bandwidth of around 200 Å per spectrum. The spectrometer has been used for atomic spectroscopy on electron beam ion traps and for plasma spectroscopy on magnetic confinement devices. Here we describe the design of the SFFS and the spectrometer setup at the sustained spheromak physics experiment in Livermore. © *2008 American Institute of Physics.*
[DOI: 10.1063/1.2965776]

I. INTRODUCTION

Plasma spectroscopy is an important diagnostic for laboratory plasmas studied in magnetic confinement fusion.[1–3] In these high-temperature plasmas, the extreme ultraviolet (EUV) interval 25–400 Å of the electromagnetic spectrum is a regime where a multitude of prominent lines from plasma impurities fall. The EUV includes *L*-shell transitions from Be through Cl and *M*-shell transitions from mid-*Z* ions such as Ti, Fe, and Cu.

There has been a number of different spectrometers used for EUV diagnostics on magnetic fusion devices. In fact, extreme ultraviolet and vacuum ultraviolet (400–1200 Å) spectrometers are standard instruments on most magnetic fusion experiments.[2] One of the most frequently used spectrometer designs is the survey poor resolution extended domain (SPRED) spectrometer, an instrument employing up to three different gratings with a total wavelength coverage from 100 up to 1700 Å with a resolution from 0.4 to 3 Å.[4,5] The benefit of this instrument is the wide spectral coverage. However, the poor resolution can make line identifications an uncertain process. Another often used spectrometer is the soft x-ray multichannel spectrometer designed for the 5–340 Å range with $\Delta\lambda=0.08$ Å using a 600 lines/mm grating.[6] Additional examples of EUV spectrometers on magnetic confinement devices include the grazing–incidence time resolving spectrometer that covers 15–360 Å with a wavelength resolution $\Delta\lambda=0.7$ Å;[7,8] the EUV spectrometers (10–130 Å and 50–500 Å) at the LHD stellarator with $\Delta\lambda=0.08$ and 0.24 Å, respectively;[9,10] and the x-ray and extreme ultraviolet spectrometer (XEUS) at the NSTX tokamak, employing a 2400 lines/mm grating for the 6–65 Å range with $\Delta\lambda=0.1$ Å.[11]

Flat field gratings, such as the gratings used on the SPRED (toroidal grating), XEUS (spherical), and LHD spectrometers (spherical), are attractive dispersive elements since they both diffract and focus the radiation to a plane, allowing for the use of planar electronic detectors, such as charged-coupled device (CCD) cameras or multichannel plates, enabling wider wavelength coverage without loss of spectral focus.

Here, we present a sister instrument to the XEUS spectrometer for use on high-temperature fusion plasmas. The spectrometer known as the silver flat field spectrometer (SFFS) is a high-resolution grazing-incidence instrument with a reflective grating. With its wide wavelength coverage, the SFFS is designed for greater flexibility than the XEUS spectrometer. As several other instruments employed at magnetic fusion energy facilities,[12] the SFFS was designed at the Livermore EBIT facility,[13] originally for use on electron beam ion traps. An earlier version of the spectrometer used on EBIT is described in Ref. 14. The adaption we describe here has proven to be an important diagnostic for spheromak

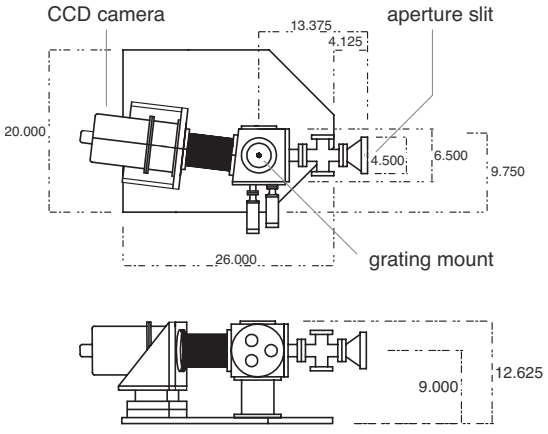

FIG. 1. SFFS outline. Top and side views. Dimensions in inches.

[a)]Contributed paper, published as part of the Proceedings of the 17th Topical Conference on High-Temperature Plasma Diagnostics, Albuquerque, New Mexico, May 2008.

[b)]Also at Atomic Physics Division, Lund Institute of Technology, P O Box 118, SE-221 00 Lund, Sweden. Electronic mail: clementson@llnl.gov.

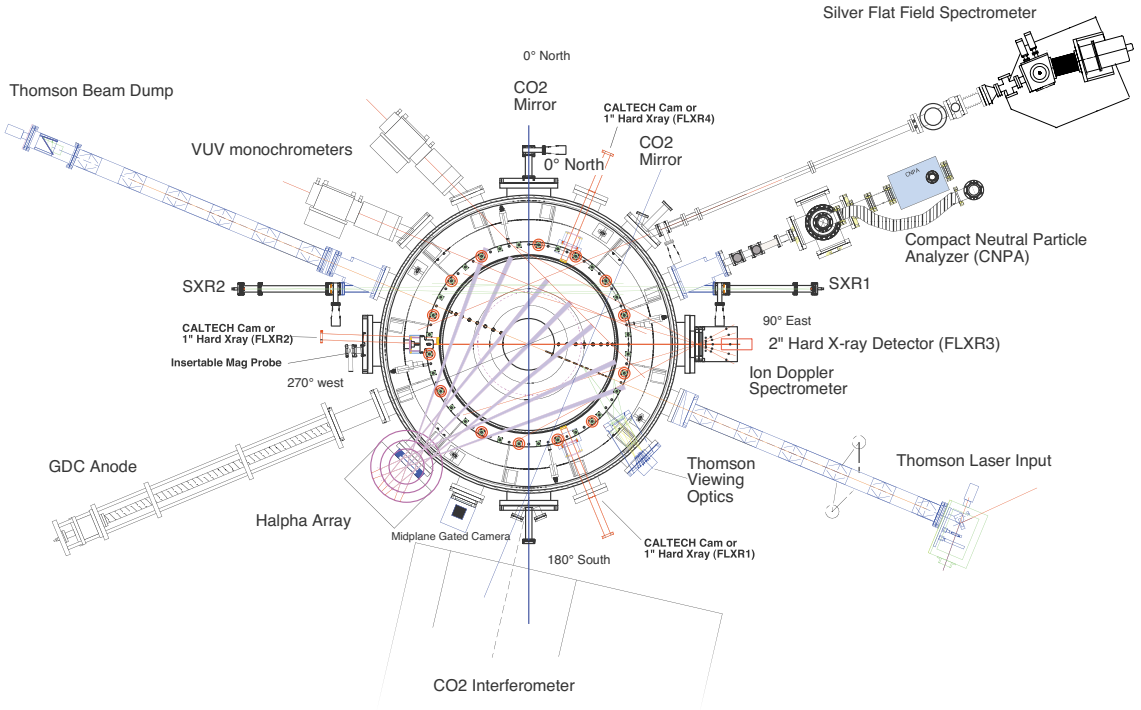

FIG. 2. (Color online) SSPX diagnostics suite. The SFFS EUV spectrometer is shown in the upper right corner, approximately 2 m from the SSPX vacuum vessel. Blueprint courtesy of H. S. McLean.

plasmas at the sustained spheromak physics experiment (SSPX) facility.[15] The SFFS spectrometer was recently moved to the NSTX tokamak in Princeton.

II. SPECTROMETER DESIGN

The silver spectrometer is a compact grazing-incidence spectrometer employing a spherical Hitachi grating (of the same type the XEUS and LHD spectrometers use) (Refs. 16 and 17) with an average groove density of 1200 lines/mm. The incident radiation impinges the grating around the blaze angle of 3.2°. The grating, originally intended for use on laser-produced plasmas, is mechanically ruled and aberration corrected, designed to produce a flat focal field in the 50–250 Å wavelength range. The gold covered surface of 30 mm groove length and 50 mm groove distance has a radius of curvature of 5649 mm.[16,17] The grating holder sits on a rotation table to enable matching of the incidence angle with the blaze angle, and is built to allow easy change of grating, e.g., the 2400 lines/mm XEUS grating.

Using a Klinger motorized linear stage and a bellows the CCD detector can be translated to cover the spectral range 25–450 Å with a bandwidth of about 200 Å per image. The detector used at the SSPX spectrometer setup was a backilluminated Photometrics CCD camera. The CCD array is made up of 1024×1024 pixels, each 25 μm in length, thus covering an area of 1 in. square. This large photon collection area enables the wide bandwidth of the spectrometer which, together with the high resolution, makes the SFFS a useful diagnostic. In order to reduce photon noise the CCD detector is cryogenically cooled with liquid nitrogen and operated at a temperature around −100 °C. The spectral background of the images thus mainly results from plasma bremsstrahlung, stray light from the spectrometer, readout noise, and high-energy cosmic rays impinging on the CCD. The CCD chip is uncoated and thus reflects optical photons, thereby preferentially selecting higher energy radiation such as ultraviolet and x-ray photons. Schematic views of the SFFS design are shown in Fig. 1.

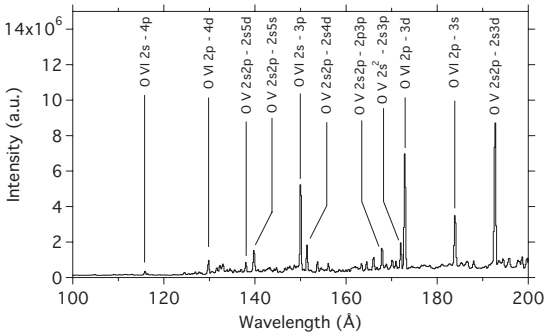

FIG. 3. SSPX shot 18360. SSPX emission above 100 Å is rich of line radiation, mainly from O IV–O VI. Some of the prominent oxygen lines are labeled.

TABLE I. SFFS measured linewidths (FWHM) from SSPX shot 18360 using a 100 μm slit.

Spectrum	Transition	λ (Å)	Δλ (Å)	λ/Δλ
O VI	$2s$-$4p$	115.9	0.35	331
O VI	$2p$-$4d$	129.9	0.28	464
O VI	$2s$-$3p$	150.1	0.27	556
O V	$2s^2$-$2s3p$	172.2	0.30	574
O VI	$2p$-$3d$	173.0	0.34	509
O V	$2s2p$-$2s3d$	192.8	0.37	521

III. SPHEROMAK SPECTROSCOPY

The SFFS has been used for plasma diagnostics and atomic physics research on the SSPX spheromak. The SSPX facility at Lawrence Livermore National Laboratory is an experiment with its main purpose to investigate magnetic field buildup and energy confinement.[18] The spheromaks are confined within a cylindrical flux conserver with diameter of 1 m and height of 0.5 m.[19] The flux conserver is made of tungsten-coated copper walls with a separation at the midplane for diagnostic access.[20] The plasma discharges last a few milliseconds and achieve electron temperatures from about 10 eV up to over 500 eV,[18] and electron densities in the range of 10^{13}–10^{15} cm^{-3}. The SSPX diagnostics suite includes a Thomson scattering system, a CO_2 laser interferometer system, magnetic probes, and an ion doppler spectrometer,[20] which together with the SFFS make the SSPX spheromak a well-diagnosed experiment. A layout of the SSPX diagnostics suite, including the location of the SFFS, is shown in Fig. 2.

With a field of view through the magnetic axis at the midplane of the toroidal spheromak plasmas, the SFFS sight line covered plasma regions of varying density and temperature. Due to the short SSPX discharges, the CCD camera recorded time-integrated images. Thus the spectra are both spatially and temporally integrated. The SFFS performed measurements during a multitude of SSPX experiments with different operating conditions, such as discharge lengths, electron temperatures and densities, and impurity concentrations.

From a diagnostics port of SSPX, the radiation entered the SFFS grating chamber roughly 2 m away through an imaging slit. Widths used were 34 and 100 μm. The low-conductivity slit together with other apertures in the beam line reduced the stray light in the spectrometer and the gas load on the differentially pumped system. The pressure in SSPX during a discharge can rise to the millitorr range, while the pressure of the SFFS grating chamber was held in the 10^{-7} Torr range by two turbomolecular pumps.

The SSPX plasmas have a multitude of line emission above 100 Å where O IV–O VI are the dominating spectra in most discharges. Figure 3 shows a typical spectrum of the 100–200 Å range (SSPX shot 18360), where a 100 μm slit was used. The wavelength resolution varies across the grating, with a measured linewidth around 0.3 Å full width at half maximum (FWHM). The resolving power, λ/Δλ, for this shot is given for some of the lines in Table I. Spectra such as that from shot 18360 are useful for collisional-radiative modeling verifications. Modeling of the oxygen EUV emission from SSPX plasmas is presented by Wilcox *et al.* in this issue.[21]

The main purpose of the SFFS spectrometer at the SSPX spheromak was to identify impurity ions present in the device. We have successfully identified a multitude of impurity ions using spectral lines from He-like B IV at 60 Å up to W lines above 400 Å. Identified emission lines also include those from Ti, Cu, N, and C. With relatively low-temperature, high-density plasmas the SSPX spheromak was a good testbed for atomic physics, providing spectra not readily attained in other devices. As an example, the SFFS was used for tungsten spectroscopy by injecting tungsten hexacarbonyl into the machine. Furthermore, the high instrumental resolution has permitted electron density and temperature measurements using line intensity ratios.[22] The SFFS has thus proven to be a very useful diagnostic for this kind of magnetic confinement experiment.

ACKNOWLEDGMENTS

This work was performed under the auspices of the United States Department of Energy by Lawrence Livermore National Laboratory under Contract Nos. W-7405-ENG-48 and DE-AC52-07NA-27344. The authors are grateful for support from the SSPX group.

[1] C. De Michelis and M. Mattioli, Rep. Prog. Phys. **47**, 1233 (1984).
[2] B. C. Stratton, M. Bitter, K. W. Hill, D. L. Hillis, and J. T. Hogan, Fusion Sci. Technol. **53**, 431 (2008).
[3] M. G. von Hellermann *et al.*, Phys. Scr., T **120**, 19 (2005).
[4] R. J. Fonck, A. T. Ramsey, and R. V. Yelle, Appl. Opt. **21**, 2115 (1982).
[5] B. C. Stratton, R. J. Fonck, K. Ida, K. P. Jaehnig, and A. T. Ramsey, Rev. Sci. Instrum. **57**, 2043 (1986).
[6] J. L. Schwob, A. W. Wouters, S. Suckewer, and M. Finkenthal, Rev. Sci. Instrum. **58**, 1601 (1987).
[7] W. L. Hodge, B. C. Stratton, and H. W. Moos, Rev. Sci. Instrum. **55**, 16 (1984).
[8] B. C. Stratton, H. W. Moos, W. L. Hodge, S. Suckewer, J. C. Hosea, R. A. Hulse, D. Q. Hwang, and J. R. Wilson, Nucl. Fusion **24**, 767 (1984).
[9] M. B. Chowdhuri, S. Morita, and M. Goto, Appl. Opt. **47**, 135 (2008).
[10] M. B. Chowdhuri, S. Morita, M. Goto, H. Nishimura, K. Nagai, and S. Fujioka, Rev. Sci. Instrum. **78**, 023501 (2007).
[11] P. Beiersdorfer, M. Bitter, L. Roquemore, J. K. Lepson, and M.-F. Cu, Rev. Sci. Instrum. **77**, 10F306 (2006).
[12] A. T. Graf *et al.*, Can. J. Phys. **86**, 307 (2008).
[13] P. Beiersdorfer *et al.*, Nucl. Instrum. Methods Phys. Res. B **205**, 173 (2003).
[14] P. Beiersdorfer, J. R. Crespo López-Urrutia, P. Springer, S. B. Utter, and K. L. Wong, Rev. Sci. Instrum. **70**, 276 (1999).
[15] E. B. Hooper, L. D. Pearlstein, and R. H. Bulmer, Nucl. Fusion **39**, 863 (1999).
[16] T. Kita, T. Harada, N. Nakano, and H. Kuroda, Appl. Opt. **22**, 512 (1983).
[17] N. Nakano, H. Kuroda, T. Kita, and T. Harada, Appl. Opt. **23**, 2386 (1984).
[18] B. Hudson *et al.*, Phys. Plasmas **15**, 056112 (2008).
[19] R. D. Wood, D. N. Hill, E. B. Hooper, H. S. McLean, D. Ryutov, and S. Woodruff, J. Nucl. Mater. **337-339**, 548 (2005).
[20] H. S. McLean *et al.*, Rev. Sci. Instrum. **72**, 556 (2001).
[21] P. G. Wilcox, A. S. Safronova, V. L. Kantsyrev, U. I. Safronova, K. M. Williamson, M. F. Yilmaz, J. Clementson, P. Beiersdorfer, and K. W. Struve, Rev. Sci. Instrum. **79**, 10F543 (2008).
[22] J. Clementson, P. Beiersdorfer, M. F. Gu, H. S. McLean, and R. D. Wood, J. Phys.: Conf. Ser. (in press).

Paper II

Laboratory Astrophysics, QED, and other Measurements using the EBIT Calorimeter Spectrometer at LLNL

G. V. Brown[*], J. S. Adams[†], P. Beiersdorfer [*], J. Clementson [*], M. Frankel [*], S. M. Kahn [**], R. L. Kelley[†], C. A. Kilbourne[†], D. Koutroumpa[†], M. Leutenegger[†], F. S. Porter[†], D. B. Thorn[‡] and E. Träbert[*]

[*]*Lawrence Livermore National Laboratory, 7000 East Avenue, Livermore, CA 94550, USA*
[†]*NASA/GSFC Code 662, Greenbelt, MD 21201, USA*
[**]*Stanford University Physics Department, Stanford, CA 94305, USA*
[‡]*GSI, Darmstadt, Germany*

Abstract. We have used the EBIT Calorimeter Spectrometer (ECS), a microcalorimeter instrument built by the calorimeter group at the NASA/Goddard Space Flight Center, to make a variety of measurements since its installation at Lawrence Livermore National Laboratory's EBIT facility. These include measurements of charge exchange between neutral gas and K- and L- shell ions, measurements of the X-ray transmission efficiency of optical blocking filters, high resolution measurements of transition energies for high-Z, highly charged ions, and measurements of M and L-shell emission from highly charged tungsten following on earlier measurements of L-shell gold. Our results will see application in the interpretation of the spectra from the Jovian atmosphere and of the diffuse soft X-ray background, in tests of QED, and in diagnosing inertial and magnetic confinement fusion plasmas. These measurements augment previous laboratory astrophysics, atomic physics, and calibration measurements made using earlier versions of NASA's microcalorimeter spectrometer.

Keywords: X-ray, X-ray spectroscopy, calorimeter, astrophysics,QED
PACS: 32.30.Rj,95.30.Dr

X-ray calorimeters built at the NASA/Goddard Space Flight Center have been used at Lawrence Livermore National Laboratory's (LLNL) Electron Beam Ion Trap (EBIT) facility beginning in 2000 [1, 2, 3]. Since then, three different versions of the NASA/GSFC calorimeter instrument have operated at LLNL, the most recent being the EBIT Calorimeter Spectrometer (ECS) [4, 5]. The ECS consists of 32 silicon thermister pixels, 18 affixed with 8 μm thick HgTe absorbers for measurements in the 0.05 to 12 keV band, and 14 affixed with 100 μm thick HgTe absorbers for measurements covering the 0.3 to 100 keV band. The 8 μm pixels have an energy resolution of $\sim$ 4.5 eV (FWHM) at 6 keV with 95% quantum efficiency, and the 100 μm pixels have a resolution of 33 eV (FWHM) at 60 keV with a QE of 32% (see [5] for more details). Because of its high spectral resolution, broad bandwidth, high quantum efficiency, and the fact that the energy resolution does not depend on the size of the X-ray source, the ECS and its predecessors have become the "workhorse" spectrometers at the LLNL EBIT facility. They have been used to measure absolute excitation cross sections [6, 7], line energies [8], spectral signatures of charge exchange recombination [9, 10], in lifetime measurements [11], in a variety of laboratory astrophysics experiments, and to measure the transmittance of optical blocking filters [12]. Here we give a brief description of a few of the more recent measurements using the microcalorimeter instruments at the LLNL EBIT facility.

EBIT was invented at LLNL and was built and developed as a tool to make high-accuracy measurements of atomic structure [13, 14, 15]. The main components of EBIT are an electron beam, a trap region, and a beam collector. The electron beam is used to radially trap, ionize, and excite ions. Ions are trapped axially by three drift tubes. Once the beam passes through the trap region, it is collected by a collector electrode. Details of the operation of EBIT can be found elsewhere [16].

Charge exchange (CX) recombination is the radiationless transfer of one or more electron from a neutral atom or molecule to an ion. X-rays are produced from CX when the transferred electron radiatively decays. CX takes place in celestial and laboratory sources. Owing to the fact that relatively little laboratory data exist, and in many cases CX spectral signatures are not well known, the diagnostic capability of CX emission has not been fully realized. To address this problem, EBIT and the ECS have been used to measure the X-ray spectral signatures of CX recombination. At EBIT, X-ray emission from charge exchange is produced using the magnetic trapping mode [17]. In this mode, the electron beam is turned off and the ions are trapped radially by the magnetic field of the superconducting magnet usually used to compress the electron beam. Neu-

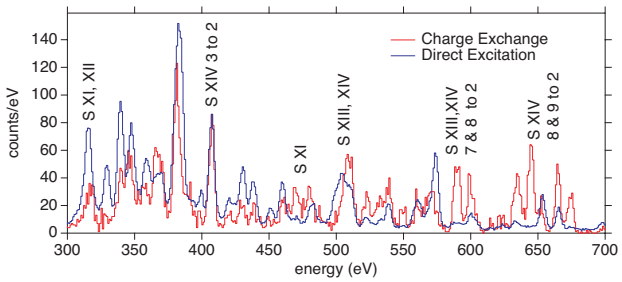

FIGURE 1. Comparison of direct excitation to charge exchange produced spectra of L-shell sulfur ions. Both spectra were measured with the EBIT Calorimeter Spectrometer. Some of the stronger lines are labelled. See [10] for a complete description of the measurement. (Color online)

tral material, introduced in the trap region using a ballistic gas injector, then interacts with the ions, CX occurs and X-rays are produced. Because the beam is not present in the magnetic mode, the ions are no longer localized to the 60 μm electron beam diameter and therefore represent an extended source of X-ray emission. The ability of the NASA/GSFC microcalorimeter to measure high-resolution spectra from extended sources without a degradation in energy resolution, and to measure time-resolved spectra, make it perfectly suited to measure the spectral signature of CX reactions produced in EBIT. Several CX measurements have been completed using the NASA/GSFC microcalorimeter instruments [9, 18, 19]. Recently, we have used the ECS to measure the CX signature of L-shell ions of sulfur. Because these transitions fall in the energy band below 500 eV, their measurement is largely facilitated by the relatively thin thermal blocking filters employed by the ECS. Figure 1 shows a comparison of the direct excitation spectrum and the spectrum produced by CX. These spectra are being used to interpret the X-ray emission from the aurora of Jupiter and also of the soft X-ray background [10, 20].

Tungsten is being employed as an internal coating for magnetic fusion devices and will be the material used for the divertor in the International Thermonuclear Experimental Reactor (ITER). As a result, it will be present in many fusion plasmas. At the temperature of the higher energy devices, several middle charge state W ions will be present. Accurate knowledge of the emission line wavelengths and excitation cross sections are crucial for tapping the W X-ray spectra of its full diagnostic potential. To provide benchmarks for atomic codes used to model these spectra, the ECS is being used to measure X-ray emission from both M-shell and L-shell inter- and intra-shell transitions. Figure 2 shows a broadband spectrum of X-ray emission from M-shell transitions in Ni-like W^{46+} and Co-like W^{47+} [21].

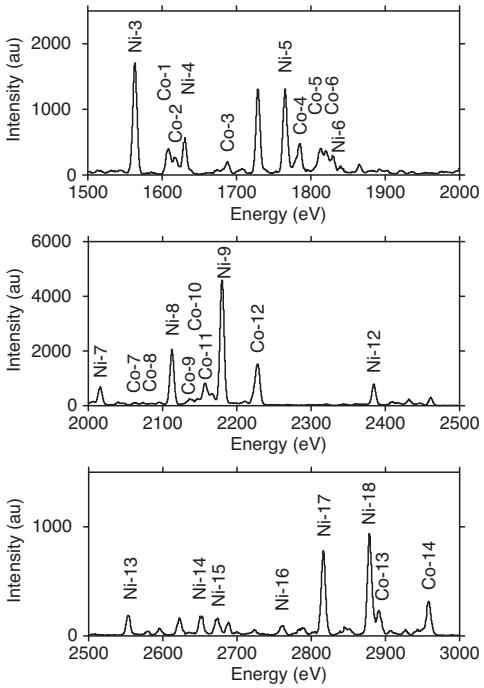

FIGURE 2. Broadband spectrum of M-shell transitions in Co- and Ni-like W. The spectrum is divided into three pieces for easier viewing. The lines are labeled according to thier charge state, i.e. Ni-3 is from Nickel-like W^{46+}. This spectrum was measured with the XRS/EBIT spectrometer, the second generation NASA/GSFC calorimeter in operation at LLNL [21].

The NASA/GSFC calorimeters have also been used to benchmark atomic codes used to interpret spectra from high-density, laser-produced plasmas and inertial con-

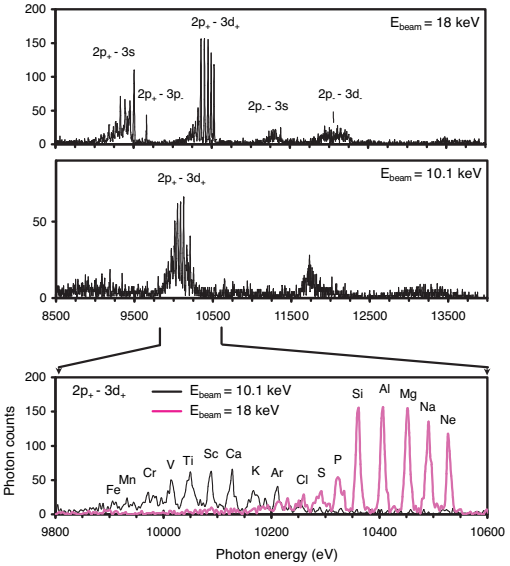

FIGURE 3. High resolution spectra of L-shell transitions in highly charged gold ions. The top figure was measured at an electron beam energy of 18 keV and shows strong emission from Si-like Au^{65+} to Ne-like Au^{69+}. The middle figure was measured at an electron beam energy of 10.1 keV and contains emission from several lower charge states between Fe-like Au^{53+} and Ar-like Au^{61+}. The bottom figure shows an expanded view of the 9800 to 10600 eV band [8].

finement fusion plasmas. Gold hohlraums are often employed as targets for inertial confinement fusion studies. In these studies, electron temperatures in the laser plasma interaction region have been predicted as high as 30 keV and Thomson scattering experiments have measured temperatures as high as 50 keV, although with high uncertainty owing to the fact that the average ionization state of gold ions is not well known. Gold L-shell radiation is produced in plasmas with electron temperatures in the 30–50 keV band. If resolved, this radiation creates a "picket-fence" spectral structure where each line or "post" is produced by a different charge state. In the past, uncertainties in the calculations have made it very challenging to unambiguously determine which charge state produced which line feature. To address this problem, we have used the calorimeter and the LLNL EBIT to measure the line energies of the L-shell transitions in highly charged gold ions. For these experiments, gold was injected using the laser ablation injection system [22], and the energy scale was calibrated using K-shell emission from Ar, Ni, and Ge. Figure 3 shows the spectra measured at 18 keV, one at 10.1 keV, and also an expanded view of the region with the strongest line emission. In the bottom figure, the "picket-fence" structure is easily seen and the emission from several different charge states is easily resolved. A detailed description of this experiment and the theoretical study can be found in [8].

In addition to the L- and M-shell transitions in high-Z ions, measurements of the transition energies of K-shell emission from high-Z ions have also been measured using the ECS. For example, the high-energy pixels have been used to measure the emission from helium-like Xe^{52+} and hydrogenic Xe^{53+} (see figure 6 of Porter et al., in these proceedings). The high resolution and QE of the high energy pixels made it possible to measure the transition energies to high accuracy, and to resolve some lines for the first time. The results of these measurements have been used to distinguish among different calculations of QED contributions to the transition energies [23].

The utility of the ECS-EBIT combination goes beyond measurements of atomic physics parameters and laboratory astrophysics studies. It has also been used to measure the absolute X-ray transmittance of thin filters [8]. Many spectral diagnostics employ thin filters of either pure metals or metalized plastic to filter out unwanted radiation or to provide energy calibration fiducials created by absorption edges. Because the X-ray transmittance of these filters is energy dependent, proper analysis of the detected radiation requires an accurate knowledge of the transmittance as a function of energy. Although manufacturers often do an excellent job of determining thickness, the quoted uncertainty in the thickness often translates to an error in transmittance larger than required to achieve experimental goals, and most manufacturers do not provide X-ray transmittance data. We have developed a system to measure the absolute transmittance of thin filters. In our method we translate the filter in and out of the line of sight of the X-ray radiation from EBIT to the ECS. By dividing the strength of the X-ray line radiation measured with the filter in by the spectrum with the filter out, the absolute filter transmission is determined. As an example, Figure 4 shows the results of a measurement of the transmittance of an aluminized lexan filter manufactured by the Luxel corporation. To span the energy range from below the carbon edge to above the aluminum edge, X-ray radiation produced by K-shell transitions in B, C, N, O, and Ne were used, as well as L-shell transitions in neon-like Kr. The advantage of using the ECS as a detector is that its high energy resolution and broad bandwidth make it possible to easily determine the X-ray transmittance at several discrete X-ray energies simultaneously; hence, the transmittance as a function of energy can be rapidly determined. The total time required to determine the complete X-ray transmittance across the 200 to 2000 eV energy band for the Luxel filter was 6 hours.

Here we have shown the large range of measurements made possible by the ECS and the previous NASA/GSFC calorimeter instruments operated at the LLNL EBIT fa-

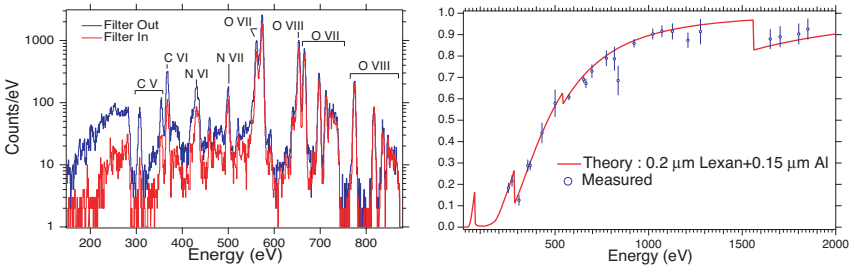

FIGURE 4. (Left) Comparison of the spectra measured by the ECS to determine the absolute X-ray transmittance of the aluminized lexan filter across the 150 to 900 eV energy band. (Right) Measured compared to theoretical transmittance. Theory based on data from the Center for X-ray optics and the nominal thickness of the filter given by the manufacturer [12].

cility. The ECS will continue to be employed as one of the primary spectrometers used daily at LLNL.

ACKNOWLEDGMENTS

This work was performed under the auspices of the U.S. Department of Energy by the Lawrence Livermore National Laboratory under contract DE-AC52-07NA27344 and is supported by NASA grants to LLNL, NASA/GSFC, and Stanford University.

REFERENCES

1. Porter, F. S., Beiersdorfer, P., Brown, G. V., Gu, M. F., Kelley, R. L., Kahn, S. M., Kilbourne, C. A., and Thorn, D. B., *J. of Physics: Conf. Series*, **163**, 012105 (2009).
2. Porter, F. S., Beiersdorfer, P., Boyce, K. R., Brown, G. V., Chen, H., Gygax, J., Kahn, S. M., Kelley, R. L., Kilbourne, C. A., Magee, E., and Thorn, D. B., *Can. J. Phys.*, **86**, 231–240 (2008).
3. Porter, F. S., Audley, M. D., Beiersdorfer, P., Boyce, K. R., Brekosky, R. P., Brown, G. V., Gendreau, K. C., Gygax, J., Kahn, S. M., Kelley, R. L., Stahle, C. K., and Szymkowiak, A. E., "Laboratory Astrophysics using a Spare XRS Microcalorimeter", in *Proceedings of the 45th annual SPIE meeting on Optical Science and Technology*, SPIE Press, p. 4140 (2000).
4. Porter, F. S., Beiersdorfer, P., Boyce, K. R., Brown, G. V., Chen, H., Gygax, J., Kahn, S. M., Kelley, R. L., Kilbourne, C. A., Magee, E., and Thorn, D. B., *Rev. Sci. Instrum.*, **79**, 10E307 (2008).
5. Porter, F. S., Adams, J. S., Beiersdorfer, P., Brown, G. V., Clementson, J., Kahn, S. M., Kelley, R. L., and Kilbourne, C. A. (2010), these proceedings.
6. Brown, G. V., Beiersdorfer, P., Boyce, K. R., Chen, H., Kelley, R. L., Kilbourne, C. A., Porter, F. S., Szymkowiak, A. E., Gu, M. F., and Kahn, S. M., *Phys. Rev. Lett.*, **96**, 253201 (2006).
7. Chen, H., Beiersdorfer, P., Scofield, J. H., Brown, G. V., Boyce, K. R., Kelley, R. L., Kilbourne, C. A., Porter, F. S., Gu, M. F., and Kahn, S. M., *Astrophys. J.*, **618**, 1086 (2005).
8. Brown, G. V., Hansen, S. B., Träbert, E., Beiersdorfer, P., Widmann, K., Chen, H., Chung, H. K., Clementson, J. H. T., Gu, M. F., and Thorn, D. B., *Phys. Rev. E*, **77**, 066406 (2008).
9. Beiersdorfer, P., Boyce, K. R., Brown, G. V., Chen, H., Kahn, S. M., Kelley, R. L., May, M., Olson, R. E., Porter, F. S., Stahle, C. K., and Tillotson, W. A., *Science*, **300**, 1558–1559 (2003).
10. Frankel, M., Beiersdorfer, P., Brown, G. V., Clementson, J., Gu, M. F., and Schweikhard, L., *J. of Physics: Conf. Series*, **163**, 012051 (2009).
11. Träbert, E., Beiersdorfer, P., Brown, G. V., Boyce, K., Kelley, R. L., Kilbourne, C. A., Porter, F. S., and Szymkowiak, A., *Phys. Rev. A*, **73**, 022508 (2006).
12. Brown, G. V., Beiersdorfer, P., Emig, J., Frankel, M., Gu, M. F., Heeter, R. F., Magee, E., Thorn, D. B., Widmann, K., Kelley, R. L., Kilbourne, C. A., and Porter, F. S., *Rev. Sci. Instrum.*, **79**, 10E309–10E309–3 (2008).
13. Beiersdorfer, P., *Can. J. Phys.*, **86**, 1–10 (2008).
14. Nilsen, J., *Can. J. Phys.*, **86**, 19–23 (2008).
15. Marrs, R., *Can. J. Phys.*, **86**, 11–18 (2008).
16. Beiersdorfer, P., *Astron. Astrophys. Review*, **41**, 343–390 (2003).
17. Beiersdorfer, P., Schweikhard, L., López-Urrutia, J. C., and Widmann, K., *Rev. Sci. Instrum.*, **67**, 3818–3826 (1996).
18. Wargelin, B. J., Beiersdorfer, P., and Brown, G. V., *Can. J. Phys.*, **86**, 151–169 (2008).
19. Brown, G. V., Beiersdorfer, P., Clementson, J., Chen, H., Frankel, M., Gu, M. F., Kelley, R. L., Kilbourne, C. A., Porter, F. S., Thorn, D. B., and Wargelin, B., *J. of Physics: Conf. Series*, **163**, 012052 (2009).
20. Frankel, M., Beiersdorfer, P., Brown, G. V., Gu, M. F., Kelley, R. L., Kilbourne, C. A., and Porter, F. S., *Astrophys. J.*, **702**, 171–177 (2009).
21. Clementson, J., Beiersdorfer, P., Brown, G. V., and Gu, M. F., *Physica Scripta* (2009), submitted.
22. Niles, A. M., Magee, E. W., Thorn, D. B., Brown, G. V., Chen, H., and Beiersdorfer, P., *Rev. Sci. Instrum.*, **77**, 10F106 (2006).
23. Thorn, D. B., Gu, M. F., Brown, G. V., Beiersdorfer, P., Kelley, R. L., Kilbourne, C. A., and Porter, F. S., *Phys. Rev. Lett.* (2009), submitted.

Paper III

Spectroscopy of $2s_{1/2}-2p_{3/2}$ transitions in W^{65+} through W^{71+}

Y. Podpaly,* J. Clementson, P. Beiersdorfer, J. Williamson,† G. V. Brown, and M. F. Gu
Physics Division, Lawrence Livermore National Laboratory, Livermore, California 94550, USA
(Received 28 August 2009; published 11 November 2009)

A high-resolution flat-crystal spectrometer was used on the SuperEBIT electron beam ion trap to measure the energies of the $2s_{1/2}-2p_{3/2}$ transitions in lithiumlike through fluorinelike tungsten. These transitions are strongly affected by energy shifts due to quantum electrodynamics (QED). SuperEBIT was run at an electron energy of 103.2 ± 0.5 keV and an electron beam current of 150 mA to generate the respective charge states; hydrogenlike aluminum and neonlike krypton were used as calibration elements. The spectra were analyzed with and the results compared to calculations based on the flexible atomic code. Good agreement was found. The measurements yielded line positions with a precision of 1–2 eV, which test QED calculations to 5%–10%.

DOI: 10.1103/PhysRevA.80.052504 PACS number(s): 32.30.Rj, 52.70.La

I. INTRODUCTION

Spectral studies of ions of heavy elements provide data that are invaluable in a variety of fields including atomic physics, astronomy, and high-temperature plasma diagnostics. In atomic physics, transition energies provide a test of the predictions of quantum electrodynamics (QED) as well as a handle on the nature of multielectron atomic structure. The QED contribution to the $2s_{1/2}-2p_{3/2}$ transition has been measured for high-Z elements such as thorium, uranium, and, more recently, lead [1–4] and for mid-Z elements such as xenon [5]; additional experiments are being planned as well such as those on the GSI storage ring [6]. QED processes are generally more pronounced with higher charge, since the effects scale as Z^4. However, QED plays a large role in determining the transition energies of all of these heavy ions. The present work, which focuses on the $2s_{1/2}-2p_{3/2}$ transitions in highly charged tungsten ions, proceeds to fill uncharted territory in mid-to-high-Z elements, i.e., the region in atomic number between Xe ($Z=54$) and Pb ($Z=82$) for which no measurements exist.

Measurements of tungsten have recently become significantly more important due to the start of construction of the ITER tokamak, where tungsten plasma-facing components and high electron temperatures, on the order of 25 keV, possibly reaching as high as 30–40 keV under certain operating conditions [7,8], are expected to produce highly ionized tungsten within the plasma. In fact, line radiation of L-shell tungsten ions may serve as a diagnostic of the ion temperature and the bulk velocity of the plasma core, where such highly charged ions are predicted to exist. Moreover, plasma energy losses can become significant due to radiation, so there has been research on the intensities and energies of the tungsten emissions, mostly in the euv and vuv, covering charge states from W^{64+} and below [9–16]. These investigations have been important both for tokamak and Z pinch plasmas [17,18]. None of these works, however, have focused on QED effects. An exception is the recent measurement of 3–3 transitions in sodiumlike tungsten and neighboring ions with lower charge (W^{58+}-W^{61+}). These measurements achieved an accuracy sufficient to constrain QED calculations at the 10% level [19].

The overall objective of the work described in this paper is to measure with high resolution the $2s_{1/2}-2p_{3/2}$ transitions of highly ionized tungsten L-shell ions, identify the spectral lines, and compare the measured energies to theoretical values. We find that these transitions are the strongest lines in the x-ray spectrum of open L-shell tungsten ions. The QED contribution is expected to be about 17 eV for the $2s_{1/2}-2p_{3/2}$ transition of Li-like tungsten [20]; since our measurement has an accuracy of about 1 eV, it provides a gauge of the QED contribution at the 6% level.

II. EXPERIMENTAL SETUP

The SuperEBIT electron beam ion trap at the Lawrence Livermore National Laboratory (LLNL) [21] was used to make these measurements in a Doppler-shift free, tungsten dominated environment. An electron beam ion trap employs a set of drift tubes and uses the space charge effect of the electron beam to create an electrostatic potential trap to confine the ions to be studied. A 3 T axial magnetic field is used to further confine the ions. Due to the possible buildup of impurities in the trap, the axial well is emptied at a given frequency to purge all confined ions. For these measurements the electron beam energy was set to 103.2 ± 0.5 keV and the timing cycle was chosen to produce the best tungsten charge balance, which was found to be 27 s. Beam currents were maintained around approximately 150 mA. Tungsten was injected into the trap with a metal vapor vacuum arc. There were trace amounts of argon and silicon in the trap; these elements acted as low-Z cooling ions and provided x-ray calibration lines. At these machine parameters, the 2–2 transitions of tungsten are the most significant emission seen, as illustrated in the spectrum recorded with the EBIT x-ray calorimeter spectrometer (ECS) in Fig. 1. The ECS [22,23] has an energy resolution of approximately 5 eV across the energy range 0.5–15 keV. It does not have the resolution of a crystal spectrometer, but it is an exceptional survey diagnostic.

*Permanent address: MIT Plasma Science and Fusion Center, Cambridge, MA 02139.
†Department of Physics, Florida A&M University, Tallahassee, FL 32307.

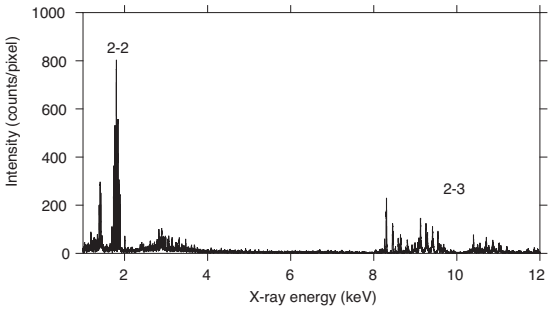

FIG. 1. Spectrum of tungsten from SuperEBIT recorded with the EBIT calorimeter spectrometer (ECS). Transitions between levels of principal quantum number n are labeled.

The crystal spectrometer we employed for the present measurement used a 11-cm-long, 1.2-cm-wide flat ammonium dihydrogen phosphate (ADP, $2d=10.640$ Å) crystal 38 cm from the electron beam and set to a central Bragg angle of $\theta=39°$. X rays were detected with an ORDELA model 1100XF position-sensitive proportional counter placed at a distance of 25 cm from the crystal. The detector was filled with 760 Torr P-10 gas (90% argon, 10% methane). The detector's vacuum window consisted of 4 μm polyimide coated with 200–400 Å aluminum. Further descriptions of the spectrometer are available in [24,25]. The crystal reflects x rays based on their wavelengths, λ, following Bragg's law, $n\lambda=2d\sin(\theta)$, where n is the order of reflection. The position on the detector, thus, can give precise wavelength information. The spectrometer was operated with a chamber pressure on the order of 10^{-7} Torr, which is a factor of 10^4 higher than the ambient EBIT chamber pressure. This pressure gradient is maintained using a 5076 Å thick polyimide filter. The detector is connected to an event-mode-type data acquisition system [26].

The spectrometer was calibrated initially with a 1.69 mCi ^{55}Fe source, which allowed setting the gates of the data acquisition system to remove background noise; the ^{55}Fe source was also used to set the proper detector voltage. Spectral lines from hydrogenlike aluminum and neonlike krypton generated in SuperEBIT were used to get a calibration of the energy scale as detailed in the next section. Due to possible drifts in the spectrometer, data from each day were analyzed separately and errors were increased to account for possible drifts.

III. CALIBRATION

The energy calibration of the crystal spectrometer was accomplished by the injection of tri-methyl aluminum (TMA) and krypton gas into the trap. The results of the aluminum calibration are shown in Fig. 2. The spectrum also shows lines from silicion, an intrinsic impurity. The intensity of the silicon emission was too low for both the He-like w and z lines, corresponding to the transitions $1s_{1/2}2p_{3/2}\rightarrow 1s^2$ and $1s_{1/2}2s_{1/2}\rightarrow 1s^2$, respectively, to provide an accurate calibration; however, the w line was located where it was expected. Neonlike krypton has the four strong, well known lines $3F$, $3D$, $3C$, and $3A$ within the region of interest. These lines correspond to the transitions from the upper configurations $2s^22p_{1/2}2p^4_{3/2}3s_{1/2}$, $2s^22p^2_{1/2}2p^3_{3/2}3d_{5/2}$, $2s^22p_{1/2}2p^4_{3/2}3d_{3/2}$, and $2s_{1/2}2p^63p_{3/2}$, respectively, to the ground state $2s^22p^6$. There are numerous other krypton lines in the region as well, mostly from fluorinelike krypton; however, these lines were overly blended to use for calibration. The krypton measurement is shown in Fig. 3. Since each x-ray energy is directly related via Bragg's law to a unique angle on the detector face, the calibration curve was calculated as a relation between angle and channel number.

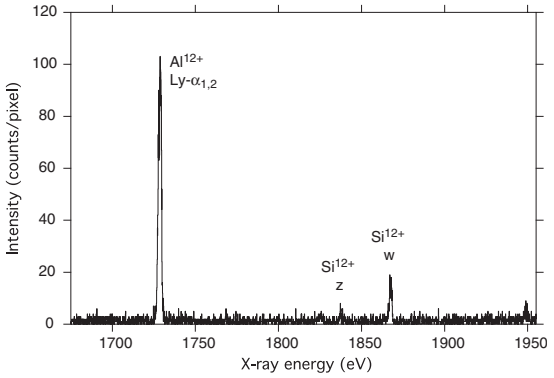

FIG. 2. Spectrum of hydrogenlike aluminum recorded on SuperEBIT with the flat-crystal spectrometer. Additional lines from heliumlike silicon are marked as well. These lines are used for wavelength calibrations.

Due to the geometry of the flat crystal and detector arrangement, the curve of angle versus channel number is expected to be a weak quadratic polynomial. The energies of the aluminum lines were set to the values given in [27]. The spectral fitting procedures assumed that the widths of the two Lyman alpha lines were identical, since the linewidth in our case was almost exclusively determined by the detector res-

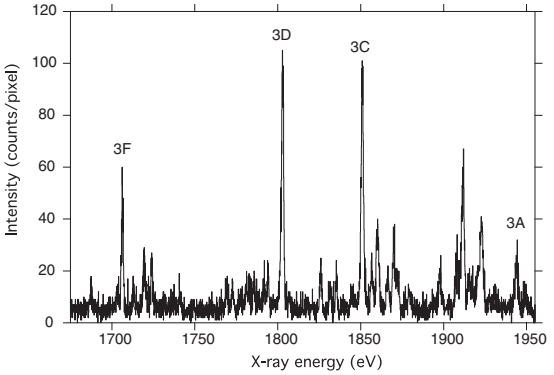

FIG. 3. Spectrum of neonlike krypton recorded on SuperEBIT with the flat-crystal spectrometer. Unlabeled lines are mostly from fluorinelike krypton. The neonlike krypton lines are used for wavelength calibrations.

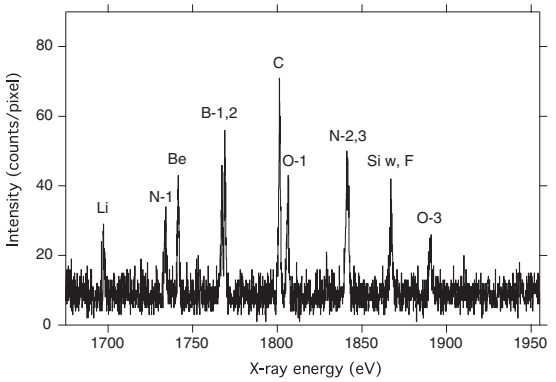

FIG. 4. Spectrum of the $2_{1/2}-2p_{3/2}$ transitions of tungsten recorded on SuperEBIT with the flat-crystal spectrometer. The lines are labeled using the isoelectronic notation from Table I.

olution. The krypton line energies were taken from [28]; and we again fitted them with equal widths. To test this, all lines were also fit individually, but none of the fits suggested an asymmetric detector response, and all lines had equal widths unless they were blended with other lines. The statistical errors for the line centroids in channel number and the published uncertainties for the energies of the krypton and aluminum calibration lines yielded an error box, the area of which was taken as the inverse weight of the point. Due to the large error bars on the krypton reference lines, the highest justifiable order of the fitting polynomial was 1 (linear). The calibration curve was found to be

$$\lambda = 10.640 \sin(45.76 \pm 0.03 - C \times 0.003\,227 \pm 1.836 \times 10^{-5}), \quad (1)$$

where C is the detector channel number and the units are angstroms.

IV. RESULTS AND ANALYSIS

Tungsten data from five run days were analyzed. No noticeable drift in the line and, thus, spectrometer position was found. The spectra were, therefore, summed; the resulting spectrum is shown in Fig. 4. Line positions, however, were obtained by taking each individual day's data, assuming equal widths, and finding the average centroid by weighting the results by the number of counts in the line of each day. Using the flexible atomic code (FAC) [29] and published references, the transitions giving rise to these peaks were identified. FAC is a self-contained fully relativistic code capable of calculating various atomic characteristics such as atomic levels, autoionization, and electron impact excitation. FAC calculates the atomic levels, which were used in this paper, by solving the Dirac-Coulomb Hamiltonian and including QED effects such as retardation and recoil; vacuum polarization and self-energy effects are implemented using a screened hydrogenic approximation.

Unfortunately, the intrinsic silicon impurities in the trap blended with two nitrogenlike tungsten peaks near 1840 eV and the fluorinelike tungsten peak. The fluorinelike tungsten peak was only resolvable for one of the run days, when the silicon admixture to the plasma was negligible. Hence, that value was taken and has been listed in Table I. From the calibration data, it was seen that the contribution from line z of He-like silicon to the nitrogenlike peaks was around 25 counts per day, which ended up being approximately 17% of the total line area. Due to the presence of two nitrogenlike peaks and uncertainties in the actual number of silicon w counts, deconvolution was not possible and the error bars on the nitrogenlike transitions had to be widened to account not only for their overlap but also for the blend with the silicon peak. Further uncertainties were approximated by analyzing the individual run days' data for deviations from a perfect Gaussian line profile.

The lithiumlike line was situated outside of the calibrated interval. The uncertainty in the inferred energy of this line

TABLE I. Summary of measured tungsten lines and comparison with theoretical values. Errors and theoretical source are shown. All energies are in eV, intensities in arbitrary units, and Einstein coefficients in s^{-1}.

Measured value	Theoretical[a]	Amplitude	A_{ij} (units of 10^{13})	Transition	Stage
1697.34 ± 1.03	1695.9956[b],1697.6	16.904 ± 1.63	0.7988	$(1s^22s_{1/2})_{J=1/2}-(1s^22p_{3/2})_{J=3/2}$	Li
1733.55 ± 1.20	1735.5	24.444 ± 1.64	0.294	$(1s^22s^22p_{1/2}^2 2p_{3/2})_{J=3/2}-(1s^22s_{1/2}2p_{1/2}^2 2p_{3/2}^2)_{J=5/2}$	N-1
1741.08 ± 1.25	1743.8	30.824 ± 1.66	1.156	$(1s^22s^2)_{J=0}-(1s^22s_{1/2}2p_{3/2})_{J=1}$	Be
1766.62 ± 1.39	1769.4	25.946 ± 1.72	1.283	$(1s^22s^22p_{1/2})_{J=1/2}-(1s^22s_{1/2}2p_{1/2}2p_{3/2})_{J=1/2}$	B-2
1768.71 ± 1.40	1771.2	37.127 ± 1.74	1.173	$(1s^22s^22p_{1/2})_{J=1/2}-(1s^22s_{1/2}2p_{1/2}2p_{3/2})_{J=3/2}$	B-1
1801.07 ± 1.60	1803.9	48.787 ± 1.72	1.266	$(1s^22s^22p_{1/2}^2)_{J=0}-(1s^22s_{1/2}2p_{1/2}^2 2p_{3/2})_{J=1}$	C
1805.91 ± 1.63	1808.4	29.777 ± 1.66	1.020	$(1s^22s^22p_{1/2}^2 2p_{3/2}^2)_{J=2}-(1s^22s_{1/2}2p_{1/2}^2 2p_{3/2}^3)_{J=2}$	O-1
1840.44 ± 1.90	1842.6	17.977 ± 1.63	1.091	$(1s^22s^22p_{1/2}^2 2p_{3/2})_{J=3/2}-(1s^22s_{1/2}2p_{1/2}^2 2p_{3/2}^2)_{J=1/2}$	N-2
1841.84 ± 1.88	1844.1	14.614 ± 2.98	2.023	$(1s^22s^22p_{1/2}^2 2p_{3/2})_{J=3/2}-(1s^22s_{1/2}2p_{1/2}^2 2p_{3/2}^2)_{J=3/2}$	N-3
1871.16 ± 2.10	1869.9	N/A[c]	2.232	$(1s^22s^22p_{1/2}^2 2p_{3/2}^3)_{J=3/2}-(1s^22s_{1/2}2p_{1/2}^2 2p_{3/2}^4)_{J=1/2}$	F
1891.01 ± 2.25	1893.3	17.977 ± 1.63	1.886	$(1s^22s^22p_{1/2}^2 2p_{3/2}^2)_{J=2}-(1s^22s_{1/2}2p_{1/2}^2 2p_{3/2}^3)_{J=1}$	O-3

[a]Calculations performed using FAC.
[b]Value from Kim *et al.* [20].
[c]Data were only available from one day, so comparing this count rate to that of the other transitions is not possible.

was increased by the uncertainty given by extrapolating the calibration curve, approximately 0.12 eV.

The data are summarized in Table I along with theoretical predictions and the line identifications. All uncertainties stated refer to one standard deviation; the 95% confidence interval is found by multiplying the given errors by approximately 1.96.

The observed tungsten lines were identified based on several criteria. First, since the SuperEBIT trap is filled with a low-density plasma, most observed lines are from transitions connecting to the ground state. Second, the most likely transitions are selected based on the FAC calculated transition energies and transition probabilities. Furthermore, extensive studies, both experimental and theoretical, of the line intensities have been made for uranium and thorium [1,30], and the strong lines expected in tungsten are presumed to not differ much from those in thorium and uranium, although their relative positions may move and are, in fact, seen to interchange. The previous research on thorium suggests the existence of a third oxygenlike line within this transition band at approximately 20% the intensity of the strong line. Calculations place that line around 1832 eV with an Einstein coefficient of 6.5×10^{12} s^{-1}; this line cannot be resolved from the background with sufficient certainty; however, it does appear to exist visually at the predicted location.

The tungsten line intensities were obtained by analyzing the heights above background as found from the summed data. Comparing the measured relative line intensities within an ionization stage with the Einstein coefficients as calculated by FAC show good agreement, which indicates that direct electron-impact excitation is the dominant line formation mechanism for these dipole-allowed transitions. The two nitrogenlike lines near 1840 eV, unfortunately, are blended, so their relative intensity measurements are not certain. The fluorinelike line intensity was only seen in one run day, so its intensity could not be extrapolated to the full run period. The constants that were used here in order to convert wavelength and energy are $h=6.626\,068\,96\times10^{-34}$ J s, $c=2.997\,924\,58\times10^{8}$ m/s, and $e=1.602\,176\,487\times10^{-19}$ C.

V. SUMMARY AND DISCUSSION

The line positions of the resonance lines in lithiumlike through fluorinelike tungsten have been measured. This work has extended the lithiumlike isoelectronic sequence, which has only a single valence electron, into the region of atomic number between xenon ($Z=54$) and lead ($Z=82$), where no data were available. The $2s_{1/2}-2p_{3/2}$ line position is affected by a QED contribution of about 17 eV. Our measurements are sensitive to 6% of this effect. Providing data in this range of atomic number is even more important for the beryllium-like to fluorinelike charge states of tungsten. For these ionic states no highly accurate theoretical calculations are yet available and electron-electron correlations strongly affect the energy levels, as discussed in a recent review by Cheng *et al.* [31]

The knowledge of the energies of the tungsten $2s_{1/2}-2p_{3/2}$ lines is very important for diagnostics of hot plasmas. As our line survey has shown in Fig. 1, these are the brightest x-ray lines from open *L*-shell tungsten ions. These lines appear at high electron temperatures, and similarly high ion temperatures in a thermal plasma significantly broaden the lines. At 30–40 keV ion temperature, which is not unrealistic in the ITER tokamak, the linewidths will be approximately 2 eV. Because different charge states exist in different albeit neighboring locations in the plasma, measurement of the $2s_{1/2}-2p_{3/2}$ spectrum of tungsten can yield temperature values at different locations in the plasma. Furthermore, the shift in the position of the line is a diagnostic for plasma rotation [32]. The data presented in this paper can serve as a basis for using these lines as a diagnostic tool.

ACKNOWLEDGMENTS

The authors would like to recognize D. Thorn, M. Frankel, E. Magee, and E. Träbert for their technical support and advice. Y.P. would also like to thank J. E. Rice for his support and comments. This work was performed at Lawrence Livermore National Laboratory under the auspices of the Department of Energy under Contract No. DE-AC52-07NA-27344 and was supported by the Laboratory Directed Research and Development program under Project No. 09-ERD-013. Y.P. acknowledges support from the Fusion Energy Sciences Program, administered by Oak Ridge Institute of Science and Education under a contract between the U.S. Department of Energy and the Oak Ridge Associated Universities. J. W. acknowledges support by NSF Grant HRD-0630370.

[1] P. Beiersdorfer, D. Knapp, R. E. Marrs, S. R. Elliott, and M. H. Chen, Phys. Rev. Lett. **71**, 3939 (1993).
[2] P. Beiersdorfer, A. L. Osterheld, and S. R. Elliott, Phys. Rev. A **58**, 1944 (1998).
[3] X. Zhang, N. Nakamura, C. Chen, M. Andersson, Y. Liu, and S. Ohtani, Phys. Rev. A **78**, 032504 (2008).
[4] P. Beiersdorfer, S. R. Elliott, A. L. Osterheld, T. Stöhlker, J. Autrey, G. V. Brown, A. J. Smith, and K. Widmann, Phys. Rev. A **53**, 4000 (1996).
[5] T. Mooney, E. Lindroth, P. Indelicato, E. G. Kessler, and R. D. Deslattes, Phys. Rev. A **45**, 1531 (1992).
[6] M. Trassinelli, D. Banaś, H. F. Beyer, P. Jagodz'nski, A. Kumar, M. Pajek, and T. Stöhlker, Can. J. Phys. **85**, 441 (2007).
[7] C. Gormezano *et al.*, Nucl. Fusion **47**, S285 (2007).
[8] A. J. H. Donné *et al.*, Nucl. Fusion **47**, S337 (2007).
[9] R. Neu, K. B. Fournier, D. Schlögl, and J. Rice, J. Phys. B **30**, 5057 (1997).
[10] Y. Ralchenko, I. N. Draganic, J. N. Tan, J. D. Gillaspy, J. M. Pomeroy, J. Reader, U. Feldman, and G. E. Holland, J. Phys. B **41**, 021003 (2008).
[11] T. Pütterich, R. Neu, C. Biedermann, R. Radtke, and the ASDEX Upgrade Team, J. Phys. B **38**, 3071 (2005).

[12] C. Biedermann, R. Radtke, J.-L. Schwob, P. Mandelbaum, R. Doron, T. Fuchs, and G. Fußmann, Phys. Scr. **T92**, 85 (2001).
[13] P. Neill, C. Harris, A. S. Safranova, S. Hamasha, S. Hansen, U. I. Safronova, and P. Beiersdorfer, Can. J. Phys. **82**, 931 (2004).
[14] S. B. Utter, P. Beiersdorfer, and E. Träbert, Can. J. Phys. **80**, 1503 (2002).
[15] C. H. Skinner, Can. J. Phys. **86**, 285 (2008).
[16] J. Clementson, P. Beiersdorfer, G. V. Brown, and M. F. Gu (unpublished).
[17] A. S. Safronova *et al.*, Can. J. Phys. **86**, 267 (2008).
[18] N. J. Peacock, M. G. O'Mullane, R. Barnsley, and M. Tarbutt, Can. J. Phys. **86**, 277 (2008).
[19] J. D. Gillaspy, I. N. Draganic, Y. Ralchenko, J. Reader, J. N. Tan, J. M. Pomeroy, and S. M. Brewer, Phys. Rev. A **80**, 010501(R) (2009).
[20] Y.-K. Kim, D. H. Baik, P. Indelicato, and J. P. Desclaux, Phys. Rev. A **44**, 148 (1991).
[21] D. A. Knapp, R. E. Marrs, S. R. Elliott, E. W. Magee, and R. Zasadzinski, Nucl. Instrum. Methods Phys. Res. A **334**, 305 (1993).
[22] F. S. Porter *et al.*, J. Low Temp. Phys. **151**, 1061 (2008).
[23] F. S. Porter *et al.*, Can. J. Phys. **86**, 231 (2008).
[24] G. V. Brown, P. Beiersdorfer, and K. Widmann, Rev. Sci. Instrum. **70**, 280 (1999).
[25] P. Beiersdorfer, G. V. Brown, R. Goddard, and B. J. Wargelin, Rev. Sci. Instrum. **75**, 3720 (2004).
[26] P. Beiersdorfer, G. V. Brown, L. Hildebrandt, K. L. Wong, and R. Ali, Rev. Sci. Instrum. **72**, 508 (2001).
[27] W. R. Johnson and G. Soff, At. Data Nucl. Data Tables **33**, 405 (1985).
[28] J. E. Rice, K. B. Fournier, J. A. Goetz, E. S. Marmar, and J. L. Terry, J. Phys. B **33**, 5435 (2000).
[29] M. F. Gu, Can. J. Phys. **86**, 675 (2008).
[30] P. Beiersdorfer, A. Osterheld, S. R. Elliott, M. H. Chen, D. Knapp, and K. Reed, Phys. Rev. A **52**, 2693 (1995).
[31] K. T. Cheng, M. H. Chen, W. R. Johnson, and J. Sapirstein, Can. J. Phys. **86**, 33 (2008).
[32] M. Bitter, G. Bertschinger, W. Biel, R. Jaspers, I. Ahmad, J. Weinheimer, and H.-J. Kunze, *27th Conference on Controlled Fusion and Plasma Physics, 2000*, Europhysics Conference Abstracts Vol. 24B, p. 840 (2000).

Paper IV

Wavelength measurement of $n = 3$ to $n = 3$ transitions in highly charged tungsten ions

J. Clementson* and P. Beiersdorfer
Lawrence Livermore National Laboratory, Livermore, California 94550, USA
(Received 16 March 2010; published xxxxx)

$3s_{1/2}$-$3p_{3/2}$ and $3p_{1/2}$-$3d_{3/2}$ transitions have been studied in potassiumlike W^{55+} through neonlike W^{64+} ions at the electron-beam ion trap facility in Livermore. The wavelengths of the lines have been measured in high resolution relative to well-known reference lines from oxygen and nitrogen ions. Using the high-energy SuperEBIT electron-beam ion trap and an $R = 44.3$ m grazing-incidence soft-x-ray spectrometer, the lines were observed with a cryogenic charge-coupled device camera. The wavelength data for the sodiumlike and magnesiumlike tungsten lines are compared with theoretical predictions for ions along the isoelectronic sequences.

DOI: 10.1103/PhysRevA.00.002500 PACS number(s): 32.30.Rj

I. INTRODUCTION

Multielectron ions of high-Z elements are of interest in atomic structure theory [1]. Accurate modeling of these systems needs to include electron correlation and relativistic effects in addition to quantum electrodynamic (QED) corrections [2,3]. Relativistic and QED effects are strongly dependent on the nuclear charge Z, which makes highly charged heavy ions suitable for investigations of high-order QED effects [4]. However, the problem of accurately calculating the structure of highly charged ions becomes challenging as the number of electrons increases. Among many-electron systems, ions with only a few valence electrons outside the last closed shell are the simplest, and those high-Z ions isoelectronic to sodium and magnesium thus represent useful stepping stones for testing QED calculations in multielectron systems.

The $3s_{1/2}$-$3p_{3/2}$ resonance transition along the sodium isoelectronic sequence has been calculated by several authors. For instance, Ivanov and Ivanova used a model potential method and extrapolated experimental data to high-Z ions [5]. Kim and Cheng calculated the wavelengths for a few high-Z ions using Dirac-Fock wave functions [6]. Johnson *et al.* performed relativistic many-body perturbation theory (RMBPT) calculations [7] from which Seely and Wagner calculated semiempirical wavelengths [8]. Predictions were also given by Kim *et al.* after investigating relativistic electron-correlation energies [2]. Baik *at al*. performed single-configuration Dirac-Fock calculations [9], whereas Seely *et al.* calculated multiconfiguration Dirac-Fock (MCDF) wavelengths [10]. Blundell added QED corrections to RMBPT calculations and studied the resonance transition for a few selected high-Z ions [11]. Theoretical wavelengths for the resonance line of magnesiumlike spectra include results of MCDF calculations by Cheng and Johnson [12], relativistic random-phase approximation (RRPA) calculations by Shorer *et al.* [13], relativistic perturbation theory using a model potential by Ivanova *et al.* [14], MCDF calculations of Marques *et al.* [15], relativistic configuration-interaction (RCI) calculations by Chen and Cheng [16], and multiconfiguration Dirac-Hartree-Fock (MCDHF) of Zou and Froese Fischer [17].

Up to xenon ($Z = 54$), the $3s_{1/2}$-$3p_{3/2}$ line has been measured for most ions isoelectronic to sodium, but for higher Z rather few measurements are reported [10,18–23]. Experimental high-precision wavelengths for the corresponding transition in magnesiumlike high-Z ions are even less common [18,19,22]. Chen *et al.* measured the $3s_{1/2}$-$3p_{3/2}$ transition in P-like through Na-like U at the Livermore EBIT-I electron-beam ion trap and found excellent agreement with RCI calculations [24]. Recently, Gillaspy *et al.* measured the $3s_{1/2}$-$3p_{3/2}$ and the $3s_{1/2}$-$3p_{1/2}$ transitions in Na-like high-Z ions, including tungsten, together with the $3s_{1/2}$-$3p_{3/2}$ transition in Mg-like and the $3p_{1/2}$-$3d_{3/2}$ transition in Al- and Si-like ions, at the electron-beam ion trap facility at the National Institute of Standards and Technology [25]. The measured $3s_{1/2}$-$3p_{3/2}$ line positions, however, did not have the accuracies required to differentiate between theories.

In the present paper, the wavelengths of the $3s_{1/2}$-$3p_{3/2}$ and $3p_{1/2}$-$3d_{3/2}$ resonance transitions in Na-, Mg-, Al-, and Si-like W ions are measured in high resolution, together with the equivalent transitions from lower-charge states down to K-like W^{55+}. The measured tungsten spectra have been analyzed using theoretical spectra calculated by using the flexible atomic code (FAC) [26]. The FAC-calculated $3s_{1/2}$-$3p_{3/2}$ wavelengths are compared with results from the general-purpose relativistic atomic structure program (GRASP2) [27,28]. The measured line positions of the sodium- and magnesiumlike resonance transitions are evaluated with calculated wavelengths from several codes, including a recent result from RCI calculations [29].

II. THEORY

The structure and spectra of calciumlike W^{54+} through fluorinelike W^{65+} ions have been calculated using FAC v.1.1.1 [26,30]. FAC is a relativistic configuration-interaction program for computation of atomic radiative and collisional processes. The one-electron wave functions are derived using a modified Dirac-Fock-Slater method. QED effects are taken into account using hydrogenic approximations for the self-energy and vacuum polarization. The Breit interaction is treated in the zero-energy limit for the exchanged photon. Continuum processes are calculated using the distorted-wave approximation. The ions have been modeled with K-shell cores. Autoionization has been included for all charge states lower than neonlike from all levels to the ground and low-lying configurations

*clementson@llnl.gov; also at Atomic Physics Division, Lund University, SE-221 00 Lund, Sweden.

ACC. CODE AQ10555 AUTHOR Clementson

TABLE I. Configuration state functions used in the FAC calculations with K-shell core. $l = 0,1,\ldots,n-1$; $l^* = s,p$; $n = 3,4,5$; $n^* = 4,5$.

F-like W^{65+}	Ne-like W^{64+}	Na-like W^{63+}	Mg-like W^{62+}
$2s^22p^5$	$2s^22p^6$	$2s^22p^6nl$	$2s^22p^63lnl$
$2s2p^6$	$2s^22p^5nl$	$2s^22p^53lnl$	$2s^22p^53l3lnl$
$2s^22p^4nl$	$2s2p^6nl$	$2s2p^63lnl$	$2s2p^63l3lnl$
$2s2p^5nl$			
$2p^6nl$			
Al-like W^{61+}	**Si-like W^{60+}**	**P-like W^{59+}**	**S-like W^{58+}**
$2s^22p^63l3lnl$	$2s^22p^63l3l3lnl$	$2s^22p^63l3l3l3l3l$	$2s^22p^63l3l3l3l3l3l$
$2s^22p^53s^23l3l$	$2s^22p^53s^23l3l3l$	$2s^22p^63l^*3l^*3l^*3ln^*l$	$2s^22p^63l^*3l^*3l^*3l^*3ln^*l$
$2s^22p^53l^*3l^*3l^*n^*l$	$2s^22p^53l^*3l^*3l^*3l^*n^*l$	$2s^22p^53s^23p^3nl$	$2s^22p^53s^23p^4nl$
$2s2p^63s^23l3l$	$2s2p^63s^23l3l3l$	$2s2p^63s^23p^3nl$	$2s2p^63s^23p^4nl$
$2s2p^63l^*3l^*3l^*n^*l$	$2s2p^63l^*3l^*3l^*3l^*n^*l$		
Cl-like W^{57+}	**Ar-like W^{56+}**	**K-like W^{55+}**	**Ca-like W^{54+}**
$2s^22p^63l3l3l3l3l3l3l$	$2s^22p^63l^*3l^*3l^*3l^*3l3l3l3l$	$2s^22p^63l^*3l^*3l^*3l^*3l3l3l3l3l$	$2s^22p^63l^*3l^*3l^*3l^*3l3l3l3l3l3l$
$2s^22p^63l^*3l^*3l^*3l^*3l^*3ln^*l$	$2s^22p^63l^*3l^*3l^*3l^*3l^*3l^*3ln^*l$	$2s^22p^63l^*3l^*3l^*3l^*3l^*3l^*3l^*3ln^*l$	$2s^22p^63l^*3l^*3l^*3l^*3l^*3l^*3l^*3l3ln^*l$
$2s^22p^53s^23p^5nl$	$2s^22p^53s^23p^6nl$	$2s^22p^63s^23p^63dnl$	$2s^22p^53s^23p^63d^2nl$
$2s2p^63s^23p^5nl$	$2s2p^63s^23p^6nl$	$2s2p^63s^23p^63dnl$	$2s2p^63s^23p^63d^2nl$

of the daughter ion. Configuration state functions used in the FAC calculations are listed in Table I. In addition, the $\Delta n = 0$ M-shell transitions in K-like W^{55+} through Ne-like W^{64+} ions have also been calculated with GRASP2 [27,28]. GRASP is a multiconfiguration Dirac-Fock code for relativistic atomic calculations. The Breit interaction, self-energy, and vacuum polarization are added perturbatively. The program was run in the extended average level (EAL) calculation mode, where the radial wave functions are obtained from an average configuration approximation. Included configuration state functions are tabulated in Table II. The theoretical $3s_{1/2}$-$3p_{3/2}$ wavelengths from FAC and GRASP2 are compared with experimental line positions in Fig. 1. High-precision calculations of the sodiumlike $3s_{1/2}$-$3p_{3/2}$ line have been performed by Sapirstein *et al.* [29]. Here, the transition energy has been calculated by using the RCI and RMBPT codes and equals 537.51 eV, including electron-correlation energy. To this energy, corrections for mass polarization (−0.01 eV) and QED effects (−4.42 eV) have been added, resulting in a total energy of 533.08(4) eV, where the uncertainty is estimated to be mainly caused by the neglect of two-loop Lamb shifts and negative energy states. This transition energy corresponds to a wavelength of 23.258(2) Å.

TABLE II. Configuration state functions used in the GRASP2 calculations with filled K shell (Ne-like W) and L shell (Na- through K-like W).

Ne-like W^{64+}	Na-like W^{63+}	Mg-like W^{62+}	Al-like W^{61+}	Si-like W^{60+}
$2s^22p^6$	$3s$	$3s^2$	$3s^23p$	$3s^23p^2$
$2s^22p^53s$	$3p$	$3s3p$	$3s^23d$	$3s^23p3d$
$2s^22p^53p$	$3d$	$3s3d$	$3s3p^2$	$3s^23d^2$
$2s^22p^53d$			$3s3p3d$	$3s3p^3$
$2s2p^63s$				$3s3p^23d$
$2s2p^63p$				$3s3p3d^2$
$2s2p^63d$				
P-like W^{59+}	**S-like W^{58+}**	**Cl-like W^{57+}**	**Ar-like W^{56+}**	**K-like W^{55+}**
$3s^23p^3$	$3s^23p^4$	$3s^23p^5$	$3s^23p^6$	$3s^23p^63d$
$3s^23p^23d$	$3s^23p^33d$	$3s^23p^43d$	$3s^23p^53d$	$3s^23p^53d^2$
$3s3p^4$	$3s3p^5$	$3s3p^6$	$3s3p^63d$	$3s3p^63d^2$
$3s3p^33d$	$3s3p^43d$	$3s3p^53d$		

III. MEASUREMENT AND ANALYSIS

The experiment employed the SuperEBIT electron-beam ion trap at the Lawrence Livermore National Laboratory [31,32]. Tungsten was supplied to the trap using a metal vapor vacuum arc (MEVVA) injector, which injects few-times ionized tungsten into SuperEBIT. Trapped by electric and magnetic fields, the ions reached higher charge states under the bombardment by a narrow ($\leqslant 60$ μm) electron beam of energy 23.5 keV and beam currents around 55 mA.

The spectrometer employed for the measurement was a very high-resolution soft-x-ray grating spectrometer [33]. The

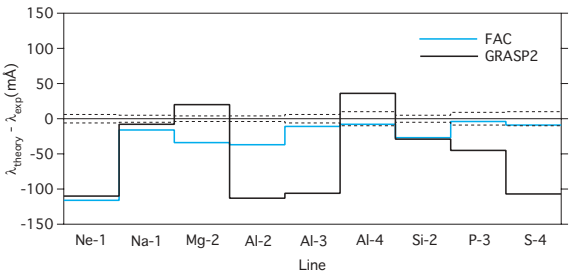

FIG. 1. (Color online) Differences between theoretical $3s_{1/2}$-$3p_{3/2}$ FAC and GRASP2 wavelengths and observed line positions in highly charged tungsten ions. Experimental uncertainties are marked with dashed lines.

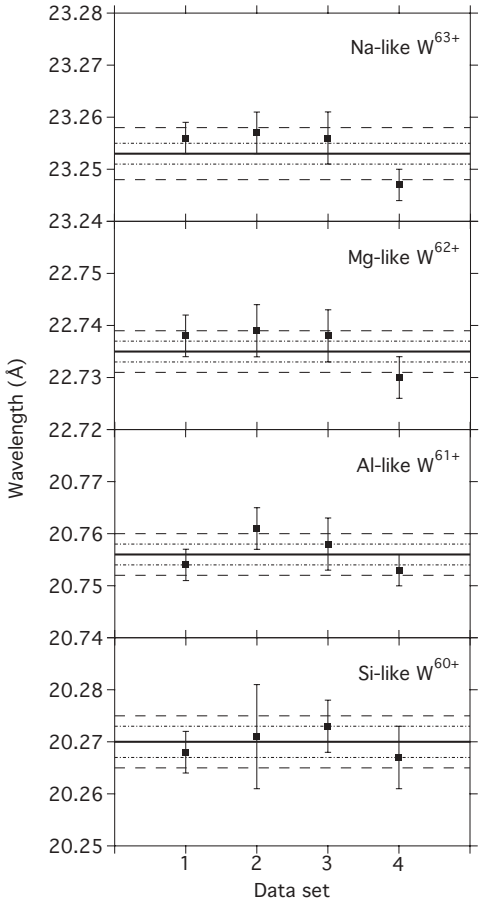

FIG. 2. Wavelengths of the Na-like through Si-like W resonance lines in the four data sets. The solid lines display the average wavelengths. Dashed lines represent the statistical and line-blend error bars, and the long-dashed lines show the final wavelength uncertainties.

instrument uses a 2400 lines/mm spherical $R = 44.3$ m grating operated at a grazing angle of 2°. The flat-field images were recorded using a cryogenically cooled Princeton Instruments charge-coupled device (CCD) detector. The back-illuminated CCD chip is made up of 1300 × 1340 pixels, each of size $20 \times 20\ \mu\text{m}^2$. The spectrometer was set up to cover the 18.5–26.5 Å soft-x-ray band. The instrument was not in best focus because of constraints placed on its use by other experiments before and after.

Nitrogen and carbon dioxide gases were supplied to the trap by a gas injector to provide accurate reference wavelengths in first order. A second-degree polynomial dispersion function of wavelength versus detector channel position was determined by using the theoretical line positions of N VII Ly-α and Ly-β, N VI $K\beta$, O VIII Ly-α, and O VII $K\alpha$ (w and z). The H-like wavelengths are taken from Garcia and Mack [34], the He-like $K\alpha$ lines from Drake [35], and the He-like $K\beta$ transition from Vainshtein and Safronova [36]. The wavelengths of the He-like ions are believed to be accurate to better than 0.6 mÅ [37]. The present measurement is thus similar to the measurement of the $2s_{1/2}$-$2p_{1/2}$ Li-like U^{89+} where the O VII lines were used as reference lines in second order [38–40].

Tungsten spectra were acquired during four days. The half-hour and one-hour exposure CCD images were rotated to correct for a slight tilt in the alignment of the CCD camera before the cosmic-ray and stray-light counts were filtered out, keeping only single-photon counts. The data from each day were added and analyzed separately. The $3s_{1/2}$-$3p_{3/2}$ transitions in Na- and Mg-like W and the $3p_{1/2}$-$3d_{3/2}$ in Al- and Si-like W were of sufficient strength so that they could be analyzed in each of these data sets. The wavelength dispersion determined from the nitrogen and oxygen spectra was applied to these tungsten spectra and anchored to the position of line w from He-like O VII, which showed in each spectrum, because oxygen existed in the trap as an impurity. The inferred line positions from all the data sets

TABLE III. Measured positions of the Na-like W^{63+} $3s_{1/2}$-$3p_{3/2}$ transition, error contributions, and average wavelength. Wavelengths in Å.

Data set	1	2	3	4
Wavelength	23.2556	23.2568	23.2562	23.2466
Statistics	0.0015	0.0015	0.0022	0.0016
O w statistics	0.0023	0.0036	0.0039	0.0027
Reference	0.0006			
Dispersion	0.0031			
Result		23.253 ± 0.005		

TABLE IV. Measured positions of the Mg-like W^{62+} $3s_{1/2}$-$3p_{3/2}$ transition, error contributions, and average wavelength. Wavelengths in Å.

Data set	1	2	3	4
Wavelength	22.7377	22.7391	22.7379	22.7299
Statistics	0.0016	0.0015	0.0023	0.0015
O w statistics	0.0023	0.0036	0.0039	0.0027
Line blend	0.0023	0.0026		0.0017
Reference	0.0006			
Dispersion	0.0022			
Result		22.735 ± 0.004		

TABLE V. Measured positions of the Al-like W^{61+} $3p_{1/2}$-$3d_{3/2}$ transition, error contributions, and average wavelength. Wavelengths in Å.

Data set	1	2	3	4
Wavelength	20.7544	20.7608	20.7581	20.7533
Statistics	0.0021	0.0025	0.0034	0.0021
O w statistics	0.0023	0.0036	0.0039	0.0027
Reference	0.0006			
Dispersion	0.0017			
Result		20.756 ± 0.004		

TABLE VI. Measured positions of the Si-like W^{60+} $3p_{1/2}$-$3d_{3/2}$ transition, error contributions, and average wavelength. Wavelengths in Å.

Data set	1	2	3	4
Wavelength	20.2681	20.2708	20.2730	20.2673
Statistics	0.0021	0.0029	0.0030	0.0018
O *w* statistics	0.0023	0.0036	0.0039	0.0027
Line blend	0.0031	0.0093		0.0049
Reference	0.0006			
Dispersion	0.0026			
Result		20.270 ± 0.005		

(see Fig. 2) were averaged to give the resulting wavelengths in Tables III, IV, V, and VI. The uncertainties in the four line positions were evaluated in each data set. The uncertainty associated with the counting statistics of each line was added to the statistical uncertainty in the O *w* reference-line position. The Mg- and Si-like W lines were not fully resolved, and the additional line-position uncertainties were estimated by fitting the lines separately (resonance line plus blending line) and blended (one centroid) and taking the wavelength difference as the line-blend error. These errors were added in quadrature with the statistical uncertainties. The resulting line-position uncertainties from the data sets were then averaged. To this average, the uncertainty in the theoretical reference wavelengths was added in quadrature, followed by the linear addition of the dispersion uncertainty in the calibration polynomial. The contributions to the line-position uncertainties are listed in Tables III–VI. Here, the statistical uncertainties for the lines are listed with the statistical uncertainties of the O *w* reference line. The reference-line error is the the uncertainty of the theoretical wavelengths used for the calibration, which have been validated by measurements to agree within about 0.6 mÅ [37]. The dispersion error is the uncertainty in the linear term in the dispersion function multiplied by the distance between each line and the O *w* position used to anchor the dispersion.

For the weaker tungsten lines, the analysis was done after the four data sets had been summed (see Fig. 3). As with the individual data sets, the wavelength dispersion was

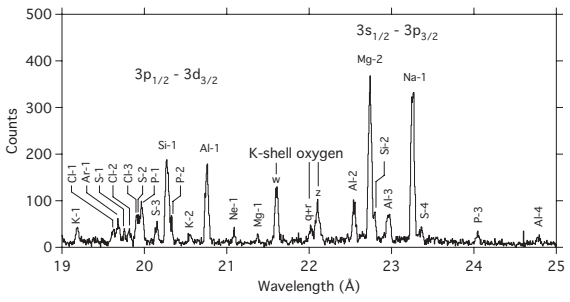

FIG. 3. Soft-x-ray spectrum of highly charged tungsten measured with an $R = 44.3$ m grazing-incidence spectrometer at the Livermore SuperEBIT electron-beam ion trap. The spectrum represents the coadded data from four run days.

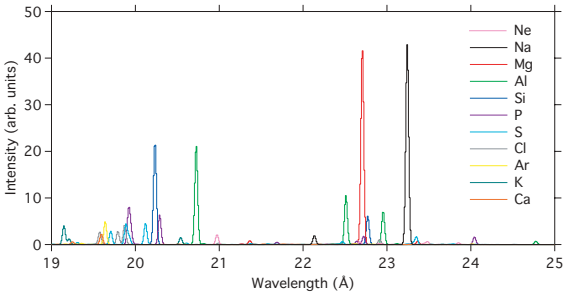

FIG. 4. (Color online) Theoretical soft-x-ray spectrum of highly charged tungsten. The spectrum is modeled with a resolution of 40 mÅ FWHM at an electron energy of 23.5 keV and a density of 5×10^{11} cm^{-3}. The charge balance is inferred from the best agreement with the spectral data in Fig. 3 and is shown in Fig. 5.

anchored to the O *w* line position. To identify the lines, a synthetic spectrum was calculated for an electron energy of 23.5 keV and an electron density of 5×10^{11} cm^{-3}. This spectrum is shown in Fig. 4, where the lines are modeled with an instrumental resolution of 40 mÅ full width at half maximum (FWHM). The tungsten charge balance was estimated from the measured number of counts in the observed lines and the corresponding calculated line emissivities. The resulting charge balance relative to the sodiumlike tungsten ion is shown in Fig. 5. The uncertainties in the abundances are difficult to estimate. For the ions with only a single line, the uncertainties are based on the statistics of the measured line intensities. For ions with several observed lines, the errors are estimated from both the counting statistics and the spread of the number of ions derived from each individual line. Comparison of the experimental and theoretical spectra allowed for the identification of lines from potassiumlike through neonlike tungsten. Although no calciumlike lines were observed, the abundance of Ca-like W^{54+} was set equal to that of K-like W^{55+} to account for the maximum possible influence of line blends. To estimate line-blend effects, the centroid of each line was fitted in the theoretical one-charge state spectrum and in the synthetic spectrum where lines from all ions were present. The wavelength differences were taken as the blend errors. These uncertainties were added in quadrature

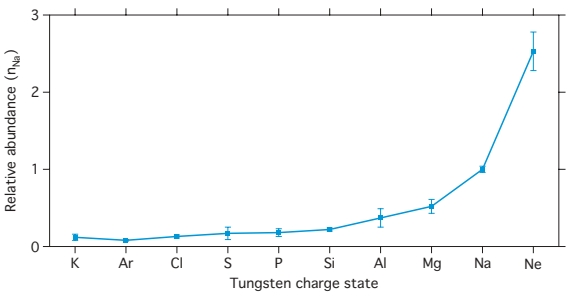

FIG. 5. (Color online) Inferred tungsten charge state distribution in SuperEBIT at an electron-beam energy of $E_b = 23.5$ keV. The charge state fractions are normalized to that of Na-like W^{63+}.

TABLE VII. Experimental and theoretical tungsten wavelengths in Å. The lines are labeled according to charge state (cf. Fig. 3). Theory from FAC, GRASP2, and RCI [29] calculations.

Key	Transition	Experiment	FAC	GRASP2	RCI
K-1	$(3s^2 3p^6 3d_{3/2})_{3/2}$-$(3s^2 3p_{1/2} 3p^4_{3/2} 3d^2_{3/2})_{3/2}$	19.184(8)	19.143	19.078	
Cl-1	$(3s^2 3p^2_{1/2} 3p^3_{3/2})_{3/2}$-$(3s^2 3p_{1/2} 3p^3_{3/2} 3d_{3/2})_{1/2}$	19.62(1)	19.570	19.442	
Ar-1	$(3s^2 3p^6)_0$-$(3s^2 3p_{1/2} 3p^4_{3/2} 3d_{3/2})_1$	19.679(7)	19.636	19.607	
S-1	$(3s^2 3p^2_{1/2} 3p^2_{3/2})_2$-$(3s^2 3p_{1/2} 3p^2_{3/2} 3d_{3/2})_1$	19.752(8)	19.702	19.592	
Cl-2	$(3s^2 3p^2_{1/2} 3p^3_{3/2})_{3/2}$-$(3s^2 3p_{1/2} 3p^3_{3/2} 3d_{3/2})_{3/2}$	19.814(9)	19.786	19.726	
Cl-3	$(3s^2 3p^2_{1/2} 3p^3_{3/2})_{3/2}$-$(3s^2 3p_{1/2} 3p^3_{3/2} 3d_{3/2})_{5/2}$		19.867	19.789	
S-2	$(3s^2 3p^2_{1/2} 3p^2_{3/2})_2$-$(3s^2 3p_{1/2} 3p^2_{3/2} 3d_{3/2})_2$		19.883	19.755	
	$(3s^2 3p^2_{1/2} 3p^2_{3/2})_0$-$(3s^2 3p_{1/2} 3p^2_{3/2} 3d_{3/2})_1$		19.922	19.852	
P-1	$(3s^2 3p^2_{1/2} 3p_{3/2})_{3/2}$-$(3s^2 3p_{1/2} 3p_{3/2} 3d_{3/2})_{3/2}$		19.916	19.789	
	$(3s^2 3p^2_{1/2} 3p_{3/2})_{3/2}$-$(3s^2 3p_{1/2} 3p_{3/2} 3d_{3/2})_{1/2}$		19.942	19.846	
S-3	$(3s^2 3p^2_{1/2} 3p^2_{3/2})_2$-$(3s^2 3p_{1/2} 3p^2_{3/2} 3d_{3/2})_3$	20.147(6)	20.116	20.006	
Si-1	$(3s^2 3p^2_{1/2})_0$-$(3s^2 3p_{1/2} 3d_{3/2})_1$	20.270(5)	20.229	20.200	
P-2	$(3s^2 3p^2_{1/2} 3p_{3/2})_{3/2}$-$(3s^2 3p_{1/2} 3p_{3/2} 3d_{3/2})_{5/2}$	20.319(5)	20.285	20.187	
K-2	$(3s^2 3p^6 3d_{3/2})_{3/2}$-$(3s^2 3p_{1/2} 3p^4_{3/2} 3d^2_{3/2})_{5/2}$	20.552(7)	20.536	20.575	
Al-1	$(3s^2 3p_{1/2})_{1/2}$-$(3s^2 3d_{3/2})_{3/2}$	20.756(4)	20.721	20.637	
Ne-1	$(2s^2 2p^2_{1/2} 2p^3_{3/2} 3s_{1/2})_1$-$(2s^2 2p^2_{1/2} 2p^3_{3/2} 3p_{3/2})_0$	21.085(6)	20.969	20.975	
Mg-1	$(3s_{1/2} 3p_{1/2})_1$-$(3s_{1/2} 3d_{3/2})_2$	21.372(6)	21.360	21.622	
Al-2	$(3s^2 3p_{1/2})_{1/2}$-$(3s_{1/2} 3p_{1/2} 3p_{3/2})_{1/2}$	22.543(4)	22.506	22.430	
Mg-2	$(3s^2)_0$-$(3s_{1/2} 3p_{3/2})_1$	22.735(4)	22.701	22.755	
Si-2	$(3s^2 3p^2_{1/2})_0$-$(3s_{1/2} 3p^2_{1/2} 3p_{3/2})_1$	22.793(5)	22.766	22.764	
Al-3	$(3s^2 3p_{1/2})_{1/2}$-$(3s_{1/2} 3p_{1/2} 3p_{3/2})_{3/2}$	22.961(6)	22.950	22.855	
Na-1	$3s_{1/2}$-$3p_{3/2}$	23.253(5)	23.237	23.245	23.258(2)
S-4	$(3s^2 3p^2_{1/2} 3p^2_{3/2})_2$-$(3s_{1/2} 3p^2_{1/2} 3p^3_{3/2})_2$	23.35(1)	23.345	23.247	
P-3	$(3s^2 3p^2_{1/2} 3p_{3/2})_{3/2}$-$(3s_{1/2} 3p^2_{1/2} 3p^2_{3/2})_{5/2}$	24.042(9)	24.038	23.997	
Al-4	$(3s^2 3p_{1/2})_{1/2}$-$(3s_{1/2} 3p_{1/2} 3p_{3/2})_{3/2}$	24.78(1)	24.770	24.814	

with the statistics of each line and O w and the reference-line uncertainty, followed by a linear addition of the dispersion uncertainty. All identified lines are listed in Table VII with experimental wavelengths and theoretical line positions from FAC and GRASP2. The three lines Cl-3, S-2, and P-1 have been identified in the theoretical model. However, because the line positions overlap, a determination of these experimental wavelengths is not possible.

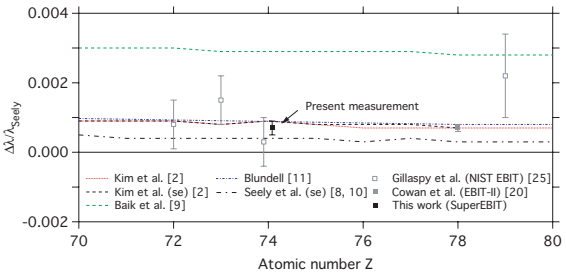

FIG. 6. (Color online) (color online) Observed $3s_{1/2}$-$3p_{3/2}$ line positions of Na-like high-Z ions [20,25] compared to theoretical line positions given by Kim *et al.* [2], Baik *et al.* [9], and Blundell [11] and to semiempirical (se) values by Kim *et al.* [2] and Seely *et al* [8,10]. Wavelengths are normalized to the theory by Seely *et al.* [10]. Note that the wavelengths by Blundell have been interpolated. Calculations from Johnson *et al.* [7], Ivanov and Ivanova [5], and Kim and Cheng [6] are off the scale. Observed values are from measurements at the NIST EBIT [25], the Livermore EBIT-II [20], and the Livermore SuperEBIT (this work).

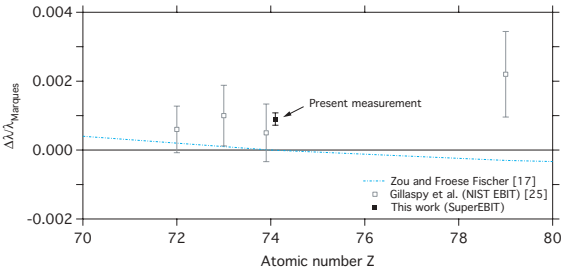

FIG. 7. (Color online) Observed $3s^2$-$3s_{1/2}3p_{3/2}$ line positions of Mg-like high-Z ions compared to theoretical line positions by Zou and Froese Fischer [17]. Wavelengths are normalized to the theory by Marques *et al.* [15]. Note that wavelengths by Zou and Froese Fischer have been interpolated. Predictions from Cheng and Johnson [12], Shorer *et al.* [13], and Ivanova *et al.* [14] are off the scale. The experimental data are from the NIST EBIT [25] and the Livermore SuperEBIT (present work).

Constants used are $hc = 12\,398.42$ Å eV $= 8065.5410$ eVcm and 1 Ry $= 13.60569$ eV.

IV. SUMMARY AND CONCLUSION

The measurement yields wavelengths for 20 soft-x-ray $\Delta n = 0$ M-shell lines in highly charged tungsten ions between 19 and 25 Å (see Table VII and Fig. 3). Lines from potassiumlike W^{55+} to neonlike W^{64+} are measured in high resolution and identified using theoretical spectra calculated using FAC(cf. Fig. 4). Comparisons with FAC and GRASP2 calculations are made for the $3s_{1/2}$-$3p_{3/2}$ transitions in K-like W^{55+} through Ne-like W^{64+} ions (see Fig. 1). The comparison shows that our FAC calculations on average do a better job in reproducing the measured values than our GRASP2 calculations. Both do poorly for the neonlike line (cf. previous work on the $2s_{1/2}$-$2p_{3/2}$ transitions in Li-like Th^{80+} and U^{82+} [39,40]). Overall, the theoretical wavelengths are too short, but not consistently.

Several calculations have been made for the resonance line in sodiumlike ions, and the observed $3s_{1/2}$-$3p_{3/2}$ tungsten line position is compared with these in Fig. 6, where sodiumlike ions with $70 \leqslant Z \leqslant 80$ are shown. The experimental wavelength of 23.253(5) Å agrees well with the *ab initio* calculations by Kim *et al.* [2], Blundell [11], and the recent *ab initio* value by Sapirstein *et al.* [29]. The latter comparison is shown in Table VII. The calculations by Kim *et al.* [2] and Blundell [11] are also in good agreement with the high-precision measurement of Na-like Pt^{67+} by Cowan *et al.* [20] performed at the Livermore EBIT-II electron-beam ion trap.

A comparison between measurements and theory of the magnesiumlike resonance line displayed in Fig. 7 shows that the measured Mg-like W^{62+} wavelength of 22.735(4) does not agree with available theoretical predictions. This contrasts with the measurement by Gillaspy *et al.* [25], whose larger error bars show consistency with the two calculations. We note that the predictions from the MCDF [12], RRPA [13], and model-potential relativistic perturbation theory [14] codes are off the scale and, therefore, not shown in Fig. 7. Magnesiumlike ions are more difficult to calculate with accuracy, and additional high-precision measurements of the $3s^2$-$3s_{1/2}3p_{3/2}$ transition in high-Z ions are needed to guide theory.

ACKNOWLEDGMENTS

This work was performed under the auspices of the United States Department of Energy by Lawrence Livermore National Laboratory under Contract No. DE-AC52-07NA-27344. The authors would like to thank Todd Chambers, Miriam Frankel, Dr. Jaan Lepson, Debbie Miller, Yuri Podpaly, Ed Magee, and Professor Elmar Träbert for assistance with the measurement. The authors furthermore would like to thank Dr. K. T. Cheng, Dr. Mau Chen, and Dr. Jonathan Sapirstein for making unpublished results available. Joel Clementson would like to thank Dr. Hans Lundberg, Dr. Sven Huldt, Professor Sune Svanberg, and Professor Tomas Brage for their support.

[1] I. Martinson, Nucl. Instrum. Methods Phys. Res. B **43**, 323 (1989).
[2] Y.-K. Kim, D. H. Baik, P. Indelicato, and J. P. Deslaux, Phys. Rev. A **44**, 148 (1991).
[3] K. T. Cheng, M. H. Chen, W. R. Johnson, and J. Sapirstein, Can. J. Phys. **86**, 33 (2008).
[4] P. Beiersdorfer, J. Phys. B (to be published).
[5] L. N. Ivanov and E. P. Ivanova, At. Data Nucl. Data Tables **24**, 95 (1979).
[6] Y.-K. Kim and K.-T. Cheng, J. Opt. Soc. Am. **68**, 836 (1978).
[7] W. R. Johnson, S. A. Blundell, and J. Sapirstein, Phys. Rev. A **38**, 2699 (1988).
[8] J. F. Seely and R. A. Wagner, Phys. Rev. A **41**, 5246 (1990).
[9] D. H. Baik, Y. G. Ohr, K. S. Kim, J. M. Lee, P. Indelicato, and Y.-K. Kim, At. Data Nucl. Data Tables **47**, 177 (1991).
[10] J. F. Seely, C. M. Brown, U. Feldman, J. O. Ekberg, C. J. Keane, B. J. MacGowan, D. R. Kania, and W. E. Behring, At. Data Nucl. Data Tables **47**, 1 (1991).
[11] S. A. Blundell, Phys. Rev. A **47**, 1790 (1993).
[12] K. T. Cheng and W. R. Johnson, Phys. Rev. A **16**, 263 (1977).
[13] P. Shorer, C. D. Lin, and W. R. Johnson, Phys. Rev. A **16**, 1109 (1977).
[14] E. P. Ivanova, L. N. Ivanov, and M. A. Tsirekidze, At. Data Nucl. Data Tables **35**, 419 (1986).
[15] J. P. Marques, F. Parente, and P. Indelicato, At. Data Nucl. Data Tables **55**, 157 (1993).
[16] M. H. Chen and K. T. Cheng, Phys. Rev. A **55**, 3440 (1997).
[17] Y. Zou and C. Froese Fischer, J. Phys. B **34**, 915 (2001).
[18] J. F. Seely, U. Feldman, C. M. Brown, M. C. Richardson, D. D. Dietrich, and W. E. Behring, J. Opt. Soc. Am. B **5**, 785 (1988).
[19] E. Träbert, P. Beiersdorfer, J. K. Lepson, and H. Chen, Phys. Rev. A **68**, 042501 (2003).
[20] T. E. Cowan, C. L. Bennett, D. D. Dietrich, J. V. Bixler, C. J. Hailey, J. R. Henderson, D. A. Knapp, M. A. Levine, R. E. Marrs, and M. B. Schneider, Phys. Rev. Lett. **66**, 1150 (1991).
[21] A. Simionovici, D. D. Dietrich, R. Keville, T. Cowan, P. Beiersdorfer, M. H. Chen, and S. A. Blundell, Phys. Rev. A **48**, 3056 (1993).
[22] P. Beiersdorfer and B. J. Wargelin, Rev. Sci. Instrum. **65**, 13 (1994).
[23] P. Beiersdorfer, E. Trabert, H. Chen, M. H. Chen, M. J. May, and A. L. Osterheld, Phys. Rev. A **67**, 052103 (2003).
[24] M. H. Chen, K. T. Cheng, P. Beiersdorfer, and J. Sapirstein, Phys. Rev. A **68**, 022507 (2003).
[25] J. D. Gillaspy, I. N. Draganić, Y. Ralchenko, J. Reader, J. N. Tan, J. M. Pomeroy, and S. M. Brewer, Phys. Rev. A **80**, 010501(R) (2009).
[26] M. F. Gu, Can. J. Phys. **86**, 675 (2008).
[27] K. G. Dyall, I. P. Grant, C. T. Johnson, F. A. Parpia, and E. P. Plummer, Comput. Phys. Commun. **55**, 425 (1989).

Q [28] F. A. Parpia, I. P. Grant, and C. Froese Fischer (unpublished).
Q [29] J. Sapirstein, M. H. Chen, and K. T. Cheng (private communication).
[30] M. F. Gu, AIP Conf. Proc. **730**, 127 (2004).
[31] D. A. Knapp, R. E. Marrs, S. R. Elliott, E. W. Magee, and R. Zasadzinski, Nucl. Instrum. Methods Phys. Res. A **334**, 305 (1993).
[32] P. Beiersdorfer, Can. J. Phys. **86**, 1 (2008).
[33] P. Beiersdorfer, E. W. Magee, E. Träbert, H. Chen, J. K. Lepson, M.-F. Gu, and M. Schmidt, Rev. Sci. Instrum. **75**, 3723 (2004).
[34] J. D. Garcia and J. E. Mack, J. Opt. Soc. Am. **55**, 654 (1965).
[35] G. W. Drake, Can. J. Phys. **66**, 586 (1988).
[36] L. A. Vainshtein and U. I. Safronova, Phys. Scr. **31**, 519 (1985).
[37] L. Engström and U. Litzén, J. Phys. B **28**, 2565 (1995).
[38] P. Beiersdorfer, H. Chen, D. B. Thorn, and E. Träbert, Phys. Rev. Lett. **95**, 233003 (2005).
[39] P. Beiersdorfer, A. Osterheld, S. R. Elliott, M. H. Chen, D. Knapp, and K. Reed, Phys. Rev. A **52**, 2693 (1995).
[40] P. Beiersdorfer, D. Knapp, R. E. Marrs, S. R. Elliott, and M. H. Chen, Phys. Rev. Lett. **71**, 3939 (1993).

Paper V

Phys. Scr. **81** (2010) 015301 (8pp) doi:10.1088/0031-8949/81/01/015301

Spectroscopy of M-shell x-ray transitions in Zn-like through Co-like W

J Clementson[1], **P Beiersdorfer, G V Brown and M F Gu**[2]

Lawrence Livermore National Laboratory, Livermore, CA 94550, USA

E-mail: clementson@llnl.gov

Received 14 July 2009
Accepted for publication 13 November 2009
Published 24 December 2009
Online at stacks.iop.org/PhysScr/81/015301

Abstract
The M-shell x-ray emission of highly charged tungsten ions has been investigated at the Livermore electron beam ion trap facility. Using the SuperEBIT electron beam ion trap and a NASA x-ray calorimeter array, transitions connecting to levels of the ground configurations in the 1500–3600 eV spectral range of zinc-like W^{44+} through cobalt-like W^{47+} have been measured. The measured spectra are compared with theoretical line positions and emissivities calculated using the FAC code.

PACS numbers: 32.30.Rj, 31.30.J−, 52.70.La

1. Introduction

Tungsten is gaining interest in fusion engineering as a plasma-facing material in magnetic confinement devices, see e.g. [1–3]. Some present-day tokamaks are already operating with tungsten surfaces or are currently installing tungsten parts [4]. The ITER tokamak, now under construction in Cadarache, France, will have a tungsten divertor.

The use of tungsten in magnetic fusion experiments will introduce trace amounts of tungsten ions into the high-temperature, low-density plasmas. Tungsten ions that enter into a tokamak will not become fully stripped even in the hot core, resulting in strong x-ray emission over a wide range of temperatures. Provided the spectra are well understood, the tungsten ions can serve as diagnostics for plasma parameters [5, 6]. For instance, the ion temperatures of the ITER core plasmas will likely be measured using the Doppler broadening of L-shell tungsten lines [7].

Forty-six times ionized tungsten ions have 28 electrons arranged in a filled M-shell structure (unlike Ni I with a ground configuration of $3s^2 3p^6 3d^4_{3/2} 3d^4_{5/2} 4s^2$) and are therefore abundant over a large temperature range in high-temperature plasmas. This renders the nickel-like tungsten spectrum important for diagnostic purposes. The tungsten M-shell spectra of nickel-like and neighboring charge states have been extensively investigated, see for example [5, 8–29]. Further references can be found in the Kramida and Shirai review of atomic data for tungsten ions [30].

In recent years, Neill *et al* [13], Safronova *et al* [16, 17] and Ralchenko *et al* [20] have measured M-shell tungsten spectra on electron beam ion traps. Safronova *et al* and Ralchenko *et al* used x-ray calorimeter spectrometers for broadband spectral surveys. X-ray calorimeters (also known as quantum calorimeters or microcalorimeters) provide lower spectroscopic resolution than crystal spectrometers; however, the higher throughput and the very broad spectral coverage make these novel spectrometers very useful for the study of atomic spectra. Measurements of high-Z ions that have several transition bands particularly benefit from x-ray calorimeters. For instance, high charge states of Au were recently observed at the Livermore SuperEBIT, enabling line identifications and charge balance modeling [31]. In this paper, we report on the application of an x-ray calorimeter array at SuperEBIT to derive spectral line positions of M-shell x-ray transitions of W^{44+} through W^{47+}.

2. Experimental set-up

The measurements were carried out using the SuperEBIT electron beam ion trap at the Lawrence Livermore National Laboratory. SuperEBIT was operated in a low-energy configuration, making it similar to EBIT-I [32], at electron beam energies close to 3.3, 4.0 and 4.1 keV. These energies are of interest for the study of nickel-like tungsten, which is created from copper-like tungsten at 2414.1 eV and ionizes to cobalt-like at 4057 eV [33].

[1] Also at Department of Physics, Lund University, SE-221 00 Lund, Sweden.
[2] Present address: Space Sciences Laboratory, University of California, Berkeley, CA 94720, USA.

Table 1. Configuration state functions included in the structure calculations. $n = 4$, 5, 6 for Zn, Cu and Co, $n = 4$–8 for Ni; $n^* = 5$, 6; $l = 0, 1, \ldots, n-1$; $l^* =$ s, p.

Zn	Cu	Ni	Co
$3s^23p^63d^{10}4lnl$	$3s^23p^63d^{10}nl$	$3s^23p^63d^{10}$	$3s^23p^63d^9$ $3s^23p^53d^{10}$ $3s3p^63d^{10}$
$3s^23p^63d^94l4l4l$ $3s^23p^63d^94l^*4l^*n^*l$	$3s^23p^63d^94l4l$ $3s^23p^63d^94l^*n^*l$	$3s^23p^63d^9nl$	$3s^23p^63d^8nl$ $3s^23p^53d^9nl$ $3s3p^63d^9nl$
$3s^23p^53d^{10}4l4l4l$ $3s^23p^53d^{10}4l^*4l^*n^*l$	$3s^23p^53d^{10}4l4l$ $3s^23p^53d^{10}4l^*n^*l$	$3s^23p^53d^{10}nl$	$3s^23p^53d^9nl$ $3s^23p^43d^{10}nl$ $3s3p^53d^{10}nl$
$3s3p^63d^{10}4l4l4l$ $3s3p^63d^{10}4l^*4l^*n^*l$	$3s3p^63d^{10}4l4l$ $3s3p^63d^{10}4l^*n^*l$	$3s3p^63d^{10}nl$	$3s3p^63d^9nl$ $3s3p^53d^{10}nl$ $3p^63d^{10}nl$

The tungsten ions were injected into the SuperEBIT trap using one of two methods: Metal Vapor Vacuum Arc (MeVVA) injection and sublimation injection. Most of the data were acquired using the faster sublimation injection. For this method, sublimation of tungsten hexacarbonyl, $W(CO)_6$, occurred in a vial attached to one of SuperEBIT's six radial vacuum ports. Once in a gaseous form, $W(CO)_6$ molecules freely entered the trap region through the port. As tungsten carbonyl molecules continuously fill the trap, the charge state distributions typically consist of several tungsten ions. Alternatively, the MeVVA injector discharges bunches of low charge state ions into the trap from a tungsten cathode, located at the top of SuperEBIT, once every trap cycle. As a result, the EBIT plasmas have a more peaked charge state distribution. Sodium metal was also sublimated and injected as a neutral gas, which, together with low-Z plasma impurities, provided reference spectra for energy calibration.

The x-ray emission was recorded with a NASA X-ray Spectrometer (XRS) x-ray calorimeter [34–36] developed at the Goddard Space Flight Center. The XRS spectrometer is a medium-resolution energy-dispersive instrument for soft and hard x-rays made up of an array of HgTe and Bi heat absorbers. For this measurement, 23 of the HgTe pixel elements were used. The resolution of 6.5 eV full-width at half-maximum equals a resolving power $E/\Delta E = 230$–550 for the spectral interval of interest. The data from the pixel elements were corrected for individual voltage drifts and then added together.

3. Calculations and spectral modeling

Transition energies of zinc-like through cobalt-like tungsten were calculated using the fully relativistic atomic physics package FAC v1.1.1 [37]. Keeping the K and L shells closed, energy levels and transition energies were calculated for the M and N shells. Table 1 lists the included configuration state functions.

Collisional-radiative models were constructed for the spectra of the four tungsten ions. The plasmas were modeled with electron beam energies of 3.3 and 4.1 keV at an electron density of 5×10^{11} cm^{-3}. Electron impact excitation and deexcitation were included as well as autoionization for the Cu- and Zn-like charge states. The calculated spectra for an excitation energy of 4.1 keV and line widths of 6.5 eV are shown in figure 1.

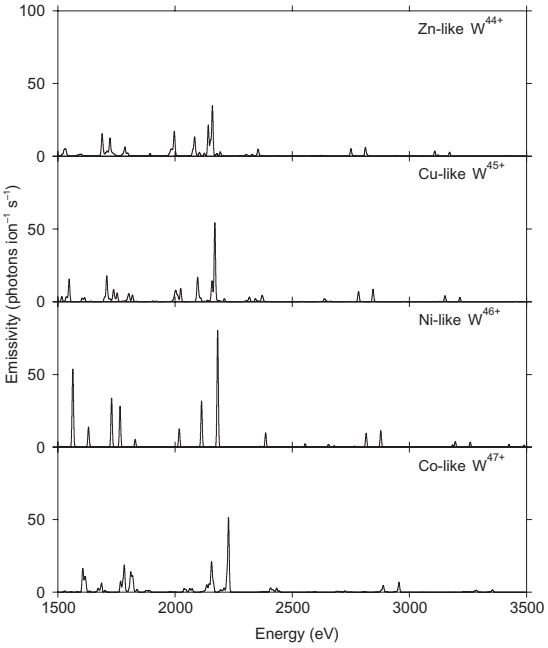

Figure 1. Calculated tungsten spectra at an excitation energy of 4.1 keV. The assumed line width is 6.5 eV.

4. Experimental tungsten spectra

The spectra analyzed comprise tungsten hexacarbonyl injection data obtained at beam energies close to 3.3, 4.0 and 4.1 keV, and MeVVA injection data obtained at an electron beam energy of 4.1 keV. The 4.1 keV carbonyl spectrum was energy calibrated with the $(3s^23p^63d^{10})_0$–$(3s^23p^63d^3_{3/2}3d^6_{5/2}4p_{1/2})_1$ Ni-like W line, which has been accurately measured at EBIT-I by Elliott *et al* [27], and with K-shell emission from low-Z elements (Na, Si, Cl, Ar and K) with transition energies calculated by Garcia and Mack [38], Drake [39] and Vainshtein and Safronova [40]. Ni-like W line positions determined from this spectrum were then used as reference lines in the other spectra. Conversion factors used were $hc = 12\,398.42$ Å eV $= 8065.5410$ eV cm.

The broadband XRS spectra are dominated by Ni-like W lines with upper levels of $n = 4$, 5, 6, 7 and 8. Lines from the lower charge states are often blended. Energies of the Co-like lines were derived from the 4.1 keV MeVVA spectrum, and the Cu- and Zn-like line positions were derived from 3.3 and 4.0 keV spectra. As far as a position of a given line was measured more than once, the results were averaged. An overview spectrum covering the 1–4 keV spectral band at a beam energy of 4.0 keV is shown in figure 2. The 3.3 keV spectrum, divided into three energy regions, is shown in figure 3, and the 4.1 keV spectrum, also divided, is shown in figure 4. The high-n transitions in Ni-like W were measured in the 4.1 keV spectrum and are shown in figure 5. This spectrum also shows lines from impurity ions.

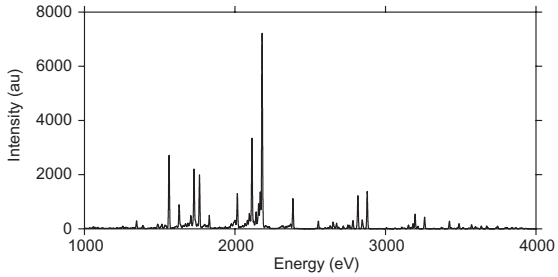

Figure 2. SuperEBIT XRS spectrum recorded at an electron beam energy of 4.0 keV.

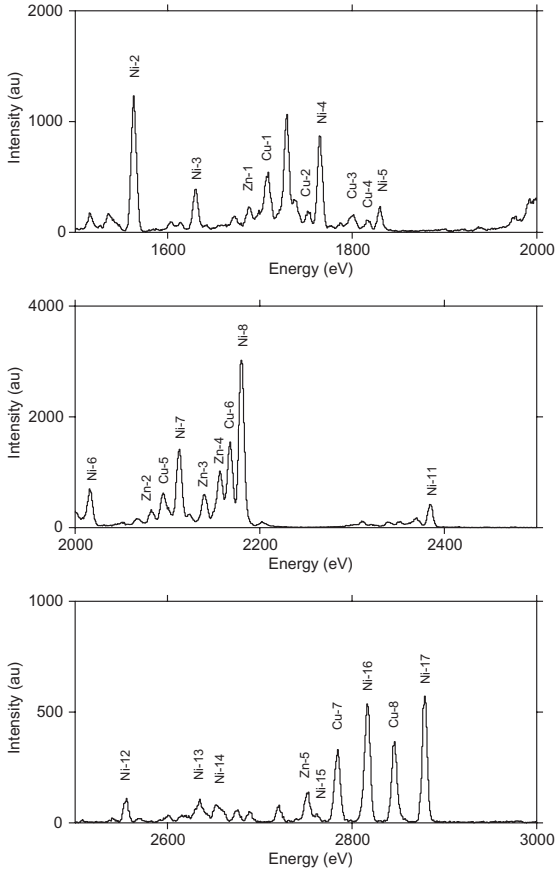

Figure 3. SuperEBIT XRS spectra recorded at an electron beam energy of 3.3 keV.

The measured lines are listed in tables 2–5 together with the theoretical line positions calculated using FAC. Most measured features have very good counting statistics and the spectroscopic accuracy is then limited by the calibration uncertainty, which varies from 0.3 to 0.5 eV. The total uncertainty of the line positions consists of the errors associated with the counting statistics and the energy scale added in quadrature. Only features that are dominated by transitions from one charge state are listed, and some features that are too broad or not fully resolved have been omitted. For the somewhat weaker or broader features the error bars have been doubled. The XRS is energy dispersive and measures

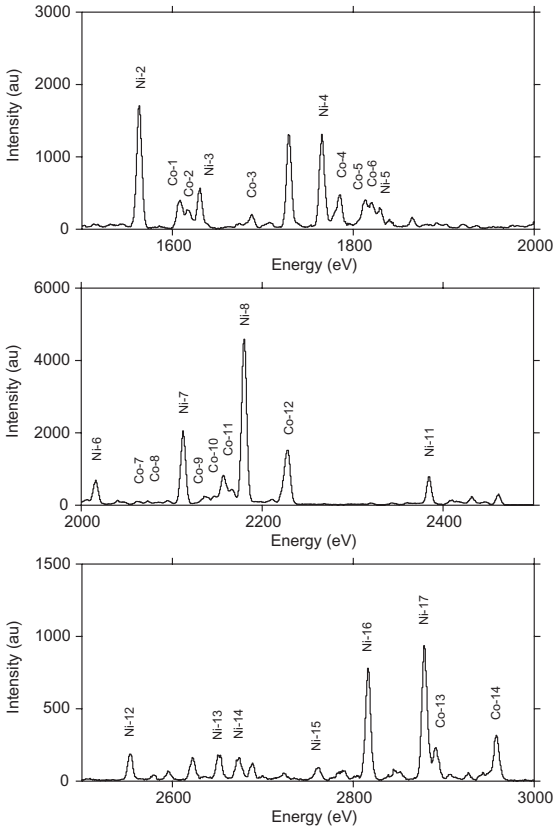

Figure 4. SuperEBIT XRS spectra recorded at an electron beam energy of 4.1 keV.

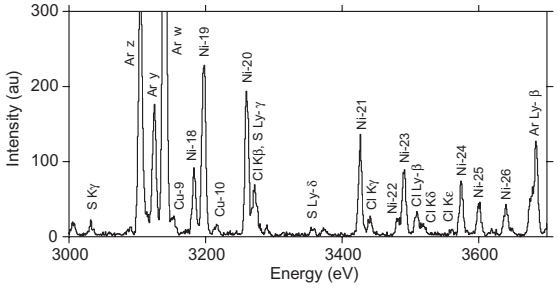

Figure 5. High-*n* transitions of Ni-like W^{46+} recorded at an electron beam energy of 4.1 keV.

photon energies, but corresponding wavelengths are also listed in the tables.

In the following, we discuss the results obtained for each of the four charge states of tungsten we have investigated.

4.1. Zn-like W^{44+}

The Zn-like lines are the weakest of the four charge states investigated. Seven lines are identified and listed in table 2. Line Zn-3 and one of the Zn-4 transitions are two-electron one-photon decays. Neill *et al* [13] observed these lines and assigned Zn-3 to be a line of Ga-like W and Zn-4 to be a resonance line from the $3d^3_{3/2}3d^6_{5/2}4s^24f_{5/2}$ configuration. As pointed out by Kramida

Table 2. Zn-like W^{44+} line positions measured with the NASA XRS spectrometer. Theoretical energies are from the present FAC calculations. [M]Mandelbaum *et al* [24], [N]Neill *et al* [13], [Ne]Neu *et al* [14], [T]Tragin *et al* [25], [Z1]Zigler *et al* [12]. *Comments on previous measurement are given in table 6.

Key	Transition lower level	upper level	Theory ΔE (eV)	Experiment ΔE (eV)	Experiment λ (Å)	Prev. Exp. λ (Å)
Zn-1	$(3s^23p^63d^{10}4s^2)_0$	$(3s^23p^63d^3_{3/2}3d^6_{5/2}4s^24p_{1/2})_1$	1688.1	1688.4(8)	7.3433(35)	7.332(3)^{M*1} 7.34^{Ne}
Zn-2	$(3s^23p^63d^{10}4s^2)_0$	$(3s^23p^63d^4_{3/2}3d^5_{5/2}4s^24f_{7/2})_1$	2082.6	2082.2(4)	5.9545(11)	
Zn-3	$(3s^23p^63d^{10}4s^2)_0$	$(3s^23p^63d^3_{3/2}3d^6_{5/2}4s_{1/2}4p_{3/2}4d_{3/2})_1$	2141.3	2139.7(8)	5.7945(22)	5.7928^{N*2}
Zn-4	$(3s^23p^63d^{10}4s^2)_0$	$(3s^23p^63d^3_{3/2}3d^6_{5/2}4s_{1/2}4p_{3/2}4d_{5/2})_1$	2150.6	2156.4(16)	5.7496(42)	5.7676^{N*3}
	$(3s^23p^63d^{10}4s^2)_0$	$(3s^23p^63d^3_{3/2}3d^6_{5/2}4s^24f_{5/2})_1$	2159.0			5.7471^{N*4}
Zn-5	$(3s^23p^63d^{10}4s^2)_0$	$(3s^23p^63d^4_{3/2}3d^5_{5/2}4s^25f_{7/2})_1$	2750.2	2750.3(10)	4.5080(16)	4.507(2)^{T*5} 4.509^{Z1*5}
Zn-6	$(3s^23p^63d^{10}4s^2)_0$	$(3s^23p^63d^4_{3/2}3d^5_{5/2}4s^26f_{7/2})_1$	3107.9	3107.8(5)	3.9895(6)	3.990(5)^{T} 3.988^{Z1}
Zn-7	$(3s^23p^63d^{10}4s^2)_0$	$(3s^23p^63d^3_{3/2}3d^6_{5/2}4s^26f_{5/2})_1$	3171.0	3171.2(6)	3.9097(7)	3.909(5)^{T} 3.909^{Z1}

Table 3. Cu-like W^{45+} line positions measured with the NASA XRS spectrometer. Theoretical energies are from the present FAC calculations. [M]Mandelbaum *et al* [24], [N]Neill *et al* [13], [Ne]Neu *et al* [14], [T]Tragin *et al* [25], [Z1]Zigler *et al* [12]. *Comments on previous measurement are given in table 6.

Key	Transition lower level	upper level	Theory ΔE (eV)	Experiment ΔE (eV)	Experiment λ (Å)	Prev. Exp. λ (Å)
Cu-1	$(3s^23p^63d^{10}4s_{1/2})_{1/2}$	$(3s^23p^63d^3_{3/2}3d^6_{5/2}4s_{1/2}4p_{1/2})_{3/2}$	1707.3	1707.4(6)	7.2616(26)	7.262(3)^{M} 7.26^{Ne}
		$(3s^23p^63d^3_{3/2}3d^6_{5/2}4s_{1/2}4p_{1/2})_{1/2}$	1708.4			7.262(3)^{M} 7.26^{Ne}
Cu-2	$(3s^23p^63d^{10}4s_{1/2})_{1/2}$	$(3s^23p^63d^4_{3/2}3d^5_{5/2}4s_{1/2}4p_{3/2})_{3/2}$	1752.6	1751.9(8)	7.0771(32)	7.075(3)^{M*6}
Cu-3	$(3s^23p^63d^{10}4s_{1/2})_{1/2}$	$(3s^23p^63d^3_{3/2}3d^6_{5/2}4s_{1/2}4p_{3/2})_{1/2}$	1797.6	1799.7(8)	6.8892(31)	6.896(3)^{M}
		$(3s^23p^63d^3_{3/2}3d^6_{5/2}4s_{1/2}4p_{3/2})_{3/2}$	1801.4			6.884(3)^{M}
	$(3s^23p^63d^{10}4p_{3/2})_{3/2}$	$(3s^23p^63d^3_{3/2}3d^6_{5/2}4s_{1/2}4d_{3/2})_{1/2}$	1803.8			
Cu-4	$(3s^23p^63d^{10}4s_{1/2})_{1/2}$	$(3s^23p^63d^3_{3/2}3d^6_{5/2}4s_{1/2}4p_{3/2})_{1/2}$	1817.2	1816.6(10)	6.8251(38)	6.827(3)^{M}
	$(3s^23p^63d^{10}4p_{3/2})_{3/2}$	$(3s^23p^63d^3_{3/2}3d^6_{5/2}4p^2_{3/2})_{1/2}$	1818.4			6.816(3)^{M*7}
Cu-5	$(3s^23p^63d^{10}4s_{1/2})_{1/2}$	$(3s^23p^63d^4_{3/2}3d^5_{5/2}4s_{1/2}4f_{7/2})_{3/2}$	2094.9	2094.8(5)	5.9187(14)	5.9127^{N*8}
		$(3s^23p^63d^4_{3/2}3d^5_{5/2}4s_{1/2}4f_{7/2})_{1/2}$	2097.7			5.9127^{N*8}
Cu-6	$(3s^23p^63d^{10}4s_{1/2})_{1/2}$	$(3s^23p^63d^3_{3/2}3d^6_{5/2}4s_{1/2}4f_{5/2})_{1/2}$	2168.6	2167.5(4)	5.7201(11)	5.7240^{N*9}
		$(3s^23p^63d^3_{3/2}3d^6_{5/2}4s_{1/2}4f_{5/2})_{3/2}$	2169.8			5.7191^{N*10}
Cu-7	$(3s^23p^63d^{10}4s_{1/2})_{1/2}$	$(3s^23p^63d^4_{3/2}3d^5_{5/2}4s_{1/2}5f_{7/2})_{1/2}$	2780.5	2783.0(8)	4.4551(13)	4.457(5)^{T*11}
		$(3s^23p^63d^4_{3/2}3d^5_{5/2}4s_{1/2}5f_{7/2})_{3/2}$	2783.1			4.457(5)^{T*11} 4.458^{Z1*11}
Cu-8	$(3s^23p^63d^{10}4s_{1/2})_{1/2}$	$(3s^23p^63d^3_{3/2}3d^6_{5/2}4s_{1/2}5f_{5/2})_{1/2}$	2843.4	2845.1(4)	4.3578(6)	4.359(5)^{T}
		$(3s^23p^63d^3_{3/2}3d^6_{5/2}4s_{1/2}5f_{5/2})_{3/2}$	2844.7			4.359(5)^{T} 4.358^{Z1}
Cu-9	$(3s^23p^63d^{10}4s_{1/2})_{1/2}$	$(3s^23p^63d^4_{3/2}3d^5_{5/2}4s_{1/2}6f_{7/2})_{1/2}$	3150.7	3152.5(5)	3.9329(6)	3.933(2)^{T*12}
		$(3s^23p^63d^4_{3/2}3d^5_{5/2}4s_{1/2}6f_{7/2})_{3/2}$	3151.9			3.933(2)^{T*12} 3.932^{Z1}
Cu-10	$(3s^23p^63d^{10}4s_{1/2})_{1/2}$	$(3s^23p^63d^3_{3/2}3d^6_{5/2}4s_{1/2}6f_{5/2})_{3/2}$	3214.7	3215.8(5)	3.8555(6)	3.856(5)^{T}
		$(3s^23p^63d^3_{3/2}3d^6_{5/2}4s_{1/2}6f_{5/2})_{1/2}$	3215.0			3.856(5)^{T}

and Shirai [30], the two lines should be two-electron one-photon decays to the ground state. Kramida and Shirai suggest the lines to be from $3d^3_{3/2}3d^6_{5/2}4s_{1/2}4p_{3/2}4d_{3/2}$. Here, the FAC collisional-radiative model suggests that one of those lines instead is from $3d^3_{3/2}3d^6_{5/2}4s_{1/2}4p_{3/2}4d_{5/2}$. The calculations also suggest the Zn-4 line to be blended with two two-electron one-photon resonance decays in Cu-like W (from upper level $(3s^23p^63d^3_{3/2}3d^6_{5/2}4p_{3/2}4d_{3/2})_{3/2}$ at 2155.2 and 2158.3 eV). Zn-3 possibly blends with two Ga-like transitions ($3d^{10}4s^24p_{1/2}$–$3d^3_{3/2}3d^6_{5/2}4s^24p_{1/2}4f_{5/2}$), and Zn-5 possibly blends with a Ge-like line ($3d^{10}4s^24p^2_{1/2}$–$3d^3_{3/2}3d^6_{5/2}4s^24p^2_{1/2}5f_{5/2}$). The error bars of the energies associated with Zn-3, Zn-4 and Zn-5 have therefore been doubled.

4.2. Cu-like W^{45+}

Ten Cu-like features are reported in table 3. The lines are measured in the 3.3 and 4.0 keV spectra. Cu-8 is

Table 4. Ni-like W^{46+} line positions measured with the NASA XRS spectrometer. Theoretical energies are from the present FAC calculations. [B]Butzbach *et al* [43], [K]Klapisch *et al* [23], [M]Mandelbaum *et al* [24], [N]Neill *et al* [13], [Ne]Neu *et al* [14], [R]Ralchenko *et al* [20], [T]Tragin *et al* [25], [W]Wyart *et al* [44], [Z1]Zigler *et al* [12], [Z2]Zigler *et al* [11]. *Comments on previous measurement are given in table 6.

Key	Transition lower level	upper level	Theory ΔE (eV)	Experiment ΔE (eV)	Experiment λ (Å)	Prev. Exp. λ (Å)
Ni-1	$(3s^23p^63d^3_{3/2}3d^6_{5/2}4p_{1/2})_1$	$(3s^23p^63d^3_{3/2}3d^6_{5/2}6d_{3/2})_0$	1487.0	1488.2(4)	8.3312(22)	8.326(11)[R]
Ni-2	$(3s^23p^63d^{10})_0$	$(3s^23p^63d^4_{3/2}3d^5_{5/2}4s_{1/2})_3$	1562.2	1562.9(3)	7.9330(15)	7.930(5)[R]
		$(3s^23p^63d^4_{3/2}3d^5_{5/2}4s_{1/2})_2$	1564.1			7.930(5)[R]
						7.93[Ne]
Ni-3	$(3s^23p^63d^{10})_0$	$(3s^23p^63d^3_{3/2}3d^6_{5/2}4s_{1/2})_2$	1630.0	1629.8(3)	7.6073(14)	7.607(6)[R]
Ni-4	$(3s^23p^63d^{10})_0$	$(3s^23p^63d^4_{3/2}3d^5_{5/2}4p_{3/2})_1$	1764.8	1764.6(3)	7.0262(12)	7.028(3)[M]
						7.030(4)[R]
						7.024(5)[Z2]
						7.028[K*13]
Ni-5	$(3s^23p^63d^{10})_0$	$(3s^23p^63d^3_{3/2}3d^6_{5/2}4p_{3/2})_1$	1829.4	1829.6(4)	6.7766(15)	6.779(3)[M]
						6.785(5)[R]
						6.775(5)[Z2]
						6.779[K*14]
Ni-6	$(3s^23p^63d^{10})_0$	$(3s^23p^2_{1/2}3p^3_{3/2}3d^{10}4s_{1/2})_1$	2017.4	2015.4(3)	6.1518(9)	6.155(4)[R]
						6.154(5)[Z2]
Ni-7	$(3s^23p^63d^{10})_0$	$(3s^23p^63d^4_{3/2}3d^5_{5/2}4f_{7/2})_1$	2112.6	2112.2(3)	5.8699(8)	5.867[N*15]
						5.872(2)[R]
						5.871(3)[Z2]
						5.8715(8)[B]
Ni-8	$(3s^23p^63d^{10})_0$	$(3s^23p^63d^3_{3/2}3d^6_{5/2}4f_{5/2})_1$	2181.4	2179.7(4)	5.6881(10)	5.690[N*16]
						5.691(2)[R]
						5.689(3)[Z2]
						5.6913(8)[B]
Ni-9	$(3s^23p^63d^{10})_0$	$(3s^23p_{1/2}3p^4_{3/2}3d^{10}4s_{1/2})_1$	2323.6	2320.3(6)	5.3435(14)	
Ni-10	$(3s^23p^63d^{10})_0$	$(3s^23p^2_{1/2}3p^3_{3/2}3d^{10}4d_{3/2})_1$	2361.8	2360.7(7)	5.2520(16)	5.2509[N*17]
						5.255(2)[T]
Ni-11	$(3s^23p^63d^{10})_0$	$(3s^23p^2_{1/2}3p^3_{3/2}3d^{10}4d_{5/2})_1$	2386.0	2384.2(4)	5.2002(9)	5.1963[N*18]
						5.203(2)[T]
						5.203(3)[R]
Ni-12	$(3s^23p^63d^{10})_0$	$(3s^23p^2_{1/2}3p^3_{3/2}3d^{10}4f_{7/2})_2$	2554.7	2553.0(4)	4.8564(8)	4.857(2)[T]
						4.857[W]
Ni-13	$(3s^23p^63d^{10})_0$	$(3s_{1/2}3p^63d^{10}4p_{1/2})_1$	2655.0	2651.3(4)	4.6764(7)	4.680(2)[T]
Ni-14	$(3s^23p^63d^{10})_0$	$(3s^23p_{1/2}3p^4_{3/2}3d^{10}4d_{3/2})_1$	2678.6	2673.7(6)	4.6372(10)	4.638(2)[T]
Ni-15	$(3s^23p^63d^{10})_0$	$(3s_{1/2}3p^63d^{10}4p_{3/2})_1$	2765.6	2760.7(5)	4.4910(8)	4.493(2)[T]
Ni-16	$(3s^23p^63d^{10})_0$	$(3s^23p^63d^4_{3/2}3d^5_{5/2}5f_{7/2})_1$	2814.9	2816.1(3)	4.4027(5)	4.406(2)[T]
						4.403(2)[R]
						4.409[Z1*19]
Ni-17	$(3s^23p^63d^{10})_0$	$(3s^23p^63d^3_{3/2}3d^6_{5/2}5f_{5/2})_1$	2877.3	2878.2(3)	4.3077(4)	4.309(2)[R]
						4.309(2)[T]
						4.311[Z1]
Ni-18	$(3s^23p^63d^{10})_0$	$(3s^23p^2_{1/2}3p^3_{3/2}3d^{10}5d_{5/2})_1$	3183.9	3182.7(4)	3.8956(5)	3.895(2)[T]
Ni-19	$(3s^23p^63d^{10})_0$	$(3s^23p^63d^4_{3/2}3d^5_{5/2}6f_{7/2})_1$	3195.5	3196.8(3)	3.8784(4)	3.877(2)[T]
						3.878(2)[R]
						3.879[Z1]
Ni-20	$(3s^23p^63d^{10})_0$	$(3s^23p^63d^3_{3/2}3d^6_{5/2}6f_{5/2})_1$	3258.9	3259.9(3)	3.8033(4)	3.803(2)[T]
						3.800(2)[R]
						3.803[Z1]
Ni-21	$(3s^23p^63d^{10})_0$	$(3s^23p^63d^4_{3/2}3d^5_{5/2}7f_{7/2})_1$	3424.4	3426.0(4)	3.6189(4)	3.618(2)[T]
Ni-22	$(3s^23p^63d^{10})_0$	$(3s^23p_{1/2}3p^4_{3/2}3d^{10}5d_{3/2})_1$	3482.7	3480.9(7)	3.5618(7)	3.551(2)[T]
Ni-23	$(3s^23p^63d^{10})_0$	$(3s^23p^63d^3_{3/2}3d^6_{5/2}7f_{5/2})_1$	3488.9	3490.2(4)	3.5524(4)	3.551(2)[T]
Ni-24	$(3s^23p^63d^{10})_0$	$(3s^23p^63d^4_{3/2}3d^5_{5/2}8f_{7/2})_1$	3572.5	3574.1(5)	3.4690(5)	3.469(2)[T]
Ni-25	$(3s^23p^63d^{10})_0$	$(3s^23p^2_{1/2}3p^3_{3/2}3d^{10}6d_{5/2})_1$	3600.9	3600.0(6)	3.4440(6)	3.445(2)[T*20]
Ni-26	$(3s^23p^63d^{10})_0$	$(3s^23p^63d^3_{3/2}3d^6_{5/2}8f_{5/2})_1$	3637.7	3639.5(6)	3.4066(6)	

Table 5. Co-like W^{47+} line positions measured with the NASA XRS spectrometer. Theoretical energies are from the present FAC calculations. [K] Klapisch *et al* [23], [M] Mandelbaum *et al* [24], [N] Neill *et al* [13], [T] Tragin *et al* [25]. *Comments on previous measurement are given in table 6.

Key	Transition lower level	upper level	Theory ΔE (eV)	Experiment ΔE (eV)	Experiment λ (Å)	Prev. Exp. λ (Å)
Co-1	$(3s^23p^63d^4_{3/2}3d^5_{5/2})_{5/2}$	$(3s^23p^63d^4_{3/2}3d^4_{5/2}4s_{1/2})_{9/2}$	1604.9	1607.6(4)	7.7124(19)	
		$(3s^23p^63d^4_{3/2}3d^4_{5/2}4s_{1/2})_{7/2}$	1608.0			
Co-2	$(3s^23p^63d^4_{3/2}3d^5_{5/2})_{5/2}$	$(3s^23p^63d^4_{3/2}3d^4_{5/2}4s_{1/2})_{5/2}$	1614.5	1617.2(10)	7.6666(47)	
		$(3s^23p^63d^4_{3/2}3d^4_{5/2}4s_{1/2})_{3/2}$	1616.0			
	$(3s^23p^2_{1/2}3p^3_{3/2}3d^{10})_{3/2}$	$(3s^23p^63d^3_{3/2}3d^5_{5/2}4d_{3/2})_{5/2}$	1618.2			
	$(3s^23p^63d^3_{3/2}3d^6_{5/2})_{3/2}$	$(3s^23p^63d^3_{3/2}3d^5_{5/2}4s_{1/2})_{7/2}$	1619.7			
Co-3	$(3s^23p^63d^4_{3/2}3d^5_{5/2})_{5/2}$	$(3s^23p^63d^3_{3/2}3d^5_{5/2}4s_{1/2})_{9/2}$	1685.9	1686.8(5)	7.3503(22)	
Co-4	$(3s^23p^63d^4_{3/2}3d^5_{5/2})_{5/2}$	$(3s^23p^63d^3_{3/2}3d^5_{5/2}4p_{1/2})_{7/2}$	1783.0	1783.8(8)	6.9506(31)	6.949(3)[M]
						6.949[K]
		$(3s^23p^63d^3_{3/2}3d^5_{5/2}4p_{1/2})_{3/2}$	1783.1			6.949(3)[M]
						6.949[K]
Co-5	$(3s^23p^63d^4_{3/2}3d^5_{5/2})_{5/2}$	$(3s^23p^63d^4_{3/2}3d^4_{5/2}4p_{3/2})_{7/2}$	1810.1	1812.4(8)	6.8409(30)	6.844(3)[M]
						6.844[K]
		$(3s^23p^63d^4_{3/2}3d^4_{5/2}4p_{3/2})_{5/2}$	1810.5			6.844(3)[M]
						6.844[K]
Co-6	$(3s^23p^63d^4_{3/2}3d^5_{5/2})_{5/2}$	$(3s^23p^63d^4_{3/2}3d^4_{5/2}4p_{3/2})_{5/2}$	1816.5	1820.6(8)	6.8101(30)	
		$(3s^23p^63d^4_{3/2}3d^4_{5/2}4p_{3/2})_{3/2}$	1820.3			6.806(3)[M*21]
						6.806[K]
Co-7	$(3s^23p^63d^4_{3/2}3d^5_{5/2})_{5/2}$	$(3s^23p^2_{1/2}3p^3_{3/2}3d^4_{3/2}3d^5_{5/2}4s_{1/2})_{7/2}$	2060.8	2062.4(10)	6.0116(29)	
		$(3s^23p^2_{1/2}3p^3_{3/2}3d^4_{3/2}3d^5_{5/2}4s_{1/2})_{5/2}$	2064.3			
Co-8	$(3s^23p^63d^4_{3/2}3d^5_{5/2})_{5/2}$	$(3s^23p^2_{1/2}3p^3_{3/2}3d^4_{3/2}3d^5_{5/2}4s_{1/2})_{3/2}$	2072.7	2072.9(10)	5.9812(29)	
Co-9	$(3s^23p^63d^4_{3/2}3d^5_{5/2})_{5/2}$	$(3s^23p^63d^4_{3/2}3d^4_{5/2}4f_{5/2})_{5/2}$	2131.1	2137.1(10)	5.8015(27)	
		$(3s^23p^63d^4_{3/2}3d^4_{5/2}4f_{5/2})_{7/2}$	2133.6			
	$(3s^23p^2_{1/2}3p^3_{3/2}3d^{10})_{3/2}$	$(3s^23p^2_{1/2}3p^3_{3/2}3d^4_{3/2}3d^5_{5/2}4f_{5/2})_{1/2}$	2133.7			
		$(3s^23p^2_{1/2}3p^3_{3/2}3d^4_{3/2}3d^5_{5/2}4f_{5/2})_{5/2}$	2134.9			
	$(3s^23p^63d^4_{3/2}3d^5_{5/2})_{5/2}$	$(3s^23p^63d^4_{3/2}3d^4_{5/2}4f_{5/2})_{3/2}$	2135.6			
	$(3s^23p^2_{1/2}3p^3_{3/2}3d^{10})_{3/2}$	$(3s^23p^2_{1/2}3p^3_{3/2}3d^4_{3/2}3d^5_{5/2}4f_{5/2})_{3/2}$	2135.9			
	$(3s^23p^63d^4_{3/2}3d^5_{5/2})_{5/2}$	$(3s^23p^63d^4_{3/2}3d^4_{5/2}4f_{7/2})_{7/2}$	2137.7			
Co-10	$(3s^23p^63d^4_{3/2}3d^5_{5/2})_{5/2}$	$(3s^23p^63d^4_{3/2}3d^4_{5/2}4f_{7/2})_{5/2}$	2143.5	2146.9(10)	5.7750(27)	
		$(3s^23p^63d^4_{3/2}3d^4_{5/2}4f_{7/2})_{3/2}$	2145.1			5.7744[N*22]
Co-11	$(3s^23p^63d^4_{3/2}3d^5_{5/2})_{5/2}$	$(3s^23p^63d^4_{3/2}3d^4_{5/2}4f_{7/2})_{5/2}$	2153.5	2156.8(4)	5.7485(11)	5.7531[N*23]
		$(3s^23p^63d^4_{3/2}3d^4_{5/2}4f_{7/2})_{7/2}$	2155.4			5.7482[N*23]
		$(3s^23p^63d^4_{3/2}3d^4_{5/2}4f_{5/2})_{5/2}$	2158.0			
	$(3s^23p^63d^3_{3/2}3d^6_{5/2})_{3/2}$	$(3s^23p^63d^3_{3/2}3d^5_{5/2}4f_{7/2})_{5/2}$	2158.2			
Co-12	$(3s^23p^63d^4_{3/2}3d^5_{5/2})_{5/2}$	$(3s^23p^63d^3_{3/2}3d^5_{5/2}4f_{5/2})_{3/2}$	2220.8	2227.1(4)	5.5671(10)	5.5811[N*24]
		$(3s^23p^63d^3_{3/2}3d^5_{5/2}4f_{7/2})_{5/2}$	2225.0			5.5713[N*25]
		$(3s^23p^63d^3_{3/2}3d^5_{5/2}4f_{5/2})_{7/2}$	2227.5			5.5686[N*26]
		$(3s^23p^63d^3_{3/2}3d^5_{5/2}4f_{5/2})_{5/2}$	2228.4			5.5641[N*27]
Co-13	$(3s^23p^63d^4_{3/2}3d^5_{5/2})_{5/2}$	$(3s^23p^63d^4_{3/2}3d^4_{5/2}5f_{7/2})_{5/2}$	2887.0	2890.3(5)	4.2897(7)	4.289(2)[T*28]
		$(3s^23p^63d^4_{3/2}3d^4_{5/2}5f_{7/2})_{7/2}$	2888.5			4.289(2)[T*28]
Co-14	$(3s^23p^63d^4_{3/2}3d^5_{5/2})_{5/2}$	$(3s^23p^63d^3_{3/2}3d^5_{5/2}5f_{5/2})_{3/2}$	2954.0	2957.9(4)	4.1916(6)	4.192(2)[T*29]
		$(3s^23p^63d^3_{3/2}3d^5_{5/2}5f_{5/2})_{7/2}$	2955.3			4.192(2)[T*29]
		$(3s^23p^63d^3_{3/2}3d^5_{5/2}5f_{5/2})_{5/2}$	2955.5			4.192(2)[T*29]

possibly blended with a Ga-like resonance transition (from the $3d^3_{3/2}3d^6_{5/2}4p_{1/2}5f_{5/2}$ configuration), and hence, the error bar has been doubled.

4.3. Ni-like W^{46+}

Twenty-six nickel-like tungsten lines are identified and listed in table 4. They were mostly measured in the 4.1 keV spectrum, although many are average line positions from several spectra. Ni-1 is a weak N-shell transition, whereas the other observed lines are M-shell transitions. Ni-2 is made up of two energetically close dipole-forbidden transitions (cf [41]); a magnetic octupole and an electric quadrupole transition. These lines have recently been resolved with high-resolution crystal spectrometers [42]. The Ni-9 line position has been predicted by [11, 30], but has not previously been observed (here it is one of the weakest lines). A previously doubly classified line observed by Tragin *et al* [25] (also discussed in [30]), is resolved in this work, Ni-22 and Ni-23. As noted by Kramida and Shirai [30], the previously doubly classified line Ni-25 [25] should be dominated by the $(3s^23p^63d^{10})_0$–$(3s^23p^2_{1/2}3p^3_{3/2}3d^{10}6d_{5/2})_1$ transition.

4.4. Co-like W^{47+}

The features from cobalt-like tungsten were all measured in the 4.1 keV MeVVA spectrum and are listed in table 5. Co-like W has many transitions and only the dominating transitions

Table 6. Comments on the selection of the lines from previous work (PW) and earlier line assignments.

Key	Reference	Comment
*1	Mandelbaum *et al* [24]	Average λ of a broad feature. PW assigned several transitions to feature.
*2	Neill *et al* [13]	Average λ from five line lists. PW assigned the line to Ga-like W.
*3	Neill *et al* [13]	Average λ from three line lists. PW has different assignment.
*4	Neill *et al* [13]	Average λ from four line lists.
*5	Tragin *et al* [25] Zigler *et al* [12]	PW assigned feature blended with Ge-like W line.
*6	Mandelbaum *et al* [24]	PW assigned several transitions to feature.
*7	Mandelbaum *et al* [24]	PW assigned two transitions to feature.
*8	Neill *et al* [13]	Average λ from seven line lists.
*9	Neill *et al* [13]	Average λ from three line lists.
*10	Neill *et al* [13]	Average λ from seven line lists.
*11	Tragin *et al* [25] Zigler *et al* [12]	PW assigned feature blended with Ga-like W line.
*12	Tragin *et al* [25]	PW assigned two transitions to feature.
*13	Klapisch *et al* [23]	PW has no line assignment.
*14	Klapisch *et al* [23]	PW has no line assignment.
*15	Neill *et al* [13]	Average λ from ten line lists.
*16	Neill *et al* [13]	Average λ from ten line lists.
*17	Neill *et al* [13]	Average λ from five line lists.
*18	Neill *et al* [13]	Average λ from ten line lists.
*19	Zigler *et al* [12]	PW assigned two transitions to feature.
*20	Tragin *et al* [25]	PW assigned two transitions to feature.
*21	Mandelbaum *et al* [24]	PW assigned two transitions to feature.
*22	Neill *et al* [13]	Average λ from five line lists.
*23	Neill *et al* [13]	Average λ from five line lists.
*24	Neill *et al* [13]	Average λ from seven line lists.
*25	Neill *et al* [13]	Average λ from five line lists. PW has different assignment.
*26	Neill *et al* [13]	Average λ from eight line lists.
*27	Neill *et al* [13]	Average λ from six line lists.
*28	Tragin *et al* [25]	PW has no line assignment.
*29	Tragin *et al* [25]	PW has no line assignment.

in each feature are tabulated. The error bars for some of the weaker features have been doubled. Co-4 blends with two transitions at slightly lower energy giving the line a shoulder.

According to our FAC calculations, previous identifications for Co-12 [13, 30] are not correct. The 2225.0 eV transition is misidentified in [13] and the identifications for the 2225.0 eV and the 2228.4 eV transitions seem to be interchanged in [30].

5. Summary

The M-shell spectra of Zn-like through Co-like W ions have been measured using an x-ray calorimeter spectrometer at the SuperEBIT electron beam ion trap. Spectra were studied at excitation energies 3.3, 4.0 and 4.1 keV and show strong line emission in the 1500–3600 eV soft x-ray range. Line positions determined in our measurement are generally in good agreement with previous measurements when available and have significantly higher accuracies. Some of our lines have similar positions and error bars to those found earlier, but have been assigned to different transitions. This is likely to be due to the higher electron densities of the earlier experiments. A few lines, however, disagree with the work of Neill *et al* [13], although their measurements were performed at similar densities to ours. In addition, many lines have been presented which have been identified for the first time.

Relativistic atomic structure and collisional-radiative calculations have been performed using the FAC atomic physics code. Theoretical spectra are presented for Zn-like W^{44+} through Co-like W^{47+}. Very good agreement is established between calculated and observed spectra.

Acknowledgments

This work was performed under the auspices of the United States Department of Energy by Lawrence Livermore National Laboratory under contract DE-AC52-07NA-27344. The authors would like to acknowledge assistance with the experiment from Phil D'Antonio, Ed Magee, Dr Daniel Thorn, and Professor Elmar Träbert. Joel Clementson would like to thank Dr Hans Lundberg, Dr Sven Huldt and Professor Sune Svanberg for their support.

References

[1] Peacock N J, O'Mullane M G, Barnsley R and Tarbutt M 2008 Anticipated x-ray and VUV spectroscopic data from ITER with appropriate diagnostic implementation *Can. J. Phys.* **86** 277–84

[2] Skinner C H 2008 Applications of EBIT to magnetic fusion diagnostics *Can. J. Phys.* **86** 285–90

[3] Skinner C H 2009 Atomic physics in the quest for fusion energy and ITER *Phys. Scr.* T **134** 014022

[4] Neu R *et al* 2005 Tungsten: an option for divertor and main chamber plasma facing components in future fusion devices *Nucl. Fusion* **45** 209–18

[5] Biedermann C, Radtke R, Seidel R and Pütterich T 2009 Spectroscopy of highly charged tungsten ions relevant to fusion plasmas *Phys. Scr.* T **134** 014026

[6] Reader J 2009 Spectral data for fusion energy: from W to W *Phys. Scr.* T **134** 014023

[7] Beiersdorfer P *et al* 2010 *J. Phys. B: At. Mol. Phys.* submitted

[8] Dong C Z, Fritzsche S and Xie L Y 2003 Energy levels and transition probabilities for possible x-ray laser lines of highly charged Ni-like ions *J. Quant. Spectrosc. Radiat. Transfer* **76** 447–65

[9] Aggarwal K M, Norrington P H, Bell K L, Keenan F P, Pert G J and Rose S J 2000 Radiative rates for allowed transitions in Ni-like Nd, Sm, Eu, Ta, and W *At. Data Nucl. Data Tables* **74** 157–255

[10] Fournier K B 1998 Atomic data and spectral line intensities for highly ionized tungsten (Co-like W^{47+} to Rb-like W^{37+}) in a high-temperature, low-density plasma *At. Data Nucl. Data Tables* **68** 1–48

[11] Zigler A, Zmora H, Spector N, Klapisch M, Schwob J L and Bar-Shalom A 1980 Identification of spectra of Hf XLV, Ta XLVI, W XLVII, and Re XLVIII isoelectronic to Ni I in laser-produced plasmas *J. Opt. Soc. Am.* **70** 129–32

[12] Zigler A, Klapisch M and Mandelbaum P 1986 Interpretation of laser produced Au and W x-ray spectra in the 3 KeV range *Phys. Lett.* A **117** 31–5

[13] Neill P, Harris C, Safronova A S, Hamasha S, Hansen S, Safronova U I and Beiersdorfer P 2004 The study of x-ray *M*-shell spectra of W ions from the Lawrence Livermore National Laboratory electron beam ion trap *Can. J. Phys.* **82** 931–42

[14] Neu R, Fournier K B, Schlögl D and Rice J 1997 Observations of x-ray spectra from highly charged tungsten ions in tokamak plasmas *J. Phys. B: At. Mol. Opt. Phys.* **30** 5057–67

[15] Neu R, Fournier K B, Bolshukhin D and Dux R 2001 Spectral lines from highly charged tungsten ions in the soft-x-ray region for quantitative diagnostics of fusion plasmas *Phys. Scr.* T **92** 307–10

[16] Safronova A S *et al* 2008 The importance of EBIT data for z-pinch plasma diagnostics *Can. J. Phys.* **86** 267–76

[17] Shlyaptseva A, Fedin D, Hamasha S, Harris C, Kantsyrev V, Neill P, Ouart N and Safronova U I 2004 Development of M-shell x-ray spectroscopy and spectropolarimetry of z-pinch tungsten plasmas *Rev. Sci. Instrum.* **75** 3750–2

[18] Osborne G C, Safronova A S, Kantsyrev V L, Safronova U I, Yilmaz M F, Williamson K M, Shrestha I and Beiersdorfer P 2008 Diagnostic of charge balance of high-temperature tungsten plasmas using LLNL EBIT *Rev. Sci. Instrum.* **79** 10E308

[19] Loch S D, Pindzola M S, Ballance C P, Griffin C P, Whiteford A D and Pütterich T 2006 Modeling the spectral emission from tungsten in tokamaks *Spectral Line Shapes: 18th Int. Conf.* ed E Oks and M Pindzola (New York: AIP) **874** 233–241

[20] Ralchenko Y, Tan J N, Gillasy J D, Pomeroy J M and Silver E 2006 Accurate modeling of benchmark x-ray spectra from highly charged ions of tungsten *Phys. Rev.* A **74** 042614

[21] Ralchenko Y 2007 Density dependence of the forbidden lines in Ni-like tungsten *J. Phys. B: At. Mol. Opt. Phys.* **40** F175–F180

[22] Hamasha S M, Shlyaptseva A S and Safronova U I 2004 E1, E2, M1, and M2 transitions in the nickel isoelectronic sequence *Can. J. Phys.* **82** 331–56

[23] Klapisch M, Mandelbaum P, Barshalom A, Schwob J L, Zigler A and Jackel S 1981 Identification of 3d-4p transitions in Co-like W XLVIII and Tm XLIII and in Cu-like W XLVI and Tm XLI from laser-produced plasmas *J. Opt. Soc. Am.* **71** 1276–81

[24] Mandelbaum P, Klapisch M, Bar-Shalom A, Schwob J L and Zigler A 1983 Classification of x-ray spectra from laser produced plasmas of atoms from Tm to Pt in the range 6–9 Å *Phys. Scr.* **27** 39–53

[25] Tragin N, Geindre J P, Monier P and Gauthier J C 1988 Extended analysis of the x-ray spectra of laser-irradiated elements in the sequence from tantalum to lead *Phys. Scr.* **37** 72–82

[26] Burkhalter P G, Dozier C M and Nagel D J 1977 X-ray spectra from exploded-wire plasmas *Phys. Rev.* A **15** 700–17

[27] Elliott S R, Beiersdorfer P, MacGowan B J and Nilsen J 1995 Measurements of line overlap for resonant spoiling of x-ray lasing transitions in nickel-like tungsten *Phys. Rev.* A **52** 2689–92

[28] Pütterich T, Neu R, Dux R, Whiteford A D, O'Mullane M G and the ASDEX Upgrade Team 2008 Modelling of measured tungsten spectra from ASDEX upgrade and predictions for ITER *Plasma Phys. Control. Fusion* **50** 1–27

[29] Ballance C P and Griffin D C 2006 Relativistic radiatively damped R-matrix calculation of the electron-impact excitation of W^{46+} *J. Phys. B: At. Mol. Opt. Phys.* **39** 3617–28

[30] Kramida A E and Shirai T 2009 Energy levels and spectral lines of tungsten, W III through W LXXIV *At. Data Nucl. Data Tables* **95** 305–474

[31] Brown G V, Hansen S B, Träbert E, Beiersdorfer P, Widmann K, Chen H, Chung H K, Clementson J H T, Gu M F and Thorn D B 2008 Investigation of the $2p_{3/2}$–$3d_{5/2}$ line emission of Au^{53+}-Au^{69+} for diagnosing high energy density plasmas *Phys. Rev.* E **77** 066406

[32] Levine M A, Marrs R E, Henderson J R, Knapp M B and Schneider D A 1988 The electron beam ion trap: a new instrument for atomic physics measurements *Phys. Scr.* T **22** 157–63

[33] Kramida A E and Reader J 2006 Ionization energies of tungsten ions: W^{2+} through W^{71+} *At. Data Nucl. Data Tables* **92** 457–79

[34] Porter F S *et al* 2004 The Astro-E2 x-ray spectrometer/EBIT microcalorimeter x-ray spectrometer *Rev. Sci. Instrum.* **75** 3772–4

[35] Brown G V *et al* 2006 Laboratory astrophysics and atomic physics using the NASA/GSFC microcalorimeter spectrometers at the LLNL electron beam ion trap and radiation properties facility *Nucl. Instrum. Methods Phys. Res.* A **559** 623–5

[36] Porter F S *et al* 2008 The XRS microcalorimeter spectrometer at the Livermore electron beam ion trap *Can. J. Phys.* **86** 231–40

[37] Gu M F 2008 The flexible atomic code *Can. J. Phys.* **86** 675–89

[38] Garcia J D and Mack J E 1965 Energy level and line tables for one-electron atomic spectra *J. Opt. Soc. Am.* **55** 654–85

[39] Drake G W 1988 Theoretical energies for the $n = 1$ and 2 states of the helium isoelectronic sequence up to $Z = 100$ *Can. J. Phys.* **66** 586–611

[40] Vainshtein L A and Safronova U I 1985 Energy levels of He- and Li-like ions (states $1snl$, $1s^2nl$ with $n = 2$–5) *Phys. Scr.* **31** 519–32

[41] Beiersdorfer P, Osterheld A L, Scofield J, Wargelin B and Marrs R E 1991 Observation of magnetic octupole decay in atomic spectra *Phys. Rev. Lett.* **67** 2272–5

[42] Clementson J, Beiersdorfer P and Gu M F 2009 X-ray spectroscopy of E2 and M3 transitions in Ni-like W *Phys. Rev.* A submitted

[43] Butzbach R *et al* 1999 Spatially resolved high resolution spectroscopy of 4f-3d emission lines of Ni- and Co-like ions from Yb, Hf, Ta and W x-ray plasmas Paper presented at *X-ray Lasers Conf, Kyoto, Japan, 31 August–4 September 1998*, no. 159 (Institute of Physics) p 463

[44] Wyart J-F, Bauche-Arnoult C, Gauthier J-C, Geindre J-P, Monier P, Klapisch M, Bar-Shalom A and Cohn A 1986 Density-sensitive electric quadrupole decays in Ni-like ions observed in laser-produced plasmas *Phys. Rev.* A **34** 701

Paper VI

Theoretical spectra of Ge-like through V-like W ions

J. Clementson[1,2], P. Beiersdorfer[1,3], T. Brage[2], and M. F. Gu[3]

[1] *Lawrence Livermore National Laboratory, Livermore, CA 94550, USA*

[2] *Department of Physics, Lund University, SE-221 00 Lund, Sweden*

[3] *Space Sciences Laboratory, University of California, Berkeley, CA 94720, USA*

Abstract

The atomic structure and spectra of ten tungsten ions have been calculated using the Flexible Atomic Code (FAC). In particular, the ions isoelectronic to germanium through vanadium have been investigated and the calculations yield energy levels, spectral line positions, transition probabilities, and line emissivities. These multi-electron heavy ions are of importance in nuclear fusion research where their spectra could provide diagnostics on magnetically confined plasmas

Preprint submitted to Atomic Data and Nuclear Data Tables *May 16, 2010*

Contents

List of Tables

List of Figures

1. Introduction

Tungsten is being implemented in magnetic fusion experiments as an erosion-resistant material on surfaces expected to receive high heat loads. Small amounts of tungsten sputters off these plasma-facing surfaces and enters into the plasmas. Energies in excess of 80 keV are required to strip the last of the seventy-four electrons from tungsten [1]. The core plasmas of present-day tokamak experiments have typical temperatures of a few keV, and tungsten particles that enter into these high-temperature plasmas will therefore ionize to M-shell charge states. Future machines, such as the ITER tokamak, will operate at temperatures around 25 keV [2, 3, 4, 5] and, consequently, the tungsten ionization balance will peak at the L-shell charge states. The tungsten emission from tokamaks could provide useful diagnostics of plasma parameters that are not otherwise easily assessable. For instance, it is likely that the ion temperatures of the ITER core plasmas will be measured by using the Doppler broadening of tungsten L-shell lines [5]. The M-shell line emission of tungsten can provide diagnostics for plasmas in current fusion experiments or in the initial ohmic phase of ITER.

M-shell spectra of highly charged tungsten ions have been observed at the ASDEX Upgrade tokamak [6, 7] and studied at electron beam ion traps at the Lawrence Livermore National Laboratory [8, 9, 10] and the National Institute of Standards and Technology [11], and at Z-pinches at the University of Nevada, Reno [9].

This paper presents *ab initio* atomic data on ten tungsten ions from germaniumlike W^{42+} through vanadiumlike W^{51+}, i.e. all the ions having ground configurations with $3d_{5/2}$, $4s_{1/2}$, and $4p_{1/2}$ valence electrons. The structure and dynamics are calculated by using the fully relativistic Flexible Atomic Code (FAC) [12, 13]. The atomic structure of these ions have been modeled up to $n = 6$ with closed K and L shells. The calculations yield energy levels, transition energies, wavelengths, oscillator strengths, and transition probabilities. The spectra have been calculated using collisional-radiative models, and autoionization for the germaniumlike through copperlike ions has been included. Line emissivities for the strong lines in a typical tokamak plasma are presented.

There have been several theoretical studies on M-shell tungsten, see e.g. [6, 7, 8, 9, 10, 11, 14, 15] of which the most comprehensive set of data is presented by Fournier, who modeled the spectra of Rb-like W^{37+} through Co-like W^{47+} [15]. In particular, the structure of Ni-like W^{46+} has been

extensively investigated by several authors using the codes RELAC [15], GRASP [16], DFS [17], RMBPT [18], Cowan [18], GRASP92 [19], and R-matrix [20]. The 106 energy levels with $3l4l'$ configurations calculated with FAC are listed with values from the seven previous calculations and compared to high-resolution measurements in Table 2.

Conversion factors used are $hc = 12398.42$ Å·eV $= 8065.5410$ eV·cm and 1 Ry $= 13.60569$ eV.

2. Structure calculations

The atomic structure and spectral modeling are performed by using the Flexible Atomic Code, FAC v1.1.1 [12, 13]. FAC is a fully relativistic package based on the Dirac equation for calculations of various atomic radiative and collisional parameters.

FAC calculates the atomic structure by diagonalizing the relativistic Hamiltonian which, in atomic units, can be written

$$H = \sum_{i=1}^{N} H_D(i) + \sum_{i<j}^{N} \frac{1}{r_{ij}}$$

where $H_D(i)$ describes the one-electron Dirac Hamiltonian. QED effects are included with the Breit interaction in the zero energy limit for the exchanged photon, and hydrogenic approximations for self-energy and vacuum polarization effects. The configuration state functions Φ consist of antisymmetric sums of products of N one-electron Dirac spinors $\varphi_{n\kappa m}$

$$\varphi_{n\kappa m} = \begin{pmatrix} P_{n\kappa}(r)\chi_{\kappa m}(\theta,\phi,\sigma) \\ iQ_{n\kappa}(r)\chi_{-\kappa m}(\theta,\phi,\sigma) \end{pmatrix}$$

where $\chi_{\kappa m}$ is the spin-angular function. The radial orbitals, $P_{n\kappa}$ and $Q_{n\kappa}$ are obtained using a Dirac-Fock-Slater method. The atomic state functions ψ are then constructed by summation of the configuration state functions of the same symmetry

$$\psi = \sum_{\nu} b_\nu \Phi_\nu$$

with b_ν being the mixing coefficient, which are derived by diagonalizing the Hamiltonian.

Line emissivities usually peak at energies higher than the temperature for which the abundance of the radiating ion is largest, and therefore the spectra are modeled at electron temperatures approximately 50 % above the peak abundance temperature. The charge balance for highly ionized tungsten has been calculated by Pütterich et al. [21]. The calculated line emissivities are listed in the tables where all transitions having emissivities larger than 1 % of the strongest line have been included. The full spectra are shown in Fig. 1, 2, 3, 4 with a resolution of 2 eV full width half maximum. All spectra are modeled at $n_e = 10^{14}$ cm^{-3}.

3. Summary

The atomic structure and spectra of the ten tungsten ions isoelectronic to germanium, W^{42+}, through vanadium, W^{51+}, have been calculated and modeled under tokamak plasma conditions. The work extends the database on highly charged tungsten ions relevant to tokamak plasma diagnostics from that of Fournier [15]. M-shell lines with $\Delta n = 0$, 1, 2, and 3 are calculated and presented together with some weaker N-shell transitions in the 1 - 4 keV x-ray range. The calculated wavelengths compare well with measurements, see e.g. the tungsten data compilation by Kramida and Shirai [22].

Acknowledgments

This work was performed under the auspices of the United States Department of Energy by Lawrence Livermore National Laboratory under Contract DE-AC52-07NA-27344 and supported by LLNL Laboratory Directed Research and Development Contract 09-ERD-016. The authors acknowledge assistance from Alexander Dixon. Joel Clementson would like to thank Dr. Hans Lundberg, Dr. Sven Huldt, and Prof. Sune Svanberg for their support.

[1] Kramida A E and Reader J 2006 *At. Data Nucl. Data Tables* **92** 457–479

[2] Peacock N J, O'Mullane M G, Barnsley R and Tarbutt M 2008 *Can. J. Phys.* **86** 277–284

[3] Skinner C H 2008 *Can. J. Phys.* **86** 285–290

[4] Skinner C H 2009 *Phys. Scr.* **T134** 014022

[5] Beiersdorfer P, Clementson J, Dunn J, Gu M F, Morris K, Podpaly Y, Wang E, Bitter M, Feder R, Hill K W, Johnson D and Barnsley R 2010 *J. Phys. B: At. Mol. Opt. Phys.* Submitted

[6] Neu R, Fournier K B, Schlögl D and Rice J 1997 *J. Phys. B: At. Mol. Opt. Phys.* **30** 5057–5067

[7] Neu R, Fournier K B, Bolshukhin D and Dux R 2001 *Phys. Scr.* **T92** 307–310

[8] Neill P, Harris C, Safronova A S, Hamasha S, Hansen S, Safronova U I and Beiersdorfer P 2004 *Can. J. Phys.* **82** 931–942

[9] Safronova A S, Kantsyrev V L, Neill P, Safronova U I, Fedin D A, Ouart N D, Yilmaz M F, Osborne G, Shrestha I, Williamson K, Hoppe T, Harris C, Beiersdorfer P and Hansen S 2008 *Can. J. Phys.* **86** 267–276

[10] Clementson J, Beiersdorfer P, Brown G V and Gu M F 2010 *Phys. Scr.* **81** 015301

[11] Ralchenko Y, Tan J N, Gillaspy J D and Pomeroy J M 2006 *Phys. Rev. A* **74** 042514

[12] Gu M F 2004 *AIP Conf. Proc.* **730** 127–136

[13] Gu M F 2008 *Can. J. Phys.* **86** 675–689

[14] Osborne G C, Safronova A S, Kantsyrev V L, Safronova U I, Yilmaz M F, Williamson K M, Shrestha I and Beiersdorfer P 2008 *Rev. Sci. Instrum.* **79** 10E308

[15] Fournier K B 1998 *At. Data Nucl. Data Tables* **68** 1–48

[16] Aggarwal K M, Norrington P H, Bell K L, Keenan F P, Pert G J and Rose S J 2000 *At. Data Nucl. Data Tables* **74** 157–255

[17] Zhang H L, Sampson D H and Fontes C J 1991 *At. Data Nucl. Data Tables* **48** 91–163

[18] Safronova U I, Safronova A S, Hamasha S M and Beiersdorfer P 2006 *At. Data Nucl. Data Tables* **92** 47–104

[19] Dong C Z, Fritzsche S and Xie L Y 2003 *J. Quant. Spectr. Rad. Transfer* **76** 447

[20] Ballance C P and Griffin D C 2006 *J. Phys. B: At. Mol. Opt. Phys.* **39** 3617–3628

[21] Pütterich T, Neu R, Dux R, Whiteford A D, O'Mullane M G and the ASDEX Upgrade team 2008 *Plasma Phys. Control. Fusion* **50** 085016

[22] Kramida A E and Shirai T 2009 *At. Data Nucl. Data Tables* **95** 305–474

[23] Clementson J, Beiersdorfer P and Gu M F 2010 *Phys. Rev. A* **81** 012505

[24] Elliott S R, Beiersdorfer P, MacGowan B J and Nilsen J 1995 *Phys. Rev. A* **52** 2689–2692

Explanation of tables

Table 1. Configuration state functions

Configuration state functions used in the modeling of each ion.

n	principal quantum number, n = 4, 5, 6
n^*	principal quantum number, n^* = 4, 5
l	electron angular momentum, l = 0, 1, ..., n - 1
l^*	electron angular momentum, l^* = *s, p*

Table 2. Comparison of energy levels in Ni-like W^{46+}

Energies of the atomic state functions with $3l4l'$ configurations. Present FAC calculations compared with results from the RELAC [15], GRASP [16], DFS [17], RMBPT [18], Cowan [18], GRASP92 [19], and R-matrix [20] codes, and experiment energy levels.

Table 3. Energy levels in Ga-like W^{43+}

Energy levels to which the radiative transitions of Table 4 connect.

Index	energy level number
Configuration	electron configuration in jj coupling
J	total electronic angular momentum in $\hbar$
Energy	energy in electron volt (eV)

Table 4. Radiative transitions in Ga-like W^{43+}

Radiative transitions in the Zn-like W^{44+} spectrum for lines in the 1 - 4 keV x-ray interval with intensities higher than 1 % of the strongest line.

i, k	lower and upper energy level index, respectively, as defined in Table 3
ΔE	transition energy in electron volt (eV)
λ	wavelength in ångström (Å)
gf	weighted absorption oscillator strength, g = 2J + 1
A_{ki}	transition probability from level k to level i in per second (s^{-1})
ϵ_{line}	line emissivity in photons per ion per second ($ion^{-1}s^{-1}$)

Table 5. Energy levels in Zn-like W^{44+}

Energy levels to which the radiative transitions of Table 6 connect.

Index	energy level number
Configuration	electron configuration in jj coupling
J	total electronic angular momentum in $\hbar$
Energy	energy in electron volt (eV)

Table 6. Radiative transitions in Zn-like W^{44+}

Radiative transitions in the Zn-like W^{44+} spectrum for lines in the 1 - 4 keV x-ray interval with intensities higher than 1 % of the strongest line.

i, k	lower and upper energy level index, respectively, as defined in Table 5
ΔE	transition energy in electron volt (eV)
λ	wavelength in ångström (Å)
gf	weighted absorption oscillator strength, g = 2J + 1
A_{ki}	transition probability from level k to level i in per second (s^{-1})
ϵ_{line}	line emissivity in photons per ion per second ($ion^{-1}s^{-1}$)

Table 7. Energy levels in Cu-like W^{45+}

Energy levels to which the radiative transitions of Table 8 connect.

Index	energy level number
Configuration	electron configuration in jj coupling
J	total electronic angular momentum in $\hbar$
Energy	energy in electron volt (eV)

Table 8. Radiative transitions in Cu-like W^{45+}

Radiative transitions in the Cu-like W^{45+} spectrum for lines in the 1 - 4 keV x-ray interval with intensities higher than 1 % of the strongest line.

i, k	lower and upper energy level index, respectively, as defined in Table 7
ΔE	transition energy in electron volt (eV)
λ	wavelength in ångström (Å)
gf	weighted absorption oscillator strength, g = 2J + 1
A_{ki}	transition probability from level k to level i in per second (s^{-1})
ϵ_{line}	line emissivity in photons per ion per second ($ion^{-1}s^{-1}$)

Table 9. Energy levels in Ni-like W^{46+}

Energy levels to which the radiative transitions of Table 10 connect.

Index	energy level number
Configuration	electron configuration in jj coupling
J	total electronic angular momentum in $\hbar$
Energy	energy in electron volt (eV)

Table 10. Radiative transitions in Ni-like W^{46+}

Radiative transitions in the Ni-like W^{46+} spectrum for lines in the 1 - 4 keV x-ray interval with intensities higher than 1 % of the strongest line.

i, k	lower and upper energy level index, respectively, as defined in Table 9
ΔE	transition energy in electron volt (eV)
λ	wavelength in ångström (Å)
gf	weighted absorption oscillator strength, g = 2J + 1
A_{ki}	transition probability from level k to level i in per second (s^{-1})
ϵ_{line}	line emissivity in photons per ion per second ($ion^{-1}s^{-1}$)

Table 11. Energy levels in Co-like W^{47+}

Energy levels to which the radiative transitions of Table 12 connect.

Index	energy level number
Configuration	electron configuration in jj coupling
J	total electronic angular momentum in $\hbar$
Energy	energy in electron volt (eV)

Table 12. Radiative transitions in Co-like W^{47+}

Radiative transitions in the Co-like W^{47+} spectrum for lines in the 1 - 4 keV x-ray interval with intensities higher than 1 % of the strongest line.

i, k	lower and upper energy level index, respectively, as defined in Table 11
ΔE	transition energy in electron volt (eV)
λ	wavelength in ångström (Å)
gf	weighted absorption oscillator strength, g = 2J + 1
A_{ki}	transition probability from level k to level i in per second (s^{-1})
ϵ_{line}	line emissivity in photons per ion per second ($ion^{-1}s^{-1}$)

Table 13. Energy levels in Fe-like W^{48+}

Energy levels to which the radiative transitions of Table 14 connect.

Index	energy level number
Configuration	electron configuration in jj coupling
J	total electronic angular momentum in $\hbar$
Energy	energy in electron volt (eV)

Table 14. Radiative transitions in Fe-like W^{48+}

Radiative transitions in the Fe-like W^{48+} spectrum for lines in the 1 - 4 keV x-ray interval with intensities higher than 1 % of the strongest line.

i, k	lower and upper energy level index, respectively, as defined in Table 13
ΔE	transition energy in electron volt (eV)
λ	wavelength in ångström (Å)
gf	weighted absorption oscillator strength, g = 2J + 1
A_{ki}	transition probability from level k to level i in per second (s^{-1})
ϵ_{line}	line emissivity in photons per ion per second ($ion^{-1}s^{-1}$)

Explanation of figures

Figure 1. Zn-like W^{44+}

The 1 - 4 keV spectrum of zinclike W XLV at an electron temperature of 3180 eV. Spectral resolution is 2 eV fwhm.

Figure 2. Cu-like W^{45+}

The 1 - 4 keV spectrum of copperlike W XLVI at an electron temperature of 3550 eV. Spectral resolution is 2 eV fwhm.

Figure 3. Ni-like W^{46+}

The 1 - 4 keV spectrum of nickellike W XLVII at an electron temperature of 4250 eV. Spectral resolution is 2 eV fwhm.

Figure 4. Co-like W^{47+}

The 1 - 4 keV spectrum of cobaltlike W XLVIII at an electron temperature of 5180 eV. Spectral resolution is 2 eV fwhm.

Figure 5. Fe-like W^{48+}

The 1 - 4 keV spectrum of ironlike W XLIX at an electron temperature of 5830 eV. Spectral resolution is 2 eV fwhm.

Table 1: Configuration state functions

Zn-like W^{44+}	Cu-like W^{45+}	Ni-like W^{46+}	Co-like W^{47+}
$3s^2 3p^6 3d^{10} 4lnl$	$3s^2 3p^6 3d^{10} nl$	$3s^2 3p^6 3d^{10}$	$3s^2 3p^6 3d^9$
			$3s^2 3p^5 3d^{10}$
			$3s3p^6 3d^{10}$
$3s^2 3p^6 3d^9 4l4l4l$	$3s^2 3p^6 3d^9 4l4l$	$3s^2 3p^6 3d^9 nl$	$3s^2 3p^6 3d^8 nl$
$3s^2 3p^6 3d^9 4l^* 4l^* nl$	$3s^2 3p^6 3d^9 4l^* nl$		$3s^2 3p^5 3d^9 nl$
			$3s3p^6 3d^9 nl$
$3s^2 3p^5 3d^{10} 4l4l4l$	$3s^2 3p^5 3d^{10} 4l4l$	$3s^2 3p^5 3d^{10} nl$	$3s^2 3p^5 3d^9 nl$
$3s^2 3p^5 3d^{10} 4l^* 4l^* nl$	$3s^2 3p^5 3d^{10} 4l^* nl$		$3s^2 3p^4 3d^{10} nl$
			$3s3p^5 3d^{10} nl$
$3s3p^6 3d^{10} 4l4l4l$	$3s3p^6 3d^{10} 4l4l$	$3s3p^6 3d^{10} nl$	$3s3p^6 3d^9 nl$
$3s3p^6 3d^{10} 4l^* 4l^* nl$	$3s3p^6 3d^{10} 4l^* nl$		$3s3p^5 3d^{10} nl$
			$3p^6 3d^{10} nl$

Fe-like W^{48+}	Mn-like W^{49+}	Cr-like W^{50+}	V-like W^{51+}
$3s^2 3p^6 3d^8$	$3s^2 3p^6 3d^7$	$3s^2 3p^6 3d^6$	$3s^2 3p^6 3d^5$
$3s^2 3p^6 3d^7 nl$	$3s^2 3p^6 3d^6 nl$	$3s^2 3p^6 3d^5 n^* l$	$3s^2 3p^6 3d^4 n^* l$
$3s^2 3p^5 3d^9$	$3s^2 3p^5 3d^8$	$3s^2 3p^5 3d^7$	$3s^2 3p^5 3d^6$
$3s^2 3p^5 3d^8 nl$	$3s^2 3p^5 3d^7 nl$	$3s^2 3p^5 3d^6 n^* l$	$3s^2 3p^5 3d^5 n^* l$
$3s3p^6 3d^9$	$3s3p^6 3d^8$	$3s3p^6 3d^7$	$3s3p^6 3d^6$
$3s3p^6 3d^8 nl$	$3s3p^6 3d^7 nl$	$3s3p^6 3d^6 n^* l$	$3s3p^6 3d^5 n^* l$

Table 2: Comparison of energy levels in Ni-like W^{46+}

Level	FAC[a]	RELAC[b]	GRASP[c]	DFS[d]	RMBPT[e]	Cowan[e]	GRASP92[f]	R-matrix[g]	Experiment
$(3s^23p^63d^4_{3/2}3d^5_{5/2}4s_{1/2})_{J=3}$	1562.15	1560.56	1559.78	1560.0				1560.31	1562.0(1)[h]
$(3s^23p^63d^4_{3/2}3d^5_{5/2}4s_{1/2})_{J=2}$	1564.07	1562.43	1561.67	1561.9	1563.63	1566.49	1561.11	1562.14	1563.9(1)[h]
$(3s^23p^63d^3_{3/2}3d^6_{5/2}4s_{1/2})_{J=1}$	1628.75	1627.15	1626.11	1626.4	1628.42	1633.09	1625.54	1627.99	
$(3s^23p^63d^3_{3/2}3d^6_{5/2}4s_{1/2})_{J=2}$	1629.99	1628.49	1627.33	1627.7	1629.62	1634.19	1626.77	1629.28	1629.8(3)[i]
$(3s^23p^63d^4_{3/2}3d^5_{5/2}4p_{1/2})_{J=2}$	1658.59	1657.56	1656.96	1657.2				1657.24	
$(3s^23p^63d^4_{3/2}3d^5_{5/2}4p_{1/2})_{J=3}$	1659.78	1658.96	1658.13	1658.4				1658.62	
$(3s^23p^63d^3_{3/2}3d^6_{5/2}4p_{1/2})_{J=2}$	1725.20	1724.42	1723.30	1723.7				1725.20	
$(3s^23p^63d^3_{3/2}3d^6_{5/2}4p_{1/2})_{J=1}$	1728.69	1727.77	1726.72	1727.1	1728.13	1730.57	1727.19	1728.49	1728.4(1)[j]
$(3s^23p^63d^4_{3/2}3d^5_{5/2}4p_{3/2})_{J=4}$	1761.59	1760.75	1759.74	1760.0				1761.41	
$(3s^23p^63d^4_{3/2}3d^5_{5/2}4p_{3/2})_{J=2}$	1763.58	1762.58	1761.72	1762.0				1763.20	
$(3s^23p^63d^4_{3/2}3d^5_{5/2}4p_{3/2})_{J=1}$	1764.83	1763.75	1762.83	1763.2	1764.28	1769.03	1763.20	1764.30	1764.6(3)[i]
$(3s^23p^63d^4_{3/2}3d^5_{5/2}4p_{3/2})_{J=3}$	1766.79	1765.85	1764.91	1765.3				1766.41	
$(3s^23p^63d^3_{3/2}3d^6_{5/2}4p_{3/2})_{J=0}$	1824.86	1823.75	1822.76	1823.1				1825.53	
$(3s^23p^63d^3_{3/2}3d^6_{5/2}4p_{3/2})_{J=1}$	1829.45	1828.51	1827.31	1827.7	1829.11	1835.58	1827.68	1830.20	1829.6(4)[i]
$(3s^23p^63d^3_{3/2}3d^6_{5/2}4p_{3/2})_{J=3}$	1829.69	1828.94	1827.55	1828.0				1830.62	
$(3s^23p^63d^3_{3/2}3d^6_{5/2}4p_{3/2})_{J=2}$	1832.38	1831.51	1830.25	1830.7				1833.16	
$(3s^23p^63d^4_{3/2}3d^5_{5/2}4d_{3/2})_{J=1}$	1904.93		1903.61	1903.6	1905.12	1906.70	1904.04	1905.40	
$(3s^23p^63d^4_{3/2}3d^5_{5/2}4d_{3/2})_{J=4}$	1909.87	1909.42	1908.52	1908.7				1910.72	
$(3s^23p^63d^4_{3/2}3d^5_{5/2}4d_{3/2})_{J=2}$	1911.28	1910.56	1909.95	1910.1	1911.15	1912.01	1910.42	1911.89	
$(3s^23p^63d^4_{3/2}3d^5_{5/2}4d_{3/2})_{J=3}$	1913.62	1912.99	1912.29	1912.5				1914.27	
$(3s^23p^63d^4_{3/2}3d^5_{5/2}4d_{5/2})_{J=1}$	1928.92	1928.29	1927.54	1927.6	1928.93	1931.14	1927.99	1930.16	
$(3s^23p^63d^4_{3/2}3d^5_{5/2}4d_{5/2})_{J=5}$	1930.53	1930.10	1929.14	1929.3				1931.91	
$(3s^23p^63d^4_{3/2}3d^5_{5/2}4d_{5/2})_{J=3}$	1934.49	1933.83	1933.12	1933.3				1935.63	
$(3s^23p^63d^4_{3/2}3d^5_{5/2}4d_{5/2})_{J=2}$	1935.73	1934.92	1934.32	1934.5	1935.68	1936.68	1934.79	1936.66	

[a]This work, [b]Fournier [15], [c]Aggarwal *et al.* [16], [d]Zhang *et al.* [17], [e]Safronova *et al.* [18], [f]Dong *et al.* [19], [g]Ballance and Griffin [20], [h]Clementson *et al.* [23], [i]Clementson *et al.* [10], [j]Elliottt *et al.* [24]

Table 2 –Comparison of energy levels in Ni-like W^{46+} continued

Level	FAC[a]	RELAC[b]	GRASP[c]	DFS[d]	RMBPT[e]	Cowan[e]	GRASP92[f]	R-matrix[g]	Experiment
$(3s^23p^63d^4_{3/2}3d^5_{5/2}4d_{5/2})_{J=4}$	1936.39	1935.80	1935.02	1935.2				1937.55	
$(3s^23p^63d^4_{3/2}3d^5_{5/2}4d_{5/2})_{J=0}$	1950.97		1949.40	1949.4	1950.09	1951.18	1950.30	1951.85	
$(3s^23p^63d^3_{3/2}3d^6_{5/2}4d_{3/2})_{J=1}$	1975.52	1974.96	1973.92	1974.1	1975.38	1978.41	1974.37	1977.42	
$(3s^23p^63d^3_{3/2}3d^6_{5/2}4d_{3/2})_{J=3}$	1975.86	1975.42	1974.25	1974.5				1977.85	
$(3s^23p^63d^3_{3/2}3d^6_{5/2}4d_{3/2})_{J=2}$	1981.68	1981.07	1980.05	1980.4	1981.35	1983.41	1980.53	1983.42	
$(3s^23p^63d^3_{3/2}3d^6_{5/2}4d_{5/2})_{J=1}$	1995.63	1994.76	1993.98	1994.2	1995.72	1999.19	1994.43	1997.68	
$(3s^23p^63d^3_{3/2}3d^6_{5/2}4d_{5/2})_{J=4}$	1998.76	1998.40	1997.09	1997.4				2001.23	
$(3s^23p^63d^3_{3/2}3d^6_{5/2}4d_{5/2})_{J=2}$	2000.54	1999.94	1998.89	1999.2	2000.47	2003.59	1999.37	2002.78	
$(3s^23p^63d^3_{3/2}3d^6_{5/2}4d_{5/2})_{J=3}$	2002.43	2001.90	2000.80	2001.1				2004.72	
$(3s^23p^2_{1/2}3p^3_{3/2}3d^{10}4s_{1/2})_{J=2}$	2014.09		2013.25	2012.9				2016.40	
$(3s^23p^2_{1/2}3p^3_{3/2}3d^{10}4s_{1/2})_{J=1}$	2017.39	2017.16	2016.49	2016.3	2179.24	2179.98	2016.34	2019.67	2015.4(3)[i]
$(3s^23p^63d^3_{3/2}3d^6_{5/2}4d_{3/2})_{J=0}$	2023.02		2020.82	2019.1	2014.93	2012.11	2018.84	2023.44	
$(3s^23p^63d^4_{3/2}3d^5_{5/2}4f_{5/2})_{J=0}$	2080.57		2078.65	2078.8				2081.09	
$(3s^23p^63d^4_{3/2}3d^5_{5/2}4f_{5/2})_{J=1}$	2083.49		2081.63	2081.8	2014.60	2008.01	2082.36	2084.36	
$(3s^23p^63d^4_{3/2}3d^5_{5/2}4f_{5/2})_{J=5}$	2087.56	2086.79	2085.84	2086.0				2089.11	
$(3s^23p^63d^4_{3/2}3d^5_{5/2}4f_{5/2})_{J=2}$	2088.32		2086.59	2091.8				2089.41	
$(3s^23p^63d^4_{3/2}3d^5_{5/2}4f_{5/2})_{J=3}$	2091.47		2089.86	2090.1				2092.83	
$(3s^23p^63d^4_{3/2}3d^5_{5/2}4f_{7/2})_{J=6}$	2091.83	2090.88	2089.97	2090.1				2093.55	
$(3s^23p^63d^4_{3/2}3d^5_{5/2}4f_{5/2})_{J=4}$	2092.57		2091.01	2091.2				2093.98	
$(3s^23p^63d^4_{3/2}3d^5_{5/2}4f_{7/2})_{J=2}$	2093.33	2092.08	2091.58	2086.8				2094.72	
$(3s^23p^63d^4_{3/2}3d^5_{5/2}4f_{7/2})_{J=4}$	2097.39	2096.35	2095.72	2095.9				2099.05	
$(3s^23p^63d^4_{3/2}3d^5_{5/2}4f_{7/2})_{J=5}$	2098.85	2097.93	2097.24	2097.5				2100.58	
$(3s^23p^63d^4_{3/2}3d^5_{5/2}4f_{7/2})_{J=3}$	2099.46	2098.44	2097.93	2098.2				2101.07	
$(3s^23p^2_{1/2}3p^3_{3/2}3d^{10}4p_{1/2})_{J=1}$	2111.07		2110.94	2110.7	2108.29	2100.07	2111.77	2113.96	
$(3s^23p^2_{1/2}3p^3_{3/2}3d^{10}4p_{1/2})_{J=2}$	2112.04	2112.55	2111.90	2111.7	2109.42	2101.01	2112.74	2115.19	

[a]This work, [b]Fournier [15], [c]Aggarwal *et al.* [16], [d]Zhang *et al.* [17], [e]Safronova *et al.* [18], [f]Dong *et al.* [19], [g]Ballance and Griffin [20], [h]Clementson *et al.* [23], [i]Clementson *et al.* [10], [j]Elliottt *et al.* [24]

Table 2 –Comparison of energy levels in Ni-like W^{46+} continued

Level	FAC[a]	RELAC[b]	GRASP[c]	DFS[d]	RMBPT[e]	Cowan[e]	GRASP92[f]	R-matrix[g]	Experiment
$(3s^23p^63d^4_{3/2}3d^5_{5/2}4f_{7/2})_{J=1}$	2112.57	2111.56	2111.25	2111.2	2082.89	2085.17	2111.54	2114.56	2112.2(3)[i]
$(3s^23p^63d^3_{3/2}3d^6_{5/2}4f_{5/2})_{J=4}$	2153.90		2151.84	2152.1				2156.39	
$(3s^23p^63d^3_{3/2}3d^6_{5/2}4f_{5/2})_{J=2}$	2155.36	2154.16	2153.29	2157.0				2157.71	
$(3s^23p^63d^3_{3/2}3d^6_{5/2}4f_{7/2})_{J=2}$	2158.70		2156.68	2153.6				2161.22	
$(3s^23p^63d^3_{3/2}3d^6_{5/2}4f_{7/2})_{J=5}$	2160.84		2158.83	2159.1				2163.69	
$(3s^23p^63d^3_{3/2}3d^6_{5/2}4f_{5/2})_{J=3}$	2160.93	2160.04	2159.11	2162.4				2163.51	
$(3s^23p^63d^3_{3/2}3d^6_{5/2}4f_{7/2})_{J=3}$	2163.93		2162.05	2159.5				2166.72	
$(3s^23p^63d^3_{3/2}3d^6_{5/2}4f_{7/2})_{J=4}$	2165.25		2163.39	2163.7				2168.12	
$(3s^23p^63d^3_{3/2}3d^6_{5/2}4f_{5/2})_{J=1}$	2181.36	2181.55	2180.88	2180.3	2112.08	2112.57	2180.36	2185.81	2179.7(4)[i]
$(3s^23p^2_{1/2}3p^3_{3/2}3d^{10}4p_{3/2})_{J=3}$	2213.58		2213.24	2213.0				2217.75	
$(3s^23p^2_{1/2}3p^3_{3/2}3d^{10}4p_{3/2})_{J=1}$	2213.69		2213.34	2213.1	2211.16	2206.94	2214.07	2217.63	
$(3s^23p^2_{1/2}3p^3_{3/2}3d^{10}4p_{3/2})_{J=2}$	2218.82		2218.45	2218.3	2216.14	2211.26	2219.18	2222.68	
$(3s^23p^2_{1/2}3p^3_{3/2}3d^{10}4p_{3/2})_{J=0}$	2239.71		2238.60	2237.2	2317.37	2326.18	2238.19	2242.37	
$(3s^23p_{1/2}3p^4_{3/2}3d^{10}4s_{1/2})_{J=0}$	2321.22		2319.65	2319.4				2326.08	
$(3s^23p_{1/2}3p^4_{3/2}3d^{10}4s_{1/2})_{J=1}$	2323.64		2322.00	2321.9	2319.63	2328.54	2321.55	2328.61	2320.3(6)[i]
$(3s^23p^2_{1/2}3p^3_{3/2}3d^{10}4d_{3/2})_{J=0}$	2358.45		2358.57	2358.2				2363.09	
$(3s^23p^2_{1/2}3p^3_{3/2}3d^{10}4d_{3/2})_{J=1}$	2361.82		2361.97	2361.6	2359.39	2351.37	2362.85	2366.61	2360.7(7)[i]
$(3s^23p^2_{1/2}3p^3_{3/2}3d^{10}4d_{3/2})_{J=3}$	2362.53		2362.70	2362.3				2367.57	
$(3s^23p^2_{1/2}3p^3_{3/2}3d^{10}4d_{3/2})_{J=2}$	2365.62		2365.81	2365.5				2370.45	
$(3s^23p^2_{1/2}3p^3_{3/2}3d^{10}4d_{5/2})_{J=4}$	2383.45		2383.58	2383.2				2388.94	
$(3s^23p^2_{1/2}3p^3_{3/2}3d^{10}4d_{5/2})_{J=2}$	2385.43	2386.10	2385.58	2385.2				2390.72	
$(3s^23p^2_{1/2}3p^3_{3/2}3d^{10}4d_{5/2})_{J=1}$	2386.03	2386.88	2386.10	2385.8	2383.71	2375.77	2386.98	2391.43	2384.2(4)[i]
$(3s^23p^2_{1/2}3p^3_{3/2}3d^{10}4d_{5/2})_{J=3}$	2388.63	2389.38	2388.78	2388.5				2393.99	
$(3s^23p_{1/2}3p^4_{3/2}3d^{10}4p_{1/2})_{J=1}$	2418.84		2417.94	2417.8	2414.80	2422.70	2418.47	2424.79	
$(3s^23p_{1/2}3p^4_{3/2}3d^{10}4p_{1/2})_{J=0}$	2435.61		2434.62	2433.5	2356.07	2348.76	2434.60	2440.82	

[a]This work, [b]Fournier [15], [c]Aggarwal *et al.* [16], [d]Zhang *et al.* [17], [e]Safronova *et al.* [18], [f]Dong *et al.* [19], [g]Ballance and Griffin [20], [h]Clementson *et al.* [23], [i]Clementson *et al.* [10], [j]Elliottt *et al.* [24]

Table 2 –Comparison of energy levels in Ni-like W^{46+} continued

Level	FAC[a]	RELAC[b]	GRASP[c]	DFS[d]	RMBPT[e]	Cowan[e]	GRASP92[f]	R-matrix[g]	Experiment
$(3s^2 3p_{1/2} 3p^4_{3/2} 3d^{10} 4p_{3/2})_{J=1}$	2520.34		2519.32	2519.2	2515.94	2524.28	2519.91	2526.92	
$(3s^2 3p_{1/2} 3p^4_{3/2} 3d^{10} 4p_{3/2})_{J=2}$	2523.83		2522.71	2522.6	2519.55	2528.01	2523.16	2530.67	
$(3s^2 3p^2_{1/2} 3p^3_{3/2} 3d^{10} 4f_{5/2})_{J=1}$	2534.39		2534.18	2730.6	2531.52	2527.98	2535.02	2539.95	
$(3s^2 3p^2_{1/2} 3p^3_{3/2} 3d^{10} 4f_{5/2})_{J=2}$	2539.17		2539.03	2721.8	2536.68	2532.10	2539.92	2544.89	
$(3s^2 3p^2_{1/2} 3p^3_{3/2} 3d^{10} 4f_{5/2})_{J=4}$	2539.97		2539.93	2721.0				2545.76	
$(3s^2 3p^2_{1/2} 3p^3_{3/2} 3d^{10} 4f_{7/2})_{J=5}$	2543.35		2543.15	2731.2				2549.31	
$(3s^2 3p^2_{1/2} 3p^3_{3/2} 3d^{10} 4f_{5/2})_{J=3}$	2543.78		2543.81	2732.9				2549.49	
$(3s^2 3p^2_{1/2} 3p^3_{3/2} 3d^{10} 4f_{7/2})_{J=3}$	2547.29	2547.67	2547.23	2722.7				2553.24	
$(3s^2 3p^2_{1/2} 3p^3_{3/2} 3d^{10} 4f_{7/2})_{J=4}$	2551.01	2551.54	2551.06	2733.7				2557.04	
$(3s^2 3p^2_{1/2} 3p^3_{3/2} 3d^{10} 4f_{7/2})_{J=2}$	2554.73	2555.61	2555.02	2733.3	2552.02	2543.59	2555.80	2560.99	2553.0(4)[i]
$(3s_{1/2} 3p^6 3d^{10} 4s_{1/2})_{J=1}$	2565.06		2565.52	2565.3	2560.48	2563.93	2568.24	2572.10	
$(3s_{1/2} 3p^6 3d^{10} 4s_{1/2})_{J=0}$	2574.71		2574.91	2573.5	2566.74	2570.08	2577.40	2581.20	
$(3s_{1/2} 3p^6 3d^{10} 4p_{1/2})_{J=1}$	2655.04		2655.62	2717.3	2674.81	2679.58	2658.89	2662.52	2651.3(4)[i]
$(3s_{1/2} 3p^6 3d^{10} 4p_{1/2})_{J=0}$	2659.22		2660.50	2715.5				2666.70	
$(3s^2 3p_{1/2} 3p^4_{3/2} 3d^{10} 4d_{3/2})_{J=2}$	2671.08		2670.49	2691.2				2680.35	
$(3s^2 3p_{1/2} 3p^4_{3/2} 3d^{10} 4d_{3/2})_{J=1}$	2678.60		2678.64	2678.5	2649.66	2653.45	2679.89	2686.23	2673.7(6)[i]
$(3s^2 3p_{1/2} 3p^4_{3/2} 3d^{10} 4d_{5/2})_{J=2}$	2692.05		2691.45	2718.6				2699.91	
$(3s^2 3p_{1/2} 3p^4_{3/2} 3d^{10} 4d_{5/2})_{J=3}$	2694.08		2693.44	2717.8				2701.63	
$(3s_{1/2} 3p^6 3d^{10} 4p_{3/2})_{J=2}$	2763.90		2764.93	2804.2				2772.54	
$(3s_{1/2} 3p^6 3d^{10} 4p_{3/2})_{J=1}$	2765.65		2766.65	2814.9	2760.14	2765.51	2770.49	2774.21	2760.7(5)[i]
$(3s^2 3p_{1/2} 3p^4_{3/2} 3d^{10} 4f_{5/2})_{J=3}$	2848.83		2847.91	2909.6				2857.14	
$(3s^2 3p_{1/2} 3p^4_{3/2} 3d^{10} 4f_{5/2})_{J=2}$	2853.66		2853.03	2909.0			2853.62	2863.02	
$(3s^2 3p_{1/2} 3p^4_{3/2} 3d^{10} 4f_{7/2})_{J=3}$	2854.06		2853.14	2910.4				2863.29	
$(3s^2 3p_{1/2} 3p^4_{3/2} 3d^{10} 4f_{7/2})_{J=4}$	2856.17		2855.31	2911.1				2864.84	
$(3s_{1/2} 3p^6 3d^{10} 4d_{3/2})_{J=1}$	2910.52		2912.10	2911.9	2905.76	2907.09	2916.03		
$(3s_{1/2} 3p^6 3d^{10} 4d_{3/2})_{J=2}$	2911.83		2913.37	2913.3	2907.15	2908.30	2917.27		

[a]This work, [b]Fournier [15], [c]Aggarwal *et al.* [16], [d]Zhang *et al.* [17], [e]Safronova *et al.* [18], [f]Dong *et al.* [19], [g]Ballance and Griffin [20], [h]Clementson *et al.* [23], [i]Clementson *et al.* [10], [j]Elliottt *et al.* [24]

Table 2 –Comparison of energy levels in Ni-like W^{46+} continued

Level	FAC[a]	RELAC[b]	GRASP[c]	DFS[d]	RMBPT[e]	Cowan[e]	GRASP92[f]	R-matrix[g]	Experiment
$(3s_{1/2}3p^6 3d^{10}4d_{5/2})_{J=3}$	2933.06		2934.59	2934.4					
$(3s_{1/2}3p^6 3d^{10}4d_{5/2})_{J=2}$	2933.97		2935.49	2935.3	2929.26	2931.22	2939.44		
$(3s_{1/2}3p^6 3d^{10}4f_{5/2})_{J=2}$	3087.27		3088.59	3087.8					
$(3s_{1/2}3p^6 3d^{10}4f_{5/2})_{J=3}$	3088.49		3089.83	3089.1					
$(3s_{1/2}3p^6 3d^{10}4f_{7/2})_{J=4}$	3092.88		3094.15	3093.4					
$(3s_{1/2}3p^6 3d^{10}4f_{7/2})_{J=3}$	3097.32		3098.81	3098.2					

[a]This work, [b]Fournier [15], [c]Aggarwal *et al.* [16], [d]Zhang *et al.* [17], [e]Safronova *et al.* [18], [f]Dong *et al.* [19], [g]Ballance and Griffin [20], [h]Clementson *et al.* [23], [i]Clementson *et al.* [10], [j]Elliottt *et al.* [24]

Table 3: Energy levels in Ga-like W^{43+}

Index	Configuration	J	Energy (eV)
0	$3s^2 3p^6 3d^{10} 4s^2 4p_{1/2}$	1/2	0.0
1	$3s^2 3p^6 3d^{10} 4s_{1/2} 4p_{1/2}^2$	1/2	96.7
2	$3s^2 3p^6 3d^{10} 4s^2 4p_{3/2}$	3/2	98.1
3	$3s^2 3p^6 3d^{10} 4s_{1/2} 4p_{1/2} 4p_{3/2}$	3/2	181.2
4	$3s^2 3p^6 3d^{10} 4s_{1/2} 4p_{1/2} 4p_{3/2}$	5/2	189.9
5	$3s^2 3p^6 3d^{10} 4s_{1/2} 4p_{1/2} 4p_{3/2}$	3/2	202.3
6	$3s^2 3p^6 3d^{10} 4s_{1/2} 4p_{1/2} 4p_{3/2}$	1/2	205.3
7	$3s^2 3p^6 3d^{10} 4s^2 4d_{3/2}$	3/2	259.5
8	$3s^2 3p^6 3d^{10} 4s^2 4d_{5/2}$	5/2	273.3
11	$3s^2 3p^6 3d^{10} 4s_{1/2} 4p_{3/2}^2$	1/2	303.0
12	$3s^2 3p^6 3d^{10} 4s_{1/2} 4p_{3/2}^2$	3/2	307.2
14	$3s^2 3p^6 3d^{10} 4s_{1/2} 4p_{1/2} 4d_{3/2}$	5/2	341.6
19	$3s^2 3p^6 3d^{10} 4s_{1/2} 4p_{1/2} 4d_{5/2}$	5/2	374.0
20	$3s^2 3p^6 3d^{10} 4s_{1/2} 4p_{1/2} 4d_{5/2}$	3/2	374.0
24	$3s^2 3p^6 3d^{10} 4s_{1/2} 4p_{3/2} 4d_{3/2}$	5/2	439.9
34	$3s^2 3p^6 3d^{10} 4s_{1/2} 4p_{3/2} 4d_{3/2}$	1/2	465.5
35	$3s^2 3p^6 3d^{10} 4s_{1/2} 4p_{3/2} 4d_{5/2}$	3/2	466.7
687	$3s^2 3p^6 3d^{10} 4s^2 5d_{3/2}$	3/2	1010.1
689	$3s^2 3p^6 3d^{10} 4s_{1/2} 4p_{1/2} 5p_{3/2}$	3/2	1023.4
690	$3s^2 3p^6 3d^{10} 4s_{1/2} 4p_{1/2} 5p_{3/2}$	1/2	1026.6
692	$3s^2 3p^6 3d^{10} 4s_{1/2} 4p_{1/2} 5p_{3/2}$	3/2	1031.6
706	$3s^2 3p^6 3d^{10} 4s_{1/2} 4p_{1/2} 5d_{3/2}$	3/2	1104.0
3751	$3s^2 3p^6 3d^{10} 4s^2 6p_{1/2}$	1/2	1329.1
3754	$3s^2 3p^6 3d^{10} 4s^2 6d_{3/2}$	3/2	1394.2
3756	$3s^2 3p^6 3d^{10} 4s_{1/2} 4p_{1/2} 6s_{1/2}$	1/2	1397.0
3761	$3s^2 3p^6 3d^{10} 4s^2 6f_{5/2}$	5/2	1440.2
3767	$3s^2 3p^6 3d^{10} 4s^2 6g_{7/2}$	7/2	1465.7
3778	$3s^2 3p^6 3d^{10} 4s_{1/2} 4p_{1/2} 6d_{5/2}$	3/2	1493.1
3791	$3s^2 3p^6 3d^{10} 4s_{1/2} 4p_{1/2} 6f_{5/2}$	7/2	1533.4
3794	$3s^2 3p^6 3d^{10} 4s_{1/2} 4p_{1/2} 6f_{7/2}$	5/2	1535.1
3796	$3s^2 3p^6 3d^{10} 4s_{1/2} 4p_{1/2} 6f_{7/2}$	7/2	1535.5
7797	$3s^2 3p^6 3d_{3/2}^4 3d_{5/2}^5 4s^2 4p_{1/2}^2$	5/2	1603.6
7798	$3s^2 3p^6 3d_{3/2}^3 3d_{5/2}^6 4s^2 4p_{1/2}^2$	3/2	1670.6
7799	$3s^2 3p^6 3d_{3/2}^4 3d_{5/2}^5 4s^2 4p_{1/2} 4p_{3/2}$	7/2	1695.6
7800	$3s^2 3p^6 3d_{3/2}^4 3d_{5/2}^5 4s^2 4p_{1/2} 4p_{3/2}$	3/2	1698.5
7802	$3s^2 3p^6 3d_{3/2}^4 3d_{5/2}^5 4s^2 4p_{1/2} 4p_{3/2}$	9/2	1700.6
7803	$3s^2 3p^6 3d_{3/2}^4 3d_{5/2}^5 4s^2 4p_{1/2} 4p_{3/2}$	3/2	1702.6
7804	$3s^2 3p^6 3d_{3/2}^4 3d_{5/2}^5 4s^2 4p_{1/2} 4p_{3/2}$	5/2	1703.0
7805	$3s^2 3p^6 3d_{3/2}^4 3d_{5/2}^5 4s^2 4p_{1/2} 4p_{3/2}$	1/2	1703.2
7806	$3s^2 3p^6 3d_{3/2}^4 3d_{5/2}^5 4s^2 4p_{1/2} 4p_{3/2}$	7/2	1704.5
7807	$3s^2 3p^6 3d_{3/2}^3 3d_{5/2}^6 4s^2 4p_{1/2} 4p_{3/2}$	1/2	1759.6

Table 3 – Energy levels in Ga-like W^{43+} continued

Index	Configuration	J	Energy (eV)
7808	$3s^2 3p^6 3d^3_{3/2} 3d^6_{5/2} 4s^2 4p_{1/2} 4p_{3/2}$	3/2	1763.7
7809	$3s^2 3p^6 3d^3_{3/2} 3d^6_{5/2} 4s^2 4p_{1/2} 4p_{3/2}$	5/2	1764.3
7810	$3s^2 3p^6 3d^3_{3/2} 3d^6_{5/2} 4s^2 4p_{1/2} 4p_{3/2}$	7/2	1766.7
7811	$3s^2 3p^6 3d^3_{3/2} 3d^6_{5/2} 4s^2 4p_{1/2} 4p_{3/2}$	1/2	1768.4
7812	$3s^2 3p^6 3d^3_{3/2} 3d^6_{5/2} 4s^2 4p_{1/2} 4p_{3/2}$	5/2	1770.3
7813	$3s^2 3p^6 3d^3_{3/2} 3d^6_{5/2} 4s^2 4p_{1/2} 4p_{3/2}$	3/2	1771.0
7816	$3s^2 3p^6 3d^4_{3/2} 3d^5_{5/2} 4s_{1/2} 4p^2_{1/2} 4p_{3/2}$	3/2	1794.5
7818	$3s^2 3p^6 3d^4_{3/2} 3d^5_{5/2} 4s_{1/2} 4p^2_{1/2} 4p_{3/2}$	1/2	1796.0
7825	$3s^2 3p^6 3d^4_{3/2} 3d^5_{5/2} 4s_{1/2} 4p^2_{1/2} 4p_{3/2}$	3/2	1807.9
7846	$3s^2 3p^6 3d^4_{3/2} 3d^5_{5/2} 4s^2 4p_{1/2} 4d_{5/2}$	3/2	1874.2
7854	$3s^2 3p^6 3d^4_{3/2} 3d^5_{5/2} 4s^2 4p_{1/2} 4d_{5/2}$	3/2	1878.5
7855	$3s^2 3p^6 3d^4_{3/2} 3d^5_{5/2} 4s^2 4p_{1/2} 4d_{5/2}$	7/2	1878.7
7857	$3s^2 3p^6 3d^4_{3/2} 3d^5_{5/2} 4s^2 4p_{1/2} 4d_{5/2}$	5/2	1879.7
7858	$3s^2 3p^6 3d^4_{3/2} 3d^5_{5/2} 4s_{1/2} 4p_{1/2} 4p^2_{3/2}$	1/2	1884.5
7861	$3s^2 3p^6 3d^4_{3/2} 3d^5_{5/2} 4s_{1/2} 4p_{1/2} 4p^2_{3/2}$	3/2	1892.7
7863	$3s^2 3p^6 3d^4_{3/2} 3d^5_{5/2} 4s_{1/2} 4p_{1/2} 4p^2_{3/2}$	1/2	1893.3
7869	$3s^2 3p^6 3d^4_{3/2} 3d^5_{5/2} 4s^2 4p_{1/2} 4d_{5/2}$	1/2	1900.6
7883	$3s^2 3p^6 3d^3_{3/2} 3d^6_{5/2} 4s^2 4p_{1/2} 4d_{3/2}$	3/2	1915.6
7884	$3s^2 3p^6 3d^3_{3/2} 3d^6_{5/2} 4s^2 4p_{1/2} 4d_{3/2}$	5/2	1918.6
7885	$3s^2 3p^6 3d^3_{3/2} 3d^6_{5/2} 4s^2 4p_{1/2} 4d_{3/2}$	1/2	1925.9
7888	$3s^2 3p^6 3d^3_{3/2} 3d^6_{5/2} 4s^2 4p_{1/2} 4d_{3/2}$	3/2	1937.6
7894	$3s^2 3p^6 3d^3_{3/2} 3d^6_{5/2} 4s^2 4p_{1/2} 4d_{5/2}$	3/2	1943.5
7898	$3s^2 3p^6 3d^3_{3/2} 3d^6_{5/2} 4s^2 4p_{1/2} 4d_{5/2}$	5/2	1946.0
7907	$3s^2 3p^6 3d^4_{3/2} 3d^5_{5/2} 4s^2 4p_{3/2} 4d_{3/2}$	1/2	1957.1
7911	$3s^2 3p^6 3d^4_{3/2} 3d^5_{5/2} 4s^2 4p_{3/2} 4d_{3/2}$	1/2	1959.7
7930	$3s^2 3p^6 3d^4_{3/2} 3d^5_{5/2} 4s^2 4p_{3/2} 4d_{3/2}$	1/2	1969.4
7951	$3s^2 3p^6 3d^3_{3/2} 3d^6_{5/2} 4s_{1/2} 4p_{1/2} 4p^2_{3/2}$	1/2	1977.9
7956	$3s^2 3p^6 3d^3_{3/2} 3d^6_{5/2} 4s_{1/2} 4p_{1/2} 4p^2_{3/2}$	1/2	1980.8
8039	$3s^2 3p^6 3d^4_{3/2} 3d^5_{5/2} 4s_{1/2} 4p_{1/2} 4p_{3/2} 4d_{3/2}$	3/2	2042.4
8090	$3s^2 3p^6 3d^4_{3/2} 3d^5_{5/2} 4s_{1/2} 4p_{1/2} 4p_{3/2} 4d_{3/2}$	1/2	2059.1
8092	$3s^2 3p^6 3d^4_{3/2} 3d^5_{5/2} 4s_{1/2} 4p_{1/2} 4p_{3/2} 4d_{3/2}$	3/2	2059.5
8095	$3s^2 3p^6 3d^4_{3/2} 3d^5_{5/2} 4s_{1/2} 4p_{1/2} 4p_{3/2} 4d_{3/2}$	1/2	2060.4
8105	$3s^2 3p^6 3d^4_{3/2} 3d^5_{5/2} 4s_{1/2} 4p_{1/2} 4p_{3/2} 4d_{5/2}$	1/2	2062.8
8106	$3s^2 3p^2_{1/2} 3p^3_{3/2} 3d^{10} 4s^2 4p^2_{1/2}$	3/2	2062.8
8111	$3s^2 3p^6 3d^4_{3/2} 3d^5_{5/2} 4s_{1/2} 4p_{1/2} 4p_{3/2} 4d_{5/2}$	3/2	2066.3
8113	$3s^2 3p^6 3d^4_{3/2} 3d^5_{5/2} 4s_{1/2} 4p_{1/2} 4p_{3/2} 4d_{5/2}$	1/2	2066.8
8116	$3s^2 3p^6 3d^4_{3/2} 3d^5_{5/2} 4s_{1/2} 4p_{1/2} 4p_{3/2} 4d_{5/2}$	3/2	2067.9
8120	$3s^2 3p^6 3d^4_{3/2} 3d^5_{5/2} 4s_{1/2} 4p_{1/2} 4p_{3/2} 4d_{5/2}$	3/2	2068.7
8124	$3s^2 3p^6 3d^4_{3/2} 3d^5_{5/2} 4s_{1/2} 4p_{1/2} 4p_{3/2} 4d_{5/2}$	1/2	2071.8

Table 3 – Energy levels in Ga-like W^{43+} continued

Index	Configuration	J	Energy (eV)
8147	$3s^23p^63d^4_{3/2}3d^5_{5/2}4s_{1/2}4p_{1/2}4p_{3/2}4d_{5/2}$	1/2	2078.8
8161	$3s^23p^63d^4_{3/2}3d^5_{5/2}4s_{1/2}4p_{1/2}4p_{3/2}4d_{5/2}$	3/2	2084.3
8168	$3s^23p^63d^4_{3/2}3d^5_{5/2}4s_{1/2}4p_{1/2}4p_{3/2}4d_{5/2}$	3/2	2085.7
8169	$3s^23p^63d^4_{3/2}3d^5_{5/2}4s_{1/2}4p_{1/2}4p_{3/2}4d_{5/2}$	1/2	2085.9
8171	$3s^23p^63d^4_{3/2}3d^5_{5/2}4s_{1/2}4p_{1/2}4p_{3/2}4d_{5/2}$	3/2	2087.7
8209	$3s^23p^63d^4_{3/2}3d^5_{5/2}4s_{1/2}4p_{1/2}4p_{3/2}4d_{5/2}$	3/2	2105.6
8211	$3s^23p^63d^4_{3/2}3d^5_{5/2}4s_{1/2}4p_{1/2}4p_{3/2}4d_{5/2}$	1/2	2106.9
8232	$3s^23p^63d^3_{3/2}3d^6_{5/2}4s_{1/2}4p_{1/2}4p_{3/2}4d_{3/2}$	3/2	2117.5
8241	$3s^23p^63d^3_{3/2}3d^6_{5/2}4s_{1/2}4p_{1/2}4p_{3/2}4d_{3/2}$	3/2	2120.5
8243	$3s^23p^63d^3_{3/2}3d^6_{5/2}4s_{1/2}4p_{1/2}4p_{3/2}4d_{3/2}$	1/2	2121.1
8255	$3s^23p^63d^3_{3/2}3d^6_{5/2}4s_{1/2}4p_{1/2}4p_{3/2}4d_{3/2}$	1/2	2125.4
8257	$3s^23p^63d^3_{3/2}3d^6_{5/2}4s_{1/2}4p_{1/2}4p_{3/2}4d_{5/2}$	1/2	2126.6
8258	$3s^23p^63d^3_{3/2}3d^6_{5/2}4s_{1/2}4p_{1/2}4p_{3/2}4d_{5/2}$	3/2	2127.3
8265	$3s^23p^63d^3_{3/2}3d^6_{5/2}4s_{1/2}4p_{1/2}4p_{3/2}4d_{3/2}$	1/2	2130.5
8266	$3s^23p^63d^3_{3/2}3d^6_{5/2}4s_{1/2}4p_{1/2}4p_{3/2}4d_{3/2}$	3/2	2131.0
8275	$3s^23p^63d^3_{3/2}3d^6_{5/2}4s_{1/2}4p_{1/2}4p_{3/2}4d_{5/2}$	3/2	2135.0
8291	$3s^23p^63d^3_{3/2}3d^6_{5/2}4s^24p_{1/2}4f_{5/2}$	3/2	2140.3
8295	$3s^23p^63d^3_{3/2}3d^6_{5/2}4s^24p_{1/2}4f_{5/2}$	1/2	2140.5
8307	$3s^23p^63d^3_{3/2}3d^6_{5/2}4s_{1/2}4p_{1/2}4p_{3/2}4d_{5/2}$	1/2	2142.8
8308	$3s^23p^63d^4_{3/2}3d^5_{5/2}4s^24p_{3/2}4f_{5/2}$	3/2	2142.9
8311	$3s^23p^63d^4_{3/2}3d^5_{5/2}4s_{1/2}4p^2_{3/2}4d_{3/2}$	3/2	2143.3
8324	$3s^23p^63d^3_{3/2}3d^6_{5/2}4s_{1/2}4p_{1/2}4p_{3/2}4d_{5/2}$	1/2	2146.0
8377	$3s^23p^63d^3_{3/2}3d^6_{5/2}4s_{1/2}4p_{1/2}4p_{3/2}4d_{3/2}$	3/2	2154.8
8407	$3s^23p^63d^3_{3/2}3d^6_{5/2}4s_{1/2}4p_{1/2}4p_{3/2}4d_{5/2}$	3/2	2160.4
8415	$3s^23p^63d^3_{3/2}3d^6_{5/2}4s_{1/2}4p_{1/2}4p_{3/2}4d_{5/2}$	3/2	2161.3
8446	$3s^23p^63d^4_{3/2}3d^5_{5/2}4s_{1/2}4p^2_{3/2}4d_{3/2}$	3/2	2170.3
8447	$3s^23p^63d^4_{3/2}3d^5_{5/2}4s^24p_{3/2}4f_{7/2}$	1/2	2170.7
8486	$3s^23p^2_{1/2}3p^3_{3/2}3d^{10}4s^24p_{1/2}4p_{3/2}$	1/2	2182.0
8502	$3s^23p^63d^4_{3/2}3d^5_{5/2}4s_{1/2}4p^2_{3/2}4d_{3/2}$	3/2	2185.9
8504	$3s^23p^63d^3_{3/2}3d^6_{5/2}4p_{1/2}4p^3_{3/2}$	1/2	2186.6
9009	$3s^23p^2_{1/2}3p^3_{3/2}3d^{10}4s^24p_{1/2}4d_{3/2}$	7/2	2306.9
9132	$3s^23p^2_{1/2}3p^3_{3/2}3d^{10}4s^24p_{1/2}4d_{5/2}$	1/2	2334.9
9147	$3s^23p^2_{1/2}3p^3_{3/2}3d^{10}4s^24p_{1/2}4d_{5/2}$	3/2	2336.9
9224	$3s^23p^2_{1/2}3p^3_{3/2}3d^{10}4s^24p_{1/2}4d_{5/2}$	1/2	2349.2
9253	$3s^23p^2_{1/2}3p^3_{3/2}3d^{10}4s_{1/2}4p_{1/2}4p^2_{3/2}$	3/2	2354.4
11806	$3s^23p^63d^4_{3/2}3d^5_{5/2}4s^24p_{1/2}5f_{7/2}$	1/2	2716.9
11808	$3s^23p^63d^4_{3/2}3d^5_{5/2}4s^24p_{1/2}5f_{7/2}$	3/2	2718.1
12028	$3s^23p^63d^3_{3/2}3d^6_{5/2}4s^24p_{1/2}5f_{5/2}$	1/2	2777.9
12033	$3s^23p^63d^3_{3/2}3d^6_{5/2}4s^24p_{1/2}5f_{5/2}$	3/2	2781.2

Table 3 – Energy levels in Ga-like W^{43+} continued

Index	Configuration	J	Energy (eV)
12038	$3s^2 3p^6 3d^3_{3/2} 3d^6_{5/2} 4s_{1/2} 4p^2_{1/2} 5d_{3/2}$	1/2	2786.0
14464	$3s^2 3p^2_{1/2} 3p^3_{3/2} 3d^{10} 4s^2 4p_{1/2} 5d_{5/2}$	1/2	3088.7
14473	$3s^2 3p^2_{1/2} 3p^3_{3/2} 3d^{10} 4s^2 4p_{1/2} 5d_{5/2}$	3/2	3089.7
18686	$3s^2 3p^6 3d^4_{3/2} 3d^5_{5/2} 4s^2 4p_{1/2} 6f_{7/2}$	3/2	3062.1
18687	$3s^2 3p^6 3d^4_{3/2} 3d^5_{5/2} 4s^2 4p_{1/2} 6f_{7/2}$	1/2	3062.2
18884	$3s^2 3p^6 3d^3_{3/2} 3d^6_{5/2} 4s^2 4p_{1/2} 6f_{5/2}$	1/2	3124.8
18894	$3s^2 3p^6 3d^3_{3/2} 3d^6_{5/2} 4s^2 4p_{1/2} 6f_{5/2}$	3/2	3126.7

Table 4: Radiative transitions in Ga-like W^{43+}

i	k	ΔE (eV)	λ (Å)	gf	A_{ki} (s^{-1})	ϵ_{line} ($ion^{-1}s^{-1}$)
1	706	1007.30	12.3085	2.90×10^{-1}	3.19×10^{12}	43
0	687	1010.14	12.2739	2.20×10^{-1}	2.44×10^{12}	281
0	689	1023.44	12.1144	8.18×10^{-2}	9.30×10^{11}	53
24	3767	1025.77	12.0869	5.55×10^{-1}	3.17×10^{12}	42
0	690	1026.57	12.0775	9.90×10^{-2}	2.26×10^{12}	102
0	692	1031.59	12.0188	1.55×10^{-1}	1.78×10^{12}	167
7	3751	1069.67	11.5909	5.69×10^{-2}	1.41×10^{12}	113
20	3794	1161.12	10.6780	4.22×10^{-1}	4.11×10^{12}	49
19	3796	1161.49	10.6746	6.38×10^{-1}	4.67×10^{12}	41
7	3761	1180.76	10.5004	5.47×10^{-1}	5.52×10^{12}	154
6	3756	1191.72	10.4038	4.35×10^{-2}	1.34×10^{12}	98
14	3791	1191.74	10.4036	7.52×10^{-1}	5.79×10^{12}	41
5	3756	1194.73	10.3776	5.45×10^{-2}	1.69×10^{12}	123
6	3778	1287.84	9.6273	1.56×10^{-1}	2.81×10^{12}	40
0	3754	1394.20	8.8929	1.34×10^{-1}	2.83×10^{12}	83
5	7806	1502.28	8.2531	1.38×10^{-4}	1.69×10^{9}	57
1	7797	1506.97	8.2274	2.68×10^{-4}	4.40×10^{9}	321
4	7802	1510.72	8.2070	4.55×10^{-4}	4.51×10^{9}	242
3	7799	1514.40	8.1870	3.40×10^{-4}	4.23×10^{9}	156
4	7806	1514.67	8.1856	2.24×10^{-4}	2.78×10^{9}	95
5	7810	1564.48	7.9249	1.81×10^{-4}	2.40×10^{9}	48
2	7804	1604.86	7.7256	2.97×10^{-4}	5.54×10^{9}	56
7	7869	1641.10	7.5549	8.10×10^{-3}	4.74×10^{11}	108
7	7883	1656.10	7.4865	1.02×10^{-1}	3.04×10^{12}	84
7	7884	1659.11	7.4729	1.18×10^{-1}	2.35×10^{12}	103
12	7930	1662.18	7.4591	4.59×10^{-3}	2.75×10^{11}	97
2	7809	1666.21	7.4411	1.20×10^{-1}	2.40×10^{12}	55
7	7885	1666.44	7.4401	6.60×10^{-2}	3.98×10^{12}	168
8	7894	1670.14	7.4236	1.61×10^{-1}	4.88×10^{12}	39
2	7811	1670.27	7.4230	1.02×10^{-1}	6.19×10^{12}	46
0	7798	1670.59	7.4216	1.38×10^{-1}	4.17×10^{12}	503
2	7812	1672.19	7.4145	1.71×10^{-1}	3.46×10^{12}	41
8	7898	1672.69	7.4123	2.44×10^{-1}	4.95×10^{12}	38
2	7813	1672.89	7.4114	2.00×10^{-1}	6.08×10^{12}	94
6	7854	1673.25	7.4098	5.20×10^{-2}	1.58×10^{12}	40
12	7956	1673.53	7.4086	3.73×10^{-2}	2.27×10^{12}	239
11	7951	1674.85	7.4027	4.09×10^{-2}	2.49×10^{12}	316
34	8295	1674.99	7.4021	6.75×10^{-2}	4.11×10^{12}	42
11	7956	1677.73	7.3900	3.12×10^{-2}	1.90×10^{12}	200
7	7888	1678.12	7.3883	4.78×10^{-2}	1.46×10^{12}	46
35	8324	1679.23	7.3834	6.51×10^{-2}	3.98×10^{12}	39
6	7858	1679.24	7.3834	2.08×10^{-2}	1.27×10^{12}	60

Table 4 – Radiative transitions in Ga-like W^{43+} continued

i	k	ΔE (eV)	λ (Å)	gf	A_{ki} (s^{-1})	ϵ_{line} ($ion^{-1}s^{-1}$)
4	7855	1688.83	7.3414	4.85×10^{-2}	7.50×10^{11}	44
4	7857	1689.85	7.3370	4.60×10^{-2}	9.51×10^{11}	106
3	7846	1692.99	7.3234	1.83×10^{-2}	5.70×10^{11}	51
7	7907	1697.61	7.3035	7.74×10^{-2}	4.84×10^{12}	293
1	7816	1697.87	7.3024	1.07×10^{-1}	3.36×10^{12}	68
5	7869	1698.31	7.3005	4.19×10^{-3}	2.62×10^{11}	60
0	7800	1698.55	7.2994	1.06×10^{-1}	3.31×10^{12}	373
1	7818	1699.30	7.2962	1.38×10^{-1}	8.63×10^{12}	46
7	7911	1700.22	7.2923	4.05×10^{-2}	2.54×10^{12}	248
14	8039	1700.74	7.2900	1.67×10^{-1}	5.23×10^{12}	57
0	7803	1702.61	7.2820	2.14×10^{-1}	6.74×10^{12}	515
0	7805	1703.16	7.2797	1.40×10^{-1}	8.79×10^{12}	582
7	7930	1709.95	7.2508	1.66×10^{-2}	1.06×10^{12}	373
1	7825	1711.18	7.2455	1.79×10^{-1}	5.67×10^{12}	48
3	7861	1711.51	7.2441	1.16×10^{-1}	3.67×10^{12}	39
3	7863	1712.11	7.2416	2.43×10^{-2}	1.55×10^{12}	49
0	7807	1759.64	7.0460	5.36×10^{-3}	3.60×10^{11}	44
0	7808	1763.70	7.0298	2.52×10^{-2}	8.52×10^{11}	173
5	7930	1767.15	7.0160	3.25×10^{-3}	2.20×10^{11}	78
6	7956	1775.49	6.9831	6.46×10^{-3}	4.42×10^{11}	46
5	7951	1775.62	6.9826	6.75×10^{-3}	4.62×10^{11}	58
7	8486	1922.57	6.4489	1.64×10^{-2}	1.31×10^{12}	115
19	9147	1962.93	6.3163	2.15×10^{-1}	8.99×10^{12}	54
14	9009	1965.26	6.3088	5.60×10^{-1}	1.17×10^{13}	50
1	8106	1966.15	6.3059	3.38×10^{-1}	1.42×10^{13}	83
6	8486	1976.77	6.2721	6.72×10^{-2}	5.70×10^{12}	501
5	8486	1979.78	6.2625	1.63×10^{-1}	1.39×10^{13}	1219
0	8039	2042.37	6.0706	8.44×10^{-2}	3.82×10^{12}	41
2	8377	2056.65	6.0285	8.78×10^{-2}	4.03×10^{12}	43
0	8090	2059.10	6.0213	1.96×10^{-1}	1.81×10^{13}	181
0	8092	2059.47	6.0202	7.73×10^{-2}	3.56×10^{12}	49
0	8095	2060.44	6.0174	6.23×10^{-2}	5.74×10^{12}	52
0	8105	2062.82	6.0104	1.70×10^{-1}	1.57×10^{13}	181
0	8111	2066.27	6.0004	7.12×10^{-1}	3.30×10^{13}	812
0	8113	2066.84	5.9987	2.72×10^{-1}	2.52×10^{13}	314
0	8116	2067.95	5.9955	3.53×10^{-1}	1.64×10^{13}	369
0	8120	2068.74	5.9932	5.76×10^{-1}	2.67×10^{13}	636
0	8124	2071.75	5.9845	1.99×10^{-1}	1.85×10^{13}	207
2	8446	2072.15	5.9834	1.10×10^{-1}	5.11×10^{12}	46
2	8447	2072.53	5.9823	3.88×10^{-1}	3.62×10^{13}	116
0	8147	2078.76	5.9643	1.06×10^{-1}	9.96×10^{12}	93
0	8161	2084.33	5.9484	6.62×10^{-2}	3.12×10^{12}	46
0	8168	2085.70	5.9445	8.77×10^{-2}	4.14×10^{12}	61

Table 4 – Radiative transitions in Ga-like W^{43+} continued

i	k	ΔE (eV)	λ (Å)	gf	A_{ki} (s^{-1})	ϵ_{line} ($ion^{-1}s^{-1}$)
0	8169	2085.92	5.9439	1.59×10^{-1}	1.50×10^{13}	139
0	8171	2087.65	5.9389	1.67×10^{-1}	7.89×10^{12}	134
0	8209	2105.63	5.8882	2.49×10^{-1}	1.20×10^{13}	227
0	8211	2106.85	5.8848	8.92×10^{-2}	8.59×10^{12}	75
0	8232	2117.53	5.8551	9.04×10^{-1}	4.40×10^{13}	913
0	8241	2120.51	5.8469	1.13×10^{-1}	5.49×10^{12}	59
0	8243	2121.07	5.8454	7.54×10^{-2}	7.36×10^{12}	57
0	8255	2125.40	5.8334	1.86×10^{-1}	1.82×10^{13}	160
0	8257	2126.58	5.8302	1.80×10^{-1}	1.77×10^{13}	171
0	8258	2127.29	5.8283	1.76×10^{-1}	8.66×10^{12}	152
0	8265	2130.50	5.8195	8.01×10^{-1}	7.89×10^{13}	832
0	8266	2130.97	5.8182	5.03×10^{-1}	2.48×10^{13}	468
0	8275	2134.97	5.8073	8.40×10^{-1}	4.15×10^{13}	860
0	8291	2140.29	5.7929	3.64	1.81×10^{14}	3804
0	8295	2140.48	5.7923	9.47×10^{-1}	9.42×10^{13}	973
0	8307	2142.83	5.7860	5.51×10^{-1}	5.49×10^{13}	559
0	8308	2142.93	5.7857	1.53×10^{-1}	7.64×10^{12}	88
0	8311	2143.32	5.7847	3.70×10^{-1}	1.84×10^{13}	295
0	8324	2145.98	5.7775	5.29×10^{-1}	5.29×10^{13}	511
0	8377	2154.78	5.7539	1.25×10^{-1}	6.28×10^{12}	66
0	8407	2160.43	5.7389	1.08×10^{-1}	5.47×10^{12}	58
0	8415	2161.27	5.7366	1.10×10^{-1}	5.56×10^{12}	65
0	8446	2170.28	5.7128	1.82×10^{-1}	9.28×10^{12}	83
0	8447	2170.66	5.7118	1.95×10^{-1}	1.99×10^{13}	64
0	8502	2185.86	5.6721	8.69×10^{-2}	4.50×10^{12}	44
0	8504	2186.59	5.6702	7.29×10^{-2}	7.56×10^{12}	39
0	9132	2334.88	5.3101	4.19×10^{-1}	4.95×10^{13}	127
0	9147	2336.94	5.3054	1.21	7.19×10^{13}	430
0	9224	2349.15	5.2778	3.25×10^{-1}	3.89×10^{13}	84
0	9253	2354.36	5.2662	2.50×10^{-1}	1.51×10^{13}	41
0	11806	2716.89	4.5635	4.68×10^{-1}	7.49×10^{13}	250
0	11808	2718.08	4.5615	1.06	8.51×10^{13}	688
0	12028	2777.86	4.4633	5.26×10^{-1}	8.81×10^{13}	255
0	12033	2781.22	4.4579	1.22	1.02×10^{14}	723
0	12038	2786.03	4.4502	1.14×10^{-1}	1.92×10^{13}	43
0	18686	3062.11	4.0490	5.31×10^{-1}	5.40×10^{13}	315
0	18687	3062.22	4.0488	2.60×10^{-1}	5.29×10^{13}	140
0	14464	3088.74	4.0141	2.21×10^{-1}	4.57×10^{13}	46
0	14473	3089.75	4.0128	4.93×10^{-1}	5.10×10^{13}	115
0	18884	3124.81	3.9677	2.28×10^{-1}	4.84×10^{13}	110
0	18894	3126.72	3.9653	4.27×10^{-1}	4.53×10^{13}	213

Table 5: Energy levels in Zn-like W^{44+}

Index	Configuration	J	Energy (eV)
0	$3s^2 3p^6 3d^{10} 4s^2$	0	0.0
1	$3s^2 3p^6 3d^{10} 4s_{1/2} 4p_{1/2}$	0	86.2
2	$3s^2 3p^6 3d^{10} 4s_{1/2} 4p_{1/2}$	1	93.2
3	$3s^2 3p^6 3d^{10} 4s_{1/2} 4p_{3/2}$	2	186.2
5	$3s^2 3p^6 3d^{10} 4s_{1/2} 4p_{3/2}$	1	203.7
7	$3s^2 3p^6 3d^{10} 4p_{1/2} 4p_{3/2}$	2	292.4
9	$3s^2 3p^6 3d^{10} 4s_{1/2} 4d_{3/2}$	2	348.4
11	$3s^2 3p^6 3d^{10} 4s_{1/2} 4d_{5/2}$	2	371.7
13	$3s^2 3p^6 3d^{10} 4p_{3/2}^2$	0	403.2
16	$3s^2 3p^6 3d^{10} 4p_{1/2} 4d_{5/2}$	3	466.2
21	$3s^2 3p^6 3d^{10} 4s_{1/2} 4f_{7/2}$	3	539.4
22	$3s^2 3p^6 3d^{10} 4p_{3/2} 4d_{3/2}$	2	543.7
25	$3s^2 3p^6 3d^{10} 4p_{3/2} 4d_{3/2}$	3	553.5
84	$3s^2 3p^6 3d_{3/2}^4 3d_{5/2}^5 4s^2 4p_{1/2}$	2	1618.7
85	$3s^2 3p^6 3d_{3/2}^4 3d_{5/2}^5 4s^2 4p_{1/2}$	3	1619.7
86	$3s^2 3p^6 3d_{3/2}^3 3d_{5/2}^6 4s^2 4p_{1/2}$	2	1684.7
87	$3s^2 3p^6 3d_{3/2}^3 3d_{5/2}^6 4s^2 4p_{1/2}$	1	1688.1
90	$3s^2 3p^6 3d_{3/2}^4 3d_{5/2}^5 4s^2 4p_{3/2}$	4	1718.4
91	$3s^2 3p^6 3d_{3/2}^4 3d_{5/2}^5 4s^2 4p_{3/2}$	2	1720.4
92	$3s^2 3p^6 3d_{3/2}^4 3d_{5/2}^5 4s^2 4p_{3/2}$	1	1722.0
93	$3s^2 3p^6 3d_{3/2}^4 3d_{5/2}^5 4s^2 4p_{3/2}$	3	1723.3
97	$3s^2 3p^6 3d_{3/2}^3 3d_{5/2}^6 4s^2 4p_{3/2}$	1	1785.8
98	$3s^2 3p^6 3d_{3/2}^3 3d_{5/2}^6 4s^2 4p_{3/2}$	3	1785.9
105	$3s^2 3p^6 3d_{3/2}^4 3d_{5/2}^5 4s_{1/2} 4p_{1/2} 4p_{3/2}$	2	1812.0
118	$3s^2 3p^6 3d_{3/2}^3 3d_{5/2}^6 4s_{1/2} 4p_{1/2} 4p_{3/2}$	3	1869.6
124	$3s^2 3p^6 3d_{3/2}^4 3d_{5/2}^5 4s^2 4d_{3/2}$	2	1878.8
125	$3s^2 3p^6 3d_{3/2}^3 3d_{5/2}^6 4s_{1/2} 4p_{1/2} 4p_{3/2}$	3	1879.0
126	$3s^2 3p^6 3d_{3/2}^3 3d_{5/2}^6 4s_{1/2} 4p_{1/2} 4p_{3/2}$	2	1879.7
133	$3s^2 3p^6 3d_{3/2}^4 3d_{5/2}^5 4s^2 4d_{5/2}$	1	1892.7
136	$3s^2 3p^6 3d_{3/2}^4 3d_{5/2}^5 4s^2 4d_{5/2}$	3	1896.3
138	$3s^2 3p^6 3d_{3/2}^4 3d_{5/2}^5 4s^2 4d_{5/2}$	2	1897.8
139	$3s^2 3p^6 3d_{3/2}^4 3d_{5/2}^5 4s_{1/2} 4p_{3/2}^2$	0	1905.8
144	$3s^2 3p^6 3d_{3/2}^4 3d_{5/2}^5 4s_{1/2} 4p_{3/2}^2$	2	1917.2
191	$3s^2 3p^6 3d_{3/2}^3 3d_{5/2}^6 4s^2 4d_{3/2}$	0	1986.0
214	$3s^2 3p^6 3d_{3/2}^3 3d_{5/2}^6 4s_{1/2} 4p_{3/2}^2$	0	2001.2
292	$3s^2 3p^6 3d_{3/2}^3 3d_{5/2}^6 4s_{1/2} 4p_{1/2} 4d_{3/2}$	1	2075.1
298	$3s^2 3p_{1/2}^2 3p_{3/2}^3 3d^{10} 4s^2 4p_{1/2}$	2	2076.7
303	$3s^2 3p^6 3d_{3/2}^4 3d_{5/2}^5 4s^2 4f_{7/2}$	1	2082.6
308	$3s^2 3p^6 3d_{3/2}^4 3d_{5/2}^5 4s_{1/2} 4p_{3/2} 4d_{5/2}$	1	2085.4

Table 5 – Energy levels in Zn-like W^{44+} continued

Index	Configuration	J	Energy (eV)
327	$3s^2 3p^6 3d^4_{3/2} 3d^5_{5/2} 4s_{1/2} 4p_{3/2} 4d_{3/2}$	1	2091.0
344	$3s^2 3p^6 3d^4_{3/2} 3d^5_{5/2} 4s_{1/2} 4p_{3/2} 4d_{5/2}$	1	2103.2
365	$3s^2 3p^6 3d^4_{3/2} 3d^5_{5/2} 4s_{1/2} 4p_{3/2} 4d_{5/2}$	1	2124.6
392	$3s^2 3p^6 3d^4_{3/2} 3d^5_{5/2} 4p^3_{3/2}$	1	2139.9
394	$3s^2 3p^6 3d^3_{3/2} 3d^6_{5/2} 4s_{1/2} 4p_{3/2} 4d_{3/2}$	1	2141.3
414	$3s^2 3p^6 3d^3_{3/2} 3d^6_{5/2} 4s_{1/2} 4p_{3/2} 4d_{5/2}$	1	2150.6
418	$3s^2 3p^6 3d^3_{3/2} 3d^6_{5/2} 4s_{1/2} 4p_{3/2} 4d_{5/2}$	1	2151.0
448	$3s^2 3p^6 3d^3_{3/2} 3d^6_{5/2} 4s^2 4f_{5/2}$	1	2159.0
484	$3s^2 3p^6 3d^3_{3/2} 3d^6_{5/2} 4s_{1/2} 4p_{3/2} 4d_{5/2}$	1	2171.1
489	$3s^2 3p^6 3d^3_{3/2} 3d^6_{5/2} 4s_{1/2} 4p_{3/2} 4d_{5/2}$	1	2172.9
508	$3s^2 3p^6 3d^3_{3/2} 3d^6_{5/2} 4s_{1/2} 4p_{3/2} 4d_{5/2}$	1	2178.8
535	$3s^2 3p^6 3d^3_{3/2} 3d^6_{5/2} 4p^3_{3/2}$	1	2192.5
544	$3s^2 3p^2_{1/2} 3p^3_{3/2} 3d^{10} 4s^2 4p_{3/2}$	0	2200.1
555	$3s^2 3p^6 3d^3_{3/2} 3d^6_{5/2} 4p^3_{3/2}$	1	2204.6
630	$3s^2 3p^6 3d^3_{3/2} 3d^6_{5/2} 4s_{1/2} 4p_{1/2} 4f_{5/2}$	1	2240.1
1021	$3s^2 3p^2_{1/2} 3p^3_{3/2} 3d^{10} 4s^2 4d_{3/2}$	3	2335.6
1098	$3s^2 3p^2_{1/2} 3p^3_{3/2} 3d^{10} 4s^2 4d_{5/2}$	1	2353.5
1189	$3s^2 3p^2_{1/2} 3p^3_{3/2} 3d^{10} 4s_{1/2} 4p^2_{3/2}$	1	2370.8
2159	$3s^2 3p^2_{1/2} 3p^3_{3/2} 3d^{10} 4s_{1/2} 4p_{3/2} 4d_{3/2}$	2	2525.5
2224	$3s^2 3p^2_{1/2} 3p^3_{3/2} 3d^{10} 4s^2 4f_{7/2}$	2	2532.3
2945	$3s_{1/2} 3p^6 3d^{10} 4s^2 4p_{1/2}$	1	2624.8
4806	$3s^2 3p_{1/2} 3p^4_{3/2} 3d^{10} 4s^2 4f_{5/2}$	2	2821.6
11470	$3s^2 3p^6 3d^{10} 4s_{1/2} 5p_{3/2}$	1	1041.0
11476	$3s^2 3p^6 3d^{10} 4s_{1/2} 5d_{3/2}$	2	1117.7
11488	$3s^2 3p^6 3d^{10} 4s_{1/2} 5f_{7/2}$	3	1203.1
11699	$3s^2 3p^6 3d^{10} 4s_{1/2} 6s_{1/2}$	0	1422.9
11703	$3s^2 3p^6 3d^{10} 4s_{1/2} 6p_{3/2}$	1	1473.7
11708	$3s^2 3p^6 3d^{10} 4s_{1/2} 6d_{5/2}$	2	1519.5
11713	$3s^2 3p^6 3d^{10} 4s_{1/2} 6f_{5/2}$	3	1559.2
11715	$3s^2 3p^6 3d^{10} 4s_{1/2} 6f_{7/2}$	3	1561.1
12148	$3s^2 3p^6 3d^4_{3/2} 3d^5_{5/2} 4s_{1/2} 4p_{1/2} 5d_{3/2}$	1	2748.8
12154	$3s^2 3p^6 3d^4_{3/2} 3d^5_{5/2} 4s^2 5f_{7/2}$	1	2750.2
12276	$3s^2 3p^6 3d^3_{3/2} 3d^6_{5/2} 4s^2 5f_{5/2}$	1	2811.6
12289	$3s^2 3p^6 3d^3_{3/2} 3d^6_{5/2} 4s_{1/2} 4p_{1/2} 5d_{3/2}$	1	2819.2
13626	$3s^2 3p^2_{1/2} 3p^3_{3/2} 3d^{10} 4s^2 5d_{5/2}$	1	3121.3
13911	$3s^2 3p^2_{1/2} 3p^3_{3/2} 3d^{10} 4s^2 5f_{7/2}$	2	3199.9
15691	$3s^2 3p^6 3d^4_{3/2} 3d^5_{5/2} 4s^2 6f_{7/2}$	1	3107.9
15817	$3s^2 3p^6 3d^3_{3/2} 3d^6_{5/2} 4s^2 6f_{5/2}$	1	3171.0
17820	$3s^2 3p^2_{1/2} 3p^3_{3/2} 3d^{10} 4s^2 6d_{5/2}$	1	3517.3

Table 6: Radiative transitions in Zn-like W^{44+}

i	k	ΔE (eV)	λ (Å)	gf	A_{ki} (s^{-1})	ϵ_{line} ($ion^{-1}s^{-1}$)
2	11476	1024.48	12.1022	3.80×10^{-1}	3.46×10^{12}	269
0	11470	1041.05	11.9096	1.25×10^{-1}	1.96×10^{12}	181
11	11715	1189.34	10.4246	5.96×10^{-1}	5.23×10^{12}	131
9	11713	1210.76	10.2402	6.52×10^{-1}	5.93×10^{12}	63
5	11699	1219.16	10.1696	5.24×10^{-2}	3.38×10^{12}	250
5	11708	1315.78	9.4229	2.21×10^{-1}	3.33×10^{12}	110
0	11703	1473.71	8.4131	6.71×10^{-2}	2.11×10^{12}	72
7	98	1493.47	8.3017	4.70×10^{-4}	6.49×10^{9}	146
5	91	1516.69	8.1747	1.50×10^{-4}	2.99×10^{9}	71
5	93	1519.53	8.1594	1.21×10^{-4}	1.74×10^{9}	62
2	84	1525.51	8.1274	8.79×10^{-5}	1.78×10^{9}	78
2	85	1526.49	8.1222	3.10×10^{-4}	4.47×10^{9}	391
3	90	1532.22	8.0918	4.09×10^{-4}	4.63×10^{9}	297
1	84	1532.57	8.0900	1.36×10^{-4}	2.78×10^{9}	122
3	93	1537.06	8.0663	1.97×10^{-4}	2.89×10^{9}	104
5	98	1582.18	7.8363	1.73×10^{-4}	2.69×10^{9}	60
2	86	1591.43	7.7907	1.29×10^{-4}	2.84×10^{9}	122
1	86	1598.50	7.7563	8.99×10^{-5}	1.99×10^{9}	85
3	118	1683.44	7.3649	1.49×10^{-1}	2.61×10^{12}	61
0	87	1688.07	7.3447	1.36×10^{-1}	5.59×10^{12}	1865
3	124	1692.63	7.3249	5.68×10^{-2}	1.41×10^{12}	61
3	125	1692.75	7.3244	1.83×10^{-1}	3.25×10^{12}	61
3	126	1693.48	7.3213	1.61×10^{-1}	4.00×10^{12}	61
5	139	1702.07	7.2843	2.46×10^{-2}	3.10×10^{12}	152
3	133	1706.51	7.2654	1.04×10^{-2}	4.39×10^{11}	62
3	136	1710.05	7.2503	6.63×10^{-2}	1.20×10^{12}	62
3	138	1711.60	7.2438	5.52×10^{-2}	1.40×10^{12}	173
2	105	1718.77	7.2135	9.17×10^{-2}	2.35×10^{12}	71
0	92	1722.01	7.2000	2.30×10^{-1}	9.85×10^{12}	1492
3	144	1731.03	7.1625	2.28×10^{-1}	5.93×10^{12}	65
13	392	1736.67	7.1392	1.08×10^{-1}	4.73×10^{12}	81
5	191	1782.22	6.9567	8.21×10^{-4}	1.13×10^{11}	130
0	97	1785.84	6.9426	2.68×10^{-2}	1.24×10^{12}	703
5	214	1797.42	6.8979	3.31×10^{-3}	4.63×10^{11}	178
2	191	1892.73	6.5505	1.38×10^{-3}	2.15×10^{11}	247
25	2224	1978.81	6.2656	1.35×10^{-1}	4.57×10^{12}	98
11	1098	1981.74	6.2563	2.48×10^{-1}	1.41×10^{13}	146
22	2159	1981.77	6.2562	1.62×10^{-1}	5.51×10^{12}	62
2	298	1983.51	6.2507	4.25×10^{-1}	1.45×10^{13}	160
21	2159	1986.14	6.2425	1.90×10^{-1}	6.50×10^{12}	73
9	1021	1987.21	6.2391	5.58×10^{-1}	1.37×10^{13}	77
21	2224	1992.97	6.2211	1.09×10^{-1}	3.75×10^{12}	80

Table 6 – Radiative transitions in Zn-like W^{44+} continued

i	k	ΔE (eV)	λ (Å)	gf	A_{ki} (s^{-1})	ϵ_{line} ($ion^{-1}s^{-1}$)
5	544	1996.40	6.2104	1.32×10^{-1}	2.28×10^{13}	1667
11488	13911	1996.87	6.2089	3.22×10^{-1}	1.12×10^{13}	88
0	292	2075.15	5.9747	3.05×10^{-1}	1.90×10^{13}	649
0	303	2082.57	5.9534	7.74×10^{-1}	4.86×10^{13}	1844
0	308	2085.35	5.9455	1.86×10^{-1}	1.17×10^{13}	390
0	327	2090.99	5.9295	5.43×10^{-2}	3.43×10^{12}	62
0	344	2103.23	5.8949	2.15×10^{-1}	1.38×10^{13}	403
0	365	2124.57	5.8357	1.69×10^{-1}	1.10×10^{13}	309
0	392	2139.87	5.7940	1.16×10^{-1}	7.70×10^{12}	132
0	394	2141.32	5.7901	1.57	1.04×10^{14}	3431
0	414	2150.58	5.7651	6.36×10^{-1}	4.25×10^{13}	1374
0	418	2151.04	5.7639	1.38×10^{-1}	9.26×10^{12}	269
1	630	2153.92	5.7562	1.57	1.05×10^{14}	58
0	448	2158.98	5.7427	2.69	1.81×10^{14}	5787
0	484	2171.12	5.7106	4.59×10^{-2}	3.13×10^{12}	65
0	489	2172.86	5.7060	4.33×10^{-2}	2.96×10^{12}	64
0	508	2178.77	5.6906	1.61×10^{-1}	1.11×10^{13}	283
0	535	2192.47	5.6550	2.93×10^{-1}	2.04×10^{13}	496
0	555	2204.63	5.6238	6.68×10^{-2}	4.70×10^{12}	79
5	2224	2328.60	5.3244	1.81×10^{-1}	8.52×10^{12}	182
0	1098	2353.47	5.2682	8.25×10^{-1}	6.61×10^{13}	686
16	4806	2355.41	5.2638	3.80×10^{-1}	1.83×10^{13}	70
0	1189	2370.77	5.2297	2.12×10^{-1}	1.73×10^{13}	80
0	2945	2624.83	4.7235	4.24×10^{-1}	4.22×10^{13}	80
0	12148	2748.78	4.5105	1.58×10^{-1}	1.72×10^{13}	169
0	12154	2750.19	4.5082	5.15×10^{-1}	5.63×10^{13}	590
0	12276	2811.57	4.4098	7.87×10^{-1}	9.00×10^{13}	908
0	12289	2819.19	4.3979	1.98×10^{-1}	2.28×10^{13}	157
0	15691	3107.86	3.9894	4.10×10^{-1}	5.73×10^{13}	476
0	13626	3121.26	3.9722	3.40×10^{-1}	4.79×10^{13}	152
0	15817	3171.04	3.9099	3.69×10^{-1}	5.37×10^{13}	401
0	17820	3517.26	3.5250	1.79×10^{-1}	3.21×10^{13}	61

Table 7: Energy levels in Cu-like W^{45+}

Index	Configuration	J	Energy (eV)
0	$3s^2 3p^6 3d^{10} 4s_{1/2}$	1/2	0.0
1	$3s^2 3p^6 3d^{10} 4p_{1/2}$	1/2	97.6
2	$3s^2 3p^6 3d^{10} 4p_{3/2}$	3/2	198.9
3	$3s^2 3p^6 3d^{10} 4d_{3/2}$	3/2	349.5
4	$3s^2 3p^6 3d^{10} 4d_{5/2}$	5/2	371.0
5	$3s^2 3p^6 3d^{10} 4f_{5/2}$	5/2	532.2
6	$3s^2 3p^6 3d^{10} 4f_{7/2}$	7/2	537.7
7	$3s^2 3p^6 3d^4_{3/2} 3d^5_{5/2} 4s^2$	5/2	1547.7
8	$3s^2 3p^6 3d^3_{3/2} 3d^6_{5/2} 4s^2$	3/2	1613.9
9	$3s^2 3p^6 3d^4_{3/2} 3d^5_{5/2} 4s_{1/2} 4p_{1/2}$	5/2	1632.1
11	$3s^2 3p^6 3d^4_{3/2} 3d^5_{5/2} 4s_{1/2} 4p_{1/2}$	5/2	1639.6
13	$3s^2 3p^6 3d^3_{3/2} 3d^6_{5/2} 4s_{1/2} 4p_{1/2}$	3/2	1698.7
14	$3s^2 3p^6 3d^3_{3/2} 3d^6_{5/2} 4s_{1/2} 4p_{1/2}$	5/2	1705.9
15	$3s^2 3p^6 3d^3_{3/2} 3d^6_{5/2} 4s_{1/2} 4p_{1/2}$	3/2	1707.3
16	$3s^2 3p^6 3d^3_{3/2} 3d^6_{5/2} 4s_{1/2} 4p_{1/2}$	1/2	1708.4
18	$3s^2 3p^6 3d^4_{3/2} 3d^5_{5/2} 4s_{1/2} 4p_{3/2}$	5/2	1736.8
19	$3s^2 3p^6 3d^4_{3/2} 3d^5_{5/2} 4s_{1/2} 4p_{3/2}$	3/2	1737.0
20	$3s^2 3p^6 3d^4_{3/2} 3d^5_{5/2} 4s_{1/2} 4p_{3/2}$	7/2	1737.5
21	$3s^2 3p^6 3d^4_{3/2} 3d^5_{5/2} 4s_{1/2} 4p_{3/2}$	1/2	1738.1
24	$3s^2 3p^6 3d^4_{3/2} 3d^5_{5/2} 4s_{1/2} 4p_{3/2}$	3/2	1752.6
26	$3s^2 3p^6 3d^3_{3/2} 3d^6_{5/2} 4s_{1/2} 4p_{3/2}$	1/2	1797.6
27	$3s^2 3p^6 3d^3_{3/2} 3d^6_{5/2} 4s_{1/2} 4p_{3/2}$	3/2	1801.4
28	$3s^2 3p^6 3d^3_{3/2} 3d^6_{5/2} 4s_{1/2} 4p_{3/2}$	7/2	1801.7
31	$3s^2 3p^6 3d^3_{3/2} 3d^6_{5/2} 4s_{1/2} 4p_{3/2}$	1/2	1817.2
56	$3s^2 3p^6 3d^3_{3/2} 3d^6_{5/2} 4p_{1/2} 4p_{3/2}$	5/2	1909.8
57	$3s^2 3p^6 3d^3_{3/2} 3d^6_{5/2} 4p_{1/2} 4p_{3/2}$	3/2	1910.7
58	$3s^2 3p^6 3d^4_{3/2} 3d^5_{5/2} 4s_{1/2} 4d_{5/2}$	3/2	1911.4
64	$3s^2 3p^6 3d^4_{3/2} 3d^5_{5/2} 4s_{1/2} 4d_{5/2}$	5/2	1920.8
65	$3s^2 3p^6 3d^4_{3/2} 3d^5_{5/2} 4s_{1/2} 4d_{5/2}$	3/2	1920.8
67	$3s^2 3p^6 3d^4_{3/2} 3d^5_{5/2} 4s_{1/2} 4d_{5/2}$	1/2	1932.6
96	$3s^2 3p^2_{1/2} 3p^3_{3/2} 3d^{10} 4s^2$	3/2	2002.6
97	$3s^2 3p^6 3d^3_{3/2} 3d^6_{5/2} 4s_{1/2} 4d_{3/2}$	1/2	2002.7
111	$3s^2 3p^6 3d^3_{3/2} 3d^6_{5/2} 4p^2_{3/2}$	1/2	2017.3
145	$3s^2 3p^6 3d^4_{3/2} 3d^5_{5/2} 4s_{1/2} 4f_{7/2}$	7/2	2083.4
151	$3s^2 3p^6 3d^4_{3/2} 3d^5_{5/2} 4p_{3/2} 4d_{3/2}$	1/2	2089.4
152	$3s^2 3p^6 3d^4_{3/2} 3d^5_{5/2} 4p_{3/2} 4d_{3/2}$	3/2	2090.5
158	$3s^2 3p^6 3d^4_{3/2} 3d^5_{5/2} 4s_{1/2} 4f_{7/2}$	3/2	2094.9
159	$3s^2 3p^2_{1/2} 3p^3_{3/2} 3d^{10} 4s_{1/2} 4p_{1/2}$	3/2	2095.1

Table 7 – Energy levels in Cu-like W^{45+} continued

Index	Configuration	J	Energy (eV)
163	$3s^2 3p^6 3d^4_{3/2} 3d^5_{5/2} 4s_{1/2} 4f_{7/2}$	1/2	2097.7
168	$3s^2 3p^6 3d^4_{3/2} 3d^5_{5/2} 4p_{3/2} 4d_{3/2}$	3/2	2102.7
174	$3s^2 3p^6 3d^4_{3/2} 3d^5_{5/2} 4p_{3/2} 4d_{5/2}$	3/2	2109.3
190	$3s^2 3p^6 3d^4_{3/2} 3d^5_{5/2} 4p_{3/2} 4d_{5/2}$	3/2	2137.0
205	$3s^2 3p^6 3d^3_{3/2} 3d^6_{5/2} 4p_{3/2} 4d_{3/2}$	3/2	2155.2
206	$3s^2 3p^6 3d^3_{3/2} 3d^6_{5/2} 4p_{3/2} 4d_{3/2}$	1/2	2155.7
209	$3s^2 3p^6 3d^3_{3/2} 3d^6_{5/2} 4p_{3/2} 4d_{3/2}$	3/2	2158.3
218	$3s^2 3p^6 3d^3_{3/2} 3d^6_{5/2} 4s_{1/2} 4f_{5/2}$	1/2	2168.6
222	$3s^2 3p^6 3d^3_{3/2} 3d^6_{5/2} 4s_{1/2} 4f_{5/2}$	3/2	2169.8
238	$3s^2 3p^6 3d^3_{3/2} 3d^6_{5/2} 4p_{3/2} 4d_{5/2}$	3/2	2178.6
248	$3s^2 3p^6 3d^3_{3/2} 3d^6_{5/2} 4p_{3/2} 4d_{5/2}$	3/2	2188.4
251	$3s^2 3p^2_{1/2} 3p^3_{3/2} 3d^{10} 4s_{1/2} 4p_{3/2}$	5/2	2192.2
256	$3s^2 3p^2_{1/2} 3p^3_{3/2} 3d^{10} 4s_{1/2} 4p_{3/2}$	1/2	2197.0
262	$3s^2 3p^6 3d^3_{3/2} 3d^6_{5/2} 4p_{3/2} 4d_{3/2}$	3/2	2209.8
264	$3s^2 3p^2_{1/2} 3p^3_{3/2} 3d^{10} 4s_{1/2} 4p_{3/2}$	1/2	2222.4
417	$3s^2 3p^2_{1/2} 3p^3_{3/2} 3d^{10} 4s_{1/2} 4d_{3/2}$	1/2	2351.4
437	$3s^2 3p^2_{1/2} 3p^3_{3/2} 3d^{10} 4s_{1/2} 4d_{5/2}$	3/2	2370.0
441	$3s^2 3p^2_{1/2} 3p^3_{3/2} 3d^{10} 4s_{1/2} 4d_{5/2}$	1/2	2373.8
442	$3s^2 3p^2_{1/2} 3p^3_{3/2} 3d^{10} 4s_{1/2} 4d_{5/2}$	3/2	2375.3
454	$3s^2 3p_{1/2} 3p^4_{3/2} 3d^{10} 4s_{1/2} 4p_{1/2}$	1/2	2414.3
662	$3s^2 3p^2_{1/2} 3p^3_{3/2} 3d^{10} 4s_{1/2} 4f_{7/2}$	5/2	2541.3
663	$3s^2 3p^2_{1/2} 3p^3_{3/2} 3d^{10} 4s_{1/2} 4f_{7/2}$	3/2	2541.5
773	$3s_{1/2} 3p^6 3d^{10} 4s_{1/2} 4p_{1/2}$	3/2	2638.3
781	$3s^2 3p_{1/2} 3p^4_{3/2} 3d^{10} 4s_{1/2} 4d_{3/2}$	3/2	2663.0
907	$3s^2 3p_{1/2} 3p^4_{3/2} 3d^{10} 4s_{1/2} 4f_{5/2}$	5/2	2833.2
909	$3s^2 3p_{1/2} 3p^4_{3/2} 3d^{10} 4s_{1/2} 4f_{5/2}$	5/2	2835.4
1302	$3s^2 3p^6 3d^{10} 5p_{1/2}$	1/2	1016.2
1303	$3s^2 3p^6 3d^{10} 5p_{3/2}$	3/2	1063.7
1304	$3s^2 3p^6 3d^{10} 5d_{3/2}$	3/2	1135.4
1307	$3s^2 3p^6 3d^{10} 5f_{7/2}$	7/2	1220.3
1310	$3s^2 3p^6 3d^{10} 6s_{1/2}$	1/2	1449.7
1314	$3s^2 3p^6 3d^{10} 6d_{5/2}$	5/2	1548.5
1315	$3s^2 3p^6 3d^{10} 6f_{5/2}$	5/2	1587.3
1316	$3s^2 3p^6 3d^{10} 6f_{7/2}$	7/2	1589.2
1448	$3s^2 3p^6 3d^4_{3/2} 3d^5_{5/2} 4s_{1/2} 5f_{7/2}$	1/2	2780.5
1451	$3s^2 3p^6 3d^4_{3/2} 3d^5_{5/2} 4s_{1/2} 5f_{7/2}$	3/2	2783.1
1542	$3s^2 3p^6 3d^3_{3/2} 3d^6_{5/2} 4s_{1/2} 5f_{5/2}$	1/2	2843.4
1543	$3s^2 3p^6 3d^3_{3/2} 3d^6_{5/2} 4s_{1/2} 5f_{5/2}$	3/2	2844.7
1912	$3s^2 3p^2_{1/2} 3p^3_{3/2} 3d^{10} 4s_{1/2} 5d_{5/2}$	1/2	3150.2
1917	$3s^2 3p^2_{1/2} 3p^3_{3/2} 3d^{10} 4s_{1/2} 5d_{5/2}$	3/2	3154.7

Table 7 – Energy levels in Cu-like W^{45+} continued

Index	Configuration	J	Energy (eV)
1954	$3s^2 3p^2_{1/2} 3p^3_{3/2} 3d^{10} 4s_{1/2} 5f_{7/2}$	5/2	3231.2
2460	$3s^2 3p^6 3d^4_{3/2} 3d^5_{5/2} 4s_{1/2} 6f_{7/2}$	1/2	3150.7
2461	$3s^2 3p^6 3d^4_{3/2} 3d^5_{5/2} 4s_{1/2} 6f_{7/2}$	3/2	3151.9
2582	$3s^2 3p^6 3d^3_{3/2} 3d^6_{5/2} 4s_{1/2} 6f_{5/2}$	3/2	3214.7
2583	$3s^2 3p^6 3d^3_{3/2} 3d^6_{5/2} 4s_{1/2} 6f_{5/2}$	1/2	3215.0

Table 8: Radiative transitions in Cu-like W^{45+}

i	k	ΔE (eV)	λ (Å)	gf	A_{ki} (s^{-1})	ϵ_{line} ($ion^{-1}s^{-1}$)
6	7	1010.01	12.2756	7.81×10^{-5}	5.76×10^{8}	206
0	1302	1016.17	12.2011	2.05×10^{-1}	4.60×10^{12}	247
1	1304	1037.82	11.9466	3.04×10^{-1}	3.55×10^{12}	179
0	1303	1063.73	11.6556	1.88×10^{-1}	2.31×10^{12}	241
4	1316	1218.18	10.1778	8.90×10^{-1}	7.16×10^{12}	80
3	1315	1237.76	10.0169	6.02×10^{-1}	6.67×10^{12}	66
2	1310	1250.77	9.9126	9.85×10^{-2}	3.34×10^{12}	114
2	1314	1349.55	9.1871	3.11×10^{-1}	4.10×10^{12}	67
1	8	1516.36	8.1765	2.64×10^{-4}	6.58×10^{9}	416
1	9	1534.54	8.0796	7.10×10^{-5}	1.21×10^{9}	294
2	18	1537.86	8.0621	1.77×10^{-4}	3.03×10^{9}	54
2	20	1538.63	8.0581	1.78×10^{-4}	2.28×10^{9}	104
1	11	1541.98	8.0406	2.39×10^{-4}	4.11×10^{9}	67
0	7	1547.67	8.0110	2.79×10^{-4}	4.82×10^{9}	1726
2	28	1602.77	7.7356	2.97×10^{-4}	4.14×10^{9}	205
1	14	1608.27	7.7092	2.27×10^{-4}	4.25×10^{9}	57
0	8	1613.95	7.6820	1.78×10^{-4}	5.02×10^{9}	318
0	13	1698.73	7.2987	2.57×10^{-2}	8.04×10^{11}	379
0	15	1707.30	7.2620	1.63×10^{-1}	5.14×10^{12}	1427
0	16	1708.40	7.2573	8.61×10^{-2}	5.45×10^{12}	857
2	56	1710.85	7.2469	1.92×10^{-1}	4.06×10^{12}	74
2	57	1711.76	7.2431	1.14×10^{-1}	3.62×10^{12}	64
4	145	1712.40	7.2404	2.67×10^{-2}	4.25×10^{11}	91
2	58	1712.48	7.2400	7.42×10^{-2}	2.36×10^{12}	103
2	64	1721.93	7.2003	4.82×10^{-2}	1.03×10^{12}	75
2	65	1721.94	7.2002	2.08×10^{-2}	6.69×10^{11}	76
2	67	1733.73	7.1513	1.64×10^{-2}	1.07×10^{12}	267
0	19	1736.99	7.1379	1.24×10^{-1}	4.07×10^{12}	513
0	21	1738.13	7.1332	1.54×10^{-1}	1.01×10^{13}	517
4	174	1738.26	7.1326	1.28×10^{-1}	4.19×10^{12}	82
3	158	1745.43	7.1034	8.60×10^{-2}	2.84×10^{12}	71
0	24	1752.57	7.0744	2.09×10^{-1}	6.97×10^{12}	740
3	168	1753.17	7.0720	1.57×10^{-1}	5.22×10^{12}	100
0	26	1797.62	6.8971	5.14×10^{-3}	3.61×10^{11}	179
0	27	1801.43	6.8825	2.88×10^{-2}	1.01×10^{12}	302
2	97	1803.82	6.8734	4.62×10^{-3}	3.26×10^{11}	410
0	31	1817.19	6.8228	2.32×10^{-2}	1.66×10^{12}	229
2	111	1818.42	6.8182	1.71×10^{-2}	1.23×10^{12}	353
1	97	1905.14	6.5079	6.53×10^{-4}	5.14×10^{10}	65
2	251	1993.28	6.2201	3.00×10^{-1}	8.63×10^{12}	63
1	159	1997.50	6.2070	3.87×10^{-1}	1.67×10^{13}	68
2	256	1998.07	6.2052	2.20×10^{-1}	1.91×10^{13}	166

Table 8 – Radiative transitions in Cu-like W^{45+} continued

i	k	ΔE (eV)	λ (Å)	gf	A_{ki} (s^{-1})	ϵ_{line} ($ion^{-1}s^{-1}$)
4	437	1999.00	6.2023	4.14×10^{-1}	1.79×10^{13}	136
0	96	2002.59	6.1912	3.53×10^{-1}	1.54×10^{13}	396
6	662	2003.65	6.1879	5.15×10^{-1}	1.50×10^{13}	423
5	663	2009.24	6.1707	6.76×10^{-2}	2.96×10^{12}	152
1307	1954	2010.87	6.1657	4.72×10^{-1}	1.38×10^{13}	75
2	264	2023.50	6.1272	6.11×10^{-2}	5.42×10^{12}	1232
0	151	2089.44	5.9339	5.08×10^{-2}	4.81×10^{12}	54
0	152	2090.51	5.9308	1.16×10^{-1}	5.49×10^{12}	124
0	158	2094.94	5.9183	1.58	7.52×10^{13}	1876
0	163	2097.71	5.9104	1.04	9.97×10^{13}	1293
0	168	2102.68	5.8965	3.86×10^{-1}	1.85×10^{13}	354
0	174	2109.31	5.8780	4.05×10^{-1}	1.96×10^{13}	385
0	190	2137.04	5.8017	1.35×10^{-1}	6.67×10^{12}	130
0	205	2155.20	5.7528	7.73×10^{-1}	3.90×10^{13}	871
0	206	2155.72	5.7514	1.86×10^{-1}	1.87×10^{13}	199
0	209	2158.35	5.7444	1.55	7.85×10^{13}	1743
0	218	2168.60	5.7172	3.78	3.86×10^{14}	4236
0	222	2169.76	5.7142	4.65	2.38×10^{14}	5242
0	238	2178.58	5.6911	1.40×10^{-1}	7.20×10^{12}	136
0	248	2188.43	5.6654	1.63×10^{-1}	8.47×10^{12}	141
0	262	2209.85	5.6105	3.87×10^{-1}	2.05×10^{13}	353
1	454	2316.72	5.3517	2.97×10^{-2}	3.46×10^{12}	315
2	662	2342.40	5.2930	1.99×10^{-1}	7.90×10^{12}	224
2	663	2342.56	5.2927	2.21×10^{-2}	1.31×10^{12}	67
0	417	2351.40	5.2728	1.85×10^{-1}	2.21×10^{13}	69
0	437	2370.04	5.2313	1.34	8.14×10^{13}	617
0	441	2373.80	5.2230	5.38×10^{-1}	6.58×10^{13}	306
0	442	2375.32	5.2197	2.14×10^{-1}	1.31×10^{13}	97
2	907	2634.26	4.7066	2.47×10^{-1}	1.24×10^{13}	71
2	909	2636.48	4.7026	3.78×10^{-1}	1.90×10^{13}	62
0	773	2638.29	4.6994	5.36×10^{-1}	4.05×10^{13}	178
0	781	2662.95	4.6559	1.71×10^{-1}	1.32×10^{13}	53
0	1448	2780.50	4.4591	5.10×10^{-1}	8.55×10^{13}	360
0	1451	2783.11	4.4549	1.11	9.30×10^{13}	801
0	1542	2843.41	4.3604	6.17×10^{-1}	1.08×10^{14}	455
0	1543	2844.69	4.3584	1.37	1.20×10^{14}	928
0	1912	3150.21	3.9357	2.41×10^{-1}	5.19×10^{13}	74
0	2460	3150.67	3.9352	2.71×10^{-1}	5.83×10^{13}	181
0	2461	3151.94	3.9336	5.38×10^{-1}	5.80×10^{13}	347
0	1917	3154.74	3.9301	3.94×10^{-1}	4.26×10^{13}	89
0	2582	3214.74	3.8567	4.87×10^{-1}	5.46×10^{13}	288
0	2583	3215.02	3.8564	2.52×10^{-1}	5.65×10^{13}	165

Table 9: Energy levels in Ni-like W^{46+}

Index	Configuration	J	Energy (eV)
0	$3s^2 3p^6 3d^{10}$	0	0.0
1	$3s^2 3p^6 3d^4_{3/2} 3d^5_{5/2} 4s_{1/2}$	3	1562.1
2	$3s^2 3p^6 3d^4_{3/2} 3d^5_{5/2} 4s_{1/2}$	2	1564.1
4	$3s^2 3p^6 3d^3_{3/2} 3d^6_{5/2} 4s_{1/2}$	2	1630.0
8	$3s^2 3p^6 3d^3_{3/2} 3d^6_{5/2} 4p_{1/2}$	1	1728.7
11	$3s^2 3p^6 3d^4_{3/2} 3d^5_{5/2} 4p_{3/2}$	1	1764.8
14	$3s^2 3p^6 3d^3_{3/2} 3d^6_{5/2} 4p_{3/2}$	1	1829.4
35	$3s^2 3p^2_{1/2} 3p^3_{3/2} 3d^{10} 4s_{1/2}$	1	2017.4
50	$3s^2 3p^6 3d^4_{3/2} 3d^5_{5/2} 4f_{7/2}$	1	2112.6
58	$3s^2 3p^6 3d^3_{3/2} 3d^6_{5/2} 4f_{5/2}$	1	2181.4
71	$3s^2 3p^2_{1/2} 3p^3_{3/2} 3d^{10} 4d_{5/2}$	1	2386.0
84	$3s^2 3p^2_{1/2} 3p^3_{3/2} 3d^{10} 4f_{7/2}$	2	2554.7
87	$3s_{1/2} 3p^6 3d^{10} 4p_{1/2}$	1	2655.0
90	$3s^2 3p_{1/2} 3p^4_{3/2} 3d^{10} 4d_{3/2}$	1	2678.6
94	$3s_{1/2} 3p^6 3d^{10} 4p_{3/2}$	1	2765.6
141	$3s^2 3p^6 3d^3_{3/2} 3d^6_{5/2} 5d_{3/2}$	0	2800.1
152	$3s^2 3p^6 3d^4_{3/2} 3d^5_{5/2} 5f_{7/2}$	1	2814.9
172	$3s^2 3p^6 3d^3_{3/2} 3d^6_{5/2} 5f_{5/2}$	1	2877.3
195	$3s^2 3p^2_{1/2} 3p^3_{3/2} 3d^{10} 5d_{5/2}$	1	3183.9
286	$3s^2 3p^6 3d^4_{3/2} 3d^5_{5/2} 6f_{7/2}$	1	3195.5
326	$3s^2 3p^6 3d^3_{3/2} 3d^6_{5/2} 6f_{5/2}$	1	3258.9

Table 10: Radiative transitions in Ni-like W^{46+}

i	k	ΔE (eV)	λ (Å)	gf	A_{ki} (s^{-1})	ϵ_{line} ($ion^{-1}s^{-1}$)
8	141	1071.37	11.572	7.70×10^{-2}	3.84×10^{12}	231
0	1	1562.15	7.9368	6.05×10^{-10}	9.15×10^{3}	532
0	2	1564.07	7.9270	2.76×10^{-4}	5.86×10^{9}	4686
0	4	1629.99	7.6064	1.93×10^{-4}	4.46×10^{9}	1359
0	8	1728.69	7.1722	1.43×10^{-1}	6.17×10^{12}	4204
0	11	1764.83	7.0253	2.58×10^{-1}	1.16×10^{13}	3574
0	14	1829.45	6.7771	2.66×10^{-2}	1.29×10^{12}	570
0	35	2017.40	6.1458	3.58×10^{-1}	2.11×10^{13}	1722
0	50	2112.57	5.8689	1.98	1.28×10^{14}	5149
0	58	2181.36	5.6838	5.89	4.05×10^{14}	13257
0	71	2386.03	5.1963	1.16	9.52×10^{13}	1748
0	84	2554.73	4.8531	9.61×10^{-3}	5.44×10^{11}	348
0	87	2655.04	4.6698	4.28×10^{-1}	4.37×10^{13}	335
0	90	2678.60	4.6287	1.62×10^{-1}	1.68×10^{13}	171
0	94	2765.65	4.4830	1.31×10^{-1}	1.44×10^{13}	133
0	152	2814.90	4.4046	8.91×10^{-1}	1.02×10^{14}	1469
0	172	2877.30	4.3090	1.11	1.33×10^{14}	1769
0	195	3183.88	3.8941	4.18×10^{-1}	6.13×10^{13}	303
0	286	3195.47	3.8800	4.11×10^{-1}	6.07×10^{13}	571
0	326	3258.94	3.8044	3.80×10^{-1}	5.84×10^{13}	502

Table 11: Energy levels in Co-like W^{47+}

Index	Configuration	J	Energy (eV)
0	$3s^2 3p^6 3d^4_{3/2} 3d^5_{5/2}$	5/2	0.0
1	$3s^2 3p^6 3d^3_{3/2} 3d^6_{5/2}$	3/2	66.8
2	$3s^2 3p^2_{1/2} 3p^3_{3/2} 3d^{10}$	3/2	449.6
5	$3s^2 3p^6 3d^4_{3/2} 3d^4_{5/2} 4s_{1/2}$	9/2	1604.9
6	$3s^2 3p^6 3d^4_{3/2} 3d^4_{5/2} 4s_{1/2}$	7/2	1608.0
7	$3s^2 3p^6 3d^4_{3/2} 3d^4_{5/2} 4s_{1/2}$	5/2	1614.5
8	$3s^2 3p^6 3d^4_{3/2} 3d^4_{5/2} 4s_{1/2}$	3/2	1616.0
9	$3s^2 3p^6 3d^4_{3/2} 3d^4_{5/2} 4s_{1/2}$	1/2	1634.3
10	$3s^2 3p^6 3d^3_{3/2} 3d^5_{5/2} 4s_{1/2}$	7/2	1670.9
11	$3s^2 3p^6 3d^3_{3/2} 3d^5_{5/2} 4s_{1/2}$	5/2	1671.7
12	$3s^2 3p^6 3d^3_{3/2} 3d^5_{5/2} 4s_{1/2}$	5/2	1680.3
14	$3s^2 3p^6 3d^3_{3/2} 3d^5_{5/2} 4s_{1/2}$	3/2	1685.5
15	$3s^2 3p^6 3d^3_{3/2} 3d^5_{5/2} 4s_{1/2}$	9/2	1685.9
16	$3s^2 3p^6 3d^3_{3/2} 3d^5_{5/2} 4s_{1/2}$	7/2	1686.5
18	$3s^2 3p^6 3d^4_{3/2} 3d^4_{5/2} 4p_{1/2}$	7/2	1700.4
25	$3s^2 3p^6 3d^3_{3/2} 3d^5_{5/2} 4p_{1/2}$	7/2	1766.5
26	$3s^2 3p^6 3d^3_{3/2} 3d^5_{5/2} 4p_{1/2}$	5/2	1767.0
28	$3s^2 3p^6 3d^3_{3/2} 3d^5_{5/2} 4p_{1/2}$	3/2	1775.4
29	$3s^2 3p^6 3d^3_{3/2} 3d^5_{5/2} 4p_{1/2}$	5/2	1777.0
32	$3s^2 3p^6 3d^3_{3/2} 3d^5_{5/2} 4p_{1/2}$	7/2	1783.0
33	$3s^2 3p^6 3d^3_{3/2} 3d^5_{5/2} 4p_{1/2}$	3/2	1783.1
36	$3s^2 3p^6 3d^4_{3/2} 3d^4_{5/2} 4p_{3/2}$	7/2	1810.1
37	$3s^2 3p^6 3d^4_{3/2} 3d^4_{5/2} 4p_{3/2}$	5/2	1810.5
38	$3s^2 3p^6 3d^4_{3/2} 3d^4_{5/2} 4p_{3/2}$	5/2	1816.5
39	$3s^2 3p^6 3d^4_{3/2} 3d^4_{5/2} 4p_{3/2}$	7/2	1818.9
41	$3s^2 3p^6 3d^4_{3/2} 3d^4_{5/2} 4p_{3/2}$	3/2	1820.3
42	$3s^2 3p^6 3d^4_{3/2} 3d^4_{5/2} 4p_{3/2}$	3/2	1837.8
47	$3s^2 3p^6 3d^3_{3/2} 3d^5_{5/2} 4p_{3/2}$	5/2	1873.2
48	$3s^2 3p^6 3d^3_{3/2} 3d^5_{5/2} 4p_{3/2}$	7/2	1874.3
49	$3s^2 3p^6 3d^3_{3/2} 3d^5_{5/2} 4p_{3/2}$	3/2	1875.0
50	$3s^2 3p^6 3d^3_{3/2} 3d^5_{5/2} 4p_{3/2}$	5/2	1881.3
52	$3s^2 3p^6 3d^3_{3/2} 3d^5_{5/2} 4p_{3/2}$	3/2	1884.3
55	$3s^2 3p^6 3d^3_{3/2} 3d^5_{5/2} 4p_{3/2}$	5/2	1887.2
58	$3s^2 3p^6 3d^3_{3/2} 3d^5_{5/2} 4p_{3/2}$	7/2	1890.4
102	$3s^2 3p^2_{1/2} 3p^3_{3/2} 3d^4_{3/2} 3d^5_{5/2} 4s_{1/2}$	7/2	2038.3
109	$3s^2 3p^2_{1/2} 3p^3_{3/2} 3d^4_{3/2} 3d^5_{5/2} 4s_{1/2}$	5/2	2045.4
110	$3s^2 3p^2_{1/2} 3p^3_{3/2} 3d^4_{3/2} 3d^5_{5/2} 4s_{1/2}$	3/2	2046.8
124	$3s^2 3p^2_{1/2} 3p^3_{3/2} 3d^4_{3/2} 3d^5_{5/2} 4s_{1/2}$	7/2	2060.8

Table 11 – Energy levels in Co-like W^{47+} continued

Index	Configuration	J	Energy (eV)
125	$3s^2 3p_{1/2}^2 3p_{3/2}^3 3d_{3/2}^4 3d_{5/2}^5 4s_{1/2}$	5/2	2064.3
126	$3s^2 3p^6 3d_{3/2}^3 3d_{5/2}^5 4d_{3/2}$	5/2	2067.8
128	$3s^2 3p_{1/2}^2 3p_{3/2}^3 3d_{3/2}^4 3d_{5/2}^5 4s_{1/2}$	3/2	2072.7
155	$3s^2 3p^6 3d_{3/2}^4 3d_{5/2}^4 4f_{5/2}$	5/2	2131.1
160	$3s^2 3p^6 3d_{3/2}^4 3d_{5/2}^4 4f_{5/2}$	7/2	2133.6
161	$3s^2 3p^6 3d_{3/2}^4 3d_{5/2}^4 4f_{5/2}$	3/2	2135.6
164	$3s^2 3p^6 3d_{3/2}^4 3d_{5/2}^4 4f_{7/2}$	7/2	2137.7
170	$3s^2 3p^6 3d_{3/2}^4 3d_{5/2}^4 4f_{7/2}$	5/2	2143.5
172	$3s^2 3p^6 3d_{3/2}^4 3d_{5/2}^4 4f_{7/2}$	3/2	2145.1
174	$3s^2 3p^6 3d_{3/2}^4 3d_{5/2}^4 4f_{7/2}$	5/2	2153.5
175	$3s^2 3p^6 3d_{3/2}^4 3d_{5/2}^4 4f_{7/2}$	7/2	2155.4
178	$3s^2 3p^6 3d_{3/2}^4 3d_{5/2}^4 4f_{5/2}$	5/2	2158.0
179	$3s^2 3p^6 3d_{3/2}^4 3d_{5/2}^4 4f_{7/2}$	7/2	2164.3
186	$3s^2 3p^6 3d_{3/2}^3 3d_{5/2}^5 4f_{5/2}$	5/2	2192.8
187	$3s^2 3p^6 3d_{3/2}^3 3d_{5/2}^5 4f_{5/2}$	7/2	2194.8
200	$3s^2 3p^6 3d_{3/2}^3 3d_{5/2}^5 4f_{7/2}$	7/2	2205.2
205	$3s^2 3p^6 3d_{3/2}^3 3d_{5/2}^5 4f_{5/2}$	7/2	2208.7
206	$3s^2 3p^6 3d_{3/2}^3 3d_{5/2}^5 4f_{5/2}$	5/2	2209.1
207	$3s^2 3p^6 3d_{3/2}^3 3d_{5/2}^5 4f_{5/2}$	7/2	2209.1
222	$3s^2 3p^6 3d_{3/2}^3 3d_{5/2}^5 4f_{5/2}$	3/2	2220.8
227	$3s^2 3p^6 3d_{3/2}^3 3d_{5/2}^5 4f_{7/2}$	5/2	2225.0
228	$3s^2 3p^6 3d_{3/2}^3 3d_{5/2}^5 4f_{5/2}$	7/2	2227.5
229	$3s^2 3p^6 3d_{3/2}^3 3d_{5/2}^5 4f_{5/2}$	5/2	2228.4
230	$3s^2 3p^6 3d_{3/2}^3 3d_{5/2}^5 4f_{7/2}$	3/2	2230.5
234	$3s^2 3p_{1/2}^2 3p_{3/2}^3 3d_{3/2}^4 3d_{5/2}^5 4p_{3/2}$	5/2	2241.5
239	$3s^2 3p_{1/2}^2 3p_{3/2}^3 3d_{3/2}^4 3d_{5/2}^5 4p_{3/2}$	5/2	2252.6
284	$3s^2 3p_{1/2}^2 3p_{3/2}^3 3d_{3/2}^4 3d_{5/2}^5 4d_{5/2}$	5/2	2404.7
286	$3s^2 3p_{1/2}^2 3p_{3/2}^3 3d_{3/2}^4 3d_{5/2}^5 4d_{5/2}$	3/2	2406.7
287	$3s^2 3p_{1/2}^2 3p_{3/2}^3 3d_{3/2}^4 3d_{5/2}^5 4d_{3/2}$	5/2	2407.2
291	$3s^2 3p_{1/2}^2 3p_{3/2}^3 3d_{3/2}^4 3d_{5/2}^5 4d_{5/2}$	7/2	2408.6
295	$3s^2 3p_{1/2}^2 3p_{3/2}^3 3d_{3/2}^4 3d_{5/2}^5 4d_{5/2}$	7/2	2415.3
302	$3s^2 3p_{1/2}^2 3p_{3/2}^3 3d_{3/2}^4 3d_{5/2}^5 4d_{5/2}$	3/2	2422.3
306	$3s^2 3p_{1/2}^2 3p_{3/2}^3 3d_{3/2}^4 3d_{5/2}^5 4d_{5/2}$	5/2	2432.5
307	$3s^2 3p_{1/2}^2 3p_{3/2}^3 3d_{3/2}^4 3d_{5/2}^5 4d_{5/2}$	7/2	2433.2
309	$3s^2 3p_{1/2}^2 3p_{3/2}^3 3d_{3/2}^4 3d_{5/2}^5 4d_{5/2}$	7/2	2443.0
387	$3s^2 3p_{1/2}^2 3p_{3/2}^3 3d_{3/2}^4 3d_{5/2}^5 4f_{5/2}$	1/2	2583.3
388	$3s^2 3p_{1/2}^2 3p_{3/2}^3 3d_{3/2}^4 3d_{5/2}^5 4f_{5/2}$	5/2	2584.6
389	$3s^2 3p_{1/2}^2 3p_{3/2}^3 3d_{3/2}^4 3d_{5/2}^5 4f_{5/2}$	3/2	2585.5
400	$3s^2 3p_{1/2}^2 3p_{3/2}^3 3d_{3/2}^4 3d_{5/2}^5 4f_{7/2}$	5/2	2599.4

Table 11 – Energy levels in Co-like W^{47+} continued

Index	Configuration	J	Energy (eV)
406	$3s_{1/2}3p^6 3d^4_{3/2}3d^5_{5/2}4s_{1/2}$	5/2	2604.8
452	$3s_{1/2}3p^6 3d^4_{3/2}3d^5_{5/2}4p_{1/2}$	7/2	2690.0
457	$3s_{1/2}3p^6 3d^4_{3/2}3d^5_{5/2}4p_{1/2}$	3/2	2699.8
467	$3s^2 3p_{1/2}3p^4_{3/2}3d^4_{3/2}3d^5_{5/2}4d_{3/2}$	5/2	2724.7
854	$3s^2 3p^6 3d^4_{3/2}3d^4_{5/2}5d_{5/2}$	5/2	2817.1
902	$3s^2 3p^6 3d^3_{3/2}3d^5_{5/2}5d_{3/2}$	5/2	2878.6
905	$3s^2 3p^6 3d^4_{3/2}3d^4_{5/2}5f_{5/2}$	3/2	2880.9
907	$3s^2 3p^6 3d^4_{3/2}3d^4_{5/2}5f_{7/2}$	5/2	2881.1
919	$3s^2 3p^6 3d^4_{3/2}3d^4_{5/2}5f_{7/2}$	5/2	2887.0
920	$3s^2 3p^6 3d^4_{3/2}3d^4_{5/2}5f_{7/2}$	7/2	2888.5
980	$3s^2 3p^6 3d^3_{3/2}3d^5_{5/2}5f_{5/2}$	7/2	2947.7
994	$3s^2 3p^6 3d^3_{3/2}3d^5_{5/2}5f_{5/2}$	3/2	2954.0
998	$3s^2 3p^6 3d^3_{3/2}3d^5_{5/2}5f_{5/2}$	7/2	2955.3
1000	$3s^2 3p^6 3d^3_{3/2}3d^5_{5/2}5f_{5/2}$	5/2	2955.5
1956	$3s^2 3p^6 3d^4_{3/2}3d^4_{5/2}6f_{7/2}$	7/2	3286.2
2093	$3s^2 3p^6 3d^3_{3/2}3d^5_{5/2}6f_{5/2}$	3/2	3353.8
2095	$3s^2 3p^6 3d^3_{3/2}3d^5_{5/2}6f_{5/2}$	7/2	3354.4
2096	$3s^2 3p^6 3d^3_{3/2}3d^5_{5/2}6f_{5/2}$	5/2	3354.5

Table 12: Radiative transitions in Co-like W^{47+}

i	k	ΔE (eV)	λ (Å)	gf	A_{ki} (s^{-1})	ϵ_{line} ($ion^{-1}s^{-1}$)
38	854	1000.60	12.3910	3.85×10^{-1}	2.79×10^{12}	66
32	902	1095.64	11.3162	2.96×10^{-1}	2.57×10^{12}	112
0	5	1604.91	7.7253	6.99×10^{-5}	7.81×10^{8}	1165
1	11	1604.92	7.7252	2.67×10^{-4}	4.97×10^{9}	93
0	6	1608.03	7.7103	8.31×10^{-4}	1.17×10^{10}	815
1	12	1613.55	7.6839	1.07×10^{-4}	2.01×10^{9}	65
0	7	1614.52	7.6793	1.95×10^{-4}	3.67×10^{9}	696
0	8	1615.99	7.6723	3.17×10^{-4}	8.99×10^{9}	343
2	126	1618.19	7.6619	7.08×10^{-3}	1.34×10^{11}	227
1	14	1618.70	7.6595	9.41×10^{-5}	2.68×10^{9}	68
1	16	1619.74	7.6546	4.96×10^{-4}	7.05×10^{9}	304
0	9	1634.29	7.5864	1.07×10^{-4}	6.20×10^{9}	118
0	10	1670.95	7.4200	2.87×10^{-4}	4.35×10^{9}	280
0	12	1680.32	7.3786	1.79×10^{-4}	3.65×10^{9}	118
0	14	1685.47	7.3561	1.37×10^{-4}	4.22×10^{9}	108
0	15	1685.90	7.3542	4.52×10^{-4}	5.58×10^{9}	589
0	18	1700.37	7.2916	1.55×10^{-3}	2.44×10^{10}	129
0	25	1766.52	7.0185	3.51×10^{-2}	5.94×10^{11}	341
0	26	1767.01	7.0166	1.24×10^{-1}	2.79×10^{12}	670
0	28	1775.37	6.9836	3.41×10^{-2}	1.16×10^{12}	210
0	29	1776.99	6.9772	1.70×10^{-1}	3.87×10^{12}	711
0	32	1783.01	6.9537	3.99×10^{-1}	6.89×10^{12}	1756
0	33	1783.09	6.9533	1.66×10^{-1}	5.72×10^{12}	689
2	234	1791.91	6.9191	2.14×10^{-1}	4.98×10^{12}	94
2	239	1802.95	6.8767	3.10×10^{-1}	7.29×10^{12}	226
1	47	1806.38	6.8637	4.30×10^{-2}	1.01×10^{12}	66
1	49	1808.28	6.8565	1.85×10^{-1}	6.54×10^{12}	69
0	36	1810.14	6.8494	3.44×10^{-1}	6.11×10^{12}	1089
0	37	1810.53	6.8480	3.20×10^{-1}	7.59×10^{12}	623
1	50	1814.51	6.8329	4.35×10^{-2}	1.04×10^{12}	81
0	38	1816.45	6.8256	3.24×10^{-1}	7.73×10^{12}	779
1	52	1817.49	6.8217	1.99×10^{-1}	7.14×10^{12}	83
0	39	1818.92	6.8164	1.37×10^{-2}	2.46×10^{11}	160
0	41	1820.29	6.8112	2.84×10^{-1}	1.02×10^{13}	596
1	55	1820.44	6.8107	4.21×10^{-1}	1.01×10^{13}	116
0	42	1837.84	6.7462	4.04×10^{-2}	1.48×10^{12}	256
0	48	1874.33	6.6149	3.26×10^{-2}	6.22×10^{11}	105
0	58	1890.35	6.5588	3.17×10^{-2}	6.14×10^{11}	110
0	102	2038.31	6.0827	8.44×10^{-1}	1.90×10^{13}	422
0	109	2045.37	6.0617	2.22×10^{-1}	6.71×10^{12}	176
0	110	2046.83	6.0574	1.79×10^{-1}	8.13×10^{12}	92
0	124	2060.79	6.0164	1.77×10^{-1}	4.07×10^{12}	153

Table 12 – Radiative transitions in Co-like W^{47+} continued

i	k	ΔE (eV)	λ (Å)	gf	A_{ki} (s^{-1})	ϵ_{line} ($ion^{-1}s^{-1}$)
0	125	2064.34	6.0060	4.75×10^{-1}	1.46×10^{13}	270
0	128	2072.70	5.9818	3.13×10^{-1}	1.46×10^{13}	337
0	155	2131.08	5.8179	6.75×10^{-2}	2.22×10^{12}	77
0	160	2133.61	5.8110	4.94×10^{-2}	1.22×10^{12}	89
2	387	2133.66	5.8109	2.23×10^{-1}	2.20×10^{13}	77
2	388	2134.93	5.8074	5.41×10^{-1}	1.78×10^{13}	150
0	161	2135.59	5.8056	1.15×10^{-1}	5.70×10^{12}	78
2	389	2135.86	5.8049	5.21×10^{-1}	2.58×10^{13}	156
0	164	2137.72	5.7998	4.76×10^{-2}	1.18×10^{12}	162
0	170	2143.49	5.7842	1.35×10^{-1}	4.48×10^{12}	146
0	172	2145.12	5.7798	1.52	7.60×10^{13}	672
2	400	2149.73	5.7674	3.04×10^{-1}	1.01×10^{13}	69
0	174	2153.51	5.7573	2.58	8.65×10^{13}	1134
1	222	2153.99	5.7560	4.13×10^{-1}	2.08×10^{13}	144
2	406	2155.12	5.7530	1.98×10^{-1}	6.66×10^{12}	68
0	175	2155.44	5.7522	4.32	1.09×10^{14}	1891
0	178	2158.00	5.7453	9.14×10^{-1}	3.08×10^{13}	431
1	227	2158.19	5.7448	2.72	9.16×10^{13}	536
1	229	2161.68	5.7355	9.99×10^{-1}	3.38×10^{13}	328
1	230	2163.76	5.7300	2.74	1.39×10^{14}	298
0	179	2164.29	5.7286	7.59×10^{-1}	1.93×10^{13}	403
0	186	2192.77	5.6542	2.01×10^{-1}	6.99×10^{12}	115
0	187	2194.77	5.6491	2.15×10^{-1}	5.62×10^{12}	143
0	200	2205.23	5.6223	4.68×10^{-2}	1.23×10^{12}	66
0	205	2208.72	5.6134	2.22×10^{-1}	5.88×10^{12}	143
0	206	2209.11	5.6124	1.14×10^{-1}	4.03×10^{12}	62
0	207	2209.11	5.6124	2.93×10^{-1}	7.77×10^{12}	175
0	222	2220.76	5.5830	4.91	2.63×10^{14}	1818
0	227	2224.96	5.5724	2.87	1.03×10^{14}	602
0	228	2227.47	5.5662	1.57×10^{-1}	4.23×10^{14}	6121
0	229	2228.45	5.5637	7.77	2.79×10^{14}	2708
0	230	2230.53	5.5585	1.05	5.66×10^{13}	121
0	284	2404.66	5.1560	7.08×10^{-1}	2.96×10^{13}	181
0	286	2406.69	5.1517	8.92×10^{-1}	5.61×10^{13}	201
0	287	2407.23	5.1505	4.51×10^{-1}	1.89×10^{13}	111
0	291	2408.58	5.1476	4.64×10^{-1}	1.46×10^{13}	150
0	295	2415.31	5.1333	1.08	3.40×10^{13}	275
0	302	2422.26	5.1185	6.19×10^{-1}	3.94×10^{13}	133
0	306	2432.48	5.0970	1.20	5.12×10^{13}	265
0	307	2433.22	5.0955	1.36	4.36×10^{13}	331
0	309	2442.98	5.0751	2.72×10^{-1}	8.82×10^{12}	107
0	452	2690.03	4.6090	1.03	4.06×10^{13}	145
0	457	2699.76	4.1791	5.89×10^{-1}	4.65×10^{13}	85

Table 12 – Radiative transitions in Co-like W^{47+} continued

i	k	ΔE (eV)	λ (Å)	gf	A_{ki} (s^{-1})	ϵ_{line} ($ion^{-1}s^{-1}$)
0	467	2724.75	4.5503	4.72×10^{-1}	2.53×10^{13}	74
0	905	2880.94	4.3036	3.25×10^{-1}	2.92×10^{13}	78
0	907	2881.09	4.3034	3.13×10^{-1}	1.88×10^{13}	70
0	919	2886.98	4.2946	9.97×10^{-1}	6.01×10^{13}	276
0	920	2888.54	4.2923	1.67	7.54×10^{13}	478
0	980	2947.75	4.2061	4.40×10^{-1}	2.07×10^{13}	89
0	994	2954.00	4.1972	1.05	9.89×10^{13}	286
0	998	2955.28	4.1954	1.79	8.46×10^{13}	490
0	1000	2955.51	4.1950	1.34	8.48×10^{13}	368
0	1956	3286.18	3.7729	6.83×10^{-1}	4.00×10^{13}	159
0	2093	3353.76	3.6969	3.66×10^{-1}	4.46×10^{13}	81
0	2095	3354.44	3.6961	4.93×10^{-1}	3.01×10^{13}	102
0	2096	3354.47	3.6961	3.73×10^{-1}	3.03×10^{13}	77

Table 13: Energy levels in Fe-like W^{48+}

Index	Configuration	J	Energy (eV)
0	$3s^2 3p^6 3d^4_{3/2} 3d^4_{5/2}$	4	0.0
1	$3s^2 3p^6 3d^4_{3/2} 3d^4_{5/2}$	2	8.9
2	$3s^2 3p^6 3d^4_{3/2} 3d^4_{5/2}$	0	28.4
3	$3s^2 3p^6 3d^3_{3/2} 3d^5_{5/2}$	3	65.2
4	$3s^2 3p^6 3d^3_{3/2} 3d^5_{5/2}$	2	74.7
5	$3s^2 3p^6 3d^3_{3/2} 3d^5_{5/2}$	1	80.0
6	$3s^2 3p^6 3d^3_{3/2} 3d^5_{5/2}$	4	80.2
9	$3s^2 3p^2_{1/2} 3p^3_{3/2} 3d^4_{3/2} 3d^5_{5/2}$	4	426.9
10	$3s^2 3p^2_{1/2} 3p^3_{3/2} 3d^4_{3/2} 3d^5_{5/2}$	2	437.0
11	$3s^2 3p^2_{1/2} 3p^3_{3/2} 3d^4_{3/2} 3d^5_{5/2}$	3	453.1
35	$3s^2 3p^6 3d^4_{3/2} 3d^3_{5/2} 4s_{1/2}$	5	1656.2
36	$3s^2 3p^6 3d^4_{3/2} 3d^3_{5/2} 4s_{1/2}$	4	1659.9
37	$3s^2 3p^6 3d^4_{3/2} 3d^3_{5/2} 4s_{1/2}$	2	1670.4
38	$3s^2 3p^6 3d^4_{3/2} 3d^3_{5/2} 4s_{1/2}$	1	1671.8
39	$3s^2 3p^6 3d^4_{3/2} 3d^3_{5/2} 4s_{1/2}$	3	1677.4
40	$3s^2 3p^6 3d^4_{3/2} 3d^3_{5/2} 4s_{1/2}$	2	1679.6
41	$3s^2 3p^6 3d^3_{3/2} 3d^4_{5/2} 4s_{1/2}$	4	1722.1
43	$3s^2 3p^6 3d^3_{3/2} 3d^4_{5/2} 4s_{1/2}$	5	1729.1
49	$3s^2 3p^6 3d^3_{3/2} 3d^4_{5/2} 4s_{1/2}$	6	1737.4
52	$3s^2 3p^6 3d^3_{3/2} 3d^4_{5/2} 4s_{1/2}$	5	1739.3
57	$3s^2 3p^6 3d^4_{3/2} 3d^3_{5/2} 4p_{1/2}$	4	1750.5
58	$3s^2 3p^6 3d^4_{3/2} 3d^3_{5/2} 4p_{1/2}$	5	1752.3
63	$3s^2 3p^6 3d^4_{3/2} 3d^3_{5/2} 4p_{1/2}$	2	1771.2
64	$3s^2 3p^6 3d^4_{3/2} 3d^3_{5/2} 4p_{1/2}$	3	1772.3
75	$3s^2 3p^6 3d^3_{3/2} 3d^4_{5/2} 4p_{1/2}$	3	1816.6
76	$3s^2 3p^6 3d^3_{3/2} 3d^4_{5/2} 4p_{1/2}$	4	1817.4
77	$3s^2 3p^6 3d^3_{3/2} 3d^4_{5/2} 4p_{1/2}$	5	1824.0
78	$3s^2 3p^6 3d^3_{3/2} 3d^4_{5/2} 4p_{1/2}$	4	1824.7
79	$3s^2 3p^6 3d^3_{3/2} 3d^4_{5/2} 4p_{1/2}$	2	1827.1
81	$3s^2 3p^6 3d^3_{3/2} 3d^4_{5/2} 4p_{1/2}$	2	1827.7
83	$3s^2 3p^6 3d^3_{3/2} 3d^4_{5/2} 4p_{1/2}$	3	1831.7
86	$3s^2 3p^6 3d^3_{3/2} 3d^4_{5/2} 4p_{1/2}$	1	1832.8
87	$3s^2 3p^6 3d^3_{3/2} 3d^4_{5/2} 4p_{1/2}$	5	1833.5
89	$3s^2 3p^6 3d^3_{3/2} 3d^4_{5/2} 4p_{1/2}$	4	1839.2
90	$3s^2 3p^6 3d^3_{3/2} 3d^4_{5/2} 4p_{1/2}$	3	1840.1
91	$3s^2 3p^6 3d^3_{3/2} 3d^4_{5/2} 4p_{1/2}$	3	1844.5
92	$3s^2 3p^6 3d^3_{3/2} 3d^4_{5/2} 4p_{1/2}$	2	1845.4
94	$3s^2 3p^6 3d^4_{3/2} 3d^3_{5/2} 4p_{3/2}$	5	1860.9

Table 13 – Energy levels in Fe-like W^{48+} continued

Index	Configuration	J	Energy (eV)
95	$3s^2 3p^6 3d^3_{3/2} 3d^4_{5/2} 4p_{1/2}$	2	1862.0
96	$3s^2 3p^6 3d^4_{3/2} 3d^3_{5/2} 4p_{3/2}$	3	1864.7
97	$3s^2 3p^6 3d^3_{3/2} 3d^4_{5/2} 4p_{1/2}$	1	1865.1
98	$3s^2 3p^6 3d^4_{3/2} 3d^3_{5/2} 4p_{3/2}$	4	1865.1
101	$3s^2 3p^6 3d^4_{3/2} 3d^3_{5/2} 4p_{3/2}$	2	1874.8
102	$3s^2 3p^6 3d^4_{3/2} 3d^3_{5/2} 4p_{3/2}$	3	1874.9
104	$3s^2 3p^6 3d^4_{3/2} 3d^3_{5/2} 4p_{3/2}$	1	1878.6
105	$3s^2 3p^6 3d^4_{3/2} 3d^3_{5/2} 4p_{3/2}$	4	1881.9
106	$3s^2 3p^6 3d^4_{3/2} 3d^3_{5/2} 4p_{3/2}$	2	1882.7
107	$3s^2 3p^6 3d^4_{3/2} 3d^3_{5/2} 4p_{3/2}$	3	1884.4
108	$3s^2 3p^6 3d^4_{3/2} 3d^3_{5/2} 4p_{3/2}$	1	1887.8
123	$3s^2 3p^6 3d^3_{3/2} 3d^4_{5/2} 4p_{3/2}$	3	1929.4
126	$3s^2 3p^6 3d^3_{3/2} 3d^4_{5/2} 4p_{3/2}$	4	1933.9
127	$3s^2 3p^6 3d^3_{3/2} 3d^4_{5/2} 4p_{3/2}$	5	1934.5
131	$3s^2 3p^6 3d^3_{3/2} 3d^4_{5/2} 4p_{3/2}$	4	1938.0
136	$3s^2 3p^6 3d^3_{3/2} 3d^4_{5/2} 4p_{3/2}$	3	1942.0
137	$3s^2 3p^6 3d^3_{3/2} 3d^4_{5/2} 4p_{3/2}$	4	1942.9
140	$3s^2 3p^6 3d^3_{3/2} 3d^4_{5/2} 4p_{3/2}$	5	1943.8
144	$3s^2 3p^6 3d^3_{3/2} 3d^4_{5/2} 4p_{3/2}$	4	1949.6
146	$3s^2 3p^6 3d^3_{3/2} 3d^4_{5/2} 4p_{3/2}$	5	1950.7
212	$3s^2 3p^2_{1/2} 3p^3_{3/2} 3d^4_{3/2} 3d^4_{5/2} 4s_{1/2}$	5	2069.9
222	$3s^2 3p^2_{1/2} 3p^3_{3/2} 3d^4_{3/2} 3d^4_{5/2} 4s_{1/2}$	3	2078.6
224	$3s^2 3p^2_{1/2} 3p^3_{3/2} 3d^4_{3/2} 3d^4_{5/2} 4s_{1/2}$	4	2078.8
229	$3s^2 3p^2_{1/2} 3p^3_{3/2} 3d^4_{3/2} 3d^4_{5/2} 4s_{1/2}$	2	2080.8
234	$3s^2 3p^2_{1/2} 3p^3_{3/2} 3d^4_{3/2} 3d^4_{5/2} 4s_{1/2}$	3	2082.7
237	$3s^2 3p^2_{1/2} 3p^3_{3/2} 3d^4_{3/2} 3d^4_{5/2} 4s_{1/2}$	5	2086.1
242	$3s^2 3p^2_{1/2} 3p^3_{3/2} 3d^4_{3/2} 3d^4_{5/2} 4s_{1/2}$	4	2090.1
279	$3s^2 3p^2_{1/2} 3p^3_{3/2} 3d^4_{3/2} 3d^4_{5/2} 4s_{1/2}$	4	2112.0
285	$3s^2 3p^6 3d^3_{3/2} 3d^4_{5/2} 4d_{3/2}$	4	2114.9
287	$3s^2 3p^2_{1/2} 3p^3_{3/2} 3d^4_{3/2} 3d^4_{5/2} 4s_{1/2}$	3	2115.6
288	$3s^2 3p^2_{1/2} 3p^3_{3/2} 3d^4_{3/2} 3d^4_{5/2} 4s_{1/2}$	3	2116.2
299	$3s^2 3p^6 3d^3_{3/2} 3d^4_{5/2} 4d_{3/2}$	2	2124.7
387	$3s^2 3p^6 3d^4_{3/2} 3d^3_{5/2} 4f_{5/2}$	4	2181.3
390	$3s^2 3p^6 3d^4_{3/2} 3d^3_{5/2} 4f_{7/2}$	2	2182.2
394	$3s^2 3p^6 3d^4_{3/2} 3d^3_{5/2} 4f_{7/2}$	3	2183.9
396	$3s^2 3p^6 3d^4_{3/2} 3d^3_{5/2} 4f_{5/2}$	3	2184.1
398	$3s^2 3p^6 3d^4_{3/2} 3d^3_{5/2} 4f_{7/2}$	5	2185.2
400	$3s^2 3p^6 3d^4_{3/2} 3d^3_{5/2} 4f_{7/2}$	4	2190.7
403	$3s^2 3p^6 3d^4_{3/2} 3d^3_{5/2} 4f_{5/2}$	3	2191.8

Table 13 – Energy levels in Fe-like W^{48+} continued

Index	Configuration	J	Energy (eV)
405	$3s^2 3p^6 3d^4_{3/2} 3d^3_{5/2} 4f_{7/2}$	4	2192.2
413	$3s^2 3p^6 3d^4_{3/2} 3d^3_{5/2} 4f_{5/2}$	5	2193.8
415	$3s^2 3p^6 3d^4_{3/2} 3d^3_{5/2} 4f_{7/2}$	1	2195.0
420	$3s^2 3p^6 3d^4_{3/2} 3d^3_{5/2} 4f_{5/2}$	4	2197.6
422	$3s^2 3p^6 3d^4_{3/2} 3d^3_{5/2} 4f_{7/2}$	5	2199.2
424	$3s^2 3p^6 3d^4_{3/2} 3d^3_{5/2} 4f_{7/2}$	2	2199.4
425	$3s^2 3p^6 3d^4_{3/2} 3d^3_{5/2} 4f_{7/2}$	4	2201.1
426	$3s^2 3p^6 3d^4_{3/2} 3d^3_{5/2} 4f_{7/2}$	2	2203.7
427	$3s^2 3p^6 3d^4_{3/2} 3d^3_{5/2} 4f_{7/2}$	3	2204.2
431	$3s^2 3p^6 3d^4_{3/2} 3d^3_{5/2} 4f_{7/2}$	5	2206.1
437	$3s^2 3p^6 3d^4_{3/2} 3d^3_{5/2} 4f_{7/2}$	3	2210.1
442	$3s^2 3p^6 3d^4_{3/2} 3d^3_{5/2} 4f_{7/2}$	1	2219.7
456	$3s^2 3p^6 3d^3_{3/2} 3d^4_{5/2} 4f_{5/2}$	5	2239.1
478	$3s^2 3p^6 3d^3_{3/2} 3d^4_{5/2} 4f_{5/2}$	4	2246.0
483	$3s^2 3p^6 3d^3_{3/2} 3d^4_{5/2} 4f_{5/2}$	5	2247.5
489	$3s^2 3p^6 3d^3_{3/2} 3d^4_{5/2} 4f_{5/2}$	5	2249.4
534	$3s^2 3p^6 3d^3_{3/2} 3d^4_{5/2} 4f_{7/2}$	3	2262.7
541	$3s^2 3p^6 3d^3_{3/2} 3d^4_{5/2} 4f_{5/2}$	3	2265.7
544	$3s^2 3p^6 3d^3_{3/2} 3d^4_{5/2} 4f_{7/2}$	4	2266.8
547	$3s^2 3p^6 3d^3_{3/2} 3d^4_{5/2} 4f_{7/2}$	4	2268.2
548	$3s^2 3p^6 3d^3_{3/2} 3d^4_{5/2} 4f_{5/2}$	5	2268.3
552	$3s^2 3p^6 3d^3_{3/2} 3d^4_{5/2} 4f_{5/2}$	3	2269.1
553	$3s^2 3p^6 3d^3_{3/2} 3d^4_{5/2} 4f_{7/2}$	4	2270.9
562	$3s^2 3p^6 3d^3_{3/2} 3d^4_{5/2} 4f_{5/2}$	5	2274.1
563	$3s^2 3p^6 3d^3_{3/2} 3d^4_{5/2} 4f_{7/2}$	4	2274.4
567	$3s^2 3p^6 3d^3_{3/2} 3d^4_{5/2} 4f_{7/2}$	2	2276.0
573	$3s^2 3p^6 3d^3_{3/2} 3d^4_{5/2} 4f_{5/2}$	1	2279.3
574	$3s^2 3p^6 3d^3_{3/2} 3d^4_{5/2} 4f_{5/2}$	2	2280.2
576	$3s^2 3p^6 3d^3_{3/2} 3d^4_{5/2} 4f_{7/2}$	3	2281.1
579	$3s^2 3p^6 3d^3_{3/2} 3d^4_{5/2} 4f_{5/2}$	3	2282.4
580	$3s^2 3p^6 3d^3_{3/2} 3d^4_{5/2} 4f_{7/2}$	2	2282.7
582	$3s^2 3p^6 3d^3_{3/2} 3d^4_{5/2} 4f_{7/2}$	1	2283.7
584	$3s^2 3p^2_{1/2} 3p^3_{3/2} 3d^4_{3/2} 3d^4_{5/2} 4p_{3/2}$	4	2285.1
590	$3s^2 3p^2_{1/2} 3p^3_{3/2} 3d^4_{3/2} 3d^4_{5/2} 4p_{3/2}$	4	2287.6
597	$3s^2 3p^6 3d^3_{3/2} 3d^4_{5/2} 4f_{5/2}$	3	2291.8
602	$3s^2 3p^2_{1/2} 3p^3_{3/2} 3d^4_{3/2} 3d^4_{5/2} 4p_{3/2}$	2	2294.5
605	$3s^2 3p^2_{1/2} 3p^3_{3/2} 3d^4_{3/2} 3d^4_{5/2} 4p_{3/2}$	4	2301.8
606	$3s^2 3p^6 3d^3_{3/2} 3d^4_{5/2} 4f_{5/2}$	1	2302.9
650	$3s^2 3p^2_{1/2} 3p^3_{3/2} 3d^4_{3/2} 3d^4_{5/2} 4p_{3/2}$	4	2325.9

Table 13 – Energy levels in Fe-like W^{48+} continued

Index	Configuration	J	Energy (eV)
792	$3s^2 3p_{1/2}^2 3p_{3/2}^3 3d_{3/2}^4 3d_{5/2}^4 4d_{5/2}$	5	2436.4
795	$3s^2 3p_{1/2}^2 3p_{3/2}^3 3d_{3/2}^4 3d_{5/2}^4 4d_{5/2}$	3	2438.6
798	$3s^2 3p_{1/2}^2 3p_{3/2}^3 3d_{3/2}^4 3d_{5/2}^4 4d_{5/2}$	4	2441.0
807	$3s^2 3p_{1/2}^2 3p_{3/2}^3 3d_{3/2}^4 3d_{5/2}^4 4d_{5/2}$	5	2445.1
809	$3s^2 3p_{1/2}^2 3p_{3/2}^3 3d_{3/2}^4 3d_{5/2}^4 4d_{5/2}$	3	2446.5
820	$3s^2 3p_{1/2}^2 3p_{3/2}^3 3d_{3/2}^4 3d_{5/2}^4 4d_{5/2}$	4	2452.8
822	$3s^2 3p_{1/2}^2 3p_{3/2}^3 3d_{3/2}^4 3d_{5/2}^4 4d_{5/2}$	2	2455.1
828	$3s^2 3p_{1/2}^2 3p_{3/2}^3 3d_{3/2}^4 3d_{5/2}^4 4d_{3/2}$	4	2457.1
830	$3s^2 3p_{1/2}^2 3p_{3/2}^3 3d_{3/2}^4 3d_{5/2}^4 4d_{5/2}$	5	2457.8
831	$3s^2 3p_{1/2}^2 3p_{3/2}^3 3d_{3/2}^4 3d_{5/2}^4 4d_{5/2}$	5	2459.0
833	$3s^2 3p_{1/2}^2 3p_{3/2}^3 3d_{3/2}^4 3d_{5/2}^4 4d_{5/2}$	3	2460.1
837	$3s^2 3p_{1/2}^2 3p_{3/2}^3 3d_{3/2}^4 3d_{5/2}^4 4d_{5/2}$	2	2462.6
843	$3s^2 3p_{1/2}^2 3p_{3/2}^3 3d_{3/2}^4 3d_{5/2}^4 4d_{3/2}$	3	2465.7
849	$3s^2 3p_{1/2}^2 3p_{3/2}^3 3d_{3/2}^4 3d_{5/2}^4 4d_{5/2}$	3	2469.1
861	$3s^2 3p_{1/2}^2 3p_{3/2}^3 3d_{3/2}^4 3d_{5/2}^4 4d_{5/2}$	5	2480.6
865	$3s^2 3p_{1/2}^2 3p_{3/2}^3 3d_{3/2}^4 3d_{5/2}^4 4d_{5/2}$	4	2481.7
869	$3s^2 3p_{1/2}^2 3p_{3/2}^3 3d_{3/2}^4 3d_{5/2}^4 4d_{5/2}$	5	2484.0
871	$3s^2 3p_{1/2}^2 3p_{3/2}^3 3d_{3/2}^4 3d_{5/2}^4 4d_{5/2}$	3	2485.4
1109	$3s^2 3p_{1/2}^2 3p_{3/2}^3 3d_{3/2}^4 3d_{5/2}^4 4f_{7/2}$	3	2606.7
1115	$3s^2 3p_{1/2}^2 3p_{3/2}^3 3d_{3/2}^4 3d_{5/2}^4 4f_{7/2}$	5	2607.6
1129	$3s^2 3p_{1/2}^2 3p_{3/2}^3 3d_{3/2}^4 3d_{5/2}^4 4f_{7/2}$	4	2611.2
1133	$3s^2 3p_{1/2}^2 3p_{3/2}^3 3d_{3/2}^4 3d_{5/2}^4 4f_{7/2}$	2	2613.4
1135	$3s^2 3p_{1/2}^2 3p_{3/2}^3 3d_{3/2}^4 3d_{5/2}^4 4f_{5/2}$	3	2613.6
1201	$3s^2 3p_{1/2}^2 3p_{3/2}^3 3d_{3/2}^4 3d_{5/2}^4 4f_{7/2}$	4	2644.4
1427	$3s_{1/2} 3p^6 3d_{3/2}^4 3d_{5/2}^4 4p_{1/2}$	5	2727.2
1445	$3s_{1/2} 3p^6 3d_{3/2}^4 3d_{5/2}^4 4p_{1/2}$	3	2742.9
1447	$3s_{1/2} 3p^6 3d_{3/2}^4 3d_{5/2}^4 4p_{1/2}$	4	2745.4
1469	$3s^2 3p_{1/2} 3p_{3/2}^4 3d_{3/2}^4 3d_{5/2}^4 4d_{3/2}$	5	2759.0
1494	$3s^2 3p_{1/2} 3p_{3/2}^4 3d_{3/2}^4 3d_{5/2}^4 4d_{3/2}$	4	2770.2
1495	$3s^2 3p_{1/2} 3p_{3/2}^4 3d_{3/2}^4 3d_{5/2}^4 4d_{3/2}$	5	2770.7
2389	$3s^2 3p^6 3d_{3/2}^4 3d_{5/2}^3 5f_{7/2}$	5	2954.8
2391	$3s^2 3p^6 3d_{3/2}^4 3d_{5/2}^3 5f_{7/2}$	4	2955.7
2423	$3s^2 3p^6 3d_{3/2}^4 3d_{5/2}^3 5f_{7/2}$	5	2965.0
2444	$3s^2 3p^6 3d_{3/2}^4 3d_{5/2}^3 5f_{7/2}$	5	2973.8
2447	$3s^2 3p^6 3d_{3/2}^4 3d_{5/2}^3 5f_{7/2}$	3	2974.7
2456	$3s^2 3p^6 3d_{3/2}^4 3d_{5/2}^3 5f_{7/2}$	1	2980.0
2592	$3s^2 3p^6 3d_{3/2}^3 3d_{5/2}^4 5f_{7/2}$	4	3029.7
2596	$3s^2 3p^6 3d_{3/2}^3 3d_{5/2}^4 5f_{5/2}$	5	3030.6
2597	$3s^2 3p^6 3d_{3/2}^3 3d_{5/2}^4 5f_{5/2}$	4	3030.8

Table 13 – Energy levels in Fe-like W^{48+} continued

Index	Configuration	J	Energy (eV)
2606	$3s^2 3p^6 3d^3_{3/2} 3d^4_{5/2} 5f_{5/2}$	3	3031.9
2611	$3s^2 3p^6 3d^3_{3/2} 3d^4_{5/2} 5f_{5/2}$	4	3033.7
2633	$3s^2 3p^6 3d^3_{3/2} 3d^4_{5/2} 5f_{5/2}$	3	3043.0
2634	$3s^2 3p^6 3d^3_{3/2} 3d^4_{5/2} 5f_{5/2}$	2	3043.2
2696	$3s^2 3p^6 3d^3_{3/2} 3d^4_{5/2} 5f_{5/2}$	1	3063.6
5368	$3s^2 3p^6 3d^4_{3/2} 3d^3_{5/2} 6f_{7/2}$	5	3369.9
5369	$3s^2 3p^6 3d^4_{3/2} 3d^3_{5/2} 6f_{7/2}$	4	3370.3
5426	$3s^2 3p^6 3d^4_{3/2} 3d^3_{5/2} 6f_{7/2}$	5	3389.2
5654	$3s^2 3p^6 3d^3_{3/2} 3d^4_{5/2} 6f_{5/2}$	5	3446.4
5659	$3s^2 3p^6 3d^3_{3/2} 3d^4_{5/2} 6f_{5/2}$	3	3447.2

Table 14: Radiative transitions in Fe-like W^{48+}

i	k	ΔE (eV)	λ (Å)	gf	A_{ki} (s^{-1})	ϵ_{line} ($ion^{-1}s^{-1}$)
1	36	1650.93	7.5100	3.22×10^{-4}	4.23×10^{9}	88
2	40	1651.21	7.5087	1.99×10^{-4}	4.70×10^{9}	42
0	35	1656.20	7.4861	2.74×10^{-4}	2.96×10^{9}	638
6	49	1657.14	7.4818	9.74×10^{-5}	8.93×10^{8}	37
6	52	1659.05	7.4732	9.75×10^{-4}	1.06×10^{10}	127
0	36	1659.87	7.4695	9.50×10^{-4}	1.26×10^{10}	264
1	37	1661.41	7.4626	1.21×10^{-4}	2.91×10^{9}	58
11	285	1661.79	7.4609	2.07×10^{-2}	2.76×10^{11}	242
1	38	1662.81	7.4563	3.20×10^{-4}	1.28×10^{10}	102
0	37	1670.36	7.4226	1.89×10^{-4}	4.58×10^{9}	91
1	40	1670.63	7.4214	2.47×10^{-4}	5.98×10^{9}	54
0	39	1677.40	7.3915	3.27×10^{-4}	5.70×10^{9}	219
10	299	1687.70	7.3463	9.62×10^{-3}	2.38×10^{11}	69
9	285	1688.03	7.3449	1.04×10^{-2}	1.43×10^{11}	125
3	64	1707.06	7.2630	7.58×10^{-4}	1.37×10^{10}	36
0	41	1722.08	7.1997	1.68×10^{-4}	2.40×10^{9}	48
0	43	1729.06	7.1706	3.99×10^{-4}	4.70×10^{9}	133
0	49	1737.36	7.1364	6.06×10^{-4}	6.11×10^{9}	253
0	57	1750.51	7.0828	1.99×10^{-3}	2.94×10^{10}	93
0	58	1752.32	7.0754	7.75×10^{-4}	9.39×10^{9}	68
1	63	1762.29	7.0354	1.89×10^{-3}	5.09×10^{10}	47
1	75	1807.69	6.8587	4.11×10^{-2}	8.33×10^{11}	80
0	75	1816.64	6.8249	5.55×10^{-2}	1.13×10^{12}	109
0	76	1817.39	6.8221	4.54×10^{-2}	7.23×10^{11}	175
1	79	1818.18	6.8191	2.38×10^{-2}	6.84×10^{11}	50
1	81	1818.71	6.8171	1.84×10^{-2}	5.30×10^{11}	42
1	86	1823.83	6.7980	1.17×10^{-1}	5.65×10^{12}	101
0	77	1824.04	6.7972	3.67×10^{-2}	4.82×10^{11}	217
0	78	1824.72	6.7947	3.29×10^{-1}	5.28×10^{12}	520
1	90	1831.11	6.7710	1.55×10^{-1}	3.23×10^{12}	219
0	83	1831.66	6.7690	2.45×10^{-1}	5.09×10^{12}	349
0	87	1833.51	6.7621	5.91×10^{-1}	7.83×10^{12}	955
1	91	1835.60	6.7544	1.68×10^{-1}	3.52×10^{12}	200
1	92	1836.48	6.7512	2.01×10^{-1}	5.90×10^{12}	208
2	97	1836.72	6.7503	1.35×10^{-1}	6.57×10^{12}	130
0	89	1839.18	6.7413	6.77×10^{-2}	1.10×10^{12}	200
0	90	1840.06	6.7380	2.58×10^{-2}	5.41×10^{11}	37
11	605	1848.66	6.7067	3.35×10^{-1}	5.52×10^{12}	227
1	95	1853.07	6.6908	1.94×10^{-2}	5.78×10^{11}	64
1	96	1855.73	6.6811	2.31×10^{-1}	4.92×10^{12}	160
10	602	1857.54	6.6746	2.11×10^{-1}	6.33×10^{12}	35
9	584	1858.23	6.6722	4.32×10^{-1}	7.19×10^{12}	95

Table 14 – Radiative transitions in Fe-like W^{48+} continued

i	k	ΔE (eV)	λ (Å)	gf	A_{ki} (s^{-1})	ϵ_{line} ($ion^{-1}s^{-1}$)
2	108	1859.44	6.6678	1.67×10^{-1}	8.33×10^{12}	100
9	590	1860.77	6.6631	2.62×10^{-1}	4.37×10^{12}	48
0	94	1860.87	6.6627	1.87×10^{-1}	2.55×10^{12}	520
6	137	1862.65	6.6563	4.94×10^{-1}	8.26×10^{12}	40
6	140	1863.54	6.6532	3.82×10^{-1}	5.23×10^{12}	82
3	123	1864.15	6.6510	3.33×10^{-1}	7.17×10^{12}	36
0	96	1864.68	6.6491	1.18×10^{-1}	2.55×10^{12}	83
0	98	1865.13	6.6475	6.91×10^{-1}	1.16×10^{13}	532
1	101	1865.86	6.6449	1.84×10^{-1}	5.55×10^{12}	138
4	136	1867.33	6.6396	1.33×10^{-1}	2.88×10^{12}	46
3	126	1868.67	6.6349	2.82×10^{-1}	4.74×10^{12}	45
6	144	1869.36	6.6325	3.75×10^{-1}	6.32×10^{12}	43
1	104	1869.70	6.6312	2.84×10^{-1}	1.44×10^{13}	129
6	146	1870.48	6.6285	4.14×10^{-2}	5.72×10^{11}	43
11	650	1872.80	6.6203	1.98×10^{-2}	3.34×10^{11}	103
1	106	1873.75	6.6169	6.53×10^{-2}	1.99×10^{12}	112
0	102	1874.92	6.6128	3.44×10^{-1}	7.50×10^{12}	343
1	107	1875.42	6.6110	5.12×10^{-2}	1.12×10^{12}	75
0	105	1881.85	6.5884	4.83×10^{-2}	8.24×10^{11}	210
0	107	1884.37	6.5796	1.43×10^{-1}	3.14×10^{12}	212
0	127	1934.49	6.4091	4.09×10^{-2}	6.04×10^{11}	41
0	131	1938.04	6.3974	2.56×10^{-2}	4.63×10^{11}	36
0	212	2069.92	5.9898	1.11	1.87×10^{13}	265
1	229	2071.81	5.9843	2.89×10^{-1}	1.08×10^{13}	42
1	234	2073.71	5.9789	5.73×10^{-1}	1.53×10^{13}	90
0	222	2078.57	5.9649	1.51×10^{-1}	4.05×10^{12}	55
0	224	2078.76	5.9643	1.13×10^{-1}	2.35×10^{12}	55
0	237	2086.11	5.9433	3.00×10^{-1}	5.14×10^{12}	100
0	242	2090.13	5.9319	6.11×10^{-1}	1.29×10^{13}	135
1	287	2106.66	5.8854	2.23×10^{-1}	6.13×10^{12}	46
0	279	2112.04	5.8703	3.31×10^{-1}	7.12×10^{12}	106
0	288	2116.21	5.8588	5.93×10^{-1}	1.65×10^{13}	202
1	390	2173.23	5.7051	2.12×10^{-1}	8.69×10^{12}	51
10	1133	2176.42	5.6967	5.71×10^{-1}	2.35×10^{13}	35
10	1135	2176.62	5.6962	4.89×10^{-1}	1.43×10^{13}	42
9	1109	2179.83	5.6878	1.33	3.92×10^{13}	39
9	1115	2180.76	5.6854	7.71×10^{-1}	1.45×10^{13}	107
0	387	2181.32	5.6839	1.22×10^{-1}	2.80×10^{12}	49
0	394	2183.92	5.6771	7.84×10^{-1}	2.32×10^{13}	176
0	396	2184.07	5.6767	5.58×10^{-1}	1.65×10^{13}	134
9	1129	2184.29	5.6762	8.36×10^{-1}	1.92×10^{13}	82
0	398	2185.24	5.6737	3.81×10^{-1}	7.17×10^{12}	177
1	415	2186.10	5.6715	8.59×10^{-1}	5.94×10^{13}	127

Table 14 – Radiative transitions in Fe-like W^{48+} continued

i	k	ΔE (eV)	λ (Å)	gf	A_{ki} (s^{-1})	ϵ_{line} ($ion^{-1}s^{-1}$)
6	552	2188.84	5.6644	3.11×10^{-1}	9.23×10^{12}	41
1	424	2190.44	5.6603	6.23×10^{-1}	2.59×10^{13}	100
0	400	2190.65	5.6597	4.43×10^{-1}	1.02×10^{13}	112
11	1201	2191.25	5.6582	7.96×10^{-1}	1.84×10^{13}	62
2	442	2191.33	5.6580	1.59	1.10×10^{14}	173
0	403	2191.80	5.6567	1.54×10^{-1}	4.59×10^{12}	37
0	405	2192.20	5.6557	1.19	2.75×10^{13}	280
0	413	2193.84	5.6515	1.17×10^{-1}	2.23×10^{12}	72
1	426	2194.71	5.6492	1.06	4.41×10^{13}	145
1	427	2195.25	5.6478	1.22×10^{-1}	3.66×10^{12}	35
3	534	2197.49	5.6421	6.95×10^{-1}	2.08×10^{13}	66
0	420	2197.58	5.6419	1.38	3.21×10^{13}	295
0	422	2199.19	5.6377	2.80	5.35×10^{13}	596
3	541	2200.51	5.6343	7.23×10^{-1}	2.17×10^{13}	93
0	425	2201.09	5.6328	1.32	3.07×10^{13}	284
1	437	2201.14	5.6327	3.74	1.12×10^{14}	489
4	567	2201.32	5.6323	1.17	4.91×10^{13}	77
3	544	2201.54	5.6317	1.36	3.17×10^{13}	72
3	547	2203.00	5.6280	2.09	4.89×10^{13}	105
5	582	2203.77	5.6260	9.82×10^{-1}	6.90×10^{13}	48
3	552	2203.83	5.6259	9.76×10^{-1}	2.94×10^{13}	131
0	431	2206.09	5.6201	3.34	6.42×10^{13}	679
4	576	2206.39	5.6193	2.26	6.82×10^{13}	150
4	579	2207.71	5.6160	1.73	5.23×10^{13}	153
4	580	2208.05	5.6151	9.04×10^{-1}	3.82×10^{13}	35
3	563	2209.17	5.6122	2.03	4.79×10^{13}	237
3	576	2215.83	5.5954	8.47×10^{-1}	2.58×10^{13}	57
0	456	2239.15	5.5371	3.49×10^{-1}	6.90×10^{12}	100
0	478	2245.96	5.5203	9.87×10^{-2}	2.40×10^{12}	40
0	483	2247.49	5.5166	3.92×10^{-1}	7.81×10^{12}	117
0	489	2249.44	5.5118	1.30×10^{-1}	2.60×10^{12}	52
1	541	2256.79	5.4938	3.72×10^{-1}	1.17×10^{13}	51
1	552	2260.12	5.4857	4.84×10^{-1}	1.53×10^{13}	68
0	534	2262.72	5.4794	1.08	3.42×10^{13}	108
0	541	2265.74	5.4721	1.83	5.83×10^{13}	251
1	567	2267.04	5.4690	1.75	7.79×10^{13}	122
0	547	2268.23	5.4661	8.87×10^{-1}	2.20×10^{13}	47
0	548	2268.33	5.4659	1.53	3.11×10^{13}	290
0	552	2269.06	5.4641	5.11	1.63×10^{14}	726
1	573	2270.32	5.4611	3.02	2.25×10^{14}	335
0	553	2270.91	5.4597	8.99	2.23×10^{14}	1586
1	574	2271.20	5.4590	4.16	1.86×10^{14}	422
1	576	2272.11	5.4568	3.02	9.68×10^{13}	213

Table 14 – Radiative transitions in Fe-like W^{48+} continued

i	k	ΔE (eV)	λ (Å)	gf	A_{ki} (s^{-1})	ϵ_{line} ($ion^{-1}s^{-1}$)
1	579	2273.43	5.4536	6.92	2.22×10^{14}	648
0	562	2274.11	5.4520	1.97×10	4.02×10^{14}	3503
0	563	2274.41	5.4513	4.16	1.04×10^{14}	513
2	606	2274.56	5.4509	4.27	3.19×10^{14}	403
1	582	2274.79	5.4504	9.73×10^{-1}	7.28×10^{13}	50
0	576	2281.06	5.4354	5.74×10^{-1}	1.85×10^{13}	41
1	597	2282.80	5.4312	1.72	5.57×10^{13}	197
0	792	2436.44	5.0888	6.17×10^{-1}	1.44×10^{13}	91
1	809	2437.53	5.0865	9.25	3.41×10^{13}	74
0	795	2438.61	5.0842	1.79	6.60×10^{13}	192
0	798	2441.03	5.0792	8.30×10^{-1}	2.39×10^{13}	96
0	807	2445.13	5.0707	4.26×10^{-1}	1.00×10^{13}	65
1	822	2446.20	5.0684	4.83×10^{-1}	2.51×10^{13}	38
0	820	2452.78	5.0548	1.04	3.02×10^{13}	109
1	837	2453.61	5.0531	6.39×10^{-1}	3.34×10^{13}	41
0	828	2457.15	5.0459	8.25×10^{-1}	2.40×10^{13}	82
0	830	2457.83	5.0445	1.08	2.57×10^{13}	117
0	831	2458.97	5.0421	4.55×10^{-1}	1.09×10^{13}	56
0	833	2460.06	5.0399	3.64×10^{-1}	1.36×10^{13}	38
1	849	2460.15	5.0397	6.36×10^{-1}	2.39×10^{13}	48
0	843	2465.70	5.0283	6.93×10^{-1}	2.61×10^{13}	65
1	871	2476.46	5.0065	8.72×10^{-1}	3.31×10^{13}	60
0	861	2480.62	4.9981	1.61	3.91×10^{13}	171
0	865	2481.66	4.9960	6.20×10^{-1}	1.84×10^{13}	60
0	869	2483.95	4.9914	2.33×10^{-1}	5.68×10^{12}	50
0	1427	2727.19	4.5462	1.27	3.72×10^{13}	84
0	1445	2742.89	4.5202	9.37×10^{-1}	4.37×10^{13}	62
0	1447	2745.40	4.5161	6.39×10^{-1}	2.32×10^{13}	39
0	1469	2758.97	4.4939	4.77×10^{-1}	1.43×10^{13}	38
0	1494	2770.22	4.4756	5.96×10^{-1}	2.21×10^{13}	42
0	1495	2770.66	4.4749	5.68×10^{-1}	1.72×10^{13}	38
2	2456	2951.61	4.2006	5.82×10^{-1}	7.34×10^{13}	42
0	2389	2954.75	4.1961	7.14×10^{-1}	2.46×10^{13}	77
0	2391	2955.73	4.1947	8.41×10^{-1}	3.54×10^{13}	98
0	2423	2964.98	4.1816	8.37×10^{-1}	2.90×10^{13}	89
1	2447	2965.76	4.1805	1.03	5.64×10^{13}	85
0	2444	2973.77	4.1693	1.19	4.15×10^{13}	138
0	2592	3029.75	4.0922	5.42×10^{-1}	2.40×10^{13}	40
0	2596	3030.65	4.0910	1.99	7.20×10^{13}	244
0	2597	3030.77	4.0909		4.44×10^{13}	110
0	2606	3031.91	4.0893	1.43	8.16×10^{13}	159
0	2611	3033.67	4.0869	7.04×10^{-1}	3.12×10^{13}	55
1	2633	3034 .00	4.0865	9.78×10^{-1}	5.58×10^{13}	63

Table 14 – Radiative transitions in Fe-like W^{48+} continued

i	k	ΔE (eV)	λ (Å)	gf	A_{ki} (s^{-1})	ϵ_{line} ($ion^{-1}s^{-1}$)
1	2634	3034.26	4.0861	8.42×10^{-1}	6.73×10^{13}	59
2	2696	3035.23	4.0848	7.89×10^{-1}	1.05×10^{14}	53
0	5368	3369.86	3.6792	4.91×10^{-1}	2.20×10^{13}	45
0	5369	3370.34	3.6787	5.51×10^{-1}	3.02×10^{13}	55
0	5426	3389.24	3.6582	4.93×10^{-1}	2.23×10^{13}	44
0	5654	3446.43	3.5975	5.03×10^{-1}	2.36×10^{13}	44
0	5659	3447.21	3.5966	5.84×10^{-1}	4.30×10^{13}	57

Figure 1: Zn-like W^{44+} at $T_e = 3180$ eV.

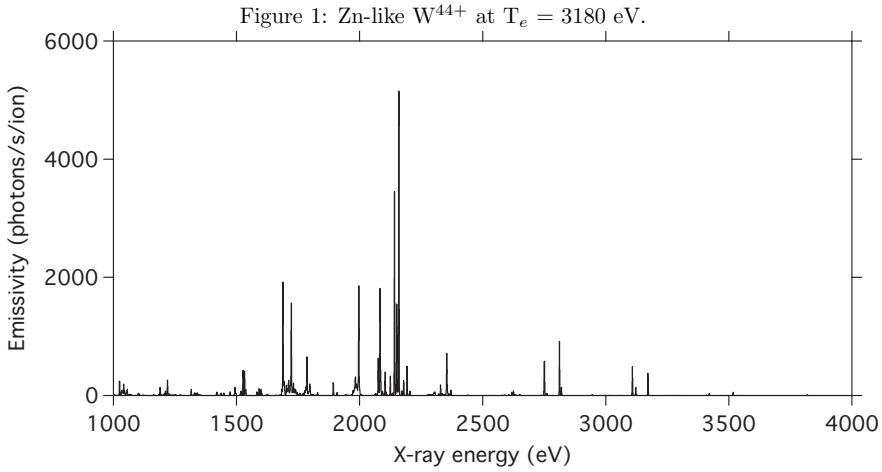

Figure 2: Cu-like W^{45+} at $T_e = 3550$ eV.

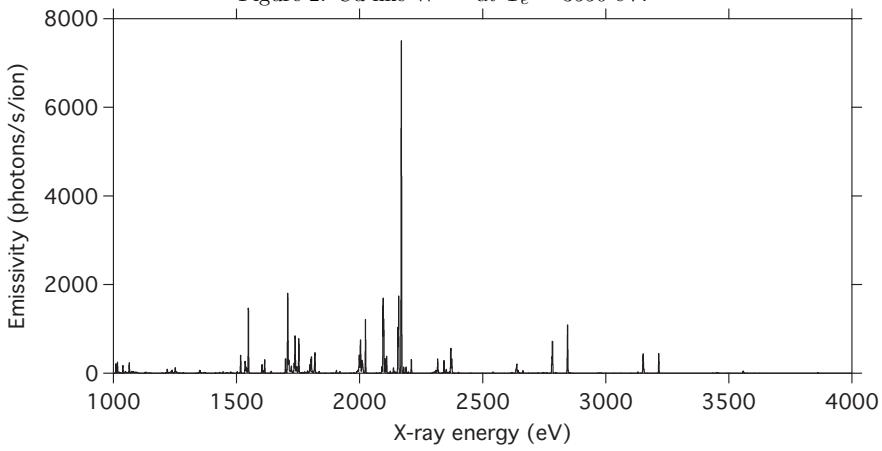

Figure 3: Ni-like W^{46+} at $T_e = 4250$ eV.

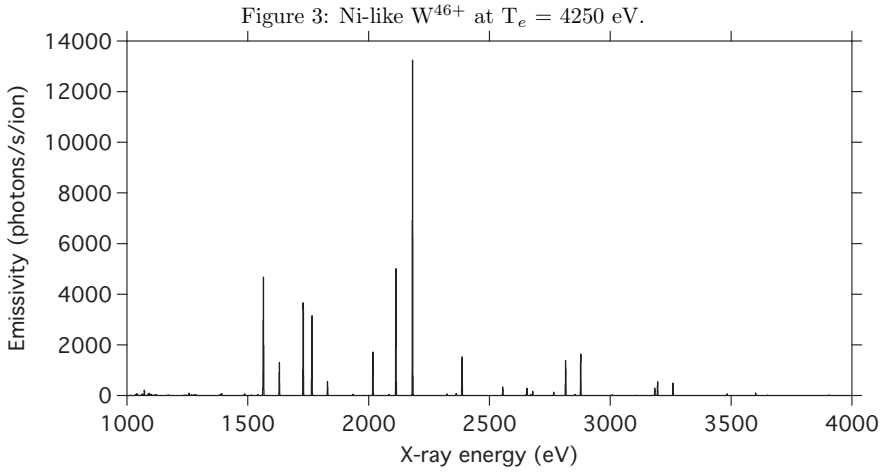

Figure 4: Co-like W^{47+} at $T_e = 5180$ eV.

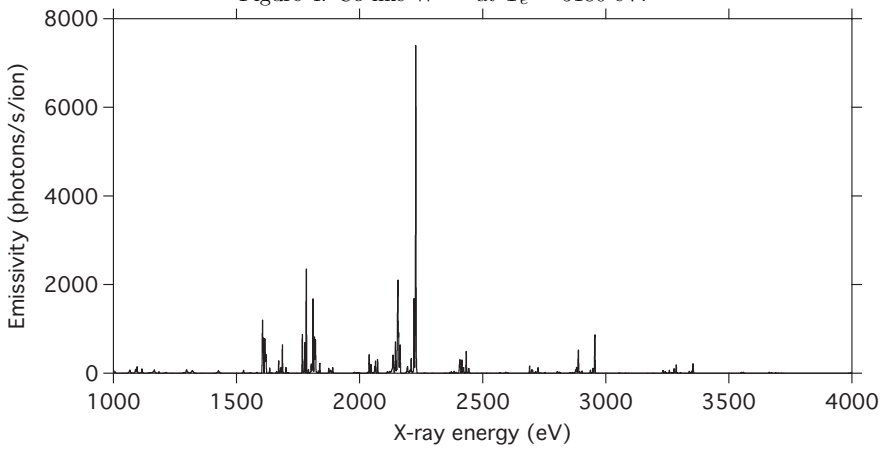

Figure 5: Fe-like W^{48+} at $T_e = 5830$ eV.

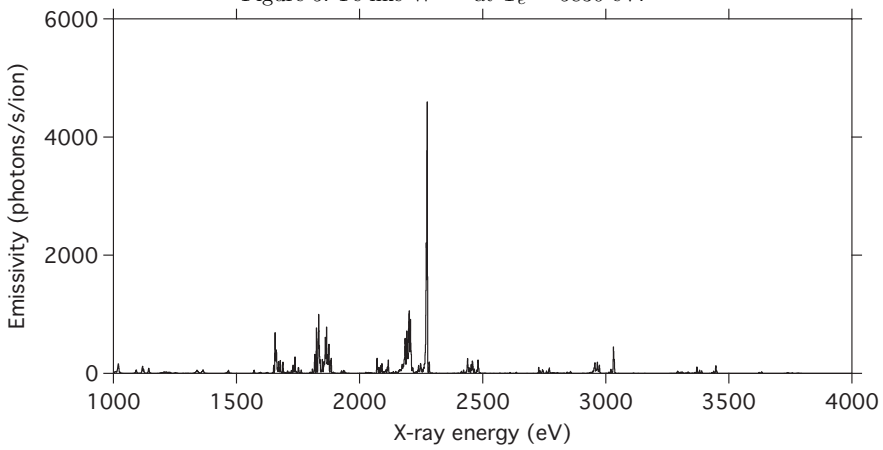

Paper VII

X-ray spectroscopy of $E2$ and $M3$ transitions in Ni-like W

J. Clementson,* P. Beiersdorfer, and M. F. Gu†
Lawrence Livermore National Laboratory, Livermore, California 94550, USA
(Received 10 November 2009; published 25 January 2010)

The electric quadrupole ($E2$) and magnetic octupole ($M3$) ground-state transitions in Ni-like W^{46+} have been measured using high-resolution crystal spectroscopy at the LLNL electron-beam ion trap facility. The lines fall in the soft x-ray region near 7.93 Å and were originally observed as an unresolved feature in tokamak plasmas. Using flat ammonium dihydrogen phosphate and quartz crystals, the wavelengths, intensities, and polarizations of the two lines have been measured for various electron-beam energies and compared to intensity and polarization calculations performed using the Flexible Atomic Code (FAC).

DOI: 10.1103/PhysRevA.81.012505 PACS number(s): 32.30.Rj, 32.70.Fw

I. INTRODUCTION

The lowest excited levels of nickellike high-Z systems are the $(3s^2 3p^6 3d^4_{3/2} 3d^5_{5/2} 4s_{1/2})_{J=3,2}$ levels. These decay to the $(3s^2 3p^6 3d^{10})_{J=0}$ ground state via a magnetic octupole ($M3$) and an electric quadrupole ($E2$) transition, respectively. The populations of metastable levels, from which electric-dipole forbidden transitions originate, are density sensitive and therefore these transitions typically do not occur in dense plasmas. However, in the spectra from low-density sources such as tokamaks and electron-beam ion traps (EBITs), electric-dipole forbidden transitions can in fact be among the strongest lines, especially from high-Z ions where their transition probabilities are higher.

Magnetic octupole transitions were first observed by Beiersdorfer *et al.* in 1991 in nickellike thorium and uranium ions [1] at the LLNL electron-beam ion trap facility, and they were later studied by Träbert *et al.* [2–4] in nickellike xenon and neighboring ions. Electric quadrupole lines have been observed in many low-density laboratory plasmas; see, e.g., Refs. [5–7].

An unresolved Ni-like W^{46+} ion feature was previously observed at 7.93 Å in the ASDEX Upgrade tokamak by Neu *et al.* [8–10] and was interpreted as the $E2$ line. Based on calculations, Loch *et al.* [11] and Ralchenko *et al.* [12,13] have suggested that this feature was actually a blend of the $M3$ and $E2$ lines. Ralchenko calculated the line positions, line intensities, and density dependences of the lines [13]. Ralchenko *et al.* also observed the unresolved line in the NIST EBIT using a 4-pixel x-ray calorimeter spectrometer [12]. The feature has also been observed in the LLNL SuperEBIT using a 36-pixel x-ray calorimeter array [14].

Several authors have calculated the two line positions, for example, Aggarwal *et al.* [15], Fournier [16], Safronova *et al.* [17], Zhang *et al.* [18], and Ballance *et al.* [19]. Other calculations are limited to the $E2$ transition [20–23].

In the present study, the x-ray feature at 7.93 Å has been resolved and shown to consist of the two electric-dipole forbidden transitions. The lines were studied using high-resolution spectroscopy at the LLNL EBIT facility, and the measurement yields wavelengths with an uncertainty of about 0.6 mÅ.

The intensities of the two lines have been studied at several electron-beam energies, and the excitation energy dependence on the relative intensities in the $3.3 - 5.4$ keV beam-energy interval has been investigated using two flat-crystal spectrometers. The measured line ratios at nearly constant electron density show that the energy has little effect on the relative intensities. However, calculations performed using the Flexible Atomic Code (FAC) show that the density dependence is very strong for plasmas of interest in magnetic fusion research.

The emitted radiation from an EBIT is in general both anisotropic and polarized. By using two crystal spectrometers the relative polarizations of the two lines could be studied as a function of electron-excitation energy and compared to the predicted polarizations calculated with FAC. It is shown that both lines have very little polarization.

II. EXPERIMENTAL SETUP

The measurements were performed using the SuperEBIT electron-beam ion trap at the Lawrence Livermore National Laboratory [24,25]. In an EBIT, the atomic element of interest is injected into an electron beam with a density around 10^{11-12} cm^{-3}, where the atoms are ionized and excited by unidirectional electron collisions. The freshly produced ions are then trapped in a small region of the electron beam by a combination of electrostatic potentials and strong magnetic fields. The atomic charge state distribution of the trapped ions is determined by the electron-beam energy, ionization and recombination cross sections, charge exchange, and various trap parameters, such as drift tube voltages and trap cycle length. In the trap, the ions have little kinetic energy and no overall direction of motion; hence the Doppler effect does not limit the spectroscopic resolution or cause any line shift. The electron beam determines the volume in which the ions are produced, excited, and confined. This narrow spatial region defines the extent of the light source which can be spectroscopically imaged without the need for a spectrometer entrance slit.

SuperEBIT was operated in its low-energy mode, which is similar to the EBIT-I device [26], at six beam energies from 3.3 keV up to 8.6 keV, to provide data for different electron collision energies (Cu-like W^{45+} has an ionization potential

*Also at Department of Physics, Lund University, SE-221 00 Lund, Sweden.; clementson@llnl.gov.
†Present address: Space Sciences Laboratory, University of California, Berkeley, California 94720, USA.

of 2414.1 eV, while Ni-like W^{46+} ionizes at 4057 eV [27]). From a vial containing the crystalline compound tungsten hexacarbonyl, $W(CO)_6$, the sublimated material was injected into SuperEBIT as a gas through one of the ports surrounding the trap. Using two of the other drift tube ports, trimethylaluminum (TMA), $Al_2(CH_3)_6$, using a ballistic gas injector, and sodium gas, using a sublimation injector, were introduced into the trap in order to provide reference wavelength lines.

The soft x rays were measured using two flat-crystal spectrometers. A crystal diffracts radiation according to the Bragg law

$$n\lambda = 2d \sin\theta,$$

where n is the diffraction order, λ the wavelength, d the crystal lattice spacing, and θ the Bragg angle, i.e., the angle of incidence measured from the crystal surface. From Bragg's law the crystal resolving power R can be determined as

$$R = \frac{\lambda}{\Delta\lambda} = \frac{1}{\Delta\theta}\tan\theta.$$

Here $\Delta\theta$ is the the angular resolution of the spectrometer, which is limited by a combination of the source width, crystal structure, and detector resolution. For a given crystal and detector, large resolving powers can therefore be achieved either at large Bragg angles or at great distances between the source and crystal.

The first crystal spectrometer used here was a broadband instrument designed by Brown *et al.* [28]. The instrument employs long, flat crystals in a vacuum environment. For this measurement, an ammonium dihydrogen phosphate (ADP) (101) crystal with a $2d$ spacing of 10.640 Å [29] was positioned at a nominal Bragg angle of 48°. An ORDELA 1100 XF position-sensitive proportional counter fed data to a CAMAC data acquisition system that was controlled by KMAX software [30]. The ADP crystal, at a distance of 38 cm from the electron beam, diffracted the radiation to the proportional counter located 25.4 cm from the crystal rotation axis. The optical plane was perpendicular to the electron beam. The resolving power R was about 1450. A spectrum obtained at an electron-beam energy of 5340 eV shows the two tungsten lines together with the aluminum calibration lines, see Fig. 1.

The second spectrometer was a very-high-resolution flat-crystal instrument [31] equipped with a quartz $(10\bar{1}0)$ crystal,

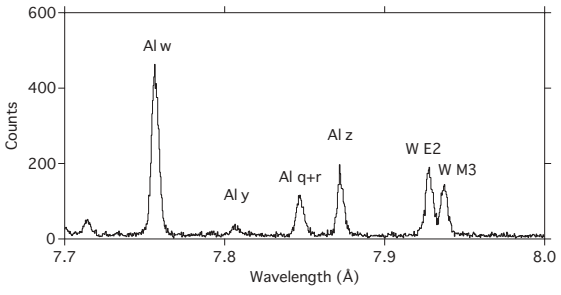

FIG. 1. Spectrum from the broadband spectrometer at a beam energy of 5340 eV showing the $M3$ and $E2$ lines of Ni-like W^{46+} together with the K-shell lines of heliumlike and lithiumlike aluminum.

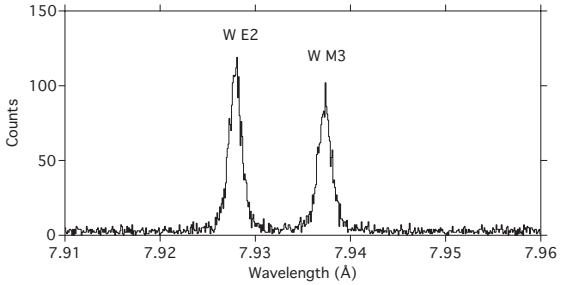

FIG. 2. Spectrum from the high-resolution spectrometer at a beam energy of 5350 eV showing the $M3$ and $E2$ lines of Ni-like W^{46+}.

and employing the same ORDELA detector. The crystal has a $2d$ spacing of 8.350 Å [32] and was positioned about 93 cm from the trap. The detector again was 25 cm from the crystal, which was set up at a Bragg angle of 72°. The spectrometer achieved a resolving power R of almost 5000. This is more than sufficient to fully resolve the two electric-dipole forbidden tungsten lines, as shown in Fig. 2.

Conversion factors used are $hc = 12398.42$ Å eV $=$ 8065.5410 eV cm, and 1 Ry $= 13.60569$ eV.

III. ANALYSIS

A. Wavelengths

The broadband spectrometer was used to determine the line positions for the $M3$ and $E2$ lines. The spectra acquired at the Bragg angle of 48° were wavelength calibrated using theoretical K-shell lines of He-like Al^{11+} (w $1s^2\,{}^1S_0$–$1s2p\,{}^1P_1$ at 7.75730 Å and z $1s^2\,{}^1S_0$–$1s2s\,{}^3S_1$ at 7.87212 Å) by Drake [33] and the Ly-γ lines of H-like Na^{10+} (8.02107 Å weighted average) by Garcia and Mack [34], cf. Fig. 1. Based on wavelength measurements of He-like O^{6+} [35] and He-like Ar^{16+} [36], the He-like Al^{11+} reference lines are believed to be accurate to 0.5 mÅ. The Bragg angle versus channel position dispersion was derived from a calibration spectrum and applied to a spectrum containing the tungsten lines together with the K-shell aluminum lines. There were small shifts of the observed Al z and Al w lines in this spectrum from the theoretical wavelengths, and the dispersion was adjusted to account for the observed average shift of the two reference lines. The uncertainties in anchoring the wavelength scale to the aluminum reference lines are estimated to be the maximum wavelength difference of the aluminum lines inferred from the calibration relative to the reference wavelengths, as well as the statistical uncertainties in the line positions of Al z and Al w. The wavelength dispersion uncertainty was evaluated for each line as a function of the distance from Al z. These uncertainties were added in quadrature with the counting statistics to give error bars of the measured line positions. The uncertainty in the splitting of the two tungsten lines is dominated by counting statistics, which, when added with the dispersion uncertainty, results in an error bar of 0.2 mÅ. In addition to the tungsten lines, the wavelength of the unresolved Li-like Al^{10+} lines q ($1s^22s^2S_{1/2}$–$1s2s2p^2P_{3/2}$) and r ($1s^22s^2S_{1/2}$–$1s2s2p^2P_{1/2}$)

TABLE I. Comparison of measured and calculated line positions of the tungsten $M3$ and $E2$ lines. Wave numbers and energies, where reported (from levels and transitions), have been converted to wavelengths.

Ni-like W^{46+}			
$M3$		$E2$	
Experiment (Å)	Theory (Å)	Experiment (Å)	Theory (Å)
7.9374(7)	7.9368[a]	7.9280(6)	7.9270[a]
	7.94883[b]		7.93921[b]
	7.9449[c]		7.9354[c]
	7.940[d]		7.930[d]
	7.938[e]		7.929[e]
	7.9477[f]		7.9380[f]
	7.94611[g]		7.93683[g]
			7.94205[h]
			7.91478[i]
			7.930[j]
			7.944[k]
Li-like Al^{10+}	Experiment (Å)	Theory (Å)	
q	7.8473(6)	7.8460[l]	
r		7.8479[l]	

[a]This work (FAC).
[b]Aggarwal *et al.* (GRASP) [15].
[c]Fournier (RELAC) [16].
[d]Ralchenko *et al.* (FAC) [12].
[e]Safronova *et al.* (RMBPT) [17].
[f]Zhang *et al.* (DFS) [18].
[g]Ballance *et al.* (*R*-matrix) [19].
[h]Dong *et al.* (GRASP) [20].
[i]Safronova (Cowan) *et al.* [17].
[j]Safronova *et al.* (FAC) [21].
[k]Pütterich *et al.* (GRASP) [23].
[l]Vainshtein and Safronova ($1/Z$ expansion) [37].

was determined. The measured wavelengths of the lines are listed in Table I together with theoretical predictions.

B. Intensities

Line intensities were studied as a function of electron impact excitation energy using the broadband and high-resolution spectrometers. Both instruments measured at electron-beam energies from 3.3 to 5.4 keV. In addition, the broadband spectrometer measured at a beam energy of 8.6 keV. The observed relative intensities of the two lines are shown in Fig. 3.

C. Polarization

The emitted radiation can be divided into two polarization components, one with the electric-field vector in the z direction parallel to the electron beam, and one with the electric field in the plane perpendicular to the beam axis, that is,

$$I = I_{\parallel} + I_{\perp}.$$

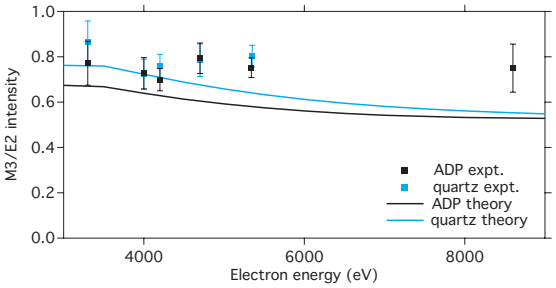

FIG. 3. (Color online) Intensity of the $M3$ vs the $E2$ line. Observed and calculated intensity ratios as a function of electron-beam energy.

Diffracting crystals have different reflectivities in the direction parallel to the beam, $R_{\parallel}$, and the direction within the dispersion plane, $R_{\perp}$. The observed intensity can then be expressed as

$$I_{\rm obs} = R_{\parallel} I_{\parallel} + R_{\perp} I_{\perp}.$$

The relative reflectivity $R = R_{\perp}/R_{\parallel}$ for ADP crystals has been calculated by Henke *et al.* [29] to be $R_{\rm ADP} = 0.06$. This reflectivity is very small, because the Bragg angle is close to 45°, where only parallel polarized light gets reflected. The reflectivities are functions of photon energy or, equivalently, of Bragg angle and can in general be modeled as $R = |\cos^m(2\theta)|$, where $1 \leqslant m \leqslant 2$ depending on whether the crystal can be considered perfect ($m = 1$) or mosaic ($m = 2$) [38]. As no published data exist on the quartz reflectivity, $R_{\rm quartz}$ is taken to be the geometric mean of the extreme cases with $m = 1$ and $m = 2$. The quartz relative reflectivity at 72° is thus taken to be $R_{\rm quartz} = 0.73$. Using this method for the ADP crystal gives a reflectivity of 0.03, which is quite close to the value by Henke *et al.* This indicates that the geometrical mean of the perfect and mosaic models makes a good estimate, which, as we show below, does not contribute a significant error to the analysis. The two tungsten lines are closely spaced, so the reflectivities are practically the same.

The measurements were carried out at an observation angle perpendicular to the electron beam. The polarization P at this angle can be expressed as

$$P = \frac{I_{\parallel} - I_{\perp}}{I_{\parallel} + I_{\perp}},$$

i.e., as the relative difference of the intensity of the radiation with electric field in the beam parallel direction and the beam perpendicular direction. The relative polarization of two lines can be measured when observed with two spectrometers. Using

$$P_{M3} = \frac{\left.\frac{I^{M3}}{I^{E2}}\right|_{\rm ADP}\left(1 + R_{\rm ADP}\frac{1-P_{E2}}{1+P_{E2}}\right)(R_{\rm quartz}+1) - \left.\frac{I^{M3}}{I^{E2}}\right|_{\rm quartz}\left(1 + R_{\rm quartz}\frac{1-P_{E2}}{1+P_{E2}}\right)(R_{\rm ADP}+1)}{\left.\frac{I^{M3}}{I^{E2}}\right|_{\rm ADP}\left(1 + R_{\rm ADP}\frac{1-P_{E2}}{1+P_{E2}}\right)(R_{\rm quartz}-1) - \left.\frac{I^{M3}}{I^{E2}}\right|_{\rm quartz}\left(1 + R_{\rm quartz}\frac{1-P_{E2}}{1+P_{E2}}\right)(R_{\rm ADP}-1)}$$

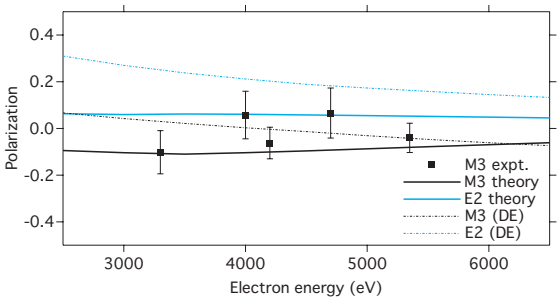

FIG. 4. (Color online) Theoretical and measured polarization of lines $M3$ and $E2$. The experimental data for the $M3$ line are tied to the theoretical polarization of the $E2$ line. Also shown are the calculated polarizations with direct excitation (DE) only.

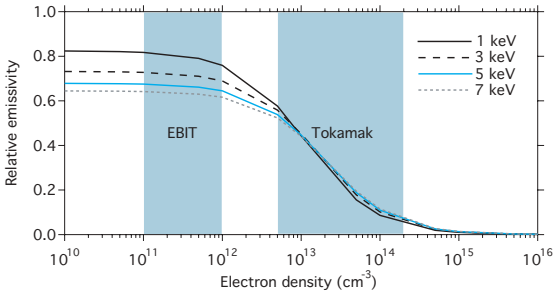

FIG. 5. (Color online) Calculated emissivity ratio of the $M3$ and $E2$ lines in a Maxwellian plasma for the temperatures listed. Typical EBIT and tokamak core densities are indicated by the shaded regions.

as shown in Ref. [39], the polarization of the $M3$ line can be expressed in terms of the polarization of the $E2$ line. The polarization of line $E2$ is taken to be a constant 5% in the interval observed, as the calculations indicate (see below). The appropriateness of choosing the geometric mean of the two limiting models for the quartz crystal reflectivity was assessed by studying the effects of this choice on the inferred polarization of the $M3$ line. Modeling the reflectivities as either perfect or mosaic resulted in changes of less than 0.02 for the inferred polarization. The largest contributions to the polarization uncertainties are from the statistics of the line intensities, giving error bars of up to 0.08. The uncertainties from the crystal reflectivities and the observed line intensities have been added in quadrature to estimate the polarization uncertainty. The inferred $M3$ polarization versus beam energy is shown together with the theoretical predictions in Fig. 4.

IV. THEORY

The spectrum of Ni-like W^{46+} was calculated using the Flexible Atomic Code, FAC v.1.1.1. FAC is a fully relativistic program for atomic-structure calculations and spectral modeling [40]. The nickellike system was modeled using configuration state functions consisting of $3s^23p^63d^{10}$, $3s^23p^63d^9nl$, $3s^23p^53d^{10}nl$, and $3s3p^63d^{10}nl$ with $n = 4$ and 5 and $l = 0, 1, \ldots, n-1$. The K and L shells were held closed in the structure calculation. To model the observed emission of the two electric-dipole forbidden lines, the intensities needed to be corrected for the crystal reflectivities, the line polarizations, and the anisotropic emission distributions from the EBIT plasma. These effects are taken into account by using the correction factor

$$G(E) = \left[1 + \frac{1-R}{1+R}P(E)\right] A(E),$$

where $P(E)$ and $A(E)$ are the calculated line polarization and anisotropy, respectively. The calculated intensities of the $M3$ versus $E2$ line at the EBIT experimental conditions are shown in Fig. 3 together with observed line ratios. The theoretical polarization is shown as a function of electron excitation energy in Fig. 4. To assess the effects of cascades on the line polarizations, a five-level model of the nickellike ion was studied with direct excitation (DE) as the only population mechanism.

Excluding polarization, the structure calculation was extended to $n = 6$, and the $M3$ and $E2$ line emissivities were studied as a function of electron density, see Fig. 5. These additional calculations were done for temperatures around 4 keV, which is the temperature when the nickellike tungsten abundance is expected to peak [23].

V. SUMMARY

The nickellike tungsten feature at 7.93 Å previously observed at the ASDEX Upgrade tokamak [8–10], the NIST EBIT [12], and the LLNL SuperEBIT [14] has now been fully resolved and shown to consist of two components: the electric-dipole forbidden ground-state transitions $M3$ at 7.9374(7) Å and $E2$ at 7.9280(6) Å. The theoretical wavelengths from our FAC calculations agree very well with the measured positions. The only other calculation that has such good agreement is the relativistic many-body perturbation theory (RMBPT) by Safronova *et al.* [17]. However, we note that the measured separation of 9.3(2) mÅ agrees better with other calculations [15,16,18]. An especially good match is achieved by the R-matrix calculation by Ballance *et al.* [19], who predicted a separation of 9.28 mÅ.

The $M3$ and $E2$ lines originate from the two lowest excited levels $(3d_{5/2}4s_{1/2})_{J=3,2}$. The calculations show that direct excitation is not the main population mechanism of the levels, but rather cascades, cf. Fig. 4. This causes the $E2$ line to have very little polarization. The calculations, which include cascades from levels as high as $n = 5$, show that the $E2$ line has a nearly constant linear polarization of only 5% over a large energy interval, which is significantly less than what results from direct excitation alone. The cascade population of the $J = 3$ level has the opposite effect, resulting in an increase in the magnitude of the polarization than what electron-impact excitation alone would cause. The measured polarization of the $M3$ line hovers around zero, appearing a bit smaller in magnitude than the predicted values, which range between -5 and -10%. Nickellike tungsten ionizes to cobaltlike tungsten at energies of 4057 eV and above, and then recombination can populate the two metastable levels in addition to the direct excitation and cascade population mechanisms. Recombination, however, is not included in

our model. Nevertheless, both the measured polarization and relative intensity values agree rather well with the calculations.

Electric-dipole forbidden lines are frequently used as plasma diagnostics, especially as a diagnostic for the electron density [41–43]. As indicated by our calculations, the two tungsten transitions can be used as a density diagnostic in plasmas of densities in the $10^{12} - 10^{15}$ cm^{-3} range. This interval coincides very well with plasmas of interest in magnetic fusion research, as illustrated in Fig. 5. For such plasmas, the temperature dependence on the relative line intensities is very weak, whereas the density dependence is strong, allowing one to make a rather robust measurement of the electron density.

The thermal line broadening in a tokamak plasma is smaller than the wavelength separation of the line pair. Doppler widths range from 1.5 mÅ at an ion temperature of 1 keV up to 4.0 mÅ at 8 keV. Spectrometers with resolving powers of 10 000 or higher may therefore be used to determine the ion temperature from the two lines in this range.

High-resolution observations of the Ni-like W^{46+} line pair could be a valuable diagnostic of magnetically confined plasmas, especially for those plasmas in which tungsten occurs as an indigenous trace element. The ITER tokamak, currently under construction, will have core temperatures in the 3–5 keV range during the initial ohmic phase. This is the interval in which W^{46+} ions are abundant in the core [23,44,45]. Diagnostics observing the $M3$ and $E2$ lines may thus play an important role in the ITER program.

ACKNOWLEDGMENTS

This work was performed under the auspices of the US Department of Energy by Lawrence Livermore National Laboratory under Contract DE-AC52-07NA-27344 and supported by LLNL Laboratory Directed Research and Development Contract 09-ERD-016. The authors would like to acknowledge support for the experiment from Dr. Greg Brown, Dr. Hui Chen, Phil D'Antonio, Miriam Frankel, Ed Magee, and Prof. Elmar Träbert. Albert Wynn from FAMU is acknowledged for assistance with the calculations. Joel Clementson would like to thank Dr. Hans Lundberg, Dr. Sven Huldt, and Prof. Sune Svanberg for their support.

[1] P. Beiersdorfer, A. L. Osterheld, J. Scofield, B. Wargelin, and R. E. Marrs, Phys. Rev. Lett. **67**, 2272 (1991).
[2] E. Träbert, P. Beiersdorfer, G. V. Brown, S. Terracol, and U. I. Safronova, Nucl. Instrum. Methods Phys. Res. B **235**, 23 (2005).
[3] E. Träbert, P. Beiersdorfer, G. V. Brown, K. Boyce, R. L. Kelley, C. A. Kilbourne, F. S. Porter, and A. Szymkowiak, Phys. Rev. A **73**, 022508 (2006).
[4] E. Träbert, P. Beiersdorfer, and G. V. Brown, Phys. Rev. Lett. **98**, 263001 (2007).
[5] M. Klapisch, J. L. Schwob, M. Finkenthal, B. S. Fraenkel, S. Egert, A. Bar-Shalom, C. Breton, C. DeMichelis, and M. Mattioli, Phys. Rev. Lett. **41**, 403 (1978).
[6] P. Beiersdorfer *et al.*, Phys. Rev. A **37**, 4153 (1988).
[7] N. K. Del Grande, P. Beiersdorfer, J. R. Henderson, A. L. Osterheld, J. H. Scofield, and J. K. Swenson, Nucl. Instrum. Methods Phys. Res. B **56-57**, 227 (1991).
[8] R. Neu, K. B. Fournier, D. Schlögl, and J. Rice, J. Phys. B **30**, 5057 (1997).
[9] R. Neu, K. B. Fournier, D. Bolshukhin, and R. Dux, Phys. Scr. **T92**, 307 (2001).
[10] R. Neu *et al.*, Plasma Phys. Control. Fusion **44**, 811 (2002).
[11] S. D. Loch, M. S. Pindzola, C. P. Ballance, D. C. Griffin, A. D. Whiteford, and T. Pütterich AIP Conf. Proc. **874**, 233 (2006).
[12] Yuri Ralchenko, Joseph N. Tan, J. D. Gillasy, Joshua M. Pomeroy, and Eric Silver, Phys. Rev. A **74**, 042514 (2006).
[13] Y. Ralchenko, J. Phys. B **40**, F175 (2007).
[14] J. Clementson, P. Beiersdorfer, G. V. Brown, and M. F. Gu, Phys. Scr. **81**, 015301 (2010).
[15] K. M. Aggarwal, P. H. Norrington, K. L. Bell, F. P. Keenan, G. J. Pert, and S. J. Rose, At. Data Nucl. Data Tables **74**, 157 (2000).
[16] K. B. Fournier, At. Data Nucl. Data Tables **68**, 1 (1998).
[17] U. I. Safronova, A. S. Safronova, S. M. Hamasha, and P. Beiersdorfer, At. Data Nucl. Data Tables **92**, 47 (2006).
[18] H. L. Zhang, D. H. Sampson, and C. J. Fontes, At. Data Nucl. Data Tables **48**, 91 (1991).
[19] C. P. Ballance and D. C. Griffin, J. Phys. B **39**, 3617 (2006).
[20] C. Z. Dong, S. Fritzsche, and L. Y. Xie, J. Quant. Spectrosc. Radiat. Transf. **76**, 447 (2003).
[21] A. S. Safronova *et al.*, Can. J. Phys. **86**, 267 (2008).
[22] S. M. Hamasha, A. S. Shlyaptseva, and U. I. Safronova, Can. J. Phys. **82**, 331 (2004).
[23] T. Pütterich, R. Neu, R. Dux, A. D. Whiteford, and M. G. O'Mullane, (ASDEX Upgrade Team), Plasma Phys. Control. Fusion **50**, 085016 (2008).
[24] P. Beiersdorfer, Can. J. Phys. **86**, 1 (2008).
[25] R. E. Marrs, Can. J. Phys. **86**, 11 (2008).
[26] M. A. Levine, R. E. Marrs, J. R. Henderson, and M. B. Knapp, and D. A. Schneider, Phys. Scr. **T22**, 157 (1988).
[27] A. E. Kramida and J. Reader, At. Data Nucl. Data Tables **92**, 457 (2006).
[28] G. V. Brown, P. Beiersdorfer, and K. Widmann, Rev. Sci. Instrum. **70**, 280 (1999).
[29] B. L. Henke, E. M. Gullikson, and J. C. Davis, At. Data Nucl. Data Tables **54**, 181 (1993).
[30] P. Beiersdorfer, G. V. Brown, L. Hildebrandt, and K. L. Wong, Rev. Sci. Instrum. **72**, 508 (2001).
[31] P. Beiersdorfer, J. R. Crespo López-Urrutia, E. Förster, J. Mahiri, and K. Widmann, Rev. Sci. Instrum. **68**, 1077 (1997).
[32] A. Burek, Space Sci. Instrum. **2**, 53 (1976).
[33] G. W. Drake, Can. J. Phys. **66**, 586 (1988).
[34] J. D. Garcia and J. E. Mack, J. Opt. Soc. Am. **55**, 654 (1965).
[35] L. Engström and U. Litzén, J. Phys. B **28**, 2565 (1995).
[36] R. D. Deslattes, H. F. Beyer, and F. Folkmann, J. Phys. B **17**, L689 (1984).
[37] L. A. Vainshtein and U. I. Safronova, At. Data Nucl. Data Tables **21**, 49 (1978).
[38] P. Beiersdorfer, J. R. Crespo López-Urrutia, V. Decaux, K. Widmann, and P. Neill, Rev. Sci. Instrum. **68**, 1073 (1997).

[39] P. Beiersdorfer, G. Brown, S. Utter, P. Neill, K. J. Reed, A. J. Smith, and R. S. Thoe, Phys. Rev. A **60**, 4156 (1999).
[40] M. F. Gu, Can. J. Phys. **86**, 675 (2008).
[41] R. W. P. McWhirter, Phys. Rep. **37**, 165 (1978).
[42] F. Bely-Dubau, Phys. Scr. **T7**, 34 (1984).
[43] H. R. Griem, *Principles of Plasma Spectroscopy* (Cambridge University Press, New York, 1997).
[44] C. H. Skinner, Can. J. Phys. **86**, 285 (2008).
[45] N. J. Peacock, M. G. O'Mullane, R. Barnsley, and M. Tarbutt, Can. J. Phys. **86**, 277 (2008).

Paper VIII

EUV spectroscopy on the SSPX spheromak

J Clementson[1,2], P Beiersdorfer[1], M F Gu[1], H S McLean[1] and R D Wood[1]

[1]Lawrence Livermore National Laboratory, Livermore, CA 94551, USA
[2]Atomic Physics Division, Lund Institute of Technology, SE-221 00 Lund, Sweden

E-mail: clementson@llnl.gov

Abstract. Extreme ultraviolet (EUV) plasma spectroscopy is one the diagnostics implemented at the Sustained Spheromak Physics Experiment (SSPX) at the Lawrence Livermore National Laboratory. A grating spectrometer covering the spectral region of 25 - 450 Å with a resolution of 0.3 Å was used as an impurity diagnostic to monitor the plasmas and to carry out atomic physics research. Several low-Z impurities have been found in the spheromak, notably B, C, N, and O. Of the heavier elements, Ti, Cu, and W were found in the plasmas. As a relatively dense and low-temperature laboratory plasma device, SSPX served as an excellent radiation source for investigation of atomic spectra in a regime not readily attained in other devices. We have injected atomic titanium and tungsten hexacarbonyl into the spheromak under different operating conditions. We also report on electron temperature and electron density measurements based on the Kα lines from B IV at 60 Å.

1. Introduction

Impurity ions serve a beneficial role in the plasmas generated for magnetic fusion research, because as trace elements they provide critical diagnostic information on the state of the plasma [1]. In large quantities, however, they may constitute a problem for magnetic confinement fusion. The presence of contaminants in a fusion device effectively cools and dilutes the plasma [2; 3], making it more difficult to achieve ignition. Impurities in large quantities, where their radiation significantly affects the power balance, may also affect the magnetic stability of the plasma [2; 3] and hence disturb the operation of the device. Being able to assess impurity concentrations via spectroscopic means is thus essential.

The atomic physics plays a crucial role for developing impurity radiation as a diagnostic. By spectroscopically studying the line radiation emitted from a plasma, information about parameters such as electron temperature, ion temperature, electron density and impurity species can be gained. For instance, certain atomic transitions are density and temperature sensitive and their line intensities can provide information of these parameters. The well known K-shell lines from He-like atoms are one such example, constituting a useful diagnostic for high-temperature plasmas [4]. The three main features of the Kα signature are the resonance line w $1s^2\ ^1S_0 - 1s2p\ ^1P_1$, the intercombination line y $1s^2\ ^1S_0 - 1s2p\ ^3P_1$, and the forbidden line z $1s^2\ ^1S_0 - 1s2s\ ^3S_1$ [5; 6]. The relative intensities in the signature can provide data about plasma densities and electron temperatures, making He-like ions very attractive diagnostics since they have the widest abundance range in high-temperature plasmas of any isoelectronic species [7].

In addition, impurities can also benefit atomic physics research, given that the optically thin magnetic confinement plasmas act as good sources of radiation [8]. These sources can provide

production of highly-charged ions difficult to attain otherwise. Magnetic confinement plasmas in near-coronal equilibrium moreover permit higher-order, i.e. dipole-forbidden, radiative transitions to occur and hence can find use as experiments of astrophysical importance [9]. Fusion experiments can therefore offer valuable atomic data for charge-balance modeling and atomic structure research.

In the extreme ultraviolet (EUV) spectral region many strong atomic transitions take place, making this region a rich area for spectroscopy. The L-shell transitions in low-Z elements such as C, N, and O fall within the EUV, as do many $n' = 3 \rightarrow n = 3$ transitions for mid-Z ions such as Ti and Cu. In moderately high-temperature plasmas, such as spheromaks, conditions are favorable for the production of charge states with ample EUV transitions.

The Sustained Spheromak Physics Experiment (SSPX) at the Lawrence Livermore National Laboratory (LLNL) was an effort in the field of innovative confinement concepts (ICC), with the main objective to explore energy confinement and current drive in spheromaks [10]. Spheromaks confine plasmas using self-organized magnetic fields [10], thus making external coils superfluous, an important advantage over the tokamak design. The toroidally shaped SSPX plasmas had a major radius of $R = 0.31$ m and a minor radius of $a = 0.23$ m, confined within a cylindrical flux conserver of diameter 1.0 m and height 0.5 m. The flux conserver was made of copper with tungsten-coated surfaces to reduce sputtering of wall material [11]. From the coaxial gun and gas injector region atop the flux conserver the plasmas were created and pushed downward into the flux conserver forming the spheromaks [11]. Plasma currents achieved magnitudes of up to 1 MA [12]. Typical SSPX plasmas lasted around 4 ms, with plasma densities of a few times 10^{14} cm^{-3} [13]. Peak electron temperatures at the magnetic axis ranged up to, and exceeded, 500 eV, a record temperature for spheromaks [12; 14].

Our diagnostic consisted of an EUV grazing-incidence spectrometer, known as the Silver Flat Field Spectrometer (SFFS). Similar to other spectroscopic instrumentation used on magnetic fusion devices [15], the instrument was developed at the Livermore EBIT facility. Its design is similar to the design described in [16]. The flat-field spectrometer employs a spherical 1200 lines/mm grating [17], giving a resolution of up to 0.3 Å FWHM over the spectral range 25 to 450 Å. The image detection was done using a back-illuminated Photometrics CCD camera, allowing a bandwidth of about 200 Å per image.

2. Measurements

The Silver Spectrometer was added to the instrumentation at the SSPX facility in 2006 to replace the Survey, Poor Resolution, Extended Domain (SPRED) spectrometer [18; 19]. With the primary purpose to study impurity ions, the SFFS was a standard part of the diagnostics suite during the last year of SSPX operations. With a field of view through the magnetic axis at the midplane of the plasma torus, the SFFS studied spheromaks under various conditions. Due to the short plasma discharges the CCD camera had to record time-integrated images. The resulting spectra thus show time-integrated lines over the spatially integrated plasma chord. For most measurements a 100 μm slit was used to image the plasmas onto the grating.

To get acquainted with the spheromak spectra in the initial phase of SFFS operations, we injected He gas into the plasmas to provide wavelength calibration. With the Rydberg series in He II and an aluminum cutoff filter in front of the grating blocking radiation below 170 Å we were able to establish the instrumental coverage.

2.1. Impurity diagnostics

Two sets of low-temperature experiments monitored by the SFFS were internal magnetic measurements to study spheromak formation and evolution. The studies were done using boron nitride covered probes [20–22] inserted into the spheromak. During the discharges the coating evaporated, which added B and N to the plasmas, thus cooling the electrons to temperatures of

some tens of eV. Spectra from these shots are rich in lines, and numerous transitions from B, C, N, and O have been identified, see Figures 1 and 2. The O ions originate mainly from water vapor inside the vacuum vessel, and are typically the most abundant contaminants in SSPX plasmas.

Another experimental campaign was undertaken with the aim to extend the flux conserver height by inserting uncoated copper rods between the upper and lower sections [14]. The SFFS recorded many interesting spectra with quite different features from earlier studies. The discharges effectively sputtered material off the exposed copper surfaces, seeding the plasmas with large amounts of Cu in various charge states.

Other impurity ions found in the spheromak were Ti and W, which we verified by injecting Ti and tungsten hexacarbonyl ($W(CO)_6$) into SSPX, as discussed below.

2.2. Injection of metals

Titanium is an abundant impurity in the spheromak, occurring in weakly ionized states (typically Ti V - VIII). With the purpose to clean the spheromak and reduce hydrogen recycling Ti is introduced on the plasma facing surfaces of the flux conserver by a vapor deposition method known as titanium gettering. We utilized this as an injection method to enhance the Ti impurity concentration and studied how the spectra changed with time, i.e. subsequent shots after titanium gettering. As expected, there existed more Ti in the plasmas immediately after gettering, and the Ti was found to successively wear off the flux conserver during subsequent discharges and to be pumped away from the vessel. By tracking various candidate Ti lines over many such discharges we could unequivocally establish them as emanating from Ti ions.

Another injection experiment we performed was to introduce the gaseous compound $W(CO)_6$ into the spheromak to study relatively weakly-ionized W. By introducing $W(CO)_6$ into the plasmas various unidentified lines observed in earlier SSPX discharges could be attributed to transitions in W. As mentioned before, W was used to coat the flux conserver. We note that the SSPX spheromak was an ideal test bed for investigating W spectra under plasma conditions similar to those of future ITER divertor plasmas, because ITER divertor plasma parameters (electron temperatures below 100 eV and densities of 10^{14} to 10^{15} cm^{-3} [23]) are essentially the same as those found in SSPX plasmas. The spectral lines produced in SSPX should prove useful as ITER divertor diagnostics.

2.3. Temperature and density diagnostic

The shortest wavelength lines so far analyzed among the SSPX data are from He-like B IV during the magnetic probe measurements, see Figure 2. The Kα line pair w at 60.3144 Å and y at 61.088 Å [24] was used to make estimates of electron temperatures and electron densities of the plasmas during one set of the magnetic probe experiments. Flexible Atomic Code [25] calculations were made as a function of electron temperature and density, as shown in Figure 3. Based on the mean value of around 0.2 of the measured y/w ratio, the atomic physics restricts the electron density to about 1×10^{12} to 2×10^{14} cm^{-3}, and a temperature interval of about 20 eV to 100 eV. The B emission therefore comes from either low-density, high-temperature regions of the spheromak or high-density, low-temperature regions. The line-averaged density through the magnetic axis of the spheromak (for shot 16644 shown in Figure 2) was determined using a CO_2 laser interferometer system [13; 26] to be between 1×10^{14} and 5×10^{14} cm^{-3} at different times during the main part of the discharge. These densities are at the high end of the values given by the calculations. This suggests that the B emission comes from the cooler edge of the plasma. We therefore hypothesize that B emission, originating from the magnetic probe at the edge of the plasma, likely has a hollow density profile due to slow diffusion. Considering that B III ionizes at 38 eV and the B IV Kα lines require energies in excess of 200 eV, along with the expected lower electron temperatures at the outer flux surfaces, we infer that only few

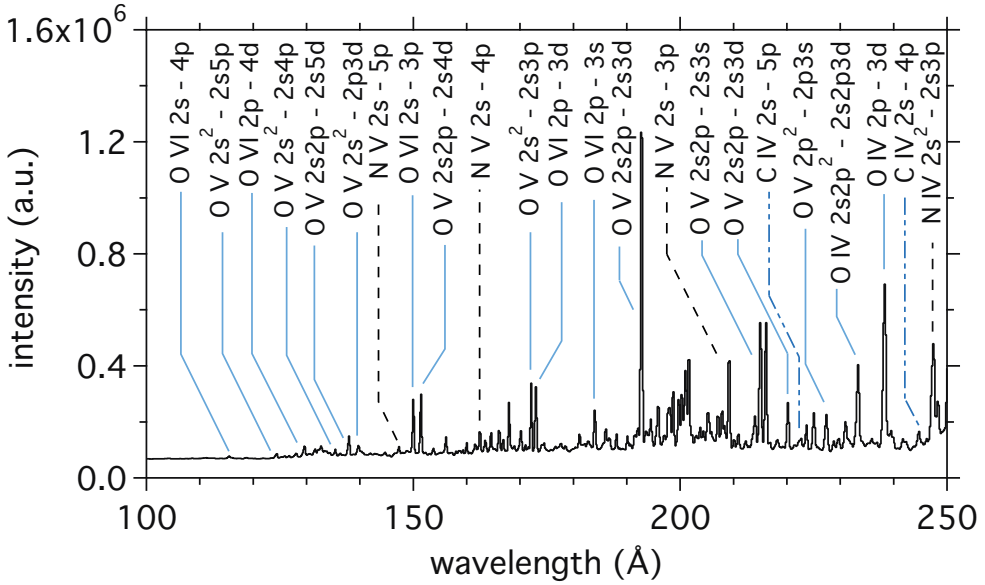

Figure 1. SSPX shot 18415. Spectral lines from O (solid blue), N (dashed black), and C (dot-dashed blue). Most of the remaining lines are from Ti, Cu, and W as described in the text.

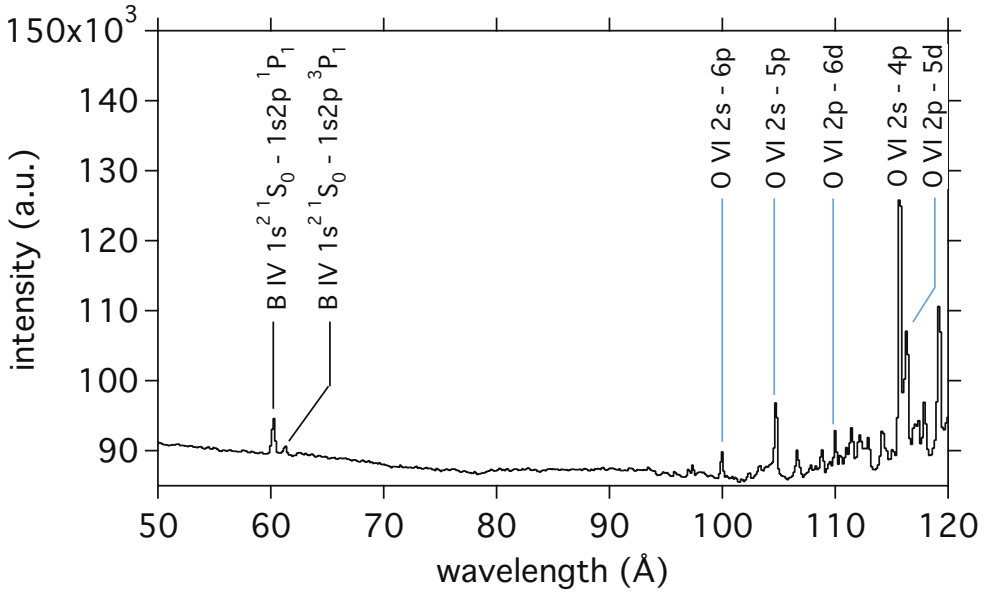

Figure 2. SSPX shot 16644. He-like B IV Kα lines (black) and Li-like O VI (blue).

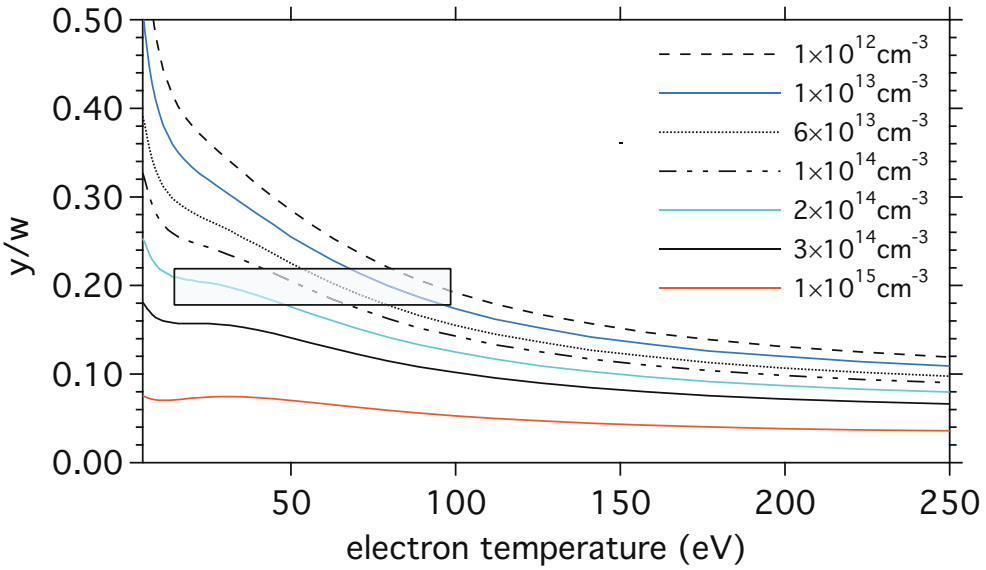

Figure 3. Flexible Atomic Code calculations of the ratio y/w as a function of electron temperature and density. The gray box shows the parameter space for the SSPX B IV emission.

high-energy electrons in the Maxwell-Boltzmann distribution are responsible for the excitation, which explains why these lines are very weak.

3. Summary

Our efforts at the SSPX facility have shown the value of spheromak spectroscopy for the study of atomic spectra believed to be of importance for future large tokamak experiments. We have performed temperature and density measurements employing the relative intensities of He-like spectral lines, and made an inventory of the impurity ions in the SSPX spheromak.

Acknowledgments

This work was performed under the auspices of the U.S. Department of Energy by Lawrence Livermore National Laboratory under contracts W-7405-ENG-48 and DE-AC52-07NA-27344. The authors are grateful for assistance from Jaan Lepson and for technical support from Ed Magee, Phil D'Antonio, and Bob Geer, and to the SSPX group for supporting the project.

References

[1] Stratton B C, Bitter M, Hill K W, Hillis D L and Hogan J T 2008 *Fusion Sci Technol* **53** 431

[2] Wesson J 1997 *Tokamaks* (Oxford University Press)

[3] Wenzel K W 1989 *Measurements of Injected Impurity Transport in TEXT Using Multiply Filtered Soft X-Ray Detectors* Ph.D. thesis Massachusetts Institute of Technology, Plasma Fusion Center

[4] Bitter M, von Goeler S, Suthoff N, Hill K, Brau K, Eames D, Goldman M, Silver E and Stodiek W 1981 *International Conference on X-Ray Processes and Inner-Shell Ionization* ed Fabian D J, Kleinpoppen H and Watson L M p 861

[5] Gabriel A H 1972 *Mon Not R Astr Soc* **160** 99

[6] Gabriel A H and Jordan C 1969 *Mon Not R Astr Soc* **145** 241

[7] Pradhan A K and Shull J M 1981 *Astrophys J* **249** 821

[8] Beiersdorfer P, von Goeler S, Bitter M and Hill K W 1989 *Nucl Instrum Meth Phys B.* **43** 347

[9] Beiersdorfer P 2003 *Ann Rev Astron Astrophys* **41** 343

[10] Wood R D, Hill D N, Hooper E B, McLean H S, Ryutov D and Woodruff S 2005 *J Nucl Mater* **337 − 339** 548

[11] Wood R D, Hill D N, Hooper E B, Woodruff S, McLean H S and Stallard B W 2005 *Nucl Fusion* **45** 1582

[12] Hudson B, McLean H S, Wood R D, Hooper E B, Hill D N, Jayakumar J, Moller J, Romero-Talamas C, Casper T A, Johnson III J A, LoDestro L L, Mezonlin E and Pearlstein L D 2008 *Phys. Plasmas* In press

[13] Wang Z, Wurden G A, Barnes C W, Buchenauer C J, McLean H S, Hill D N, Hooper E B, Wood R D and Woodruff S 2001 *Rev Sci Instrum* **72** 1059

[14] Wood R D, Hill D N, McLean H S, Hooper E B, Hudson B F and Moller J M Submitted to Phys Rev Lett

[15] Graf A T, Brockington S, Horton R, Howard S, Hwang D, Beiersdorfer P, Clementson J, Hill D, May M, McLean H, Wood R, Bitter M, Rice J, Terry J and Rowan W L 2008 *Can J Phys* **86** 307

[16] Beiersdorfer P, Crespo López-Urrutia J R, Springer P, Utter S B and Wong K L 1999 *Rev Sci Instrum* **70** 276

[17] Kita T, Harada T, Nakano N and Kuroda H 1983 *Appl Optic* **22** 512

[18] Fonck R J, Ramsey A T and Yelle R V 1982 *Appl Optic* **21** 2115

[19] Stratton B C, Fonck R J, Ida K, Jaehnig K P and Ramsey A T 1986 *Rev Sci Instrum* **57** 2043

[20] Romero-Talamás C A, Bellan P M and Hsu S C 2004 *Rev Sci Instrum* **75** 2664

[21] Romero-Talamás C A, Hooper E B, Hill D N, Cohen B I, McLean H S, Wood R D and Moller J M 2007 *J Fusion Energ.* **26** 169

[22] Romero-Talamás C A, McLean H S, Hooper E B, Wood R D, LoDestro L L and Moller J M 2007 *J Fusion Energ.* DOI 10.1007/s10894-007-9110-5

[23] Skinner C H 2008 *Can J Phys* **86** 285

[24] Kelly R L 1987 *J Phys Chem Ref Data* **16**

[25] Gu M F 2008 *Can J Phys* **86** 675

[26] McLean H S, Ahmed A, Buchenauer D, Den Hartog D, Domier C W, Hill D N, Holcomb C, Hooper E B, Morse E C, Nagata M, Roh Y, Stallard B, Wood R D, Woodruff S, Wurden G, Wang Z and Team S 2001 *Rev Sci Instrum* **72** 556

Paper IX

Journal of Physics: Conference Series **163** (2009) 012018 doi:10.1088/1742-6596/163/1/012018

Spectroscopy of multiply charged titanium ions in high-density magnetic fusion plasmas

Joel H T Clementson[1,2], Peter Beiersdorfer[1], and Reginald D Wood[1]

[1]Lawrence Livermore National Laboratory, Livermore, California 94550, USA
[2]Atomic Physics Division, Lund Institute of Technology, SE-221 00 Lund, Sweden

E-mail: clementson@llnl.gov

Abstract. The M-shell line emission from multiply charged titanium ions has been investigated at the Sustained Spheromak Physics Experiment in Livermore. Titanium was introduced into the relatively low-temperature, high-density magnetically confined spheromak plasmas using a titanium gettering system. The measurements were done using a high-resolution grazing-incidence spectrometer with a 1200 lines/mm grating and a Photometrics charged-coupled device camera. Spectral lines from the transition array $3s^2 3p^k$ - $3s^2 3p^{k-1} 3d$ in argon-like Ti^{4+}, chlorine-like Ti^{5+}, and sulfur-like Ti^{6+} have been observed in the 240 - 370 Å interval.

1. Introduction

Titanium is a transition element of interest in magnetic confinement fusion (MCF) research. Since 1974 titanium has been used in fusion experiments to reduce impurity concentrations and control hydrogen recycling [1]. As radiation losses have large effects on the energy balance in fusion plasmas, it is of utter importance to reduce ion impurities to be able to heat plasmas to thermonuclear temperatures. Titanium is deposited on plasma-facing surfaces by means of the so-called titanium gettering method. In this process titanium is evaporated inside the MCF vacuum vessel and deposited on the interior surfaces. This way the titanium will not only reduce the impurity concentrations by binding to various gas molecules present in the device, but also by burying impurities on the walls [1].

Ti has been spectroscopically investigated in many MCF experiments. Especially x-ray spectra of the K-shell emission from highly charged titanium ions have been observed in several tokamaks [2, 3, 4, 5, 6, 7], but also EUV measurements have been performed, see e.g. Ref. [8] for observations of strong Ti lines on the Princeton Large Torus (PLT) tokamak. More recently Ti lines have unexpectedly appeared in EUV spectra from the National Spherical Torus Experiment (NSTX), i.e. from plasmas where no Ti gettering is used [9]. The study of titanium spectra in fusion plasmas is also of general interest to better understand the spectra of multiply charged ions from mid-Z elements in both laboratory and astrophysical environments. When the 3p subshell gets partially stripped, starting with chlorine-like ions, the spectra get relatively complex due to the numerous coupling combinations of angular momenta.

Here we have investigated the titanium 3p - 3d M-shell EUV emission at the Sustained Spheromak Physics Experiment (SSPX) [10, 11]. The SSPX spheromak research facility, in operation from 1999 to 2007 at the Lawrence Livermore National Laboratory in California, was a project among innovative confinement concepts in magnetic fusion research, aimed at

investigating the feasibility of spheromaks as potential fusion reactors [12]. Typical electron densities of SSPX plasmas were a few times 10^{14} cm^{-3}, and were thereby denser than most tokamak core plasmas. This made SSPX a good test bed for the study of spectra not readily attainable in other devices. The objective of our investigations was to determine the radiative losses of the spheromak by identifying the impurity ions and their respective charge states present in the plasmas.

2. Measurements

The SSPX spheromak produced toroidal hydrogen plasmas confined in a copper flux conserver coated with tungsten to minimize sputtering of wall material. On the plasma-facing components a 10 nm layer of titanium was deposited by titanium gettering [12]. The titanium deposition effectively helped to reduce the amount of impurity ions, but, as a side effect, also introduced titanium ions into the spheromak plasmas. For our measurements we utilized this as a convenient injection method.

The instrument used for the titanium spectroscopy was a flat-field grating instrument as described in Ref. [13]. Employing a 1200 lines/mm grating, the high-resolution EUV spectrometer achieved a line width of around 0.3 Å full width at half maximum. The spectrometer had a tangential line of sight of the spheromak magnetic axis through the midplane of the toroidal plasmas. The spectra were time-integrated and recorded with a Photometrics charged-coupled device camera.

The spectra were wavelength calibrated using first and second order lines from oxygen ions present in SSPX [14, 15] and lines from the Lyman series in helium, which was puffed into the device to provide reference lines. By analyzing many SSPX shots we could recognize which lines belonged to Ti and which originated from other plasma impurities such as C, N, O, and W.

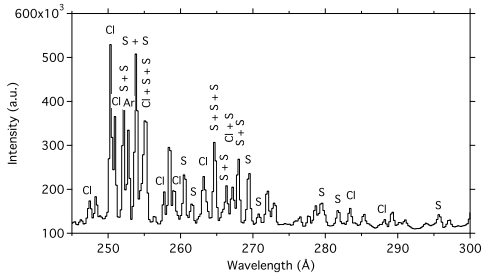

Figure 1. Spectrum from SSPX shot # 18633 showing strong titanium lines labeled according to charge state. Also shown are O V at 248.5 Å, and O IV at 272.1 and 279.8 Å.

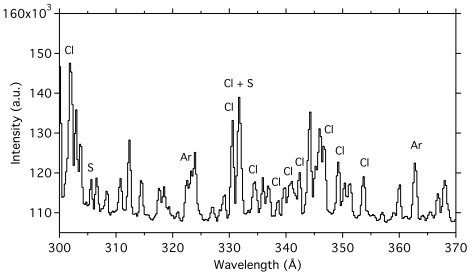

Figure 2. SSPX shot # 18633. Titanium lines, He II at 303.8 Å, C IV at 312.4 Å, and second order lines of O VI at 300.2, 346.0, 368.0 Å and O V at 303.0, 340.4, and 344.4 Å.

3. Results

By studying subsequent discharges after titanium gettering it was clear the strong line emission observed in the 240 - 280 Å interval originated from M-shell titanium ions. The lines were very strong in the first shots after the titanium deposition and got weaker as the Ti wore off the walls during discharges and got pumped out from the vacuum vessel. We have identified strong lines from four times ionized argon-like through six times ionized sulfur-like titanium. The strongest lines are of the $3s^2 3p^k$ - $3s^2 3p^{k-1} 3d$ transition array, which is listed in Table 1. We have used line lists from Kelly [16] and the NIST Atomic Spectra Database [17] to identify the observed features. The listed titanium data are taken from measurements by Svensson and Ekberg 1968 [18] and Svensson 1976 [19].

Ion	Lower level	Upper level	λ (Å)	Ion	Lower level	Upper level	λ (Å)
Ti^{4+}	$3s^23p^6\ ^1S_0$	$3s^23p^5(^2P)3d\ ^1P_1$	253.0	Ti^{6+}	$3s^23p^4\ ^3P_1$	$3s^23p^3(^2P)3d\ ^1D_2$	248.0
	$^1S_0$	$^3D_1$	323.4		$^3P_2$	$^3D_1$	250.9
	$^1S_0$	$^3P_1$	363.1		$^3P_2$	$^3D_2$	252.2
					$^1D_2$	$^1F_3$	252.3
Ti^{5+}	$3s^23p^5\ ^2P_{3/2}$	$3s^23p^4(^1D)3d\ ^2D_{3/2}$	247.5		$^1S_0$	$^1P_1$	252.6
	$^2P_{3/2}$	$^2D_{5/2}$	250.5		$^3P_1$	$^3D_1$	253.8
	$^2P_{1/2}$	$^2D_{3/2}$	251.1		$^3P_2$	$^3D_3$	254.0
	$^2P_{3/2}$	$^2P_{3/2}$	255.4		$^3P_0$	$^3D_1$	254.7
	$^2P_{1/2}$	$^2P_{1/2}$	257.9		$^3P_1$	$^3D_2$	255.1
	$^2P_{1/2}$	$^2P_{3/2}$	259.2		$^1D_2$	$^1D_2$	260.7
	$^2P_{3/2}$	$^2S_{1/2}$	263.2		$^3P_2$	$3s^23p^3(^2D)3d\ ^1P_1$	261.9
	$^2P_{1/2}$	$^2S_{1/2}$	267.3		$^3P_2$	$3s^23p^3(^2P)3d\ ^3P_1$	263.9
	$^2P_{3/2}$	$3s^23p^4(^1S)3d\ ^2D_{5/2}$	282.2		$^3P_2$	$^3P_2$	264.8
	$^2P_{3/2}$	$^2D_{3/2}$	283.6		$^3P_1$	$3s^23p^3(^2D)3d\ ^1P_1$	265.0
	$^2P_{1/2}$	$^2D_{3/2}$	288.4		$^3P_1$	$3s^23p^3(^2P)3d\ ^3P_0$	265.1
	$^2P_{3/2}$	$3s^23p^4(^1D)3d\ ^2F_{5/2}$	301.9		$^3P_0$	$3s^23p^3(^2D)3d\ ^1P_1$	266.0
	$^2P_{3/2}$	$3s^23p^4(^3P)3d\ ^2D_{5/2}$	330.7		$^3P_2$	$^3S_1$	266.5
	$^2P_{3/2}$	$^4P_{1/2}$	331.8		$^3P_1$	$3s^23p^3(^2P)3d\ ^3P_1$	267.1
	$^2P_{3/2}$	$^2D_{3/2}$	334.5		$^3P_1$	$^3P_2$	268.0
	$^2P_{1/2}$	$^4P_{1/2}$	338.3		$^3P_0$	$^3P_1$	268.1
	$^2P_{1/2}$	$^2D_{3/2}$	341.1		$^1D_2$	$^3D_2$	268.5
	$^2P_{3/2}$	$^2P_{3/2}$	342.6		$^3P_1$	$3s^23p^3(^2D)3d\ ^3S_1$	269.8
	$^2P_{3/2}$	$^2P_{1/2}$	346.7		$^3P_0$	$^3S_1$	270.7
	$^2P_{1/2}$	$^2P_{3/2}$	349.6		$^1D_2$	$^1P_1$	279.5
	$^2P_{1/2}$	$^2P_{1/2}$	353.9		$^1D_2$	$3s^23p^3(^2P)3d\ ^3P_1$	281.9
					$^1D_2$	$^3P_2$	282.9
					$^1D_2$	$3s^23p^3(^2D)3d\ ^1F_3$	296.1
					$^1S_0$	$^1P_1$	305.7
					$^1D_2$	$^1D_2$	332.1

Table 1. $3s^23p^{k-1}3d$ resonance transition arrays in Ti^{4+} through Ti^{6+}. All the data are taken from the NIST Atomic Spectra Database [17].

Shown in Figure 1 is a spectrum from SSPX shot # 18633 displaying the strong titanium lines in the 240 - 300 Å interval. In this discharge the charge balance seems to be dominated by the chlorine- and sulfur-like ions, indicating an electron temperature of around 50 - 70 eV. In the spectrum there are additional lines (some that are blended with those from titanium), mainly from oxygen. The Ti^{6+} line at 254.0 Å has previously been observed in the PLT tokamak [8].

The longer wavelengths are shown in Figure 2. The Ti lines are here much weaker and, again, lines from other plasma impurities interfere with the titanium spectra. In this interval several strong lines from O V and O VI appear in second order. The Ti^{5+} line at 338.3 Å has not previously been observed and we use the Ritz wavelength from the NIST database for our identification.

Most of the 3p - 3d transitions listed in Table 1 are observed in SSPX spectra. The identification of a few lines are somewhat uncertain due to line blends. Due to blends and overlapping lines it is a difficult task to determine the intensity of the titanium lines and the

charge state distribution. This is especially true for blends with oxygen lines, which always exist in the spectra. We are planning to further investigate the spectra from higher charge states of titanium present in SSPX as well as to perform collisional radiative modeling of the spheromak plasmas. This will help us better understand the M-shell emission from transition elements in high-density magnetic fusion plasmas.

Acknowledgments

This work was performed under the auspices of the U.S. Department of Energy by Lawrence Livermore National Laboratory under contracts W-7405-ENG-48 and DE-AC52-07NA-27344. The authors would like to thank Dr. Harry McLean for supporting the project, as well as Ed Magee for technical assistance.

References

[1] Braams C M and Stott P E 2002 *Nuclear Fusion - Half a Century of Magnetic Confinement Fusion Research* (Institute of Physics Publishing)
[2] Bely-Dubau F, Faucher P, Steenman-Clark L, Bitter M, von Goeler S, Hill K W, Camhy-Val C and Dubau J 1982 *Phys. Rev. A* **26** 3459–3469
[3] Bitter M, Hill K W, Zarnstorff M, von Goeler S, Hulse R, Johnson L C, Sauthoff N R, Sesnic S and Young K M 1985 *Phys. Rev. A* **32** 3011–3029
[4] Kato T, Morita S and Masai K 1987 *Phys. Rev. A* **36** 795–803
[5] Pacella D and Leigheb Mattioli M 1998 *Phys. Scr.* **57** 265–271
[6] Lee P, Lieber A J and Wojtowicz S S 1985 *Phys. Rev. A* **31** 3996–3998
[7] Lee P, Lieber A J and Chase R P 1985 *Phys. Rev. Lett.* **55** 386–389
[8] Davé J H, Feldman U, Seely J F, Wouters A, Suckewer S, Hinnov E and Schwob J L 1987 *J. Opt. Soc. Am. B* **4** 635–643
[9] Beiersdorfer P, Lepson J K, Bitter M, Hill K W and Roquemore L 2008 *Rev. Sci. Instrum.* **79**
[10] Hooper E B, Pearlstein L D and Bulmer R H 1999 *Nucl. Fusion* **39**
[11] Hudson B, Wood R D, McLean H S, Hooper E B, Hill D N, Jayakumar J, Moller J, Montez D, Romero-Talámas C A, Casper T A, Johnson III J A, LoDestro L L, Mezonlin E and Pearlstein L D 2008 *Phys. Plasmas* **15** 056112
[12] Wood R D, Hill D N, Hooper E B, Buchenauer D, McLean H, Wang Z, Woodruff S and Wurden G 2001 *J. Nucl. Mater.* **290-293** 513–517
[13] Clementson J, Beiersdorfer P and Magee E W 2008 *Rev. Sci. Instrum.* **79**
[14] Clementson J, Beiersdorfer P, Gu M F, McLean H S and Wood R D 2008 *J. Phys. Conf. Ser.* In press
[15] Wilcox P G, Safronova A S, Kantsyrev V L, Safronova U I, Williamson K M, Yilmaz M F, Clementson J, Beiersdorfer P and Struve K W 2008 *Rev. Sci. Instrum.* **79**
[16] Kelly R L 1987 *J. Phys. Chem. Ref. Data* **16**
[17] Ralchenko Y, Kramida A E, Reader J and NIST ASD Team (2008) NIST ASD Atomic Spectra Database (version 3.1.5) [online at http://physics.nist.gov/asd3, august 25 2008]
[18] Svensson L Å and Ekberg J O 1967 *Ark. Fys.* **37** 65–84
[19] Svensson L Å 1976 *Phys. Scr.* **13** 235–239

Paper X

J. Phys. B: At. Mol. Opt. Phys. **43** (2010) 000000 (8pp) UNCORRECTED PROOF

Tungsten spectroscopy relevant to the diagnostics of ITER divertor plasmas

J Clementson[1], P Beiersdorfer, E W Magee, H S McLean and R D Wood

Lawrence Livermore National Laboratory, Livermore, CA 94550, USA

Received 1 December 2009, in final form 25 January 2010
Published DD MMM 2010
Online at stacks.iop.org/JPhysB/43/000000

Abstract
The possibility of using extreme ultraviolet emission from low-charge states of tungsten ions to diagnose the divertor plasmas of the ITER tokamak has been investigated. Spectral modelling of Lu-like W^{3+} to Gd-like W^{10+} has been performed by using the flexible atomic code, and spectroscopic measurements have been conducted at the Sustained Spheromak Physics Experiment (SSPX) in Livermore. To simulate ITER divertor plasmas, tungsten was introduced into the SSPX spheromak by prefilling it with tungsten hexacarbonyl prior to the usual hydrogen gas injection and initiation of the plasma discharge. The tungsten emission was studied using a grazing-incidence spectrometer.

1. Introduction

The divertor of the ITER tokamak will have tungsten target plates. Tungsten ions will sputter off the surfaces of the tiles at the particle strike points and get introduced into the plasma. The divertor plasmas will be relatively cool and have large temperature gradients. According to simulations by the ITER Physics Expert Group on Divertor [1], the electron temperatures will mainly be between 25 and 100 eV with peak temperatures around 150 eV close to the X point. Considering the ionization energies of tungsten, see [2] and table 1, and neglecting transport, a large fraction of the divertor plasmas can therefore be expected to contain tungsten ions in charge states mainly from three to ten times ionized.

The spectroscopic diagnostics considered for the ITER divertor include optical spectrometers and vacuum ultraviolet (VUV) spectrometers with wavelength coverage extending down in the soft x-ray region to 10 Å [3, 4]. As demonstrated in this paper, the 150–450 Å EUV range may offer the best spectral region for monitoring of tungsten in the main divertor volume as the strong resonance lines of several low-charge state tungsten ions fall in this region. However, it should be noted that plasma transport can add higher charge states of tungsten to the divertor that also could radiate in the EUV range, making the emission more complex, see e.g. [5]. Another advantage of the EUV interval is that expected low-Z impurities, such as carbon ions, offer strong *in situ* wavelength calibration lines, which could serve to measure carbon concentrations as well. The abundance of tungsten ions in the divertor is of importance for ITER operations as too large a quantity entering the confined core plasma could affect the plasma stability and ignition because of radiation losses. EUV tungsten spectra would be suitable to infer the concentrations and flow velocities and, given enough resolution, also could be used to measure ion temperatures in the divertor.

To assess where the strong line emission from low-charge states of tungsten occurs, the structure and spectra of W^{3+}–W^{10+} have been calculated using the flexible atomic code (FAC) [6]. The spectra have been modelled under magnetic fusion plasma conditions in the 100–1100 Å spectral range. Synthetic spectra of W^{5+}–W^{16+} in the 100–500 Å region have previously been presented by Peacock *et al* in their review of anticipated x-ray and VUV radiation in ITER [7].

Previously, the spectra of neutral to six times ionized tungsten have been studied [8, 9]. However, little focus has been given on the EUV range (150–450 Å) where, for charge states above four times ionized, strong resonance transitions are expected. The VUV spectrum of trebly ionized Lu-like W IV has been studied down to 673 Å by Iglesias *et al* [10] using a sliding-spark discharge. The spectrum of quadruply ionized tungsten, W V, isoelectronic to ytterbium, was first studied by Meijer using a sliding spark, leading to the identification of lines down to 638 Å [11]. Later studies by Kildiyarova *et al* [12] and Churilov *et al* [13], also using spark sources, observed lines down to 417 and 391 Å, respectively. The sixth spectrum of tungsten, Tm-like W VI, was also first investigated by Meijer [14] and later by Kaufman and Sugar [15, 16] resulting in wavelength measurements down to 382 Å. Sugar and Kaufman also observed Er-like W VII, again using

[1] Also at Department of Physics, Lund University, SE-221 00 Lund, Sweden

Table 1. Tungsten ionization energies (IE). Excerpt from Kramida and Reader [2].

Ion	IE (eV)	Ion	IE (eV)
Neutral W	7.864	Ho-like W^{7+}	141.2
Ta-like W^{+}	16.37	Dy-like W^{8+}	160.2
Hf-like W^{2+}	26.0	Tb-like W^{9+}	179.0
Lu-like W^{3+}	38.2	Gd-like W^{10+}	208.9
Yb-like W^{4+}	51.6	Eu-like W^{11+}	231.6
Tm-like W^{5+}	64.77	Sm-like W^{12+}	258.2
Er-like W^{6+}	122.01	Pm-like W^{13+}	290.7

a sliding spark, and their measurement yielded wavelengths down to 130 Å [17]. Wyart *et al* re-examined those spectra and identified a number of lines in the 316–345 Å range [18]. A low-resolution observation of Ho-like W VIII in a tokamak plasma by Veres *et al*, indicated emission around 190 and 235 Å [19]. The spectra of higher charge states have, to our knowledge, not been investigated in any wavelength band until the tentative identification of 13 times ionized Pm-like W XIV, which Hutton *et al* may have observed at the Berlin electron-beam ion trap [20–22]. With the exception of Er-like W VII, low-charge tungsten spectra have not been studied in the EUV.

To simulate tungsten emission from ITER divertor plasmas, hydrogen discharges with trace amounts of tungsten have been produced at the Sustained Spheromak Physics Experiment facility (SSPX) at the Lawrence Livermore National Laboratory [23–25]. The SSPX spheromak, which was decommissioned in 2007, had plasma conditions comparable to those expected in the ITER divertor, with typical electron temperatures of around 100 eV and densities in the 10^{14-15} cm^{-3} range. The tungsten emission from SSPX plasmas can hence be assumed similar to those of the future ITER divertor or other magnetic fusion experiments operating in this low-temperature, high-density regime. The SSPX plasmas contained trace amounts of tungsten resulting from the usage of tungsten as a plasma-facing material coating the flux conserver. In addition to this intrinsic tungsten, a novel sublimation injector was constructed to increase the concentration of tungsten impurity ions in the spheromak plasmas. These tungsten-doped plasmas were studied spectroscopically using a 5.6 m grazing-incidence EUV spectrometer.

2. Spectral modelling

Based on ionization energies, the tungsten ions that can be expected to dominate the charge balance in the main plasma volume of the ITER divertor are Lu-like W^{3+} up to around Gd-like W^{10+}, see table 1. The spectra of these tungsten charge states have been calculated to guide the spheromak measurement and assess in which wavelength range the strong transitions occur. Some of these spectra have been studied experimentally in the past; however, those studies have been done at densities different than those found in magnetic fusion plasmas and, as such, line intensities can be quite different.

The calculations were performed using the flexible atomic code, FAC v1.1.1., written by Gu [6]. The structure of the ions was calculated with closed K, L and M shells. Depending on spectral complexity, different numbers of energy levels and configuration interactions were included. Considered transitions comprise those involving ground configurations with valence electrons in $n = 5$, and excited configurations with one electron excited from the 4f subshell to $n = 5$ or 6, and electrons excited within the $n = 5$ shell or from $n = 5$ to $n = 6$. These multi-electron spectra are quite difficult to calculate with any accuracy because configuration interaction effects are large, as noted by Sugar and Kaufman for Er-like W VII [17]. Comparisons with known line positions of W VII indicate that the calculated wavelengths are within 20 Å of the measured values. To aid the spectral analysis of the SSPX data, the low-Z impurity species were also calculated, i.e. carbon, nitrogen and oxygen. These systems were modelled with levels up to $n = 5$. Here, comparisons with known line positions listed by Kelly [26] show that most calculated line positions are within 10 Å of the experimental wavelengths.

The spectra were modelled at various electron temperatures and densities in order to have reference spectra from which to infer the SSPX temperatures. Spectra were calculated at densities of 10^{14} and 10^{15} cm^{-3}, but very little difference on the emission signatures was seen. However, as expected, the temperature had a strong effect and the spectra were therefore calculated in the 25–200 eV interval. The collisional-radiative spectral models include collisional excitation and de-excitation and autoionization. An overview of the calculated tungsten spectra is shown in figure 1 for $T_e = 100$ eV. It is clear that for charge states above four times ionized, Yb-like W V, the strong line radiation falls in the EUV region. It is also worth noting that the emissivities drop to very low values for ions above Ho-like W VIII, which means that for ITER divertor plasmas it is likely that only the very low-charge states will be of interest for spectroscopic diagnostics. The spectra of Tm-like W VI, Er-like W VII and Ho-like W VIII are presented in greater detail in figure 2, where they are modelled in the 150–450 Å range at various temperatures with a resolution of $\Delta\lambda = 0.3$ Å full width at half-maximum (FWHM). The low-Z reference spectra at $T_e = 50$ eV are also presented, see figures 3–5. All presented spectra are calculated at $n_e = 10^{14}$ cm^{-3}.

3. Experimental setup

The tungsten study was performed at the SSPX spheromak facility, a small-size fusion experiment in Livermore [23–25]. The SSPX device produced self-organized toroidal plasmas lasting a few milliseconds. The tungsten was injected into the magnetically confined plasmas in the form of tungsten hexacarbonyl, $W(CO)_6$, a crystalline compound that also has been introduced into the Livermore SuperEBIT electron-beam ion trap for spectroscopic investigations of highly charged tungsten ions [27, 28]. Here, 5 g of tungsten hexacarbonyl was placed in a 1 l volume, which had been cleaned and purged with nitrogen gas. The volume and assembly were first

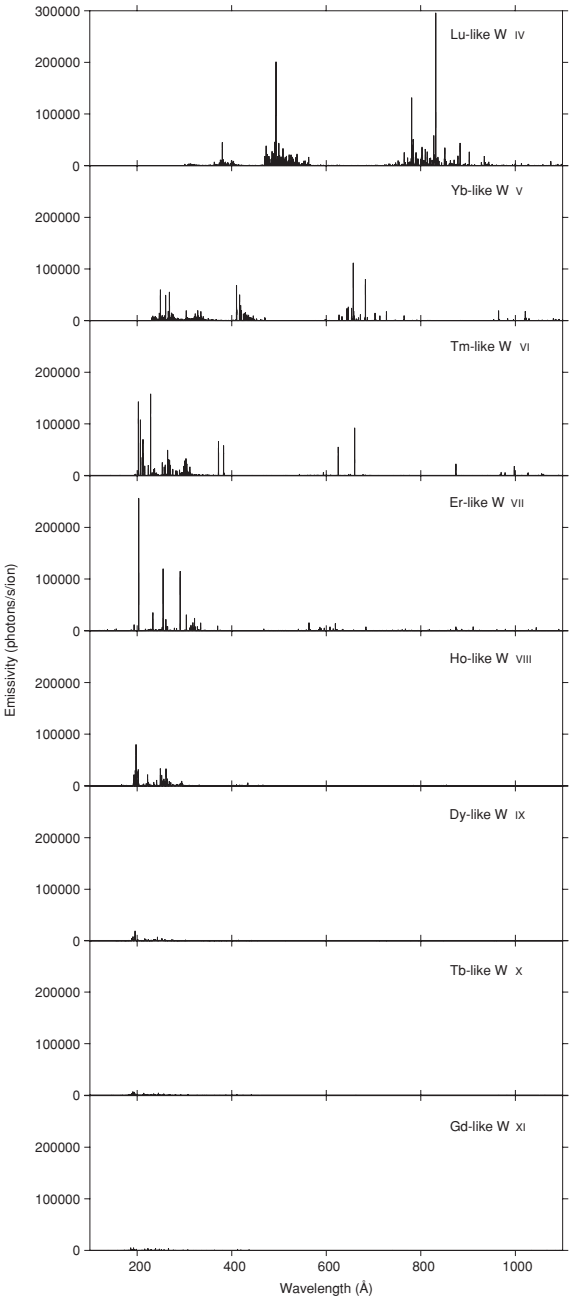

Figure 1. Calculated tungsten spectra at $T_e = 100$ eV and $n_e = 10^{14}$ cm^{-3}. The emissivity scale is set to the same value for each charge state in order to provide a direct comparison of the expected line intensities.

evacuated to approximately 10^{-5} Torr and then heated using wrapped heater tapes. The pressure increase was monitored with a vacuum gauge and pressures were varied from 0.1 to 2 Torr by changing the temperature, which was recorded with a thermocouple. The tungsten hexacarbonyl volume, which was connected to a view port of SSPX, was opened during the hydrogen prefill phase approximately 0.5 s prior to the discharge. As the tungsten gas pressures were higher than the SSPX vacuum vessel pressure, the vapour could easily stream through a solenoid-controlled valve into the spheromak.

A high-resolution grazing-incidence spectrometer was used to study the tungsten emission. The same instrument has previously been used to study titanium and low-Z plasma impurities on SSPX [29–32] and is described in detail in [33]. For this experiment, the spectrometer was equipped with a photometrics back-illuminated charge-coupled device (CCD) detector and a 30 μm entrance slit. With a field of view tangential to the magnetic axis of the spheromak, the observed emission originated from the cooler edge across to the hottest part at the centre of the plasma.

The spheromak plasmas were studied with and without tungsten injection to support the line identification process. The toroidal plasma current was used to change the electron temperature. Record peak temperatures at SSPX have been noted to exceed 500 eV [24]; however, for this experiment the temperatures were likely in the 25–100 eV range. As the Thomson-scattering electron-temperature diagnostic was offline, the plasma temperatures had to be inferred from the calculated spectra. The injection of tungsten into SSPX did not appear to have any negative effect on the spheromak performance, and plasma currents of up to around 1 MA were achieved during the few millisecond discharges.

4. Analysis and results

Figures 6–8 show SSPX spectra in three regions where tungsten lines appear. The spectra were wavelength calibrated *in situ* using L shell lines from carbon and oxygen. These lines, which also became enhanced during injection of tungsten hexacarbonyl, were observed in first and second orders. Spectra were also observed from helium, nitrogen, titanium and copper. The spectral lines were identified using the calculated spectra for line intensities and line lists from Kelly [26] for line positions. Even though the calculated wavelengths varied slightly from the measured positions, the intensities generally agreed well with the observed spectra. Lines that did not match any known spectra were likely candidates for being tungsten lines. Additionally, tungsten line identification was aided by the fact that the amounts of injected tungsten changed the observed spectra. Identified tungsten lines are listed in table 2, and unclassified candidate tungsten lines are listed in table 3.

The tungsten emission is dominated by Er-like W VII, which shows in most spectra. The Er-like lines are identified based on the classifications by Sugar and Kaufman [17]. However, the line intensities given by Sugar and Kaufman do not agree with the observed SSPX intensities, which is likely due to the different densities of the emitting plasmas. For example, in Sugar and Kaufman's line list the strongest EUV line is the 261 Å line, which is six times stronger than the 216 Å line. In the SSPX spectra, the 216 Å line is generally the strongest line followed by the 261 Å line. Sugar and Kaufman list the 302 Å line and the 188 Å line to be about

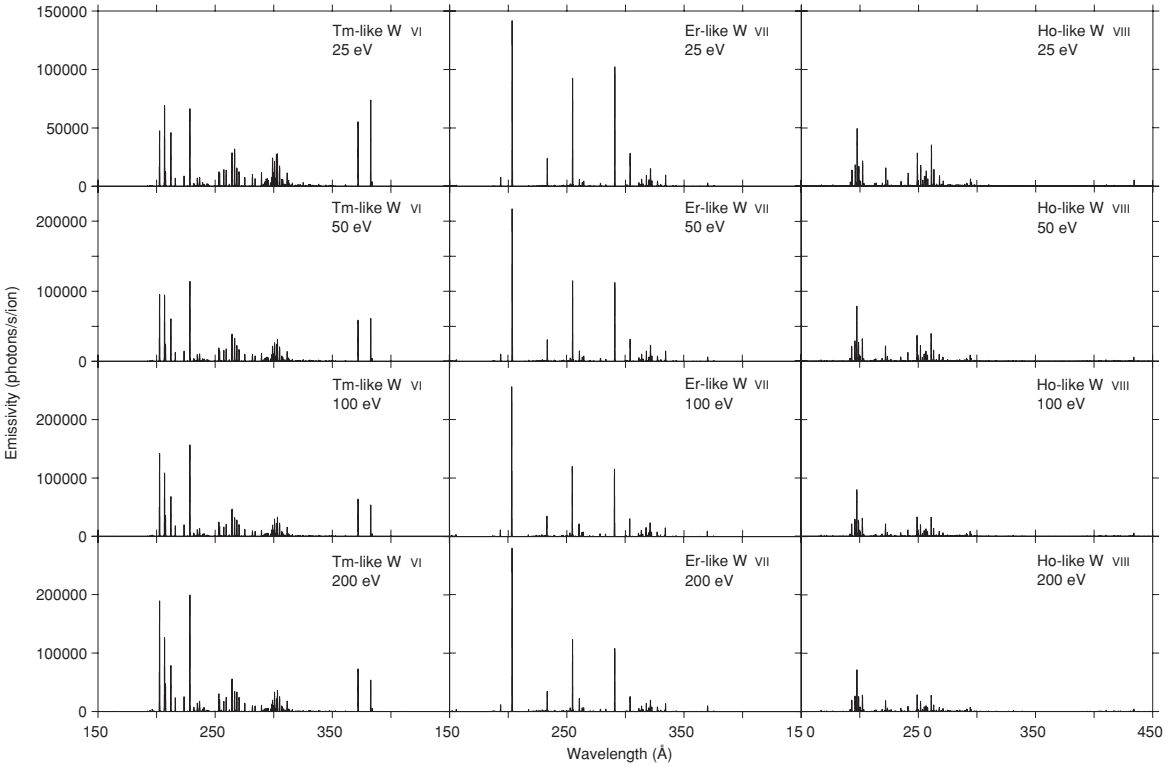

Figure 2. Calculated tungsten spectra at $n_e = 10^{14}$ cm^{-3} with $\Delta\lambda = 0.3$ Å fwhm. The spectra are labeled according to charge state and electron temperature.

Table 2. Observed tungsten lines in the SSPX spheromak.

Ion	Experiment λ (Å)	Prev. Exp. λ (Å)	Theory λ (Å)	Transition lower level	upper level
W^{6+}	188.15	188.159[a]	193.4	$(4f^{14}5s^25p^6)_0$	$(4f^{14}5s^25p_{1/2}5p^4_{3/2}6s_{1/2})_1$
W^{6+}	216.19	216.219[a]	203.2	$(4f^{14}5s^25p^6)_0$	$(4f^{14}5s^25p_{1/2}5p^4_{3/2}5d_{3/2})_1$
W^{6+}	223.82	223.846[a]	233.2	$(4f^{14}5s^25p^6)_0$	$(4f^{14}5s^25p^2_{1/2}5p^3_{3/2}6s_{1/2})_1$
W^{6+}	261.35	261.387[a]	254.9	$(4f^{14}5s^25p^6)_0$	$(4f^{14}5s^25p^2_{1/2}5p^3_{3/2}5d_{5/2})_1$
W^{6+}	289.44	289.526[a]	301.2	$(4f^{14}5s^25p^6)_0$	$(4f^5_{5/2}4f^8_{7/2}5s^25p^65d_{5/2})_1$
W^{6+}	294.37	294.376[a]	290.9	$(4f^{14}5s^25p^6)_0$	$(4f^5_{5/2}4f^8_{7/2}5s^25p^65d_{3/2})_1$
W^{6+}	302.28	302.272[a]	320.0	$(4f^{14}5s^25p^6)_0$	$(4f^6_{5/2}4f^7_{7/2}5s^25p^65d_{5/2})_1$
W^{6+}	313.64	313.573[a]	303.9	$(4f^{14}5s^25p^6)_0$	$(4f^{14}5s^25p^2_{1/2}5p^3_{3/2}5d_{3/2})_1$
W^{5+}	382.12	382.145[b]	371.9	$(4f^{14}5s^25p^65d_{3/2})_{3/2}$	$(4f^{14}5s^25p^65f_{5/2})_{5/2}$
W^{5+}	394.08	394.133[b]	382.7	$(4f^{14}5s^25p^65d_{5/2})_{5/2}$	$(4f^{14}5s^25p^65f_{7/2})_{7/2}$

[a] Sugar and Kaufman [17]
[b] Kaufman and Sugar [15, 16]

50 % more intense than the 216 line. Both these lines, however, are weaker in the SSPX spectra. The 289 Å line overlaps with a carbon line prohibiting a clear determination of its intensity, which according to the modelling should be very low. The 294 Å line is weaker and the 302 Å line much stronger than the calculations suggest. It is possible that the stronger intensity of the 302 Å line is due to a line blend. However, as noted earlier, these spectra are difficult to predict and even though Er-like W VII, with its closed shell structure, should be the easiest to calculate, it is quite possible that the calculated spectra are not that accurate. The line at 313 Å is slightly off the value given by Sugar and Kaufman [17], which could mean that it is blended, too. Some of the lines identified by Wyart *et al* [18] possibly show around 330–340 Å as weak features.

Table 3. Candidate tungsten transitions in the SSPX spheromak.

Ion	Transition lower level	Upper level	Theory λ (Å)	Exp. candidate lines λ (Å)
W^{7+}	$(4f^{14}5s^25p^2_{1/2}5p^3_{3/2})_{3/2}$	$(4f^{14}5s^25p_{1/2}5p^3_{3/2}5d_{3/2})_{3/2}$	193.2	194.5, 198.0, 198.8
W^{7+}	$(4f^{14}5s^25p^2_{1/2}5p^3_{3/2})_{3/2}$	$(4f^{14}5s^25p_{1/2}5p^3_{3/2}5d_{3/2})_{1/2}$	195.9	198.0, 198.8, 200.5
W^{7+}	$(4f^{14}5s^25p^2_{1/2}5p^3_{3/2})_{3/2}$	$(4f^{14}5s^25p_{1/2}5p^3_{3/2}5d_{3/2})_{5/2}$	197.5	201.8
W^{7+}	$(4f^{14}5s^25p_{1/2}5p^4_{3/2})_{1/2}$	$(4f^{14}5s^25p^4_{3/2}5d_{3/2})_{3/2}$	199.0	198.0, 198.8, 200.5, 205.3
W^{7+}	$(4f^{14}5s^25p^2_{1/2}5p^3_{3/2})_{3/2}$	$(4f^{14}5s^25p_{1/2}5p^3_{3/2}5d_{3/2})_{3/2}$	202.3	200.5, 205.3, 208.0
W^{5+}	$(4f^{14}5s^25p^65d_{3/2})_{3/2}$	$(4f^{14}5s^25p_{1/2}5p^4_{3/2}5d^2_{3/2})_{3/2}$	202.5	198.0, 198.8, 200.5, 201.8, 205.3, 208.0
W^{5+}	$(4f^{14}5s^25p^65d_{5/2})_{5/2}$	$(4f^{14}5s^25p_{1/2}5p^4_{3/2}5d_{3/2}5d_{5/2})_{5/2}$	206.7	205.3, 208.0, 211.0
W^{5+}	$(4f^{14}5s^25p^65d_{5/2})_{5/2}$	$(4f^{14}5s^25p_{1/2}5p^4_{3/2}5d_{3/2}5d_{5/2})_{3/2}$	206.9	205.3, 208.0, 210.2, 211.0
W^{5+}	$(4f^{14}5s^25p^65d_{5/2})_{5/2}$	$(4f^{14}5s^25p_{1/2}5p^4_{3/2}5d_{3/2}5d_{5/2})_{7/2}$	212.2	205.3, 208.0, 210.2, 211.0
W^{7+}	$(4f^{14}5s^25p_{1/2}5p^4_{3/2})_{1/2}$	$(4f^{14}5s^25p_{1/2}5p^3_{3/2}5d_{5/2})_{1/2}$	222.0	211.0, 218.4, 229.8
W^{5+}	$(4f^{14}5s^25p^65d_{3/2})_{3/2}$	$(4f^{14}5s^25p_{1/2}5p^4_{3/2}5d^2_{3/2})_{5/2}$	228.4	218.4, 229.8, 240.0, 241.8
W^{7+}	$(4f^{14}5s^25p^2_{1/2}5p^3_{3/2})_{3/2}$	$(4f^{14}5s^25p^2_{1/2}5p^2_{3/2}5d_{5/2})_{5/2}$	249.0	253.7, 254.3, 255.4, 259.3
W^{7+}	$(4f^{14}5s^25p^2_{1/2}5p^3_{3/2})_{3/2}$	$(4f^{14}5s^25p^2_{1/2}5p^2_{3/2}5d_{5/2})_{3/2}$	251.8	253.7, 254.3, 255.4, 259.3
W^{6+}	$(4f^5_{5/2}4f^8_{7/2}5s^25p^65d_{3/2})_1$	$(4f^5_{5/2}4f^8_{7/2}5s^25p^65f_{5/2})_0$	260.6	259.3, 276.2
W^{7+}	$(4f^{14}5s^25p^2_{1/2}5p^3_{3/2})_{3/2}$	$(4f^5_{5/2}4f^8_{7/2}5s^25p^2_{1/2}5p^3_{3/2}5d_{3/2})_{3/2}$	261.0	253.7, 254.3, 255.4, 259.3, 276.2
W^{7+}	$(4f^{14}5s^25p^2_{1/2}5p^3_{3/2})_{3/2}$	$(4f^6_{5/2}4f^7_{7/2}5s^25p^2_{1/2}5p^3_{3/2}5d_{5/2})_{5/2}$	263.1	253.7, 254.3, 255.4, 259.3, 276.2
W^{6+}	$(4f^{14}5s^25p^2_{1/2}5p^3_{3/2}5d_{5/2})_1$	$(4f^{14}5s^25p^2_{1/2}5p^3_{3/2}5f_{7/2})_2$	370.1	376.3

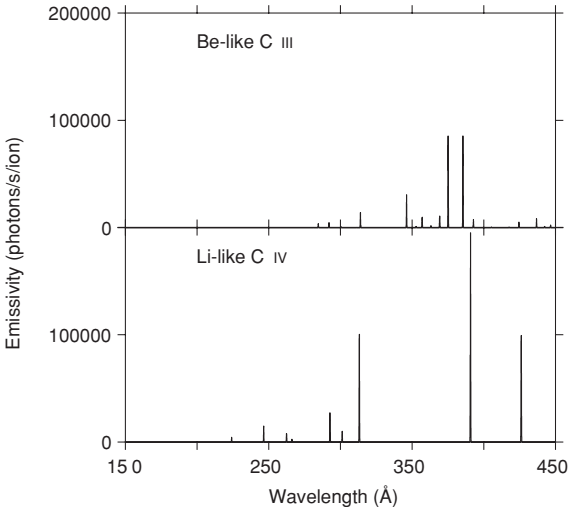

Figure 3. Calculated carbon spectra at $T_e = 50$ eV and $n_e = 10^{14}$ cm^{-3} with $\Delta\lambda = 0.3$ Å FWHM.

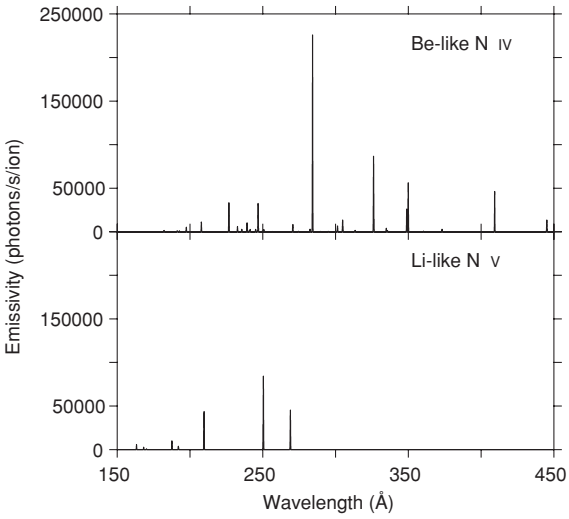

Figure 4. Calculated nitrogen spectra at $T_e = 50$ eV and $n_e = 10^{14}$ cm^{-3} with $\Delta\lambda = 0.3$ Å FWHM.

Based on the calculations, two groups of lines are believed to originate mainly from Ho-like W VIII. Ho-like W has previously been observed in a tokamak plasma at around 190 and 235 Å by Veres *et al* [19]. However, the features at around 202 and 255 Å in the SSPX spectra are shifted towards longer wavelengths relative to the tokamak spectrum. No reference lines were shown or discussed in [19], and a possible explanation of the shift could therefore be that their tokamak spectrometer had not been sufficiently calibrated.

Two 5d–5f transitions from Tm-like W VI are observed at 382 and 394 Å. Those are the shortest wavelengths previously measured in Tm-like W [15, 16]. The FAC calculations give several isolated Tm-like W lines in the EUV region, especially in the 200–240 Å range. These are not easy to identify, because there are plenty of lines in this region, including the Ho-like W candidate lines, and the calculations are not accurate enough to identify individual lines. The calculated

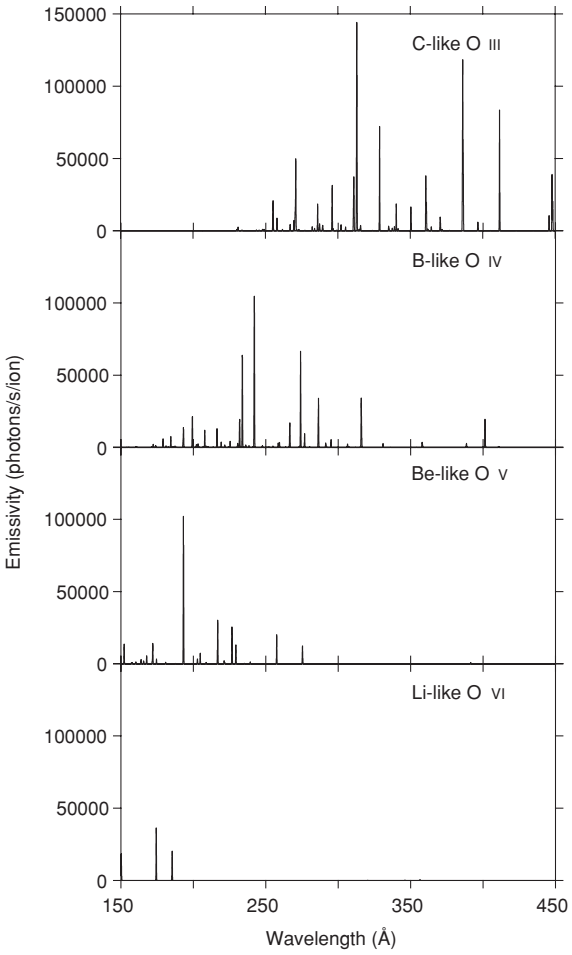

Figure 5. Calculated oxygen spectra at $T_e = 50$ eV and $n_e = 10^{14}$ cm^{-3} with $\Delta\lambda = 0.3$ Å FWHM.

lines can be both longer and shorter than the true line positions, and therefore the relative positions of the calculated lines may change. The Tm-like candidate lines could be blended or interchanged with the Ho-like W candidate lines. Since many of the tungsten ions have several transitions around 200 Å, it is also possible that contributions from other charge states are blending with the candidate lines, in addition to the intrinsic impurity ions. Several tungsten candidate lines, however, have been identified. These lines are designated with red labels in the spectra. Based on the calculations, suggested candidate transitions are listed in table 3 with suggested line positions. Considering the agreement with the Er-like W lines, it is likely that the calculated wavelengths are within 20 Å of the actual values.

5. Summary

The tungsten emission from the SSPX plasmas is dominated by Er-like W VII with likely contributions from Tm-like W VI and Ho-like W VIII. The prevalence of Er-like W is due to the closed $4f^{14}5s^25p^6$ ground configuration, making the ion abundant over a large temperature interval and concentrating the emission into a few strong lines. The fact that Er-like W has strong isolated lines makes it very suitable for plasma diagnostics, especially to infer tungsten concentrations, ion temperatures and flow velocities.

However, even though the SSPX plasmas only show three charge states, it is quite possible that transport can affect the charge balance to look somewhat different in the ITER divertor. As indicated by the FAC calculations, the 150–450 Å spectral band contains strong emission from several charge states. Accurate atomic data on these ions will be necessary in order to realize tungsten spectroscopy in this wavelength regime as a viable divertor diagnostic. Although tungsten line positions can be determined from tungsten-doped plasmas, unambiguous line identifications can prove difficult as lines from neighbouring charge states often seem to be close and may even overlap, as our measurements have shown. In order to disentangle the emission and analyse relative line intensities, we are planning to extend this investigation at the Livermore low-energy electron-beam ion trap where there is more control over the ionization balance and the excitation processes [34, 35].

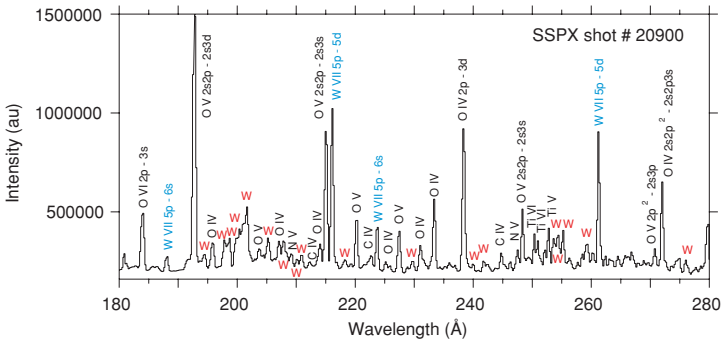

Figure 6. SSPX shot no. 20900. Low-temperature spheromak plasma with tungsten hexacarbonyl injection. Tungsten lines are designated with blue labels and tungsten candidate lines with red labels. Also shown are lines from carbon, nitrogen, oxygen and titanium.

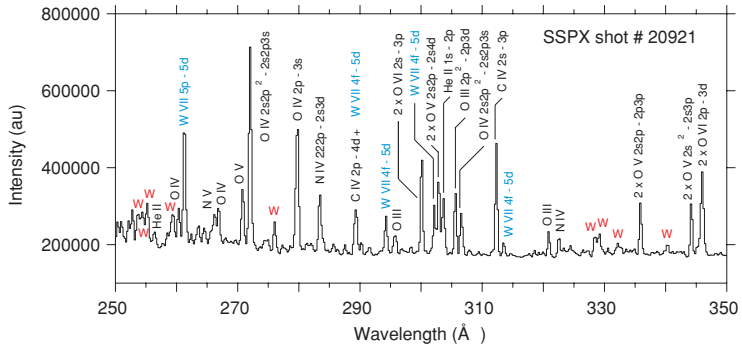

Figure 7. SSPX shot no. 20921. Low-temperature spheromak plasma with tungsten hexacarbonyl injection. Tungsten lines are designated with blue labels and tungsten candidate lines with red labels. Also shown are lines from helium, carbon, nitrogen and oxygen.

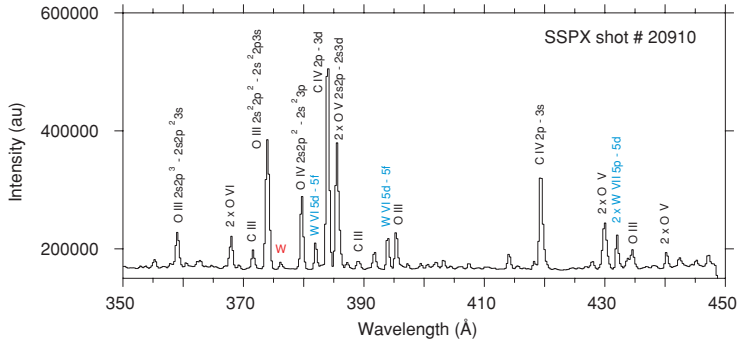

Figure 8. SSPX shot no. 20910. Low-temperature spheromak plasma with tungsten hexacarbonyl injection. Tungsten lines are designated with blue labels and tungsten candidate lines with red labels. Also shown are lines from carbon, nitrogen and oxygen.

Acknowledgments

This work was performed under the auspices of the United States Department of Energy by Lawrence Livermore National Laboratory under contract DE-AC52-07NA-27344. The authors would like to acknowledge technical, experimental and theoretical support from Bob Geer, Rick Kemptner, Steven Gordon, Josh King, Dr Ming Feng Gu and the SSPX group. Joel Clementson would like to thank Dr Hans Lundberg, Dr Sven Huldt and Professor Sune Svanberg for their support.

References

[1] ITER Physics Expert Group on Divertor 1999 *Nucl. Fusion* **39** 2391–469
[2] Kramida A E and Reader J 2006 *At. Data Nucl. Data Tables* **92** 457–79
[3] Sugie T, Costley A, Malaquias A and Walker C 2003 *J. Plasma Fusion Res.* **79** 1051–61
[4] Skinner C H 2008 *Can. J. Phys.* **86** 285–90
[5] Pütterich T, Neu R, Dux R, Whiteford A D and O'Mullane M G the ASDEX Upgrade Team 2008 *Plasma Phys. Control. Fusion* **50** 085016
[6] Gu M F 2008 *Can. J. Phys.* **86** 675–89
[7] Peacock N J, O'Mullane M G, Barnsley R and Tarbutt M 2008 *Can. J. Phys.* **86** 277–84
[8] Kramida A E and Shirai T 2006 *J. Phys. Chem. Ref. Data* **35** 423–683
[9] Kramida A E and Shirai T 2009 *At. Data Nucl. Data Tables* **95** 305–474
[10] Iglesias L, Kaufman V, Garcia-Riquelme O and Rico F R 1985 *Phys. Scr.* **31** 173–83
[11] Meijer F G 1986 *Physica* C **141** 230–6
[12] Kildiyarova R R, Churilov S S and Joshi Y N 1996 *Phys. Scr.* **53** 454–60
[13] Churilov S S, Kildiyarova R R and Joshi Y N 1996 *Can. J. Phys.* **74** 145–9
[14] Meijer F G 1974 *Physica* **73** 415–20
[15] Kaufman V and Sugar J 1976 *J. Opt. Soc. Am.* **66** 1019–25
[16] Sugar J and Kaufman V 1979 *J. Opt. Soc. Am.* **69** 141–3
[17] Sugar J and Kaufman V 1975 *Phys. Rev.* A **12** 994–1012
[18] Wyart J F, Kaufman V and Sugar J 1981 *Phys. Scr.* **23** 1069–78
[19] Veres G, Bakos J S and Kardon B 1996 *J. Quant. Spectrosc. Radiat. Transfer* **56** 295–301
[20] Hutton R, Zou Y, Reyna Almandos J, Biedermann C, Radtke R, Greier A and Neu R 2003 *Nucl. Instrum. Methods Phys. Res.* B **205** 114–8
[21] Wu S and Hutton R 2008 *Can. J. Phys.* **86** 125–9
[22] Träbert E, Vilkas M J and Ishikawa Y 2009 *J. Phys. Conf. Ser.* **163** 012017
[23] Hooper E B, Pearlstein L D and Bulmer R H 1999 *Nucl. Fusion* **39** 863–71
[24] Hudson B *et al* 2008 *Phys. Plasmas* **15** 056112

[25] Wood R D, Hill D N, Hooper E B, Woodruff S, McLean H S and Stallard B W 2005 *Nucl. Fusion* **45** 1582–8
[26] Kelly R L 1987 *J. Phys. Chem. Ref. Data* **16** 1
[27] Clementson J, Beiersdorfer P, Brown G V and Gu M F 2010 *Phys. Scr.* **81** 015301
[28] Clementson J, Beiersdorfer P and Gu M F 2010 *Phys. Rev.* A **Q2** at press
[29] Graf A T *et al* 2008 *Can. J. Phys.* **86** 307–13
[30] Clementson J, Beiersdorfer P, Gu M F, McLean H S and Wood R D 2008 *J. Phys. Conf. Ser.* **130** 012004
[31] Clementson J H T, Beiersdorfer P and Wood R D 2009 *J. Phys. Conf. Ser.* **163** 012018
[32] Wilcox P G, Safronova A S, Kantsyrev V L, Safronova U I, Williamson K M, Yilmaz M F, Clementson J, Beiersdorfer P and Struve K W 2008 *Rev. Sci. Instrum.* **79** 10F543
[33] Clementson J, Beiersdorfer P and Magee E W 2008 *Rev. Sci. Instrum.* **79** 10F538
[34] Beiersdorfer P 2008 *Can. J. Phys.* **86** 1–10
[35] Marrs R E 2008 *Can. J. Phys.* **86** 11–8